

2D Electron Systems in Undoped GaAs and InGaAs and Progress Towards Undoped GaAs Nano-Structures



Benjamin David Ramsay

Churchill College



UNIVERSITY OF
CAMBRIDGE

2020 February

A dissertation submitted for the degree of Doctor of Philosophy

DECLARATION

This thesis is the result of my own work and includes nothing which is the outcome of work done in collaboration except as declared in the Preface and specified in the text. It is not substantially the same as any that I have submitted, or, is being concurrently submitted for a degree or diploma or other qualification at the University of Cambridge or any other University or similar institution except as declared in the Preface and specified in the text. I further state that no substantial part of my thesis has already been submitted, or, is being concurrently submitted for any such degree, diploma or other qualification at the University of Cambridge or any other University or similar institution except as declared in the Preface and specified in the text. It does not exceed the prescribed word limit for the relevant Degree Committee

SUMMARY

2D Electron Systems in Undoped GaAs and InGaAs and Progress Towards Undoped GaAs Nano-Structures

Benjamin David Ramsay

The MBE growth of high-quality GaAs/AlGaAs epilayer structures has enabled the study of novel physical phenomena, such as the Quantum Hall and Fractional Quantum Hall in a 2D electron system (2DES), 1D transport, and single-electron transport in 0D systems. The wide range of systems that can be studied all start with a 2DES from which 1D and 0D systems are formed by further confining the carrier gas.

Undoped devices, which use an externally applied electric field to form a potential well for carriers, replicating the effect of dopants in a doped device, can have higher carrier mobilities and a lower charge impurity background than doped devices. This gives them advantages in specific applications such as nano-structures where charge impurities can prevent the device functioning and examining the condition of the MBE system used to grow the material. Because dopants are not needed in undoped devices, material systems where dopants are difficult to work with due to contamination of growth system or causing significant disorder resulting in low carrier mobility can be studied using undoped devices, sidestepping these difficulties.

In this thesis, undoped AlGaAs/GaAs wafers allow the fabrication of 2D electron system (2DES) for n-type, p-type and ambipolar devices for studying the Quantum Hall effect in the $\text{Al}_{0.33}\text{Ga}_{0.67}\text{As}$ and $\text{In}_{0.1}\text{Ga}_{0.9}\text{As}$ material systems. The Quantum Hall effect for electrons and holes in a $\text{In}_{0.1}\text{Ga}_{0.9}\text{As}$ quantum well showed remarkable different behaviour to GaAs quantum wells despite the low indium content.

Undoped devices have their own fabrication challenges and needed optimisation to produce n-type, p-type, and ambipolar, heterostructures and quantum wells with high enough yields of 2DES that 1D and 0D systems can be fabricated with a reasonable success rate. Functioning 1D p-type channels demonstrate the successful fabrication of undoped nano-structures.

The carrier mobility in undoped devices is limited by unintentional dopants included in the structure during growth. This means that the carrier mobility is a measure of the ‘cleanliness’ of the MBE growth system. From the carrier mobility-density curve shapes the dopant source of disorder in the structure can be determined allowing for feedback on the condition of MBE system, not possible with other device and techniques.

ACKNOWLEDGEMENTS

Firstly, I would like to thank my supervisor Prof David Ritchie for offering me a PhD as one of his students, and his continuing support during my PhD. I would like to acknowledge funding from the UK Engineering and Physical Sciences Research Council (EPSRC). Secondly I would like to thank the members of the SP group: Dr Harvey Beere and Dr James Aldous for the wafers they grew and entrusted to me to play with. Melanie Tribble, Matt Pluck and Abbie Lowe for their hard work and efforts to keep the cleanroom running. Jon Griffiths and Tom Mitchell for e-beam patterning. Dr Chong Chen for advise about InGaAs. Shakeel Fernandes and James Dann for general discussions and listening to me complain when things weren't behaving themselves. To all the people who came to tea for the many varied discussions over the years.

In particular, I must thank Dr Joanna Waldie who first got me interested in undoped GaAs/AlGaAs systems. Despite having her own research to conduct, as well as being incredibly generous with her time, skills and knowledge with everyone one she worked with, Joanna was always around and happy to offer encouragement and advice, no matter how foolish the question. Even after moving across the country and starting a new job, Joanna has always been just an email away. Joanna, despite your teasing about how long I've taken to write this thesis, it is not an exaggeration to say I would not have completed this thesis without your support. Thank you.

Finally I am grateful to my family for their encouragement. And to my wife, Madeline, thank you for everything...

CONTENTS

Declaration	iii
Summary	v
Acknowledgements	vii
Contents	ix
Presentations	xiii
Glossary	xv
1 Introduction	1
2 Background and Motivation	5
2.1 2D Electron Systems Background	5
2.2 GaAs Transport Structures	10
2.3 Undoped AlGaAs/GaAs Structures	15
2.4 InGaAs	20
2.5 Quantum Point Contacts and Quantum Dots	20
3 Undoped Heterostructure	25
3.1 Intrinsic High Electron Mobility Transistor (iHEMT)	26
3.2 Using iHEMT for Optimising MBE Growth Conditions	30
3.3 iHEMT MBE Growth Variation	40
3.4 Variation Due to Cool-down	50
3.5 Carrier Density Limit	52
3.6 Conclusions	57
4 Optimisation of Fabrication	59
4.1 Changes to previous fabrication methods	60
4.2 Contact Resistance Measurement Using ITLM	72
4.3 Surface Charge Passivisation	78
4.4 Further Work and Conclusions	83
5 Modelling of 2D Transport	85
5.1 Background	85
5.2 Motivation for Fitting Experimental Data via Non-Linear Optimisation	92

5.3	Characterisation with the Fang-Howard Wave Function	98
5.4	Analysis of iHEMT Mobility-Density Curves	99
5.5	Extension to Transport Model	109
5.6	Comparison to Numerical Solutions	115
5.7	Scattering Rate Comparison	118
5.8	C-Shaped iHEMT Devices	119
5.9	Conclusions	127
6	Low Temperature 2D Transport	133
6.1	Shubnikov De Haas Oscillations	133
6.2	Dynamic Magneto-Resistance of Hole Gases	146
6.3	Further Work and Conclusion	155
7	Undoped InGaAs Quantum Well	159
7.1	InGaAs Quantum Well	159
7.2	Double Gated Ambipolar Device	160
7.3	Characterisation	161
7.4	Shubnikov De Haas Oscillations	162
7.5	Weak Localisation	177
7.6	Absence of Spin-Orbit Coupling in InGaAs	180
7.7	Conclusions and Further Work	183
8	Undoped Nano-Structures	185
8.1	Fabrication of Low Dimensional Systems	186
8.2	Attempts to Replicate Previous Induced Quantum Dots	186
8.3	P-type 1D Quantum Point Contacts	187
8.4	iQPC Measurement at 300mK	189
8.5	Modelling with Nextnano	196
8.6	Conclusions and Further Work	201
9	Conclusions and Further Work	203
9.1	Hole Gas in an $\text{In}_{0.1}\text{Ga}_{0.9}\text{As}$ Quantum Well	203
9.2	Dynamic Magneto-Resistance of Hole Gases in GaAs Heterostructures	204
9.3	Scattering Rate Modelling - As_2 vs As_4	205
9.4	QPC in Induced Holes Gases	206
	Bibliography	209
A	Fourier Analysis of Shubnikov De Haas Oscillations	233
A.1	Fourier Transform	233
A.2	Amplitude Modulation	235
A.3	Shubnikov De Haas Oscillation Signal	236
B	Fabrication Procedure	239
B.1	Sample Cleaning	239
B.2	Photoresist Spinning	240
B.3	Photoresist Patterning and Development	240
B.4	Recessed Ohmics	240

B.5	Undoped Hall Bars	244
B.6	iQPCs and iQDs	245
C	Parameter Uncertainties Estimated from χ^2	247
C.1	Find region about minimum that corresponds to a confidence interval	247
C.2	Bounding Box of N Dimensional ellipsoid	249
D	Example Scattering Rate Modelling Input File	253
E	Nextnano input file for undoped structures	261

PRESENTATIONS

A list of presentations and talks given on the work in this thesis.

- **Poster** - Undoped 2D Electron Systems as a Tool for Optimizing MBE Growth - Semiconductors UK 2016 & MBE 2016
- **Talk** - Undoped 2D Electron systems as a tool for optimising MBE growth - Cavendish Laboratory, 11/05/16
- **Talk** - 2D Transport Measurements in Undoped Electron Systems - Cavendish Laboratory, 14/02/18
- **Talk** - Transport Experiments in Undoped GaAs and InGaAs Heterojunctions and Quantum Wells - Cavendish Laboratory, 17/10/18

ACRONYMS

- 2DEG** 2D electron gas. 5, 11, 31, 38–40, 44, 144, 186, 196
- 2DES** 2D electron system. v, 1, 2, 5–8, 16, 19–21, 59, 60, 66, 86, 88, 90, 111, 141, 146, 185
- 2DHG** 2D hole gas. 11, 31, 191
- AFM** Atomic Force Microscope. 68, 69, 84
- ALD** atomic layer deposition. 28, 30, 60–66, 68, 83, 84, 206
- CVD** chemical vapour deposition. 63, 64
- fft** fast-fourier transform. 135
- HEMT** high electron mobility transistor. 15, 26, 27, 39, 45, 50, 99, 100
- iHEMT** intrinsic high electron mobility transistor. ix, 15, 25–27, 29–33, 35, 37, 39–41, 43, 45–47, 49, 50, 52, 81, 99, 100, 108, 122, 125
- iTLM** intrinsic transmission line measurement. ix, 60, 72, 73, 75–78, 84
- MBE** Molecular Beam Epitaxy. v, ix, 1–3, 12, 16, 25, 30, 31, 33, 35, 37, 39–41, 43, 45, 47, 49, 60
- MODFET** modulated-doped field effect transistor. 25
- PL** photoluminescence. 31
- QD** quantum dot. 20, 21, 23
- QPC** quantum point contact. 20, 21, 187
- SMU** source-measurement unit. 37, 38
- TLM** transmission line measurement. 3, 60, 70, 72, 77, 207
- UHV** ultra high vacuum. 16, 17

INTRODUCTION

The Molecular Beam Epitaxy (MBE) growth of high quality GaAs/AlGaAs epilayer structures has enabled the study of novel physical phenomena, such as the Quantum Hall and fractional Quantum Hall[1] in 2D electron system (2DES), 1D transport[2] and the 0.7 anomaly[3] and single electron transport in 0D systems[4]. The wide range of systems that can be studied all use a 2DES as a base from which the 1D and 0D systems are fabricated by further confining the carrier gas of the 2DES.

The success of these 2DES systems is due to the MBE growth of high quality epilayer structures. In many of these structures, dopants are introduced to change the band structure, forming potential wells for the charge carriers. The final carrier density in these structures is controlled by fine tuning the growth parameters of the MBE systems; to dope the structure with the correct dopant density to achieve the desired carrier density, while avoiding problems such as parallel conduction [5] or forming a metallic material by over doping the wafer. The presence of these purposeful dopants causes scattering in the carrier gas and, at low carrier densities, is the dominant cause of electron scattering [6].

Through the use of an externally applied electric field, similar changes to the band structure in doped structures can be achieved without the use of dopants. These undoped structures have a few advantages over doped devices; the lack of purposeful dopants in the structure means that the scattering is dominated by unintentional dopants. The reduction in scattering from dopants potentially makes an undoped structure a better choice for certain applications such as quantum dots and quantum points contacts, where the scattering from dopants can cause decoherence effect leading to poor performance[7, 8]. Because an external electric field is used to create the

potential well for the carriers, a simple change in polarity of the applied bias allows carriers to form in the conduction band or the valence band so that an electron or hole gas can be formed in the same structure. This allows for some interesting comparisons of the dynamics of electrons and holes in the same structure in the same cool down. There may also be practical advantages for systems such as p-n junctions where the shape of the junction could be controlled through the geometry of a top contact, opening new options for design and control of such devices. Finally, because the mobility of these undoped devices is limited by unintentional dopants, the mobility of these samples is a measure of the ‘cleanliness’ of the MBE system. This provides a method to measure the background impurity concentration of an MBE, system which is not possible with doped devices due to the required purposeful dopants. However, undoped devices come with their own fabrication challenges, such as insulating the top gate contact from the bottom ohmic contacts with a dielectric without creating a non-uniform electric field and challenges in making ohmic contacts to the 2DES.

In this thesis, work with undoped devices is presented, looking at the practical use of undoped devices to provide feedback on the MBE systems used to grow the material and how standard transport measurements of the material can give information on the limiting scattering mechanisms. Much work went into the improvement of the fabrication of the undoped devices both for electrons and holes, with demonstration of functioning (although not optimal) induced quantum point contacts for hole gases. Fabrication of ambipolar Hall bars allows the study of Quantum Hall effect in GaAs and InGaAs materials for both electrons and holes looking at the difference and changes that the inclusion of materials such as Indium can have on the properties of the carriers.

For systems such as InGaAs and p-type GaAs the doping through the use of beryllium and zinc causes contamination due to the diffusion of the dopants leading to low mobility material. While other dopants such as carbon can be used without causing contamination, the growth of high mobility doped material, in particular p-type, has proved a challenge to balance the increased carrier density and therefore mobility through the inclusion of more dopants with the increased scattering and therefore reduction in mobility. Using undoped material and device allow these difficulties with dopant to be sidestepped.

Thesis Structure

The structure of this thesis is as follows. A brief review of the background of undoped devices, the Quantum Hall effect and nano-structures along with motivation for the use of undoped devices is given in chapter 2. The characterisation of undoped wafers from measurement of the carrier density and carrier mobility in an electron gas at 1.5 K is covered in chapter 3, with

a study of the affects of varying MBE growth conditions, determined from the changes in the carrier mobility-density curves.

Chapter 4 looks at the key changes and optimisation of the fabrication processes for undoped devices from previous work. The yield of low resistance n-type, p-type and ambipolar ohmic contacts was determined from the fabrication of a transmission line measurement (TLM) device for undoped wafers. The TLM gave value for the contact resistance of the undoped ohmic contacts.

Furthering the analyse of the carrier mobility-density curves from chapter 3, a Boltzmann transport model of the scattering rates in an electron gas at 1.5 K, used in previous work on undoped devices [6], is used to extract relevant parameters characterising physical properties of the wafer in chapter 5. This model allow a quantitative study of the wafers characterised in chapter 3, by implementation of an automated fitting routine to calculate best fit parameters with uncertainties. Shortcomings of the model use are discussed with extension to address some of the limitation of the model.

Chapters 6 and 7 study the Quantum Hall effect in electron and hole gases in GaAs/Al-GaAs heterostructures and quantum wells and a InGaAs quantum wells at 283 mK. Measurement of the GaAs quantum well and heterostructure establishes a base line for comparison to the InGaAs quantum well. For hole gases in a GaAs heterostructure an anomalous dynamic magneto-resistance about 0 T is reported. The InGaAs quantum well show markedly different behaviour from the GaAs quantum well despite the small amount of In in the well.

Fabrication of nano-structures with the new fabrication processes is presented in chapter 8. The new fabrication processes introduced in chapter 4 means that the geometry of previous nano-structures [9–11] may require re-optimisation. Attempts to reproduce previously successful quantum dot designs are discuss with results from working quantum point contacts in a hole gas shown.

A summary and brief discussion for further work continuing from the thesis is given in chapter 9.

BACKGROUND AND MOTIVATION

It is truly remarkable to consider the vast range of technologies that depend on the ability to control and manipulate charge. Since 1947[12], with the creation of the first point-contact transistor at Bell labs, there has been an explosion in semiconductor technology, most commonly described by Moore's law based on Si technology. In research GaAs is often used due to generally higher carrier mobility than Si[13], and therefore lower disorder as well as a wider and direct bandgap which has advantages for optical applications. While GaAs is a superior research material in many cases, for commercial applications the relative abundance of Si, leading to a lower cost, economies of scale and native oxide (SiO_2) that Si technology can take advantage of, make it difficult for GaAs to compete.

In this chapter an overview of the background of GaAs based semiconductor research is summarised. Because of the wide range of potential applications that a GaAs based 2D electron system (2DES) can have both to fundamental physics research and new technological applications, this review is an attempt to briefly introduce some of the many applications rather than give a in depth review of each.

2.1 2D Electron Systems Background

As the starting point for most of the applications in this thesis is from a 2D electron gas (2DEG)[14], it is worth summarising the key physics of such a system. Detailed derivations can be found in many articles and books, such as [15–17]. As always, the starting point is the

Schrödinger equation:

$$\hat{H} |\psi\rangle = \left[\frac{|\hat{p}|^2}{2m^*} + \hat{V} \right] |\psi\rangle = E |\psi\rangle \quad (2.1)$$

The effective mass, m^* , is defined such that the band structure can locally be approximated by the parabolic relation,

$$E(k + k_0) \approx E(k_0) + \hbar \mathbf{v}_g \cdot \mathbf{k} + \frac{\hbar^2}{2} \mathbf{k} \cdot [m^*]^{-1} \cdot \mathbf{k} + O(k^3) \quad (2.2)$$

defining the group velocity, \mathbf{v}_g , and the effective mass tensor m_{ij}^* as,

$$\mathbf{v}_g = \frac{1}{\hbar} \frac{\partial E}{\partial \mathbf{k}_i} \quad \frac{\hbar^2}{m_{ij}} = \frac{\partial^2 E}{\partial k_i \partial k_j} \quad (2.3)$$

Generally the effective mass can be anisotropic with the six components $m_{xx}, m_{yy}, m_{zz}, m_{xy}, m_{yz}, m_{xz}$, which can effect the transport properties of a device effective mass depending on crystal direction. For GaAs the effective mass tensor is approximately isotropic, although there is evidence for small anisotropy [18]. For the devices in this thesis the fermi level is close enough to the Γ point ($\mathbf{k}=0$) that the group velocity is approximately zero such that with an isotropic effective mass, m^* the energy dispersion approximates to,

$$E(k) \approx E_0 + \frac{|\mathbf{k}|^2}{2m^*} \quad (2.4)$$

The GaAs 2D electron system is formed due to a confining potential in the z direction such that the Schrödinger equation separates into,

$$\hat{H} |\psi\rangle = \left[\frac{\hat{p}_{xy}^2}{2m^*} + \hat{V}_{xy} \right] |\psi\rangle + \left[\frac{\hat{p}_z^2}{2m^*} + \hat{V}_z \right] |\psi\rangle = (E_{xy} + E_z) |\psi\rangle \quad (2.5)$$

leading to separately solving a 1D Schrödinger equation for the confinement of the 2D electron system (2DES) and a 2D Hamiltonian for the physics of the 2D system itself,

$$\begin{aligned} \hat{H} |\psi\rangle &\equiv (\hat{H}_{xy} + \hat{H}_z) |\psi_{xy}\rangle |\psi_z\rangle \\ \hat{H}_{xy} |\psi_{xy}\rangle &= E_{xy} |\psi_{xy}\rangle \\ \hat{H}_z |\psi_z\rangle &= \left[\frac{\hat{p}_z^2}{2m^*} + \hat{V}_z \right] |\psi_z\rangle = E_z |\psi_z\rangle \end{aligned} \quad (2.6)$$

Solving the 1D Schrödinger equation in z gives the shape of the confinement of the carrier gas and the sub-band energies E_z^n . The solutions for the 2D Schrödinger equation give the behaviour of the carrier gas.

2.1.1 2D Electron System - Without a magnetic field

The properties of a 2D system are significantly different to those of a 3D system, resulting in different behaviours. In this section some of the useful properties of a 2D system are summarised. For the moment, the effects of a magnetic field shall be ignored. The Schrödinger equation for the 2D system is simply,

$$\hat{H}_{xy} = \frac{\hat{p}_x^2 + \hat{p}_y^2}{2m^*} \quad (2.7)$$

therefore the eigen functions for the 2D system are the familiar plane wave functions, $\psi(x, y) \propto \exp[ik_x x + ik_y y]$ from which the standard results for a 2D electron gas are obtained. The kinetic energy of a 2D system free electron gas system is given simply by:

$$T = \frac{\hbar^2 k_f^2}{2m^*} \quad (2.8)$$

where the carrier density n_c defines the Fermi wave-vector k_f from,

$$n_c = \frac{g_s g_v}{4\pi} k_f^2 \quad (2.9)$$

with a spin and valley degeneracy g_s and g_v . From these relationships the Fermi energy of a 2D system is directly proportional to the carrier density n_c ,

$$\varepsilon_f = \frac{\hbar^2 k_f^2}{2m^*} = \frac{\hbar^2}{2\pi m^* g_s g_v} n_c \quad (2.10)$$

from which the density of states is found to be constant,

$$g(\varepsilon) = \frac{m^* g_s g_v}{2\pi \hbar^2} \quad (2.11)$$

For GaAs the spin degeneracy $g_s = 2$ and the valley degeneracy of $g_v = 1$, simplifying the above.

2.1.2 2D Electron System - With a magnetic field

Much of the interesting physical phenomena for a 2D electron system (2DES) appear when a magnetic field is applied to the system. In the presence of a magnetic field the momentum of the 2DES couples to the magnetic vector potential, \hat{A} , to give the canonical momentum of the system $\hat{\pi} = \hat{p} - q\hat{A}$, where q is the charge of the particle ($-e$ for an electron). Due to the magnetic moment of the electrons, there is also a contribution to the energy of the system from the Zeeman effect [19]. Therefore the full Hamiltonian for the 2DES is:

$$\hat{H}_{xy} = \frac{\hat{\pi}^2}{2m^*} - \hat{\mu} \cdot \nabla \times \hat{A} = \frac{(\hat{p} - q\hat{A})^2}{2m^*} - \hat{\mu} \cdot \nabla \times \hat{A} \quad (2.12)$$

where the magnetic vector potential is defined by $\nabla \times \mathbf{A} = \mathbf{B}$ and $\hat{\mu}$ is the magnetic moment of the electrons.

The Quantum Hall effect occurs when there is a component of the magnetic field perpendicular to the plane of the 2DES. Considering a system where the magnetic field is $\mathbf{B} = (0, 0, B)$ and ignoring the Zeeman effect for the moment, the Hamiltonian can be solved with energy eigenvalues $E_n = \hbar\omega_c(n + 1/2)$. Solutions for the Hamiltonian are often done using either the Landau gauge, $\mathbf{A} = (0, Bx, 0)$ or the symmetric gauge, $\mathbf{A} = (-By/2, Bx/2, 0)$. The solutions in the Landau gauge are similar to the solutions for the Harmonic oscillator, with the ‘physicists’ Hermite polynomials $H_n(x)$,

$$\psi_n^{Landau}(x, y) = \frac{1}{\sqrt{2^n n!}} \left(\frac{m^* \omega_c}{\pi \hbar} \right)^{\frac{1}{4}} H_n \left(\sqrt{\frac{m^* \omega_c}{\hbar}} \left[x + \frac{\hbar k_y}{m^* \omega_c} \right] \right) e^{-\frac{m^* \omega_c}{2\hbar} \left(x + \frac{\hbar k_y}{m^* \omega_c} \right)^2 + ik_y y} \quad (2.13)$$

In the Landau gauge the eigenstates are plane wave states in the y direction, with the eigenstates of the harmonic oscillator in the x direction centred at $x_0 = -\hbar k_y / m^* \omega_c$. The degeneracy of the Landau levels can be found by considering 2D periodic boundary conditions at L_x, L_y such that $\psi_n^{Landau}(0, 0) = \psi_n^{Landau}(L_x, L_y)$, with the area of the system $A = L_x L_y$. These boundary conditions quantise the possible values of k_y with $k_y = 2\pi n / L_y$. The values of n are limited by considering that the centre of the wave function in the x direction is $0 \leq x_0 \leq L_x$. This constraint provides the following limit of the possible values of n ,

$$0 \leq \frac{2\pi \hbar n}{m^* \omega_c} \leq L_x L_y \equiv A \quad (2.14)$$

Therefore n is a positive integer which ranges from 0 to $\phi e / h$ where $\phi \equiv BA$. Introducing the magnetic flux quanta $\phi_0 \equiv h/e$ the value of n is limited to the number of flux quanta present. With a spin degeneracy of two for electrons, the total number of electrons per Landau level is $\mathcal{N} = 2\phi / \phi_0$. Therefore the carrier density per Landau level is $n_c = 2B / \phi_0$, increasing with the strength of the magnetic field. The maximum value of density of states is unchanged by the application of the magnetic field.

In a pure system with no disorder the density of states is a series of delta functions spaced by $\hbar\omega_c$ with each Landau level contributing $2\hbar\omega_c m^* / \pi \hbar^2$ carriers per unit area. In a real system there is some level of disorder. The disorder causes the electrons to scatter thereby localising some of the electron states. The effect of the localisation broadens the density of states as shown in figure 2.1. Only the extended states at $\hbar\omega_c(n + 1/2)$ carry the current in the device, but the localised states contribute to scattering.

2.1.3 Quantum Hall Effect

The Quantum Hall effect is a phenomena where the Hall resistance of a 2DES takes quantised values at sufficiently high magnetic fields[20].

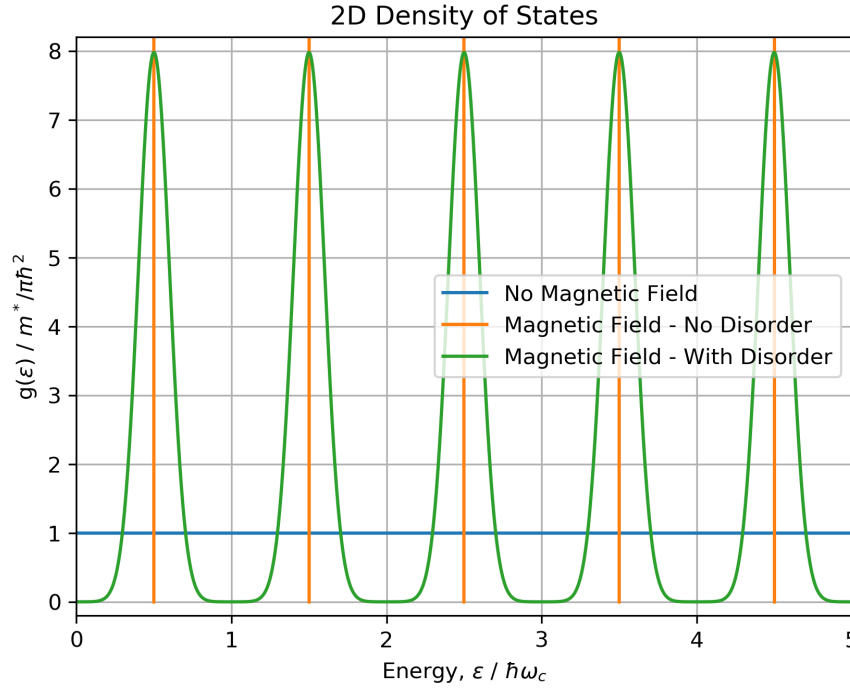


Figure 2.1: The 2D density of states in the presence of magnetic field and disorder.

The quantisation of the Hall resistance can be seen by considering the effect of applying an electric field in the x direction. The application of the electric field introduces an additional potential $V_E = -eEx$. This introduces a further shift in the eigenstates of the system $x \rightarrow x + mE/eB^2$. By calculating the current density using the Landau gauge the conductivity matrix can be found from Ohm's law $\mathbf{j} = \boldsymbol{\sigma} \cdot \mathbf{E}$. The Hall resistivity is $\rho_{xy} = h/e^2\nu$, where ν is the number of filled Landau levels. While the Hall resistivity is quantised to fractions of h/e^2 the longitudinal resistivity oscillates with minima in the resistivity coinciding with the quantised values of the Hall resistivity.

The integer Quantum Hall effect can be understood from the Landau level spectra. At low temperatures, where scattering is limited to within k_bT of the Fermi level ε_f , the resistivity is proportional to the scattering rate between states at the Fermi level and therefore from Fermi's golden rule is proportional to the density of states. When the Fermi level is in between Landau levels which are widely spaced, the density of states is zero. Therefore the resistivity falls to zero. As the Landau levels become more closely spaced, at lower magnetic field, the extended Landau level tails begin to overlap. At this point the density of states is non-zero, leading to a small but non-zero resistivity. This matches the positions of the minima in ρ_{xx} in 2.2. Looking more closely at the minima in 2.2, at low field only even filling factors ν can be seen. At high fields suppressed minima at odd filling factor ν become visible. This can be understood

by accounting for the spin of the electrons. The Zeeman splitting causes an energy splitting between the spin up and spin down state. At low field this energy splitting is smaller than the broadening of the extended Landau state, the overlap between the up and down states is so large than the density of states in between the up and down states doesn't change. As the magnetic field increases, increasing the energy split between the levels, eventually the spin split levels are far enough apart for the density of states to reduce in between the spin split levels causing the odd minima to become visible in ρ_{xx} . The resistivity ρ_{xy} has a different behaviour to that of ρ_{xx} . At low fields ρ_{xy} is linear, matching the expected classical behaviour, but at larger fields steps and plateaus of a fixed height can be resolved. From the classical picture $\rho_{xy} = B/n_c e$, but the degeneracy of the Landau levels gives the carrier density $n_c = \nu e B/h$. If these relations are both true then combining them gives, $\rho_{xy} = h/e^2 \nu \equiv R_k/\nu$, defining the Von Klitzing constant $R_k \equiv h/e^2$ [21] and the filling factor ν . This relation predicts that ρ_{xy} is inversely proportional to the number of filled Landau levels, with the plateaus observed in the ρ_{xy} traces corresponding to regions where the number of occupied Landau levels is constants.

The fractional Quantum Hall effect is similar to the integer Quantum Hall effect, but with minima and plateaus appearing at fractional filling factors. Unlike the integer Quantum Hall effects, the fractional Quantum Hall states cannot be explained with Landau level boarding due to disorder. To explain some of the fractional Quantum Hall states the effects of carrier-carrier interactions must be understood and the role of disorder included. While some of the fractional Quantum Hall states are understood, others are still the subject of on going debated. To resolve the fractional Quantum Hall states dilution fridge temperatures are usually needed for samples with a high mobility [1].

2.2 GaAs Transport Structures

Group *III:V* semiconductors have long been the materials of choice for fundamental research, due primarily to their superior mobility compared to Silicon. One of the most common material systems is the GaAs-AlGaAs system [23], with a common fraction of 0.33 for the Al, i.e. $\text{Al}_{0.33}\text{Ga}_{0.67}\text{As}$. The fraction of Al tunes the bandgap, with fractions greater than 0.4 having an indirect gap [17].

The direct band gap semiconductors, GaAs and AlGaAs, have the same crystal structure with similar lattice constants, allowing GaAs and AlGaAs to be grown on top of each other with little strain or defects, leading to a smooth interface. The interface between GaAs and AlGaAs is known as a heterointerface, and is the core of the heterostructure device. Due to the different chemical potentials in GaAs and AlGaAs, with either doping, or an electric field, the heterointerface can be engineered to produce a thin conducting layer confined in one

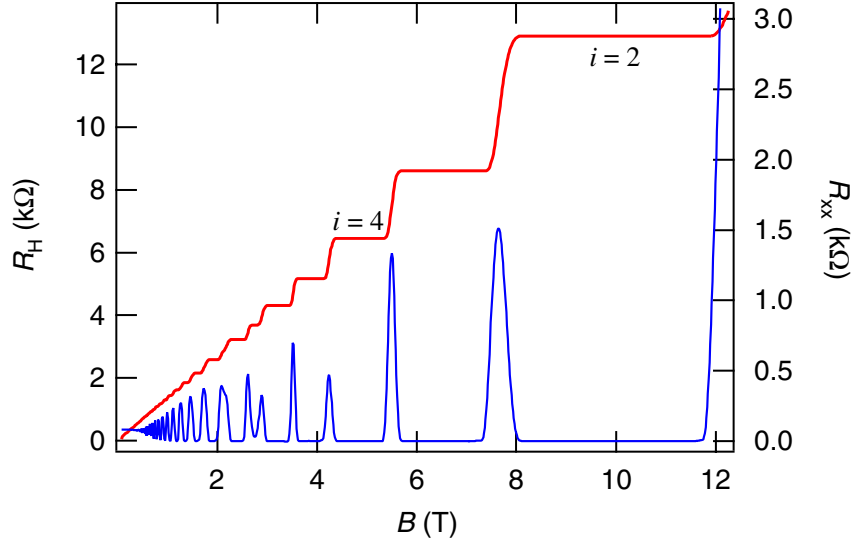


Figure 2.2: Quantum Hall data from a AlGaAs/GaAs heterostructure at 0.1 K [22], showing integer Quantum Hall effect with only even plateaus visible below ~ 2 T.

dimension, producing a 2D system, either a 2D electron gas (2DEG) or 2D hole gas (2DHG).

2.2.1 Transport / Scattering in 2D systems

The scattering in 2D systems, with small electromagnetic fields, is well described using Boltzmann transport. At equilibrium the Boltzmann transport equation states,

$$\frac{df}{dt} \equiv \frac{\partial f}{\partial t} + \frac{\partial f}{\partial \mathbf{r}} \cdot \dot{\mathbf{r}} + \frac{\partial f}{\partial \mathbf{k}} \cdot \dot{\mathbf{k}} = 0 \quad (2.15)$$

where $f(t; \mathbf{r}, \mathbf{k})$ is the carrier distribution function, generally a function of the position, \mathbf{r} in the system and the wave vector, \mathbf{k} of the carriers.

In the semi-classical limit, the transport of carriers in the presence of electric, \mathbf{E} , and magnetic, \mathbf{B} , fields are described by the Lorentz force, semi-classical relations and Newton's second law of motion[24],

$$\mathbf{F} = q(\mathbf{E} + \mathbf{v} \wedge \mathbf{B}) \quad (2.16)$$

$$\mathbf{p} = \hbar \mathbf{k} = m^* \dot{\mathbf{r}} \quad (2.17)$$

$$\epsilon = \frac{\hbar^2 |\mathbf{k}|^2}{2m^*} \quad (2.18)$$

$$\mathbf{F} \equiv \frac{d\mathbf{p}}{dt} \quad (2.19)$$

where the force, moment and energy are \mathbf{F} , \mathbf{p} and ϵ respectively.

Assuming that the distribution function does not depend on position and introducing the excess distribution function $g(t; \mathbf{k})$, such that $f(t; \mathbf{k}) \equiv f_0(\mathbf{k}) + g(t; \mathbf{k})$, where $f_0(\mathbf{k})$ is the Fermi-Dirac distribution, the linear Boltzmann equation at steady-state gives,

$$\frac{\partial g}{\partial t} + \frac{q}{m^*} \frac{\partial f_0}{\partial \epsilon} (\mathbf{k} \cdot \mathbf{E}) = 0 \quad (2.20)$$

where the semi-classical relations in (2.16) have been used to simplify the expressions and the non-linear term $\nabla_{\mathbf{k}} g \cdot \mathbf{E}$ has been removed. Working with the relaxation approximation, introducing the relaxation time, τ ,

$$\frac{\partial g}{\partial t} \sim -\frac{g}{\tau} \quad (2.21)$$

the approximation of the distribution function, $f(t; \mathbf{k})$ is,

$$f(t; \mathbf{k}) = f_0(\mathbf{k}) + \frac{q\tau}{m^*} \frac{\partial f_0}{\partial \epsilon} \mathbf{E} \cdot \mathbf{k} \quad (2.22)$$

Equating the second term to the first order term from the Taylor expansion, $\nabla_{\mathbf{k}} f_0 \cdot \Delta \mathbf{k}$, the change in wave vector, $\Delta \mathbf{k}$, can be calculated, giving a result for the drift velocity,

$$v_d = \frac{\hbar \Delta \mathbf{k}}{m^*} = \frac{q\tau}{m^*} \mathbf{E} \quad (2.23)$$

From the drift velocity the mobility of the carrier is defined,

$$\mu \equiv \frac{v_d}{\mathbf{E}} = \frac{q\tau}{m^*} \quad (2.24)$$

This relation shows that the mobility is an expression of the level of scattering in the system with the total scattering time τ given by the reciprocal sum,

$$\frac{1}{\tau} = \sum_i \frac{1}{\tau_i} \quad (2.25)$$

In chapter 5, the scattering rates, $1/\tau_i$ are calculated for the dominant sources of scattering in the GaAs-AlGaAs heterostructure at 1.5 K.

2.2.2 Molecular Beam Epitaxy (MBE)

AlGaAs/GaAs heterostructures are commonly grown using Molecular Beam Epitaxy (MBE), due to the purities of GaAs and AlGaAs needed to produce high-quality devices. MBE, in the most basic terms, is a process of depositing high purity single crystals films by the interaction of atomic or molecular beams with a heated crystalline substrate, in an ultra-high vacuum system. By manipulating the atomic or molecular beams, the growth can be controlled monolayer by monolayer. This high degree of control allows a wide variety of structures to be grown, including the AlGaAs-GaAs heterostructure. The precise details behind MBE growth are very complex [25–28], but typical GaAs is grown at 600 °C at $1\mu\text{mh}^{-1}$ with a *IV:III* flux ratio of 5-10 [29]. The molecular beams are produced by a set of material sources, which are heated and exposed to the crystal substrate via a set of control shutters, figure 2.3.

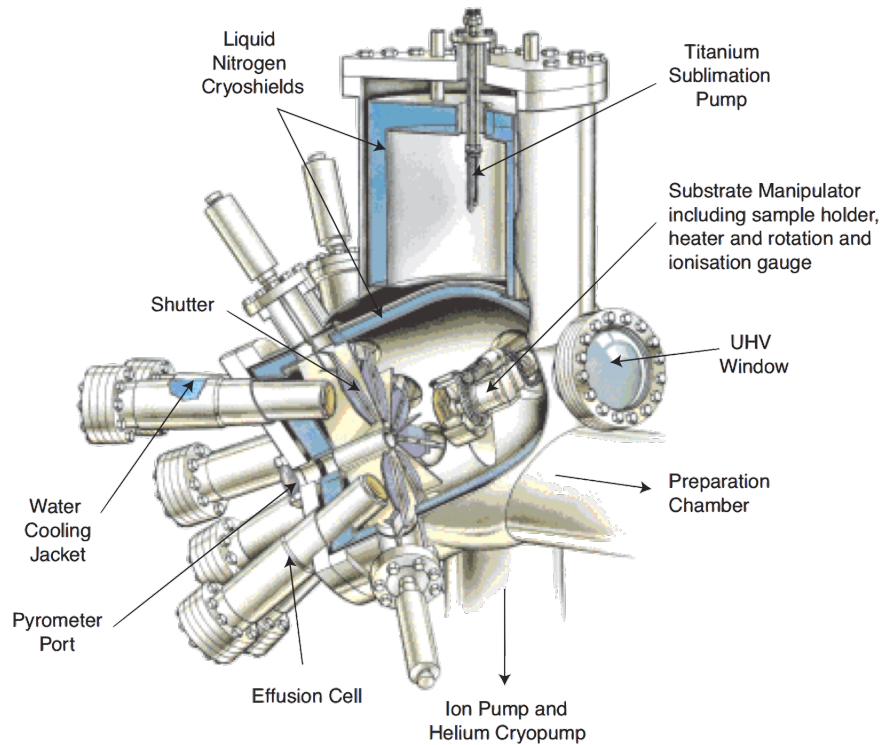


Figure 2.3: Diagram of the inside of the MBE chamber, from [29].

2.2.3 Semi-classics in 2D systems

The conditions during MBE growth govern the quality of the final device. The mobility, which is limited by scattering from the disorder in the structure, characterises the quality of the device. Disorder in a wafer structure includes background impurities, such as crystal vacancies, ionised and substitutional atoms, and the AlGaAs-GaAs interface roughness. Some of the parameters which control the disorder are substrate temperature, As overpressure and quality of vacuum. Over the years there has been continued development and improvement of MBE techniques used in the growth of heterostructure. Figure 2.4 shows mobility data over the years with each improvement. The purity of source materials is still reported as a key consideration to maximise carrier mobility[30, 31].

Figure 2.5 shows a plot of mobility data from the Cavendish Laboratory W-chamber for some nominally identical heterostructures grown over the last five years. The significant variation in mobility demonstrates how variation of the complex set of parameters involved in MBE growth can significantly change the mobility, with a factor of two between the best and worst mobilities from the W-chamber.

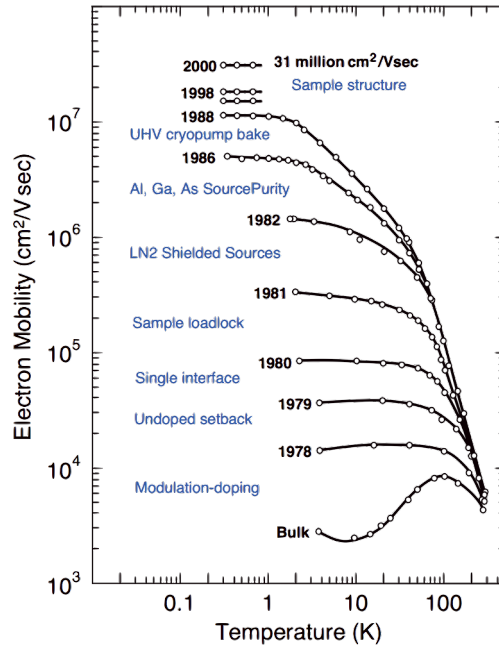


Figure 2.4: Mobility data of electrons in GaAs over 30 years, showing the improvement in MBE techniques. Taken from [32].

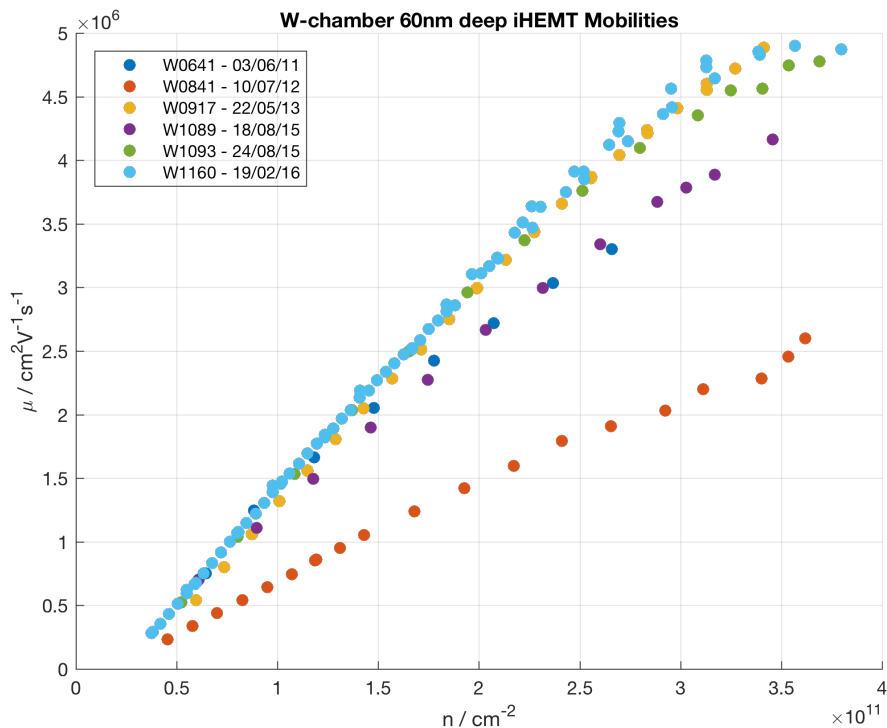


Figure 2.5: 2D electron mobility as a functions of carrier density, from 60nm deep iHEMT from 2011 to 2016, grown in the W-chamber, highlighting the large change in mobilities possible due to changing growth conditions inside the MBE chamber.

2.3 Undoped AlGaAs/GaAs Structures

The heterostructure device depends on either a doped region [33] or electric field [34] to change the band structure, producing a thin region at the AlGaAs-GaAs interface where carriers can be confined. These devices form a high electron mobility transistor (HEMT) in doped systems or intrinsic high electron mobility transistor (iHEMT) in undoped systems. Figure 2.6 contains a plot of the band structure for a modulation-doped heterostructure. While doped devices have

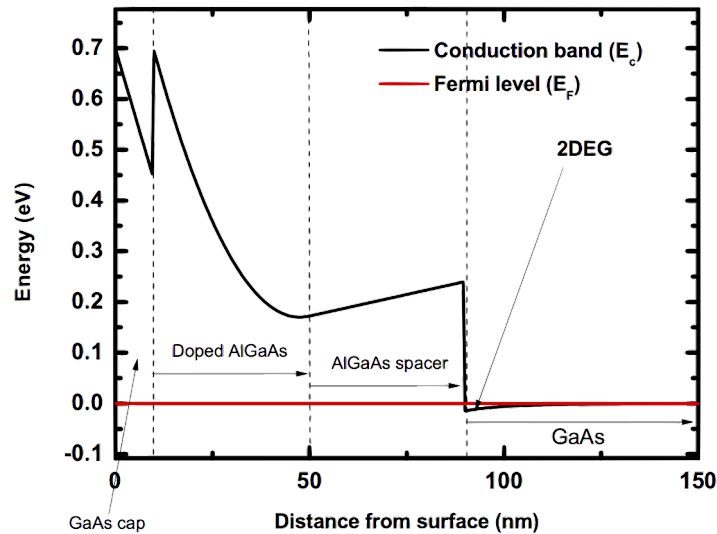


Figure 2.6: The band structure for a modulation-doped heterostructure device, with a suitable doping level for a conducting layer of electrons to form at the AlGaAs-GaAs interface. Taken from [9], using a 1D Poisson-Schödinger solver developed by Prof Greg Snider [35].

higher maximum mobilities than undoped, due to a higher carrier density from the dopants, undoped devices have several advantages over doped, motivating further research into undoped systems.

The absence of dopants results in a higher mobility at lower carrier densities, where background impurities dominate scattering, and more direct control of the carrier densities is possible through the use of an applied gate voltage. In addition to interest in carrier mobility, for the highest quality wafers, the carrier density is of interest as carrier-carrier interactions are most prominent at low carrier densities, enabling the study of many-body effects in 2D systems. The lowest carrier density measured in an undoped device was $7 \times 10^8 \text{ cm}^{-2}$ in a 2DHG [36]. The lack of scattering from impurities also has good implications for quantum dots and quantum point contacts, which suffer from coupling to nearby charge impurities. The absence of doping impurities reduces charge noise and may increase spin-coherence lifetimes [7, 8, 37–39].

While shallow 2DEGs can be made in doped systems [40, 41], they require high levels

of doping to bend the band structure enough to ensure conduction. High levels of doping tend to result in low mobilities due to scattering from the dopants. Shallow 2DEGs are more easily achieved in undoped devices, as the undoped device only requires a thin insulating layer between the gate and the device, and there are far fewer background impurities to scatter from, resulting in higher mobility shallow devices. These shallow devices [6, 42] allow finer features to be defined by surface gates, which leads to a wider range of potential applications [43].

Because the undoped devices are based on the use of a top gate to induce the conducting layer, they naturally lend themselves to ambipolar devices, where 2DEG and 2DHG can be confined in the same channel.

2.3.1 Motivation for Undoped Devices

The 2DES in doped and undoped wafers readily lend themselves to the study of 2D phenomena as well as often providing a basis from which 1D or 0D system can be created by further confining the 2DES already present. The work present in this thesis uses undoped material rather than doped, which introduces its own fabrication challenges. It is worth pausing to consider the motivation for the use of undoped material, given the wide range of high quality doped material available and the successful fabrication of novel devices with such material.

The first of four motivations for the use of undoped material is the lack of dopants required to form a 2DES. As outlined in section 2.3, doped structure use dopants to add donor or acceptor dopants to bend the conduction band to form the quantum well in which the 2DES forms. The amount of dopants required varies depending on the desired carrier density and the precise structure of the wafer, but generally dopant densities of $O(10^{18}\text{cm}^{-3})$ are used to produce 2DES with carrier densities of $O(10^{11}\text{cm}^{-2})$.

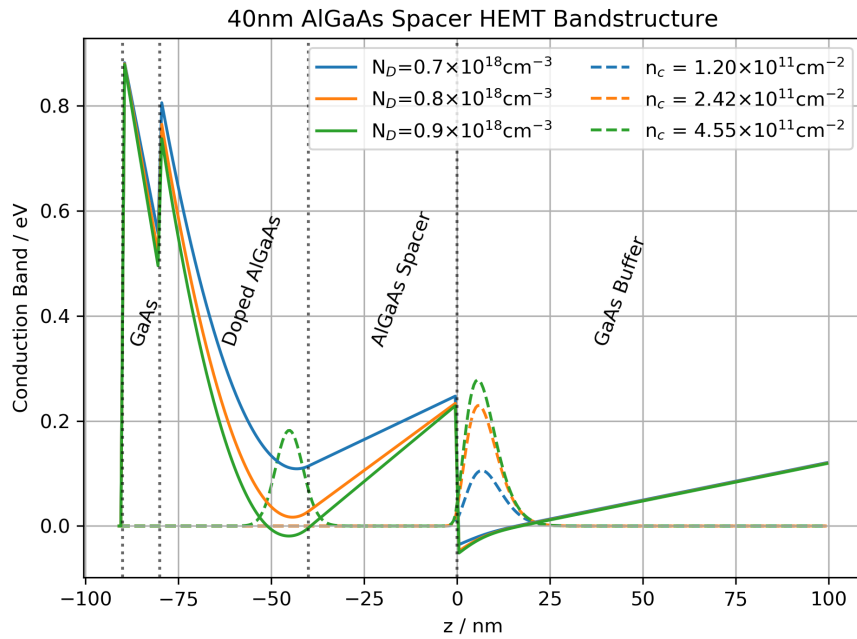
The removal of these dopants has a few benefits for certain systems and devices. The first is the reduction of scattering within the formed 2DES. While the charge centres formed by the dopants are essential for the formation of the 2DES, the dopants placed in the structure can be several orders of magnitude higher than the background level within the UHV MBE systems used for growth and the charge centre cause scattering within the 2DES formed. While the scattering from the charge centres is reduced by the use of a undoped spacer layer to position the charges away from the 2DES, the scattering from the dopants is still a significant source of scattering in these structures. Scattering within a structure is unavoidable to some extent but for many phenomena and devices the reduction of scattering improved the strength of the signal from physical phenomena or allows a device to perform better. A simple example is the Quantum Hall effect discussed in 2.1.2. Figure 2.1 show the effect of scattering in the formation of localised states and extending the Landau levels. The width of the extended Landau levels is a measure of the level of scattering in the system. If the level of scattering

is high then from figure 2.1 at a fixed magnetic field the overlap of the Landau levels would be increased compared to a system with less scattering. This makes the resolution of the oscillations in resistance more difficult as the increased overlap in the Landau levels reduces the difference in resistance when between Landau levels compared to when the Fermi level matches a Landau level. Other examples of system where reduced scattering was beneficial include measurement of the fractional Quantum Hall states, some of which required very high mobility to see the fractional states[44, 45]. From a more practical perspective, there are many examples of quantum technologies that benefit from reduced scattering. A common example is the coherent time of a spin from a trapped charge within a quantum dot. The T^{2*} time is commonly used as a metric for the quality of the quantum dot, one of the mechanisms causing the state to decohere is the presence of charge centres with the structure[37]. These charge centres can interact with the trapped charge in a dot ultimately resulting in decoherence effects.

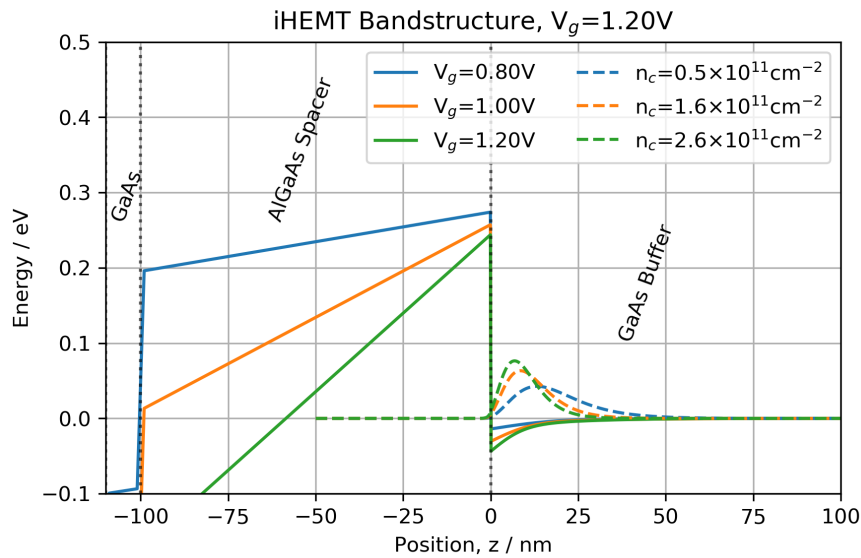
A second benefit of the lack of dopants in undoped material is the elimination of the risk of parallel conduction. Parallel conduction refers to the general situation where there is at least one other conduction path in the device in parallel with the channel formed by the 2DES. While there are many potential causes of parallel conduction, a common one is over doping within doped structures. If the doping within the doped structure is too high it is possible that the conduction band in the doped region falls below the Fermi level resulting in a conducting channel forming, see figure 2.7a. An undoped structure completely avoids this potential problem, as the lack of dopants in the structure means that parallel conduction from this type of parallel channel forming is not possible. It is worth noting that other sources of parallel conduction such as conducting layers deep in the wafer grown to help with the growth of the material e.g. superlattice and strain matching layers, can still be an issue if they are used in undoped wafers.

A third potential benefit of undoped material, is when working with material systems where dopants for either n-type or p-type carriers are either difficult to work with as they cause contamination of the UHV growth systems or cause other issues such as strain from lattice mismatching and disorder resulting in low mobility material, often the case with p-type material.

The final benefit of undoped material is the increased flexibility of the carrier types that can be formed in the potential well. Because the potential well is formed by the application of an external field the conduction band can be bend up or down in energy. Therefore a potential well for electrons can be formed by raising the Fermi level and bending the conduction band upwards, but equally by lowering the Fermi energy, a potential well for holes can be formed in the same structure. Similar effects could be achieved in doped structures because only one type of carrier (hole or electron) can be doped for. Therefore, if a wafer has been doped with n-type dopants such as silicon for electrons the application of negative potential can lower the Fermi energy and in principle form a potential well for holes but the external potential has to



(a) Bandstructure for a 40nm AlGaAs Spacer HEMT, with fully ionised dopants of $(7 - 9) \times 10^{17} \text{cm}^{-3}$. The electron densities (dashed) are shown and for doping of $9 \times 10^{17} \text{cm}^{-3}$ the conduction band in the doped region falls below the Fermi level resulting in two conducting channels being present.



(b) Bandstructure for a 100nm AlGaAs Spacer iHEMT, with an applied bias between 0.8-1.2V with the electron densities plotted (dashed).

Figure 2.7: Band structures of a modulation doped HEMT 2.7a and an undoped iHEMT 2.7b.

counteract the band bending, not present in undoped material, from the dopant in addition to forming the potential well for holes. Therefore undoped material naturally lends itself to ambipolar devices where holes and electrons can be induced in the same wafer. Another advantage that ambipolar undoped devices have is that 2DES only form directly under the gates applying the potential. This opens up the options of patterning planar p-n junctions and similar devices through patterning of gates on the surface of wafers and may prove a novel approach for certain applications.

Undoped devices come with a few disadvantages compared to modulation doped devices. These disadvantages stem from the challenges involved in fabricating a device structure that can externally apply the electric field that is produced by the modulation dopants in a doped structure. In order to create the electric field by applying a bias to the device structure, there must be some form of metallic contact to which the bias is applied without passing current into the structure. If current can flow from the metallic contact this often results in the short-circuiting of the contact with the iHEMT structure preventing the electric field from being applied. In this work a dielectric layer and metal gate are used to create this isolated metallic contact, however similar effects have been achieved by growing highly doped layers into the wafer structure to act as the metal gate [6, 46].

A second challenge when working with undoped devices is fabricating good quality ohmic contacts. The quality of an ohmic contact is somewhat subjective, but in this work a good ohmic contact is a contact with a linear IV characteristic and a resistance of the order 1 k Ω or less. A common method for creating ohmic contacts is to deposit ohmic metal on the surface of a wafer with then ‘spikes’ down when annealed. For a modulation doped structure this works well because the ‘in-built’ electric field is generated by donor charges which are trapped. Therefore when the ohmic metal spikes down through the modulation doped layer the ‘in-built’ field isn’t significantly affected and the metal makes a good electrical connection with the carrier gas. By contrast for a undoped device with the electric field applied through the use of a metallic contact, this method of annealing ohmic material to ‘spike down’ would result in short-circuiting the contact. Therefore fabrication methods for undoped devices tend to laterally diffuse ohmic material. However, because the ohmic material must make contact with the carrier gas directly under the metallic top gate, fabrication of a contact close enough to the top contact to diffuse underneath while remaining electrically isolated from the top contact to produce a good low resistance <1 k Ω presents some challenges.

Details of the fabrication of undoped devices and optimisations of the fabrication are discussed in chapter 4.

2.4 InGaAs

The InGaAs material system is of particular interest for study due to its properties being a mix of GaAs and InAs. This allows the control of some properties of InGaAs with the effective mass and the bandgap both varying based on the In content. InGaAs is of particular interest for transport experiments due to its very light electron of effective mass ($0.051m_0$)[47], however it also has application for its optical properties as its bandgap can be tuned to cover the full range of transmission bands in fibre optic cables. A final property of InGaAs which is of particular interest is the increased spin-orbit coupling that In causes. Spin-orbit coupling key for spintronics which focuses on the manipulation of control of spin within a structure in an analogous way to electronics manipulations and controls charge[48]. Spin-orbit coupling allows for the manipulation of the spin within a structure via the manipulation of the orbital momentum, therefore material system like InGaAs may prove to be useful in spintronic research.

Unlike the AlGaAs material system where the lattice constant changes by 0.1% between GaAs and AlAs, the InGaAs material system's lattice constant changes by 6% between GaAs and InAs. This lattice mismatch means that for InGaAs grown on GaAs substrates strain can play an important role in the properties of the material. The straining of grown layers has lead to study of the InGaAs system being limited to either low In fractions <30% where the strain is small enough that the growth on GaAs substrate is possible[11, 49] or high fraction 50% where InP substrates are lattice matched to $\text{In}_{0.57}\text{Ga}_{0.43}\text{As}$ and again allows for growth. The work with InGaAs in this thesis looks at undoped AlGaAs/GaAs heterostructure with a $\text{In}_{0.1}\text{Ga}_{0.9}\text{As}$ layer grown at the interface. This wafer was grown in order to study the effects of adding a small amount of In to a 2DES to modify the electrical properties of the 2DES such as the electron g-factor.

2.5 Quantum Point Contacts and Quantum Dots

Quantum point contact (QPC) and Quantum dot (QD) respectively are 1D and 0D systems where the 2DES has been further confined into lower dimensional systems. These low dimension systems are of interest due to their very different behaviour compared to typical 3D system, as has already been described for 2D systems with the Quantum Hall effect 2.1.3. While the Quantum Hall effect is remarkably stable in the presence of disorder within the system when confining system to lower dimensions the effects of disorder can become more significant as the charge centres that form disorder become comparatively larger to the smaller more confined systems. Because of these the study of 1D and 0D systems and more general nano-structures in undoped systems are of particular interest due to the reduced disorder and the potential im-

provement in the performance of nano-structures. Brief summaries of the properties of QPCs and QDs are given in the following sections.

2.5.1 Quantum point contact (QPC)

A quantum point contact (QPC) [49–51] is a one dimensional channel where the carriers have been confined to a region just a few Fermi wavelengths wide. Such channels are often formed by using a split gates on the surface of a 2DES device to apply a potential which is often approximated as parabolic potential to analyse such a system.

The defining property of such a system is the conduction staircase seen when measuring the conductance through a QPC while varying either the carrier density or the potential of the split gate, thereby changing the confining potential. The conduction traces for QPCs show a series of plateaus in the conductance when varying the split gate potential. When measuring the differential conductance to remove any in series resistance due to ohmic contacts and any 2DES present, the plateaus are found to correspond to integer values of $G_0 \approx 77\mu\text{S}$. The quantisation of the QPC conductance can be understood by considering the a 1D wire with a potential difference of V between the two ends of the wire. The infinitesimal current being injected into the wire would have the form,

$$dI_i = qv_\varepsilon f(\varepsilon, \mu) \frac{dn}{d\varepsilon} d\varepsilon \quad (2.26)$$

where q is the charge of the carriers, v_ε the group velocity, $f(\varepsilon, \mu)$ the Fermi function and $dn/d\varepsilon$ the density of states. Because the wire is a 1D system with an energy $\varepsilon = E_0 + \hbar^2 k^2 / 2m^*$ the density of states in 1D has the property, $dn/d\varepsilon = g_s / 2\pi\hbar v_\varepsilon$, hence the current carried by a 1D sub-band can be expressed as,

$$dI_i = \frac{g_s q}{h} f(\varepsilon, \mu) d\varepsilon \quad (2.27)$$

Consider the two ends of a 1D channel injecting current the net current through the channel will be,

$$\begin{aligned} dI_i &= dI_i^+ - dI_i^- = \frac{g_s q}{h} [f(\varepsilon, \mu + qV) - f(\varepsilon, \mu)] d\varepsilon \\ dI_i &= \frac{g_s q^2}{h} V \frac{\partial f}{\partial \varepsilon} d\varepsilon \end{aligned} \quad (2.28)$$

where one end of the channel has been bias with a potential V assumed to inject a positive current compared to the unbiased side injecting current in the opposite sense. Completing the sum over all sub-bands i and taking the low temperature limit the conductance is found to be $G = g_s q^2 N / h$ where N is the number of sub-bands active. The conductivity quanta is therefore $G_0 = 2e^2 / h \sim 77\mu\text{S}$ for an electron or hole with spin degeneracy $g_s = 2$. A similar result is

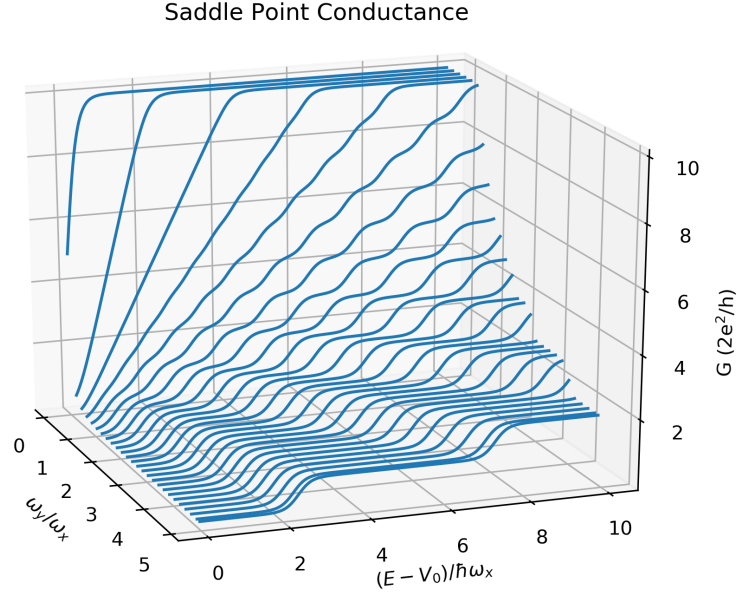


Figure 2.8: The conductance, G as a function of $E - V_0/\hbar\omega_x$ and ω_y/ω_x in units of $G_0 = 2e^2/h$. The conductance traces show a series of plateaus with the plateaus becoming more pronounced when $\omega_y \gg \omega_x$.

obtained from the Landauer formalism[52] with the conductance through a generally potential in 1D given by,

$$G = \frac{2e^2}{h} \text{Trace}[t^{+\dagger} t^+] \quad (2.29)$$

where $t^{+\dagger} t^+$ is the transmission matrix for the potential. The saddle point potential, $V(x, y) = V_0 + m^*(\omega_y^2 y^2 - \omega_x^2 x^2)/2$, is often used as a description of the type of potential formed by a split gate. The transmission matrix for such a potential is known and gives rise to a conductivity of,

$$G = \frac{2e^2}{h} \sum_n \frac{1}{1 + e^{-\pi\varepsilon_n}} \quad (2.30)$$

where $\varepsilon_n = 2(\varepsilon - V_0)/\hbar\omega_x - (2n + 1) \omega_y/\omega_x$. Figure 2.8 contains a plot of this function as a function of $(\varepsilon - V_0)/\hbar\omega_x$ and ω_y/ω_x . The function still produces a conductance staircase but the definition of the conductance plateaus now depends on $\omega_y \gg \omega_x$.

The study of such 1D channels is of interest for the highly correlated phenomena that such 1D systems exhibit, but are also of interest for practical applications as the potentially sharp increase in conductance that 1D channel shows in between conductance plateaus provides a very sensitive method for detecting local changes in the potential surrounding the 1D channel. This method has been applied to count electrons populating a quantum dot[53, 54].

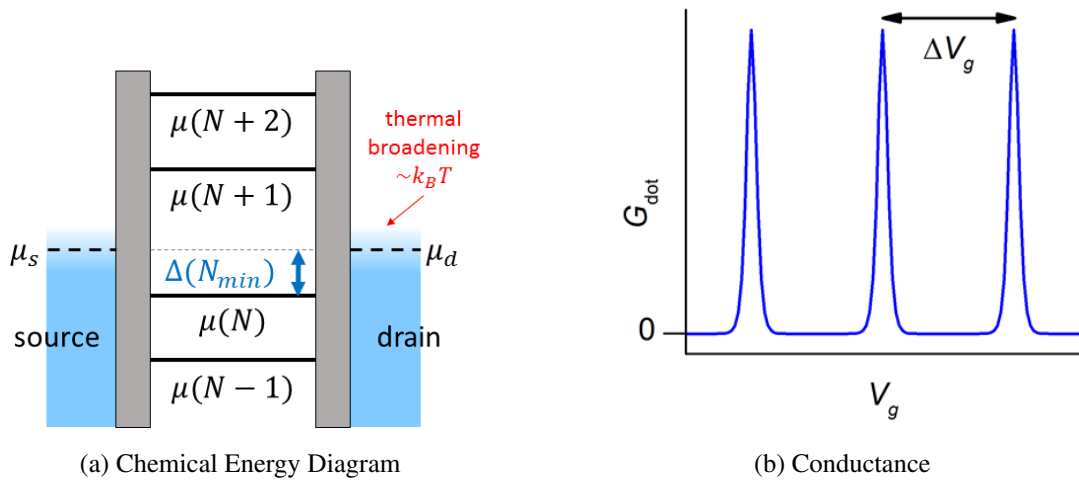


Figure 2.9: The chemical energy of a quantum hole and the conductance through the dot, taken from [59].

2.5.2 Quantum dot (QD)

A Quantum dot (QD) [55–58] is a region where the carriers have been completely confined in all three dimensions and therefore are referred to as 0D systems. As a result of the complete confinement of carriers, quantum dots have an energy structure which has been likened to that of an atom. As with 2D and 1D structures, 0D structures have unique transport properties that identify the presence of a 0D system, for quantum dots this is the phenomenon of Coulomb blockade [4].

Coulomb blockade is the general term given to transport through a 0D system like a quantum dot. The basic principles of Coulomb blockade can be understood by considering the energy levels on either side of the quantum dot and in the dot itself. Either side of the dot are carrier reservoirs which are most likely to be 2D as quantum dots often are fabricated by further confining a 2D carrier gas. The energy spectrum of the 2D reservoirs can be assumed to be a continuum of states populated up to the Fermi level when at low temperatures. The spectra of the quantum dot is similar to that of an atom with discrete energy levels, figure 2.9.

Transport through the quantum dot can only take place if the carrier from the source can tunnel through the barrier to the dot into a state within the dot. As figure 2.9 shows this depends on the source and drain being biased such that the source is aligned in energy with a state within the dot and the drain is at a lower energy to allow for tunnelling out of the dot. When these conditions are not met, carrier cannot travel through the dot which is known as Coulomb blockade.

Beyond the fundamental physics of such 0D systems, quantum dots are interesting due to many potential technological applications. Fundamentally the creation of a quantum dot

produces a series of discrete energy levels which can be tuned to some extent by changing the geometry of the dot itself. Once these discrete energy levels have been formed there are a wide range of uses of these levels, a few of which include: photon sources [60] and detectors [61], thermometry [62], quantum computing [63] and electron pumping [58]. Therefore the fabrication of quantum dots is of interest of many possible research projects.

UNDOPED HETEROSTRUCTURE

Many semiconductor devices such as the modulated-doped field effect transistor (MODFET) are based on placing additional charges within the structure by adding dopants, ultimately resulting in bending of the conduction or valence bands and creating an ‘in-built’ electric field which results in a conducting channel forming.

However, the required band bending and forming of the conducting channel can also be achieved by applying an external electric field to the semiconductor via a metal gate. These intrinsic semiconductor devices have two main advantages over equivalent doped devices: firstly, the lack of dopants removes a significant source of scattering, particularly at low carrier densities, and secondly, applying either a positive or negative voltage to the metal gate allows both electrons or holes to be induced in the same structure.

In this chapter, the structure and functions of the undoped heterostructure used to fabricate an intrinsic high electron mobility transistor (iHEMT) are discussed, including the main scattering mechanisms within an iHEMT at 1.5 K. Characterisation of the iHEMTs involves measuring the carrier density and carrier mobility using a Hall bar device, and measuring the resistivity along and across the bar. The Hall bar device and the experimental measurement are introduced in section 3.2.2. Because the mobility in an undoped device is a measure of the ‘cleanliness’ of the MBE growth system, comparison of the carrier mobility-density curves can provide feedback on the MBE system and how changes in growth parameter affect the disorder in the material. In section 3.3 the carrier mobility-density curves from a series of wafers are compared to look at the affect of changing a range of growth parameters, the variation in the MBE chamber over time and the limiting factors in carrier density and mobility.

3.1 Intrinsic High Electron Mobility Transistor (iHEMT)

The simplest intrinsic structure is that of the iHEMT, a simple AlGaAs/GaAs heterostructure. Unlike a doped HEMT which requires a doped AlGaAs region and an AlGaAs spacer, the iHEMT has only an AlGaAs spacer layer and a GaAs buffer.

Both the HEMT and iHEMT form a conducting channel at the AlGaAs/GaAs interface by creating a potential well. This potential well is formed due to different conduction band energies in the AlGaAs and GaAs causing a band offset of approximately 0.27 eV to 0.29 eV [65–67] at the AlGaAs/GaAs^a interface. This results in a potential barrier on the AlGaAs side of the interface in the conduction band. Combining this band offset with an electric field further tilts the conduction band forming an approximately triangular potential well at the interface.

The doped and undoped HEMTs generate the required electric field in different ways. The doped HEMT has a doped AlGaAs layer between the surface of the semiconductor and the GaAs layer. These dopants add additional charges to the structure causing band bending following the Poisson's equation for electro-statics $\epsilon_0 \nabla \cdot (\epsilon \nabla \phi) = -\rho(z)$. Enough charge must be placed into the semiconductor to generate a large enough 'in-built' electric field to create the triangular potential well, as shown in figure 3.1a.

An undoped iHEMT generates the electric field from a metal gate on the surface of the semiconductor, applying the field externally, shown in figure 3.1b. An undoped iHEMT does not need dopants to be added to the semiconductor; but does not have the 'in-built', always present electric field of a doped HEMT. This means that until the device is cold and a sufficient voltage applied to the top gate of the device there is no conducting channel in an iHEMT.

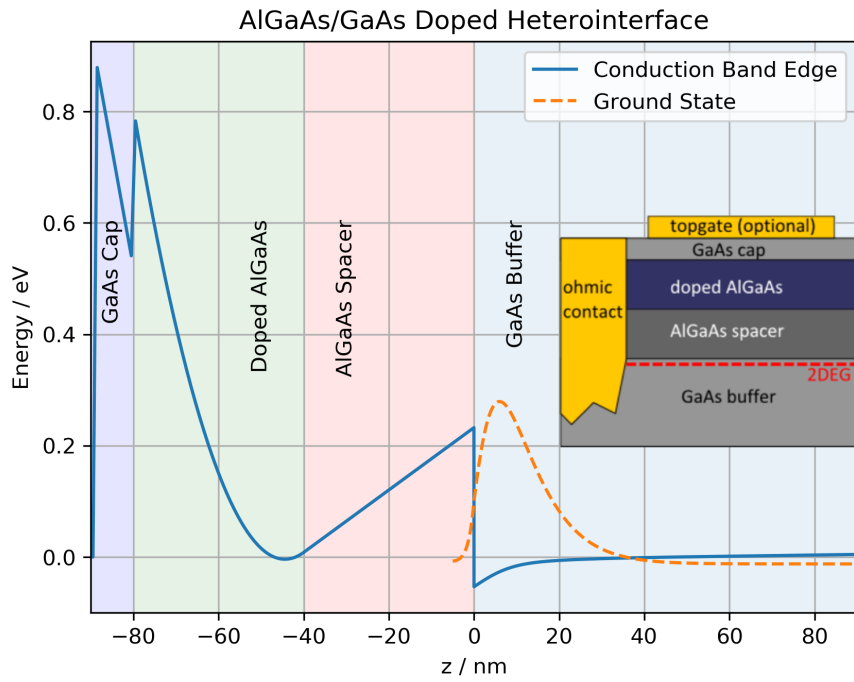
For HEMT and iHEMT devices the thickness of the AlGaAs layers are varied to change the depth of the interface relative to the surface of the structure. Because all devices have a standard 10 nm GaAs capping layer and 1 μm GaAs buffer, the thickness of the AlGaAs layer is used as a short hand for describing the depth of a devices. Therefore in this work an iHEMT referred to as a 50nm iHEMT has a 50nm AlGaAs spacer layer but with the 10nm GaAs capping layer the interface is 60nm below the surface of the device.

3.1.1 iHEMT Fabrication

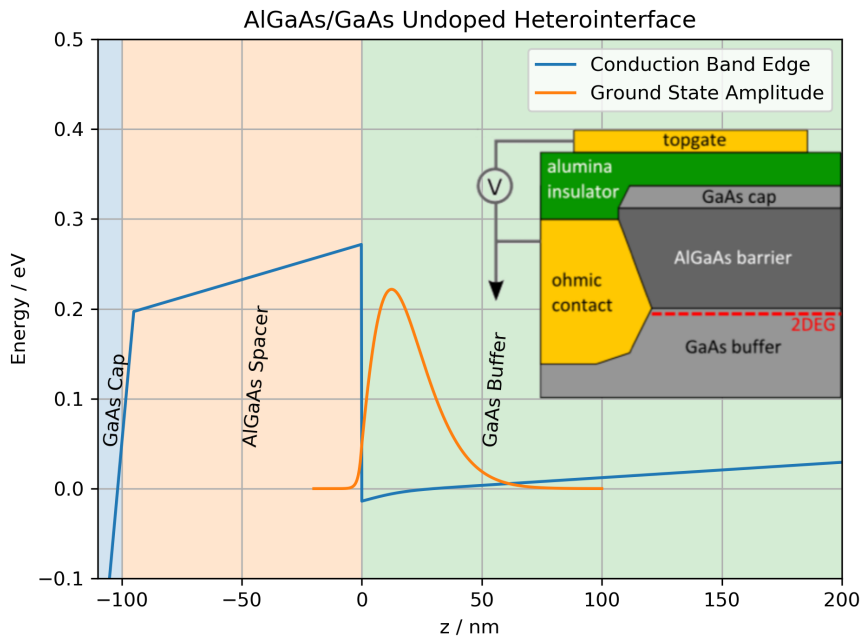
The fabrication of an iHEMT is very similar to that of a doped HEMT. However, there are a few key differences due to the different structures of the devices.

There are four main layers in the iHEMT device, an image of which is shown in figure 3.2. The MESA (grey), etched to 500 nm, creates an electrically isolated region for the device on the substrate. The ohmic layer places ten ohmic contacts (orange) around the MESA, giving

^a $x = \frac{1}{3}$ Al fraction $\text{Al}_x\text{Ga}_{1-x}\text{As}$



(a) Doped HEMT



(b) Undoped/Intrinsic HEMT

Figure 3.1: The structure and band structure of a doped and undoped HEMT. The undoped iHEMT does not require a doped layer causing band bending like a doped HEMT, instead an external gate is used to apply an electric field. Band edges calculated using nextnano[64].

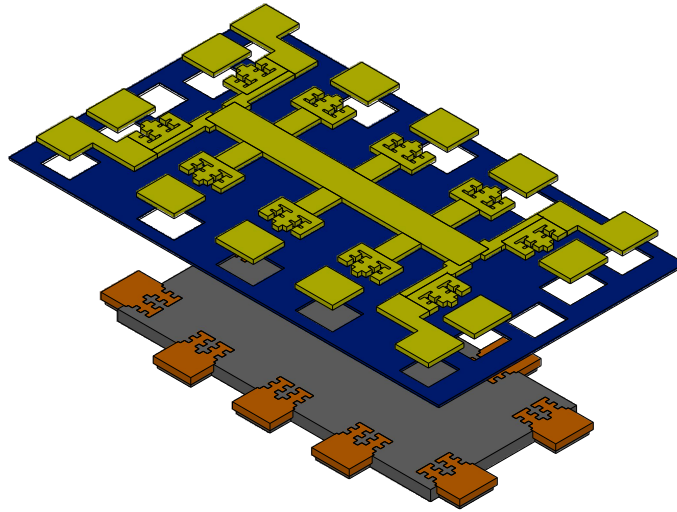


Figure 3.2: Exploded view of iHEMT Device pattern and cut through, showing the MESA (grey), ohmic(orange), alumina insulator(blue) and the top gate with bond pads(yellow).

multiple potential choices of contacts to add some redundancy for measurement. After the MESA and ohmic layers, Atomic layer deposition (ALD) is used to completely cover the device in 60nm of Al_2O_3 (blue) to act as a gate dielectric. A buffered HF acid solution is used to etch windows into the ALD layer granting access to the ohmic contacts beneath. The final layer deposits the metal gate (yellow) on the surface, covering the gate dielectric. The conducting channel forms at the AlGaAs/GaAs interface directly below the metal gate. This means the patterning of the metal gate defines the geometry of the conducting channel and therefore the device.

3.1.1.1 Key Fabrication Steps for Undoped Devices

The full and precise details of the fabrication of undoped iHEMTs in the semiconductor clean-room at the Cavendish laboratory, are in appendix B. In this section only the key fabrication steps for undoped device are discussed.

The main difference between a doped device and an undoped device is the external metal top gate covering the region where the conducting channel forms. While doped devices can optionally have top gates, used to change the carrier density, an undoped device requires a gate to form the conducting channel. The design of the undoped device differs from a doped device in two main ways. Firstly, as the conducting channel only forms directly under the metal gate, the metal gate must overlap the contacts to bring the conducting channel to the ohmic

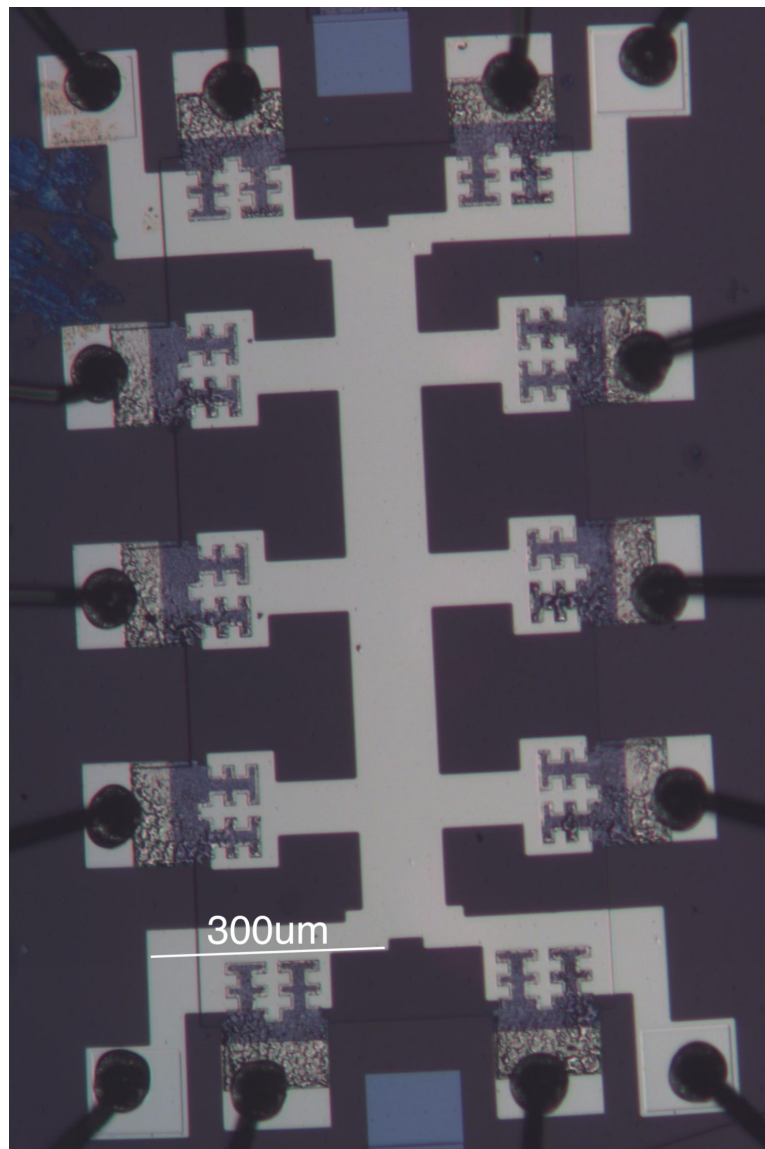


Figure 3.3: Optical image of complete iHEMT device

contacts' perimeter. If the gate does not overlap with the contacts, an intrinsic semiconducting region can form between the channel and contacts. Such an intrinsic region would cause very high contact resistances, impacting the measurement of the device. A dielectric placed in between the gate and contacts forms an insulating layer, keeping the contacts and gates separate while overlapping. The dielectric material also helps with avoiding short circuits forming from applying a high enough voltage on the metal gate to overcome the Schottky barrier at the GaAs surface. Overcoming the Schottky barrier results in charge passing into the semiconductor from the metal gate. While it is possible to apply a small enough voltage to form a conducting channel without overcoming the Schottky barrier, this would limit the maximum carrier density

in the device.

Continuing on from previous work with undoped devices[10, 68], an Al_2O_3 dielectric deposited via ALD forms the insulating layer in this work. Previously polyimide was used for the dielectric layer. The ALD process has two advantages over polyimide. Firstly, the dielectric layer can be much thinner than the polyimide at 40 nm-60 nm^b compared to 700 nm-1500 nm of polyimide. A thinner layer means that smaller voltages are required to form the conducting channel. Secondly, the ALD process creates a uniform conformal layer which provides better coverage of rough surfaces such as ohmic contacts. The more uniform the layer, the better the uniformity of the carrier density across the device, as the carrier density is set by the electric field, which in turn is controlled by the layer thickness. Coverage of the rough surfaces of the ohmic contacts is critical for undoped devices, as failing to insulate any single contact from the top gate short-circuits the device, preventing a carrier gas from forming. The conformal nature of the ALD reduces the chance of this type of short circuit occurring.

The second main design change compared to a doped device is the recessed ohmic contacts, as established in [69]. Etching pits recesses the ohmic metal down to where the conducting layer forms. In a doped structure, the conducting channel is everywhere due to the doped layer in the wafer. For doped structures depositing the correct ohmic metal on the surface and annealing causes the metal to ‘spike’ down, contacting the conducting channel. The conducting channel in an undoped device is only directly under the metal gate. Depositing ohmic metal in the same manner as used for a doped device resulted in a low yield of functioning ohmic contacts.

The recessed contacts are etched 300nm below the surface for a typical 50nm or 100nm iHEMT. The ohmic metal deposited in the etched pits is in direct contact with the GaAs layer where the conducting channel forms, meaning that the metal only needs to diffuse laterally to contact the channel. Recessing the ohmic contacts in this way produces a better yield of low resistance contacts to the channel.

3.2 Using iHEMT for Optimising MBE Growth Conditions

Every wafer grown for transport experiments in the MBE chambers at the Cavendish Laboratory undergoes standard characterisation by measuring carrier mobility and density at 1.5K. The carrier mobility is proportional to the transport lifetime of the carriers, which in turn depends on the scattering rates from the scattering mechanisms within the semiconductor. The carrier mobility is, therefore, a measure of the ‘cleanliness’ of the semiconductor material.

^bThe 40 nm-60 nm was based on fabrication processes developed in previous work. Thinner ALD dielectric layers are possible but would need implementation.

As discussed in 3.1, an undoped device has no intentional dopants. Therefore any dopants present are due to background impurities in the MBE systems. The mobility of the undoped device is, therefore, related to the background impurity density of the MBE system, allowing a qualitative measurement of the background. Measurement of the background is not possible with a doped device as the dopants in the device are a more significant source of scattering than the background impurities, and other methods for measuring background such as photoluminescence (PL), secondary ion mass spectrometry, and deep-level transient spectrometry are not sufficiently sensitive for state-of-the-art material produced in MBE chambers [70]. The undoped device mobility, therefore, allows the effect of varying growth parameters to be examined, providing complementary information to the measurements of doped devices.

Undoped devices allow for both holes and electrons in the same structure, however due to the heavier effective mass of holes in GaAs, $0.45m_0$, compared to the electrons, $0.067m_0$ the ratio of the thermal energy to the kinetic energy will be larger in a 2D hole gas (2DHG) compared to a 2DEG. This means that the range of k-states involved in the transport in a 2DHG will be larger as,

$$k_b T \approx \Delta E = \frac{\hbar^2 k_f}{m^*} \Delta k \implies \frac{\Delta k}{k_f} \approx \frac{m^* k_b T}{\hbar^2 k_f^2} \quad (3.1)$$

For a 2DEG at 1.5K with a carrier density of $1 \times 10^{11} \text{cm}^{-2}$ this relationship gives a value of $\Delta k/k_f \sim 0.18$ compared to $\Delta k/k_f \sim 1.22$ for a 2DHG with the same carrier density. This smaller range of k-states involved in the transport, in addition to other transport phenomena like the Quantum Hall effect[20], which are more pronounced at 1.5K in a 2DEG compared to a 2DHG, again due to the effective masses, make a 2DEG the better choice for examining MBE growth conditions. Unless stated otherwise, the remaining devices in this chapter are 2DEG in a iHEMT structure.

3.2.1 Scattering Mechanism with a 2DEG

The four primary sources of scattering, for a 2DEG at 1.5 K are point charge scattering from dopants and charge traps within the structure or at the GaAs surface/oxide interface, interface roughness at the AlGaAs/GaAs interface, and alloy scattering from the AlGaAs spacer layer. Other possible causes of scattering are from electron-phonon interactions or electron-electron interactions. By cooling the device to 1.5K the phonon modes are frozen out to a point where electron-phonon interactions are sufficiently rare enough that electron-phonon scattering is insignificant compared to other sources of scattering. Electron-electron interactions have an effect on the scattering rate of a 2DEG due to screening of charge. The effectiveness of the screen in an electron gas increases with the carrier density of the gas and is taken into account by the dielectric constant of the gas. The effective dielectric constant can be calculated from models

such as Thomas-Fermi screening. Additional interaction effects related to highly correlated electron systems only become significant at the lowest carrier densities due to the scaling of the kinetic energy $\propto n_c$ and Coulomb potential $\propto \sqrt{n_c}$ such that the ratio of the two is $\sqrt{n_c}$. The typical carrier densities in the wafers were $\sim 1 \times 10^{11} \text{ cm}^{-2}$, large enough that the change in the dielectric constants is the only relevant consideration of electron-electron interactions for iHEMT devices.

In chapter 5, the modelling of the dominant scattering mechanisms is discussed in detail. In this chapter, a more qualitative description of the scattering mechanisms is used to understand the experimental data from the standard characterisation of undoped devices.

3.2.1.1 Point Charge Scattering

Scattering from point charges depends on two major factors: the scattering potential V_q and the screening in the carrier gas. The screen in carrier gas is described by Lindhard theory[71], which in the static limit for a 2D system introduces an enhancement to the dielectric constant of $\epsilon(q) = 1 + q_{TF}/q$. The scattering potential V_q is proportional to $\exp[-qz]/q$ where q is the momentum transfer wavevector $q \propto n_c$ and z the distance between the point charge and carrier gas. Combining these two factors gives a scattering rate $1/\tau \propto \exp[-qz]/(q + q_{TF})$. From this expression the dependence of the scattering rate on the carrier density can be seen. At low carrier density $q \ll 1$, therefore the screening in the carrier gas increases the scattering rate but, more significantly, the exponential dependence on the momentum transfer wave vector also increases the scattering rate. It is this exponential dependence on q that means that point charge scattering will dominate at low carrier density as the other sources of scattering present have a slower dependence on q .

Scattering from point charges within an undoped device comes from two primary sources: background impurities and surface charge. Of the two, the background impurities are the dominant source of scattering[72–74], due partly to the distance of the surface from the conducting channel. The exponential dependence of the screened potential on the distance to the point charge, $V_q \propto \exp[-qd]$, defines a length scale of $k_f^{-1} = (2\pi n_c)^{-1/2} \sim 40 \text{ nm}$ for the potential. This exponential dependence means for deep conducting channels, $>100 \text{ nm}$ below the surface, the surface charge is too far away to cause significant scattering. However, for shallow devices, the surface charge is a significant source of scattering and needs to be considered. In both cases, the background impurity is the most significant source and is often the dominant source of scattering within the device. The dominance of point charge scattering is shown in the mobility-density curve, by an increased carrier mobility as the carrier density increases, due to the enhanced screening of the point charges.

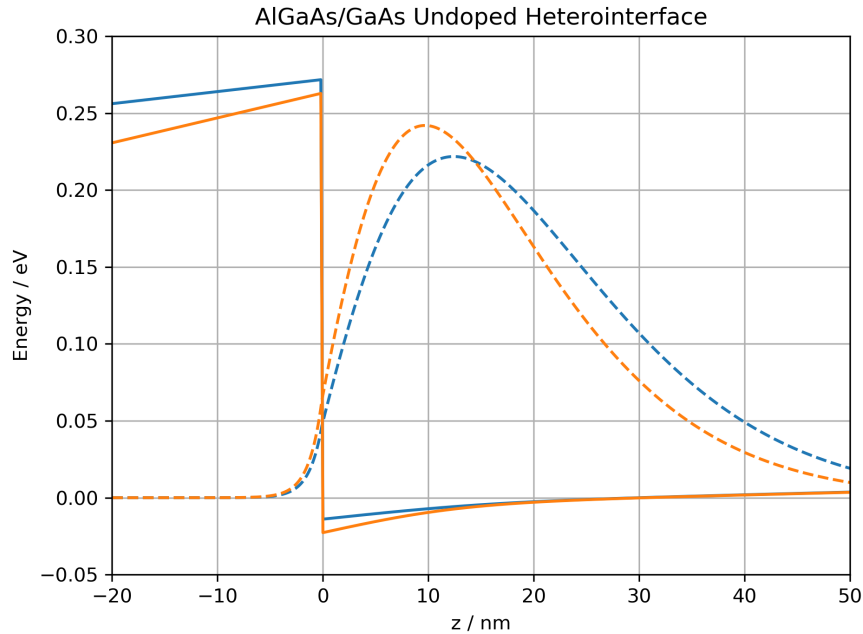


Figure 3.4: nextnano[64] simulation of the conduction band edge of an undoped AlGaAs/GaAs heterointerface at two voltages, 0.9V (blue) and 1.0V (orange). As the voltage is increased, the potential well deepens in energy and narrows towards the interface, drawing the confinement wave function (dashed) closer to the interface.

3.2.1.2 Interface Roughness

The scattering from the AlGaAs/GaAs interface roughness is due to the conduction band offset between GaAs and AlGaAs. The interface has small variations across its surface as the AlGaAs reconstructs on the GaAs. The conduction band offset causes this physical variation in the interface to produce a varying potential. The amount of scattering depends on the density of carriers at the AlGaAs/GaAs interface. As the carrier density increases, the shape of the potential changes, narrowing in space and deepening in energy, figure 3.4, with the end result that the carriers become more confined closer to the AlGaAs/GaAs interface. As with point charge scattering at screening within the carrier gas is more effective at higher carrier densities. While the screening does reduce the effect of the interface roughness unlike point charge scattering the benefit of increased screening at higher carrier density are outweighed by the increase proximity of the carriers to the interface. Therefore, interface roughness scattering becomes more significant at high carrier density, $n_c > 2 \times 10^{11} \text{cm}^{-2}$, limiting the maximum mobilities within a heterostructure[75–77].

Other structures like a quantum well, which consist of a GaAs layer sandwiched between two symmetric layers of AlGaAs, have less scattering from interface roughness. A quantum well structure forms a more square-like symmetric potential well, with the wave function more

centrally positioned. With the wave function in the centre of the potential well, less charge is near the interfaces where roughness causes scattering. For a like-for-like heterostructure and quantum well, the mobility is higher in the quantum well due to the reduced interface roughness scattering.

3.2.1.3 Alloy Scattering

Alloy scattering in a AlGaAs/GaAs heterostructure only occurs for carrier in the AlGaAs spacer near the AlGaAs/GaAs interface. This is due to the penetration of the carrier confinement wavefunction into the AlGaAs barrier. Within the AlGaAs, carriers experience a random potential due to the replacement of gallium with aluminium atoms. Alloy scattering is not significant for low aluminium content AlGaAs/GaAs devices due to the band similarity for AlAs and GaAs, and the small amount of penetration into the spacer layers in both AlGaAs/GaAs heterostructures and quantum wells. For other materials such as InGaAs, alloy scattering is more significant due to the difference in band structures of InAs and GaAs, as well as the conducting channel forming within the InGaAs, such as in an AlGaAs/InGaAs/GaAs quantum well, chapter 7.

For the AlGaAs/GaAs heterostructure, alloy scattering, like interface roughness, is more significant at higher carrier densities when the carriers are ‘pushed’ against and into the AlGaAs spacer layer. Alloy scattering has a similar dependence as interface roughness to the carrier density but has a smaller impact on the mobility.

3.2.2 Standard Assessment

The carrier mobility and density are measured using the Hall effect. A Hall bar consists of a current path with at least three voltage probes to measure the potential difference along the bar, V_x , and across the bar, V_y , figure 3.5. Section 3.2.2.1 outlines the theory of the Hall effect and section 3.2.2.2 discusses experimental considerations.

3.2.2.1 Hall Effect

For a semi-classical system with scattering described by the scattering time, τ_t , the equation of motion for the carriers in the Drude model is,

$$\frac{d\mathbf{p}}{dt} = q(\mathbf{E} + \mathbf{v}_d \wedge \mathbf{B}) - \frac{\mathbf{p}}{\tau_t} \quad (3.2)$$

where the \mathbf{p}/τ_t term accounts for scattering, along with the Lorentz force for a carrier of charge, q , in the presence of an electric, \mathbf{E} , and magnetic, \mathbf{B} , fields. Considering the steady-state

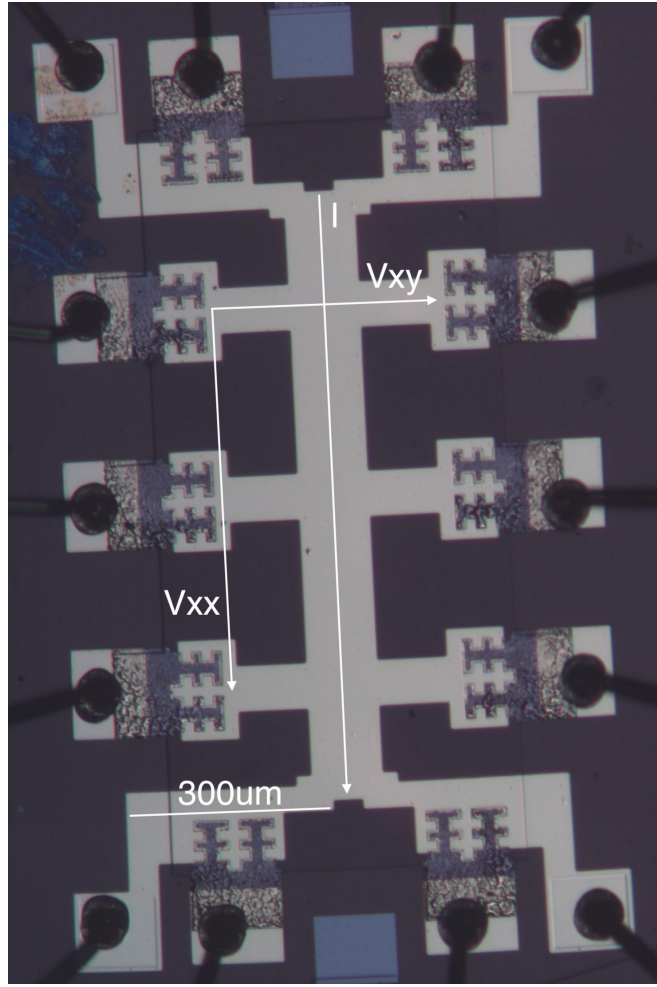


Figure 3.5: Optical image of undoped device with a Hall bar. Bar is oriented with a long edge in the x direction, with length l and width w . A current I is passed along the length of the bar with the longitudinal voltage V_x and the transverse/Hall voltage V_{yy} defined.

situation gives an expression for the electron drift velocity, (3.3).

$$\mathbf{v}_d = \frac{q\tau_t}{m^*} (\mathbf{E} + \mathbf{v}_d \wedge \mathbf{B}) \quad (3.3)$$

The Hall geometry has a magnetic field, aligned along the z-direction, with the carriers in the heterostructure free in the x-y plane. Introducing the current density, $\mathbf{j} = nq\mathbf{v}_d$, the carrier density, n , and calculating the cross product term gives,

$$\begin{pmatrix} j_x \\ j_y \end{pmatrix} = \begin{pmatrix} \sigma_0 E_x + \omega_c \tau_t j_y \\ \sigma_0 E_y - \omega_c \tau_t j_x \end{pmatrix} \quad (3.4)$$

where $\sigma_0 \equiv q^2 \tau_t n / m^*$ and $\omega_c \equiv qB / m^*$. There is no current path in the y-direction, therefore,

$$j_y = 0,$$

$$\frac{E_y}{j_x} = \frac{B}{qn} \qquad \frac{E_y}{E_x} = \omega_c \tau_t \qquad (3.5)$$

Relating these terms to the measurable values, the applied current, I , and the defined voltages V_x and V_y , yields,

$$j_x = \frac{I}{w} \qquad E_x = -\frac{V_x}{l} \qquad E_y = -\frac{V_y}{w} \qquad (3.6)$$

Combining the relations in (3.5) and (3.6) gives the following expression for the carrier density, n_c and the carrier mobility $\mu \equiv v_d E = q\tau_t/m^*$,

$$\rho_{xi}(B) = \frac{V_i(B)}{I} \qquad \rho_{xy}(B) = R_h B \qquad (3.7)$$

$$R_h = \frac{1}{qn_c} \qquad \mu = \frac{R_h}{\rho_{xx}(B=0)} \qquad (3.8)$$

defining the resistance along and across the Hall bar, R_{xi} .

The relations in (3.5) depend on the semi-classical limit and therefore are only valid in weak magnetic fields. For the carrier densities in the devices measured at $< 1.5\text{K}$ the linear relation between Hall voltage and magnetic field, predicted by the carrier density relation, breaks down with fields $> \sim 0.2\text{ T}$. For magnetic fields above this limit, the Quantum Hall effect is required to describe the behaviour of the system, as seen in figure 3.7.

3.2.2.2 Experimental Setup

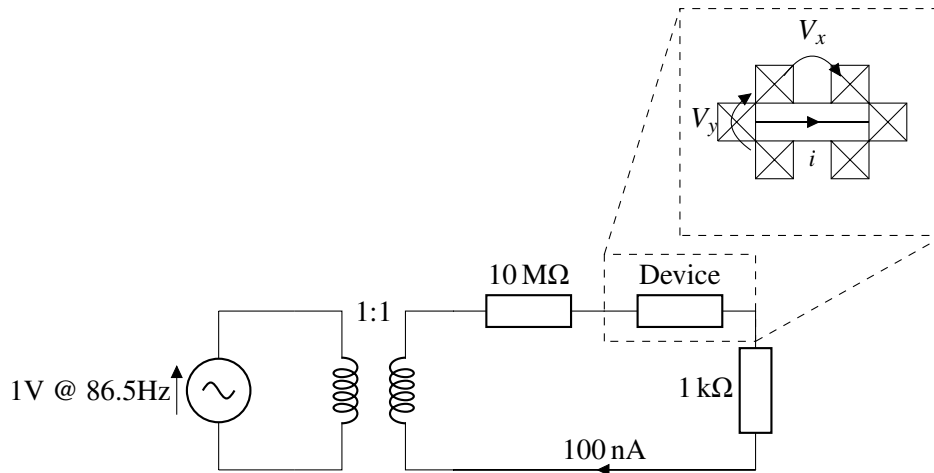


Figure 3.6: Circuit diagram for the standard assessment set up. The device is put in series with a $10\text{M}\Omega$ resistor to keep the applied current at a constant 100nA , measured by the voltage drop across the $1\text{k}\Omega$.

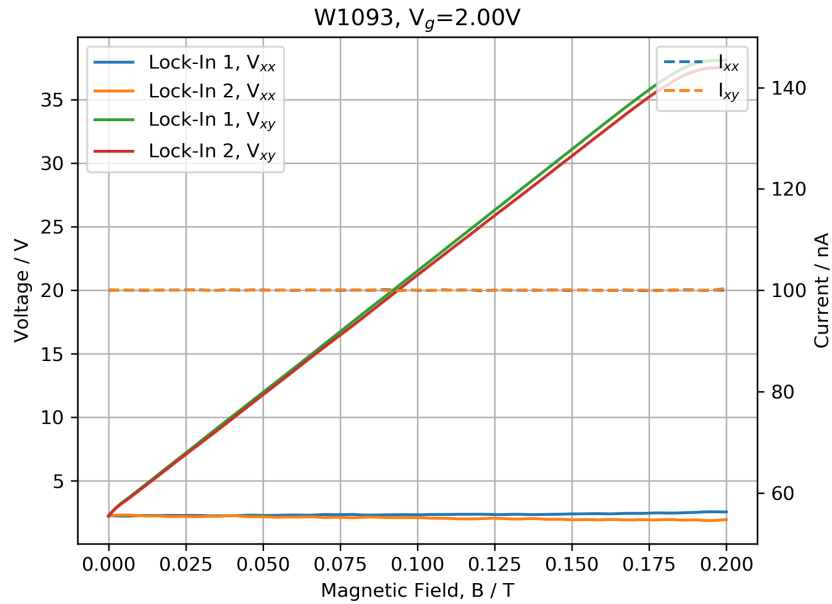


Figure 3.7: A typical set of assessment data, with two traces (solid) for the voltages V_x and V_y from either side of the Hall bar as these were measured simultaneously. The two current (dashed) traces for I_x and I_y are the current passing along the Hall bar when measuring V_x and V_y respectively. There is a small variation between the sides of the Hall bar, which is accounted for in the calculated error in the carrier mobility density data. The current is constant $100.0 \pm 0.1nA$ with the leakage current $-15 \pm 6pA$.

Figure 3.6 contains a circuit diagram of the standard assessment set up. Applying a 1V 86.5Hz AC at signal through a 1:1 transformer decouples the measurement circuit from the voltage source. The device is placed in series, with a $10M\Omega$ resistor to keep the applied current a constant 100 nA, measured by the voltage drop across the $1k\Omega$ resistor. If the resistance of the device is too large, the total resistance of the circuit increases, reducing the current below the expected 100 nA. The input impedance of the lock-in amplifiers used to measure the voltages is $10M\Omega$, therefore when the current is reduced the current path through the device will not be the expected Hall bar geometry, limiting the accuracy of the measurement.

Standard phase-sensitive detection methods with lock-in amplifiers and AC signals are used to measure the device. A source-measurement unit (SMU) is used to apply a voltage to the top gate, relative the ohmic contacts, to induce the carriers while monitoring the current from the top gate to measure any leakage. The device itself is cooled to 1.5K in a pumped 4He cryostat with a superconducting magnet capable of up to 10 T. Figure 3.7 number shows a plot of a typical assessment data set.

3.2.2.3 Operation of the Induced Device and Experimental Considerations

Unlike a doped device, without a potential applied to the top gate of the device, there is no potential well for a 2DEG to form in. By applying a potential to the gate of the device the applied electric field tilts the conduction band and when a sufficient voltage is applied the conduction band falls below the Fermi level at the GaAs/AlGaAs interface resulting in a 2DEG forming in the newly formed potential well.

Once the 2DEG has formed the device operate similarly to a parallel plate capacitor with the top gate and the 2DEG the equivalent of the plates in a capacitor. As the voltage on the gate is changed and more charge is forced onto the top gate with the carrier density in the 2DEG changing to balance the charge. The relationship between the gate voltage and the carrier density is linear, as expected from a parallel plate capacitor.

$$\frac{dn_c}{dV} = \frac{C}{eA} \quad (3.9)$$

there C/A is the capacitance per unit area of the top gate-2DEG system.

There are two chief experimental considerations: charging resulting in hysteresis in the mobility-density curve, and the effect of the cooldown rate. The cooling power of the helium cryostat used for standard assessment is adjusted by a computer-controlled needle valve to set the rate at which ^4He is bleed into the sample space. The position of the valve changes during cooldown based on the sample temperature. A standard cooldown routine adjusts the valve position to follow a reproducible temperature curve on cooldown.

When changing the applied gate voltage, the carrier density follows the linear trend as expected for a capacitor. Increasing the applied voltage past a critical value causes the carrier density to saturate at a constant value when increasing the gate voltage further. When reducing the gate voltage after passing this critical voltage, the carrier density reduces with the same linear trend but a different intercept value. Similar behaviour has been observed in other work with induced structures [78].

When increasing the gate voltage more charge is forced onto the top gate of the device, this must be balanced by an equal amount of charge being induced in the device structure. As the SMU used to apply voltage to the top gate measures a small, approximately constant, current of $\mathcal{O}(10 \text{ pA})$ there is no indication of any charge flow above the critical voltage at which the carrier density saturates. This suggests that there is a layer of trapped charge forming somewhere in the structure of the device and, above the critical voltage charge, is being trapped in this layer rather than populating the 2DEG. Once past the critical voltage, the charging remains stable on a time scale of minutes to hours. A thermal cycle removes any trapped charge and ‘resets’ the device back to the behaviour before passing the critical voltage. The charging of the undoped device sets an upper bound on the carrier density and useful ranges of gate voltage to measure.

A different form of potential charging also effects the ohmic contacts in the undoped device. Unlike a doped HEMT, there is no always-present ‘in-built’ electric field, meaning that until a sufficient voltage is applied to create the conducting channel, the ohmic contacts are all isolated from each other and therefore in principle at different potentials.. When the conducting channel forms, the isolated floating ohmic contacts become connected. The rearrangement of charge, in order to match the potentials of the ohmics contacts, can result in high resistance contacts, thought to be due to trapped charge on the contact surface.

To prevent this potential charge trapping, the standard cool down routine cools the device from room temperature to 1.5K with all contacts and the gate grounded. Grounding the contacts fixes the potential of the contacts to a known equal value. A voltage known to form a conducting channel, $\sim 0.9\text{ V} - 1.1\text{ V}$, is then applied to the top gate of the iHEMT before removing the grounding plugs from the ohmic contacts and connecting the measurement circuit. This procedure ensures that the contacts are kept at a fixed and equal potential throughout the measurement, preventing any charge trapping.

3.2.2.4 Measurement Routine

Cooling to 1.5K takes approximately 40 minutes with a standard cooling routine used for HEMTs. After inducing the 2DEG, measurement of the Hall voltage as a function of the magnetic field between 0 and 0.2T allows the carrier density to be measured. From (3.7), the Hall voltage and carrier density are inversely related. From the Hall voltage measured after inducing the 2DEG with a magnetic field at 0.2T, and the carrier density measured from the gradient of the Hall voltage as a function of magnetic field, the Hall voltage for any carrier density can be calculated.

$$V_y = R_{xy}I = \frac{BI}{qn_c} \rightarrow \frac{n'_c}{n_c} = \frac{V_y}{V'_y} \quad \text{if } B, I \text{ both constant} \quad (3.10)$$

This allows the Hall voltage for a temporary upper limit of the carrier density to be calculated and then found by changing the gate voltage with a fixed magnetic field. This procedure allows for the gate voltage at which the upper limit of carrier density is achieved to be determined quickly, without the need to take a series of magnetic field sweeps measuring the Hall voltage. To determine the lower bound on the top gate bias, the top gate bias is reduced until either the ohmic contacts stop working (indicated by a sudden jump in the phase measured on the lock-ins) or the device’s resistance increases (indicated by a change in the current from the 100nA set by the 10M Ω resistor).

With limits on the top gate voltage, the Hall voltage, V_y , is measured for a range of gate voltages between the limits. By interleaving values of the applied voltage used on the sweep

up to the upper bound on gate voltage and the sweep back to the lower bound, hysteresis or other systematic changes with time can be observed.

3.3 iHEMT MBE Growth Variation

To examine how changes to the growth parameter of the wafer can effect the scattering rate of the 2DEG, a series of wafers were grown varying the As source, Si source temperature and AlGaAs spacer thickness. Table 3.1 contains a summary of the wafers growth with details of the key differences between the wafers and when the wafers were grown. By selectively comparing the carrier mobility-density curves of subsets of these wafers the effects of the use of As₂ compared to As₄ in growth, keeping the silicon source hot throughout growth, higher background impurity density in the AlGaAs spacer only, and thicker AlGaAs spacer layers can be looked at and are detailed in the follow sections.

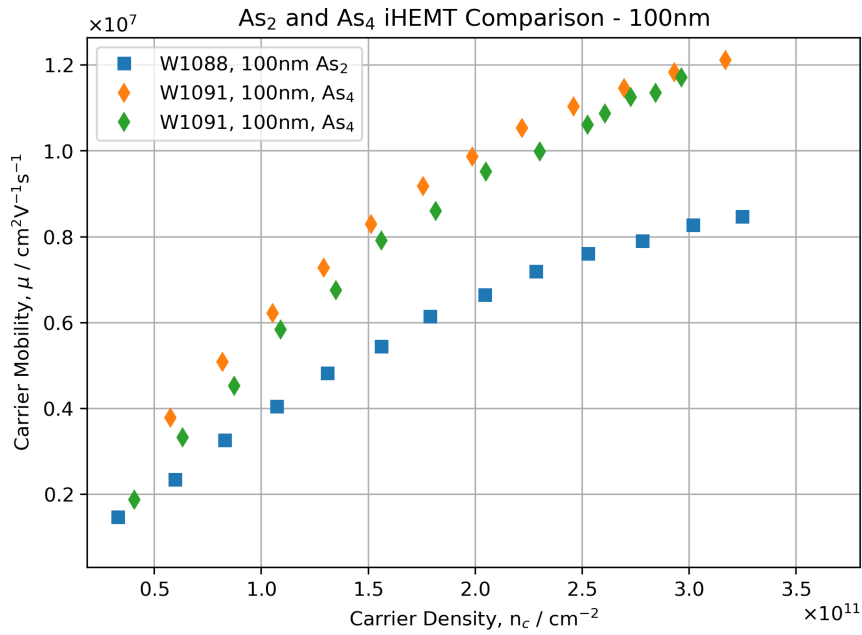
The range of carrier densities and mobilities reported in doped and undoped AlGaAs/GaAs structure varies based on the quality of the particular wafer but typically the carrier density is of the order 10^{11}cm^{-2} [79–84]. In the highest quality material the carrier mobility range between high $10^6\text{cm}^2\text{V}^{-1}\text{s}^{-1}$ and low $10^7\text{cm}^2\text{V}^{-1}\text{s}^{-1}$ [31, 75, 77, 85, 86].

3.3.1 As₂ vs As₄

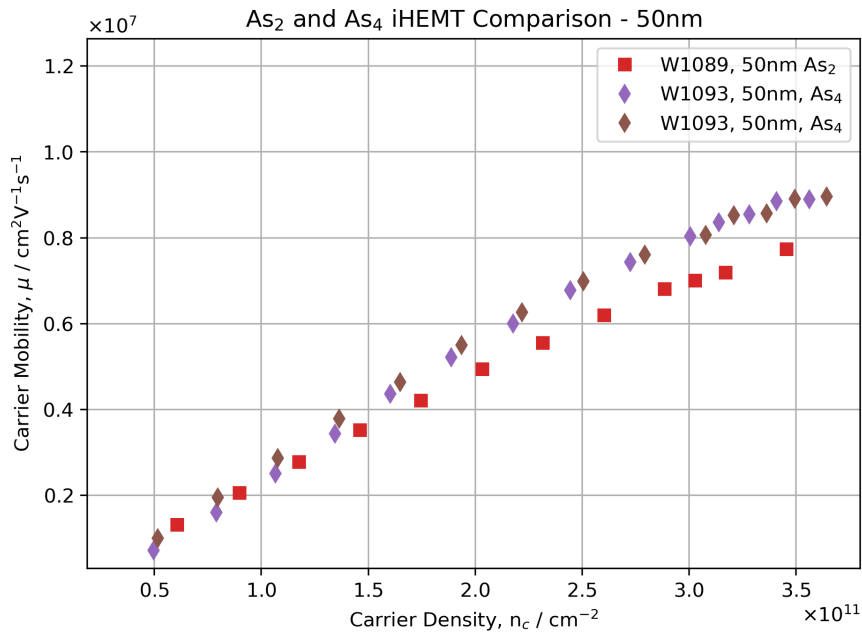
The W-chamber at the Cavendish Laboratory is equipped with a variable temperature arsenic cracker capable of producing two forms of arsenic, either di-arsenic, As₂ or tetra-arsenic, As₄, as a source for growth. The cracker is operated at $\sim 600^\circ\text{C}$ for As₄, lower than the $\sim 900^\circ\text{C}$ for As₂. The lower temperature of the As source is thought to reduce the background impurity level as there is a smaller heat load on the chamber. A series of 50nm and 100nm AlGaAs/GaAs undoped heterostructures were grown sequentially using the cracker on the W-chamber at different temperatures, to examine the difference between using As₂ as the source compared to As₄. A standard set of carrier mobility-density curves were measured at 1.5K using the method described in 3.2.2, shown in figure 3.8.

The first thing to note about the mobility-density curves in figure 3.8 is the lower mobility of the 50nm AlGaAs spacer layer devices (triangles) compared to the equivalent 100nm spacer devices (squares). This reduction in mobility is due to the increased scattering from the surface charge for a carrier gas 60nm below the surface of the device, compared to a carrier gas 110nm below the surface.

Comparing the As₂ and As₄ 100nm spacer devices, W1088 and W1091, the As₄ (W1091) has higher mobilities over the entire range of carrier densities. At the highest carrier densities, the As₄ device has a 43% increase in mobility compared to the As₂ device. At the lowest carrier



(a) 100 nm iHEMT



(b) 50 nm iHEMT

Figure 3.8: As₂ (square) and As₄ (diamond) iHEMT comparison for 100 nm and 50 nm Al_{0.33}Ga_{0.67}As/GaAs undoped heterostructures. The As₄ devices had a higher yield of working devices allow two different devices to be measured.

Wafer ID	Growth Date	AlGaAs Spacer Thickness / nm	Growth Detail	Comparison
First Batch				
W1088	18/08/2015	100	As ₂ control	Si cell and As ₂ vs As ₄
W1089	18/08/2015	50	As ₂ control	Si cell and As ₂ vs As ₄
W1090	18/08/2015	100	As ₂ , Si cell hot	Si cell
W1091	24/08/2015	100	As ₄	As ₂ vs As ₄
W1093	24/08/2015	50	As ₄	As ₂ vs As ₄
Second Batch				
W1161	19/02/2016	100	As ₄ , Si cell hot	Si cell
W1162	19/02/2016	100	As ₄ , control	Si cell
W1170	08/03/2016	100	Lightly doped AlGaAs spacer	AlGaAs spacer Background
W1171	08/03/2016	100	Control for W1170	AlGaAs spacer Background
Third Batch				
W1283	13/12/2016	225	As ₂ 225nm iHEMT	AlGaAs spacer thickness
W1284	13/12/2016	150	As ₂ 150nm iHEMT	AlGaAs spacer thickness
W1285	13/12/2016	300	As ₂ 300nm iHEMT	AlGaAs spacer thickness

Table 3.1: Summary of all undoped wafers grown to examine the effects of As source, Si cell temperature during growth, higher background impurity in AlGaAs spacer, and AlGaAs spacer thickness.

density the mobilities of the As₂ and As₄ approach the same value of $\sim 1.6 \times 10^6 \text{cm}^2 \text{V}^{-1} \text{s}^{-1}$. It is well established[31, 87–90] that background impurities are the dominate source of scattering for these types of devices at low density, however a discussed in section 3.2.1 there are multiple scattering mechanisms within these structures, makes analysis of the mobility-density curves more involved.

From Matthiessen's rule [91] the total mobility is given by $1/\mu = 1/\mu_{BI} + 1/\mu_{IR} + 1/\mu_{SC}$, considering only the contribution scattering from background impurities, interface roughness and surface charge. The scattering rates for background impurities and surface charge both scale with the density of impurities/charges respectively, therefore the mobility contributions from each can be described by $1/\mu_{BI} = Nf(n_c)$ and $1/\mu_{SC} = \sigma g(n_c)$, where N and σ are the impurity and charge densities and $f(n_c)$ and $g(n_c)$ account for the details of the scattering mechanisms and screening. Details about $f(n_c)$ and $g(n_c)$ are discussed in chapter 5 but for the moment the scaling of the scattering rates is sufficient to understand the shape of the mobility-density curves. With these scaling for the mobilities and introducing $1/\mu_{IR} = h(n_c)$ for the interface roughness, the gradient of the mobility-density curve is given by,

$$\frac{\partial \mu}{\partial n_c} = -\mu^2(Nf'(n_c) + h'(n_c) + \sigma g'(n_c)) = \frac{Ne f'(n_c) + h'(n_c) + \sigma g'(n_c)}{(Nf(n_c) + h(n_c) + \sigma g(n_c))^2} \quad (3.11)$$

Assuming that the background impurity is dominate with little contribution from surface charge, as for the 100nm spacer devices, W1088 and W1091, then this expression can be reduced to,

$$\frac{\partial \mu}{\partial n_c} = \frac{1}{Nf(n_c)} \left[\frac{f'/f + h'/Nf}{(1 + h/Nf)^2} \right] \quad (3.12)$$

This expression highlights that it is not just the absolute value of the mobility which depend on the impurity density but the gradient of the mobility-density curve as well. Therefore the gradient of the curve must also be considered when looking at the data in figure 3.8 This statement is a simplification as clearly this depends of the functions $f(n_c)$, $g(n_c)$ and $h(n_c)$, particularly their derivatives, but the more detailed analysis in chapter 3.2.1 agrees with this somewhat simplistic approach.

Therefore when considering the value of the mobility and the gradient and comparing the As₂ and As₄ wafers, although at carrier densities below $\sim 1 \times 10^{11} \text{cm}^{-2}$ the mobilities appear to tend towards the same value the greater gradient of the As₄ wafers indicates that there is a lower background impurity density in the As₄ wafers. The agreement of the mobilities below $\sim 1 \times 10^{11} \text{cm}^{-2}$ may be due to other scattering mechanisms becoming more sufficient and this is certainly true for the 50 nm spacer devices where surface charge is important. However, surface charge is not as significant for the 100 nm devices, as shown by the higher overall mobility. The better mobility in the As₄ material runs counter to Arsenic species various found in literature[92–97] all of which favoured As₂ over As₄. However these worked looked at the

mobility in doped GaAs structure and as noted by Chand et al[98] the purity of sources has improved and forces reconsideration of the conclusion from earlier works. Growth variations focusing on arsenic cracker temperatures[93, 99] show better mobility at lower cracker temperature, however it worth noting that the cracker temperature can control the As₂ to As₄ ratio depending of the design of the MBE chamber.

Another consideration for the 100 nm devices at densities $\leq 0.5 \times 10^{11} \text{cm}^{-2}$ is whether the carrier gas is fully continuous and well defined. At these low carrier densities the two terminal resistance of the device can rise slightly and it is therefore possible that the carrier gas is not as well defined as at higher carrier densities. This would have implications for the Hall bar geometry, particularly the length to width ratio which is assume to be defined by the top gate. If the length to width ratio changes at such low densities this would cause in accuracies in the mobility measurement.

In a 2DEG scattering from the interface roughness is expected to become significant at carrier densities $\gtrsim 2 - 3 \times 10^{11} \text{cm}^{-2}$ and can become the dominant source of scattering. In this dataset, it is difficult to conclude that interface roughness becomes dominant at the highest carrier densities, as the mobility curves are only just starting to approach a potential turning point and data for higher carrier densities could not be obtained due to the carrier density saturating, see 3.5 . It is difficult to see much difference between the curvature of the As₂ and As₄ as the mobility-density curve is in a region where the background impurity is more significant than the interface roughness, but the lack of clear difference in the curvature of the curves suggest that the interface roughness in As₂ and As₄ is comparable, however a more detailed analysis is required.

For both As₂ and As₄ the 50nm devices have a lower mobility than the 100nm devices due to scattering from the surface charge. Comparing the difference between the As₂ and As₄ in the 100nm and 50nm device separately, the As₄ devices have the higher mobility but the difference between the As₄ and As₂ mobility is less pronounced in the 50nm devices. The general trend of the 50nm mobility curves is the same as the 100nm devices, with the As₂ having lower mobilities over the range of carrier densities due to a higher background impurity density than the As₄ source. At the lowest carrier densities, $< 1 \times 10^{11} \text{cm}^{-2}$, the As₂ and As₄ 50nm devices' mobilities are much closer in value than the 100nm devices. The similarities of the 50nm mobilities at low carrier density are evidence that surface charge limits the mobility at these low densities.

The two 100nm As₄ devices show a small difference in the mobilities. While the difference in mobility is small, 4%, it raises the question if this variation is due to a variation in the wafer, variation in the processing, or a cool-down dependence variation.

3.3.1.1 Effect of the Si Cell

As the background impurity density limits the mobility of an undoped HEMT, it is possible to use them to examine the effects of changes in the growth parameters in the MBE system. A pair of wafers were grown on the same day to examine the effect of keeping the silicon cell hot throughout the growth. Typically, the growth of a HEMT is paused between the spacer layer and the doped region, to heat the silicon cell. While the silicon cell is hot, it may outgas significantly, adding impurities into the AlGaAs spacer, or potentially effect the reconstruction of AlGaAs on the GaAs surface at the interface. However, if the silicon cell could be kept warm throughout the growth, this would allow the uninterrupted growth of the HEMT.

For comparison to W1088, a 100nm AlGaAs spacer As₂ *i*HEMT, W1090, was grown with the same structure and using the same method but with the silicon cell at 1200 °C throughout the growth, a typical temperature for the growth of a doped HEMT. At a later date, W1161 and W1162 were grown using As₄ for the same comparison. Figure 3.9 contains the mobility-density curves for W1088, W1090, W1161 and W1162. The mobility-density curves show that there is no measurable effect due to keeping the silicon cell warm during growth, as the difference between the wafers is less than the variation seen between different devices on the same wafer.

The data in figure 3.9 appears to contradict the As₂ vs As₄ result, as both arsenic sources give the same mobility and are in good agreement at the lowest carrier densities where background impurities are the dominant scattering mechanism. However, the wafers were grown six months apart, with 71 other samples grown in the chamber in the intervening time. The agreement with all the devices at the lowest carrier densities indicated that the background impurity density in these samples is very similar, indicating the ‘cleanliness’ of the MBE chamber has reduced over the six months in between the growth of W1088 and W1161, to a point where the improved mobility seen in W1091 grown with As₄ at the same time as W1088 has now been lost. Therefore if As₂ samples had been growth at the same time as W1161 the mobility would be expected to be lower than the mobility of W1088, even if the samples were grown nominally as identical repeats of W1088.

3.3.2 Intentional Doping of the AlGaAs Spacer Layer

All of the *i*HEMT mobility-density curves are consistent with the mobility being limited by background impurities, with interface roughness scattering becoming significant at higher carrier densities, causing a decrease in the slope of the mobility curve, but not a turning point. Reducing the background impurity density within the undoped device would increase the mobilities over the whole range of carrier densities.

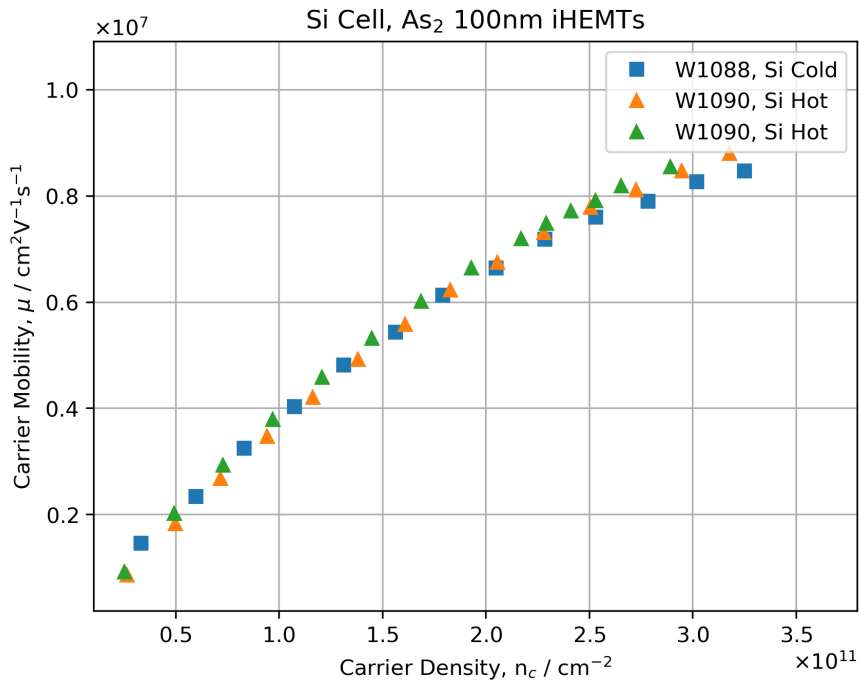
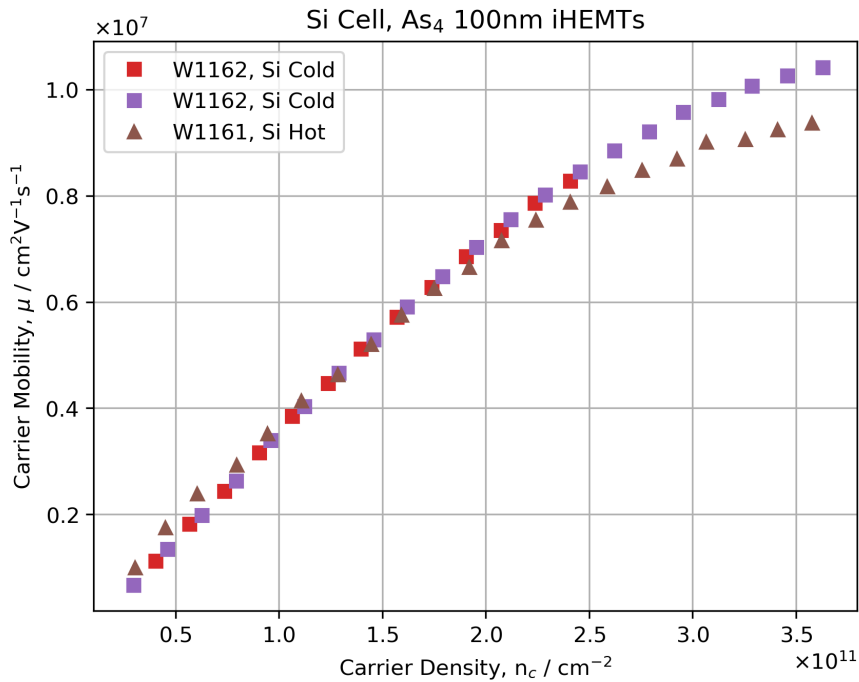
(a) As₂, 100 nm iHEMT(b) As₄, 100 nm iHEMT

Figure 3.9: Mobility-density curves from W1088 (As₂), W1090 (As₂), W1161 (As₄) and W1162 (As₄), 100 nm iHEMT devices. Comparing the effect of keeping the Si cell cold (square) or hot (triangle) during growth but with the Si cell shutter closed. The As₂ and As₄ samples were grown six months apart and an increase in the growth chambers impurities levels in that times explains the lower As₄ mobilities.

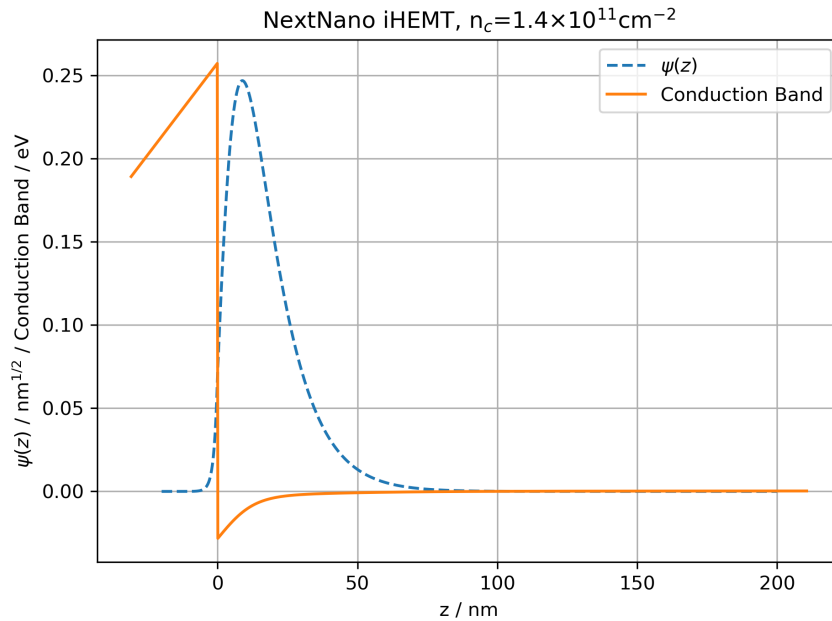


Figure 3.10: nextnano[64] output for a simulated AlGaAs/GaAs induced heterostructure, showing the ground state and the conduction band at the Γ point.

The background impurity level has two components, the density in the GaAs buffer and the density in the AlGaAs spacer. The impurity densities of the GaAs and AlGaAs are not necessarily equal, with the AlGaAs layer expected to have a higher density due to high reactivity of aluminium, and the increased growth rate: $1.5 \mu\text{m h}^{-1}$ compared to $1.0 \mu\text{m h}^{-1}$ for the GaAs buffer. Another significant difference is the confinement of the carriers in the growth direction. Figure 3.10 contains a figure of the calculated conduction band edge and (amplitude) ground state for the iHEMT structure using nextnano[64], showing that the majority of the confinement in the growth direction is in the GaAs, with only a small penetration into the AlGaAs layer. The confinement of carriers causes more scattering from the GaAs background impurities than the AlGaAs density, due to the proximity of the carriers to the impurities.

Due to the combination of higher background impurity density in the AlGaAs but a lower scattering rate due to the confinement of carriers in the growth direction, it is unclear how significant the scattering due to the AlGaAs background impurity density is. If the AlGaAs background impurity density is a significant source of the background impurity scattering, then one strategy to reduce the background scattering is to use a lower aluminium fraction such as 20% or 10%.

To measure if the AlGaAs background is a significant source of scattering a 100nm As_4 iHEMT, W1170, was grown with deliberate silicon doping nominally^c with a density of $1 \times$

^cDoping levels are based on doping of bulk GaAs grown at $1 \mu\text{m s}^{-1}$. There are secondary effects to take account

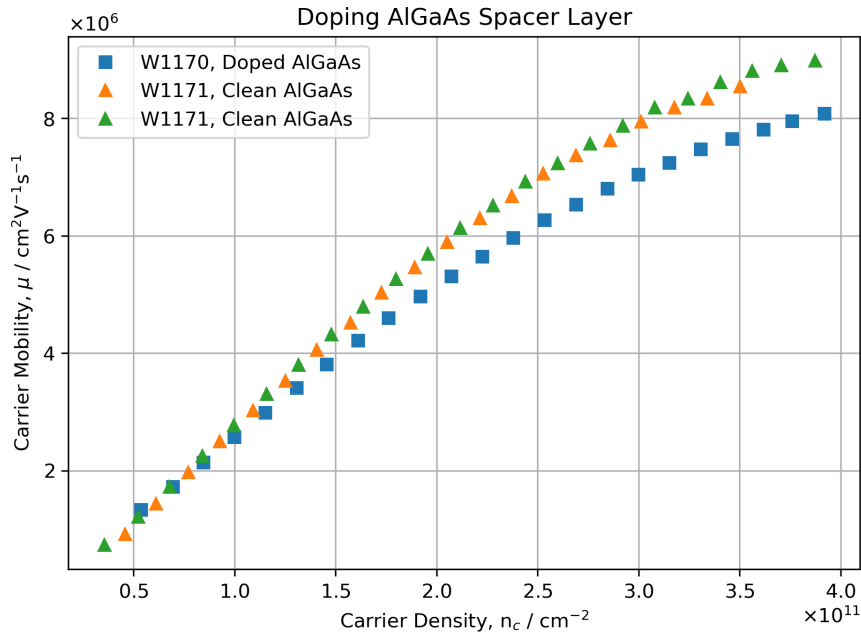


Figure 3.11: Electron mobility-density curves from W1170 and W1171, both 100nm AlGaAs spacer As_4 iHEMTs. W1170 was grown with deliberate dopants added to the AlGaAs spacer layer to increase the background dopant density in the AlGaAs only, in comparison to the control W1171.

10^{15}cm^{-3} added to the AlGaAs spacer to create a higher background density. A control wafer, W1171, was grown at the same time for comparison. The mobility-density curves are in figure 3.11. The curves show a small reduction in the mobility of W1170 compared to W1171 which based, on the gradient of the mobility curves at low carrier density, is in part due to a small increase in background impurity level. The reduction of $\sim 10\%$ in mobility at high carrier density could be due to an increase in background impurity density but also could be due to a change in the interface roughness. As with W1088 and W1091, it is difficult to form conclusions about the interface roughness, but the main difference between the two wafers is due to the added dopants. Therefore, these mobility-density curves suggest that strategies that focus on reducing impurities in the AlGaAs layer over GaAs could result in a small but notable increase in mobility.

3.3.3 Thickness of AlGaAs Spacer

Based on the result that the AlGaAs spacer background does have a small but meaningful impact on the mobility of an induced heterostructure, a series of wafers were grown to see if the thickness of the AlGaAs spacer layer impacts the mobility.

of when doping AlGaAs which make this doping an approximation

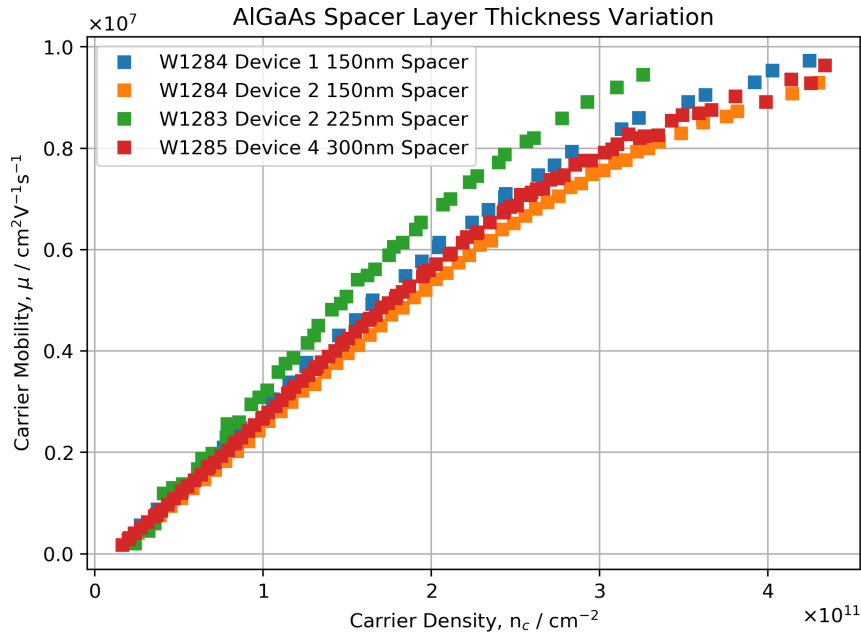


Figure 3.12: Mobility-density curves for iHEMTs with 150nm, 225nm and 300nm AlGaAs spacer thickness.

Figure 3.12 contains the mobility-density curves for three iHEMT wafers with 150nm, 225nm and 300nm AlGaAs spacer layer thicknesses. The thickness of the AlGaAs spacer does not have a significant impact on the mobility of the carrier gas for densities lower than $1 \times 10^{11} \text{cm}^{-2}$. Interestingly, the mobilities of all three wafers are very comparable, indicating that, once a carrier gas is deep enough, the surface charge is not significant and the background impurity limits the mobility.

Notably the 225 nm spacer device as a mobility which is approximately 10% higher at $\sim 3 \times 10^{11} \text{cm}^{-2}$. Based on the shape of the mobility-density curve the 225 nm spacer device appears to have a lower background impurity level than the 300 nm and 150 nm. However, it is not clear why this is the case. Assuming that the background impurity level is approximately constant throughout the structure then the effect of increasing the spacer layer thickness would be to remove the effect of surface charges by increasing the distance between the carrier gas and surface. Therefore we might expect the result of this growth variation to have the lowest mobility in the 150 nm spacer with the mobility increasing with spacer layer thickness or potentially remaining constant once the carrier gas is sufficiently deep enough that surface effects are no longer important. Similar trends have been measured in doped Quantum wells[81, 100–102].

This is all based on the assumption that the background impurities level is constants which may not be true. It is possible that the 225 nm spacer device is a balancing between improvement mobility from a deeper structure and a reduction in mobility from a thicker $\text{Al}_{0.33}\text{Ga}_{0.67}\text{As}$.

However, with measurement from the single functional 225 nm it is also possible that this device has a anomalously high mobility which is hiding the true trend that mobility is approximately constant between 150 nm and 300 nm thickness of spacer material. Equally possible that the single 300 nm device has a anomalously low mobility and could be hiding the expected trend of improved mobility for deeper structures. Without repeat measurement of new devices and a potential repeated growth variation it is difficult to draw a conclusion from this data.

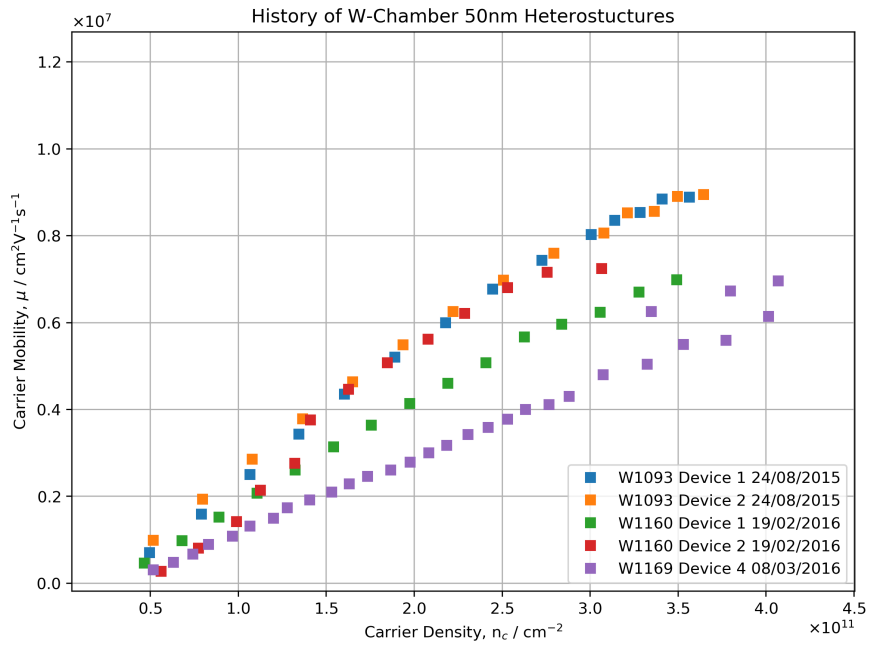
3.3.4 History of MBE Chamber

At the Cavendish Laboratory, standard doped heterostructure 3.1a are grown and processed into HEMT, which through a standard measurement similar to the one used for the iHEMT, give values for the carrier density and mobility of the HEMT device. These devices grown periodically are used to characterise the state of the chamber throughout the growth campaign. iHEMTs are not affected by dopants like the HEMT because there are no intentional dopants in the structure. Therefore characterisation with iHEMTs gives information about the background state of the MBE chamber exclusively.

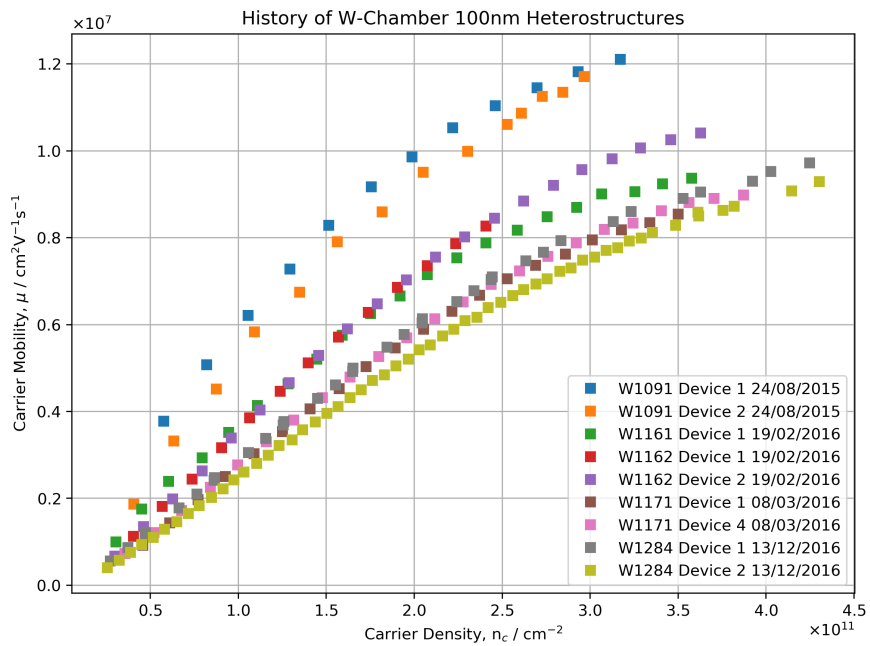
Figure 3.13 contains the density-mobility curves for all 100nm and 50nm As_4 undoped heterostructure wafers grown between October 2015. These wafers had material fabricated into iHEMTs, with carrier mobility and carrier density measured using the standard method at 1.5K. The mobility curves indicate that the background impurity level of the W-chamber increased between the end of 2015 and the end of 2016 as the mobility of the iHEMT device reduces, noting the reduction of the mobility at low carrier density to isolate the effects of background impurity density from the effect of interface roughness. The 50nm devices show the same general trend as the 100nm device.

3.4 Variation Due to Cool-down

The mobility-density curves from the iHEMT devices in the previous sections showed a variation between devices on the same wafer. These variations, while small, $\sim 5\%$, are comparable to some of the measured effect due to changes in the MBE growth conditions. As the devices are on a $7\text{ mm} \times 5\text{ mm}$ piece of the wafer, these variations are unlikely to be due to variations in the 3" wafer grown. Figure 3.15 shows the mobility-density curves from an iHEMT device from W1171 which was cooled down multiple times. The cool-down of the sample used a computer-controlled needle valve which adjusted the He flow into the sample space depending on the temperature of the sample. While this means that the cool-down is somewhat reproducible, as the temperature of the thermometry on the sample probe controls the cool-down rate, the thermometry on the probe is not in direct contact with the sample and therefore is



(a) 50nm As₄



(b) 100nm As₄

Figure 3.13: Mobility-Density curves for 100nm and 50nm As₄ iHEMTs for wafers grown between October 2015, showing how the ‘cleanliness’ of the chamber reduced in 2015 - 2016.

not necessarily in perfect thermal equilibrium. The possible difference in temperature between the sample and thermometry, combined with the limited control of the cooling power with the needle valve, causes some variation between cool-downs.

To further explore the effect of the cool-down, a sample from W1171 underwent multiple cool-downs using the standard cool-down routine, as well as cooling the sample over a more extended time. Reducing the helium flow with the needle valve slows the cooling rate, but the degree of control is limited. The temperature and cooling rate curves, figure 3.14, show an average cooling rate of $\approx 0.1\text{Ks}^{-1}$ for all three different cool-downs. Lowering the helium flow reduced the peak cooling rate, from $\approx 0.45\text{Ks}^{-1}$ to $\approx 0.25\text{Ks}^{-1}$.

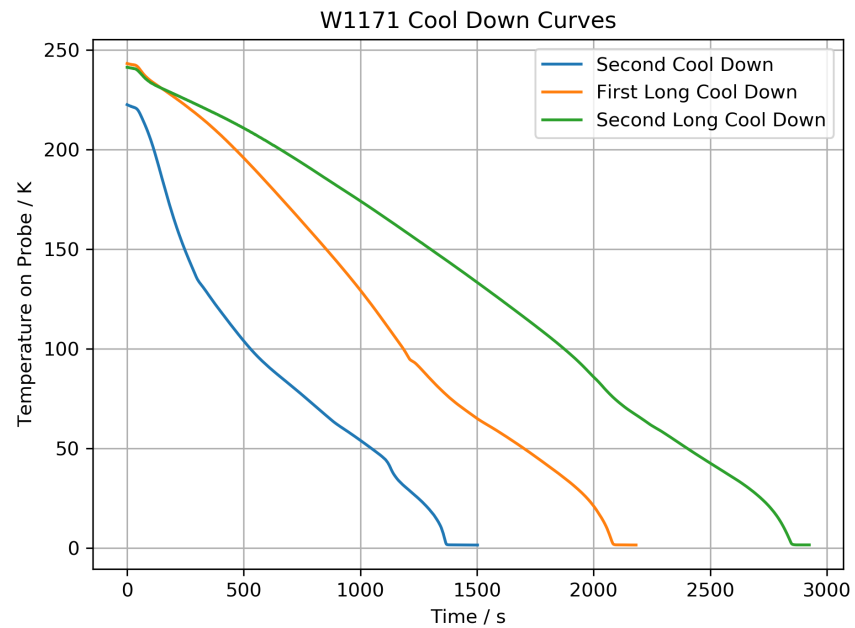
As figure 3.15a shows the mobility of the same device varies by a small amount between cool-downs. By calculating the mean mobility as a function of carrier density, the percentage variation from the mean mobility, figure 3.15b, shows a $\sim 4\%$ variation from the mean on average. The percentage variation is larger at lower carrier density due to the lower mobility. The absolute variation is $\leq 3 \times 10^5 \text{cm}^2\text{V}^{-1}\text{s}^{-1}$ for all cool downs. This variation is critical to keep in mind when interpreting the MBE growth variation results in the previous section.

As the sample cools from room temperature, charges in the structure from impurities become trapped and frozen in a particular configuration forming the background potential of the device. This results in the mobility variation seen in W1171 and the increased variation at lower density is consistent with this, as the carrier gas screening of the background potential is reduced at lower carrier densities, so background potential variations would be more significant at low carrier densities.

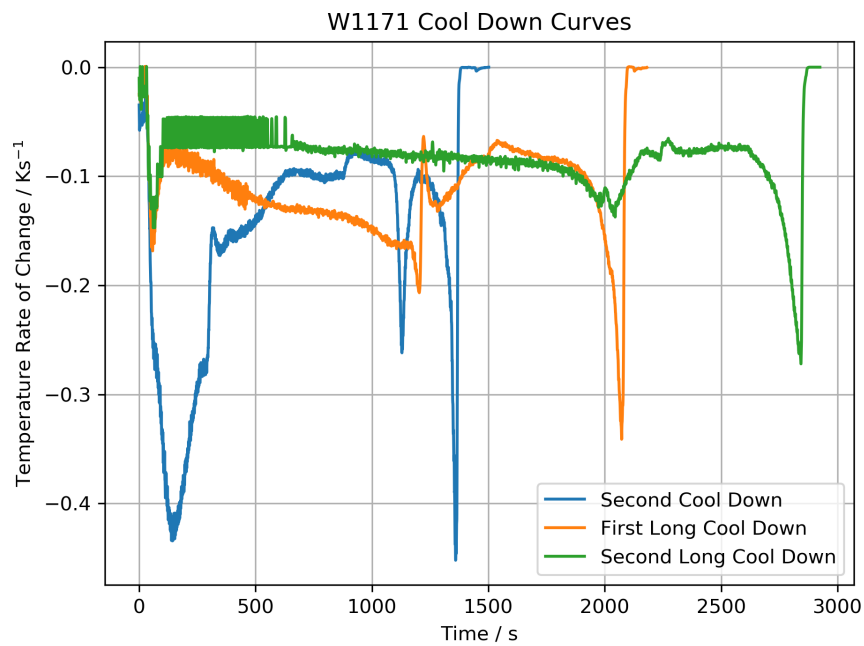
3.5 Carrier Density Limit

The point at which the iHEMT device has a resistance of the order of $10\text{M}\Omega$ sets the lowest carrier density measurable. Once the resistance of the device is comparable to $10\text{M}\Omega$ the current path through the device is ill-defined, due to the $10\text{M}\Omega$ input impedance on the lock-in amplifiers. For this design of iHEMT with a single global top gate, it's not clear if the device's resistance is due to the carrier gas no longer being continuous or if there is no longer a good ohmic contact with the carrier gas. It is, therefore, possible that iHEMTs designed with two separate gates, a set of bridging gates to induce carriers around the ohmic contacts ensuring good contact and a central gate controlling the carrier density in the Hall bar, would allow for lower carrier densities to be measured, if the ohmic contacts are the limiting factor.

Ultimately the breakdown voltage of the insulating layer between the contacts and the top gate sets the upper carrier density limit. For the Al_2O_3 used for the iHEMT device, the breakdown voltage is much higher than the voltages used for carrier densities measured, $> 10\text{V}$.

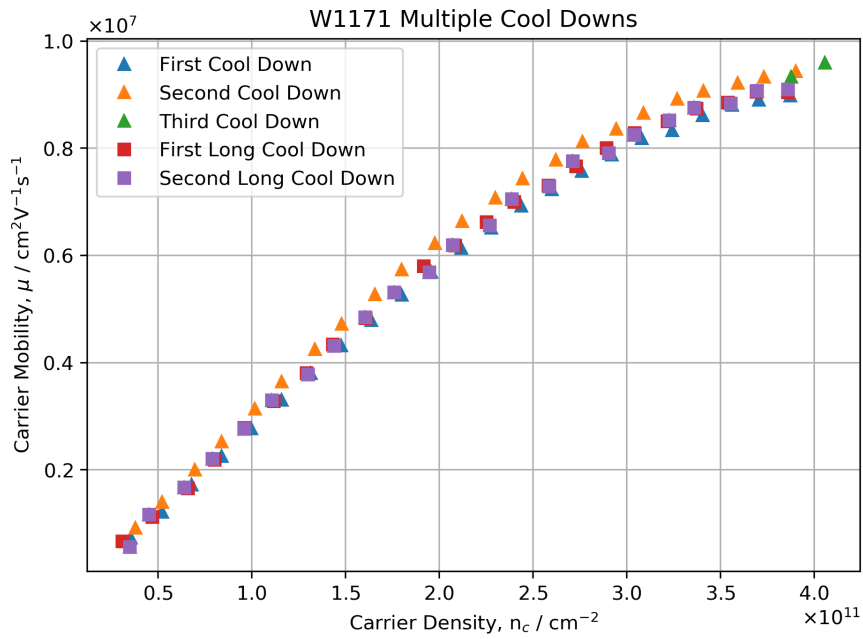


(a) Temperature

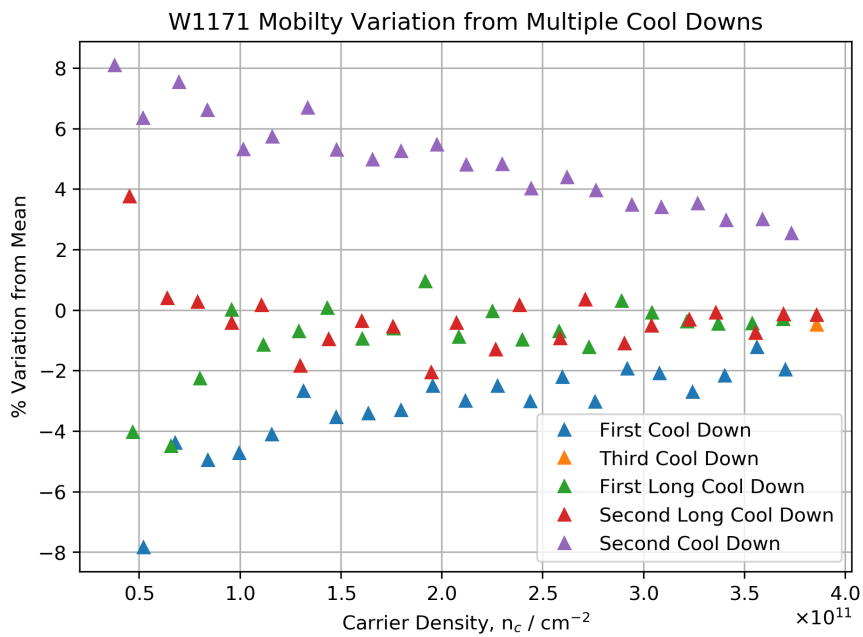


(b) Cooling Rate

Figure 3.14: The cool down curves for W1171 for the three different cool down routine performed on W1171 device 4. While the average cooling rate for all three is $\approx -0.1\text{Ks}^{-1}$, the peak cooling rate was reduced by slowing the cool-down.



(a) Mobility-Density



(b) % Variation

Figure 3.15: Carrier mobility-density curves from W1171 Device 4 for multiple cool-downs. The device was cool-down three times using the standard cool-down routine and twice using a longer cool-down by reducing the He flow use to cool the sample.

	Before Charging	After Charging
Capacitance per unit area / $\text{pF}\mu\text{m}^{-2}$	$(6.84 \pm 0.03) \times 10^{-8}$	$(6.97 \pm 0.03) \times 10^{-8}$
Voltage Offset / V	0.81 ± 0.01	0.86 ± 0.01

Table 3.2: Linear Fit parameters of carrier density as a function of gate voltage, before and after charging in W1160, 50nm AlGaAs spacer As_4 iHEMT.

The meaningful limit on the carrier density for the iHEMTs is due to charge traps within the device. For regular operation, the relation of the applied gate voltage to the carrier density induced in the device follows from a simple capacitive model. The global top gate and the carrier gas form a capacitor where the capacitor equation (3.13) relates the potential on the top gate and the charge in the carrier gas.

$$\begin{aligned}
 Q &= CV \\
 n_c eA &= C(V - V_{threshold}) \\
 \frac{dn_c}{dV} &= \frac{C}{eA}
 \end{aligned} \tag{3.13}$$

Therefore the carrier density is linearly dependent on the applied gate voltage with a gradient set by the capacitance per unit area of the device and an offset due to the finite voltage at which the carrier gas forms, where V_t is the voltage at which $n_c = 0\text{cm}^{-2}$.

At some voltage, the carrier density is no longer linearly dependent on the applied gate voltage, and the carrier density saturates at a fixed value, figure 3.16. This behaviour has been observed before in undoped devices[9] but with different insulating material. The mobility-density curve shows that the mobility increases after the carrier density has saturated, indicating that the carrier saturation may have coincided with the neutralisation of some charge traps. The carrier density-voltage graphs show the expected linear relation before and after carrier saturation. Capacitance per unit area and voltage offset are summarised in table 3.2, calculated from linear fits of the carrier density against voltage. The voltage offset shifted by 0.05V after saturation and the capacitance per unit area increased by $0.13 \times 10^{-8}\text{pF}\mu\text{m}^{-2}$.

Figure 3.16b shows that increasing the gate voltage above a critical value results in no additional carriers being induced in the conducting channel gas. Instead, the charge is becoming trapped within the device. The most likely location of these charge traps is at the GaAs surface/ Al_2O_3 interface. Once trapped, the only method to remove the charge from these traps is to cycle the device thermally. The results from W1160 indicate that, for a 50nm iHEMT, which is known to have a mobility limited by surface charge, pushing charge into the interface charge traps results in a decrease in scattering and an increase in capacitance, seen by the increased gradient in figure 3.16b.

The measured decrease in scattering and increase in capacitance seen in the increased mo-

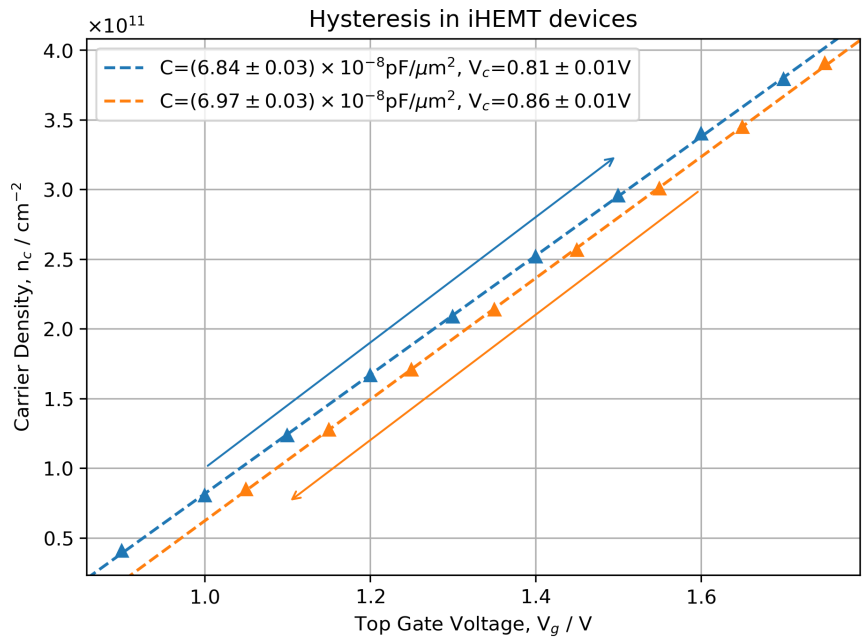
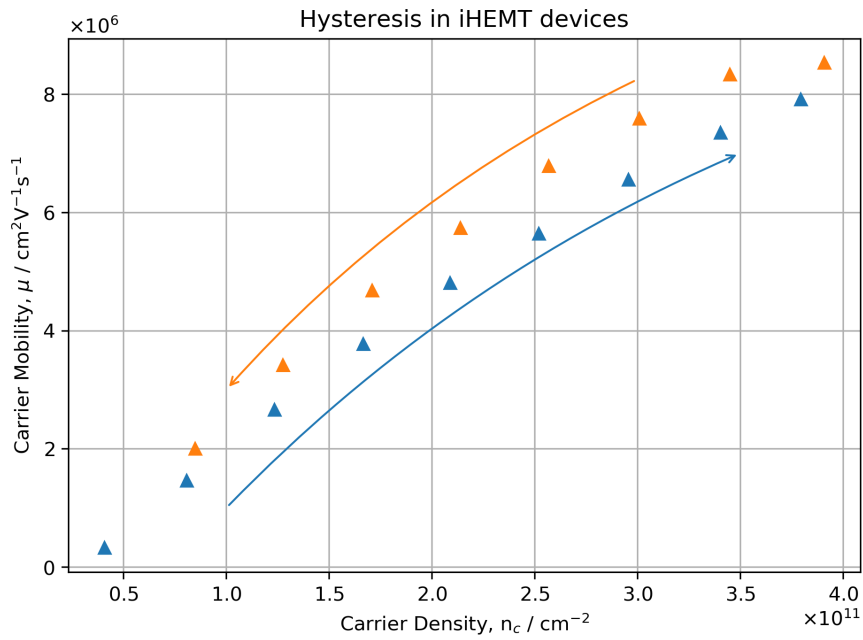


Figure 3.16: Carrier mobility-density curve and density-voltage curve for W1160 before (blue) and after (orange) carrier density saturation occurred.

bility and increased gradient from figure 3.16, may be an indication of some charge trap neutralisation by the rearrangement of the trapped charge. The increased mobility clearly indicates a reduction in the scattering in W1160, but at the lowest carrier densities the mobility remains unchanged and therefore the background impurity density is unchanged. As the increased mobility is significant at carrier densities around $1 \times 10^{11} \text{cm}^{-2}$, scattering from the interface roughness is not the cause of this change in mobility. Therefore the remaining cause of scattering is scattering due to surface charge density. The potential of neutralising interface charge traps opens up the possibility of a device tuning process by pushing the gate voltage above this critical value at which this charging occurs, to reduce scattering from interface charge traps. While this charging of the interface may be a method for increasing the mobility of shallow devices, the maximum carrier density achievable is fixed by the point at which charge no longer is pushed into the carrier gas.

3.6 Conclusions

In conclusion, point charge scattering from impurities and surface charge, and scattering from interface roughness, limit the mobility of undoped high mobility electron transistors measured at 1.5K. The surface charge is the limiting source of scattering in shallow 50nm devices. The carrier mobilities within the structures are comparable to the highest report mobilities for Al-GaAs/GaAs heterostructure[14, 89, 90, 103–105]. Point charge scattering dominates at low carrier densities, with scattering from interface roughness becoming significant at high carrier densities, limiting the maximum mobility of the devices, causing the mobilities-density curves to approach a turning point at the highest densities.

Impurities in the structures are the dominant source of scattering for deep structures $>100\text{nm}$. Standard characterisation of these deep structures measures the mobility which at low carrier density is proportional to the density of impurities. Therefore, standard characterisation of these structures gives information about the background impurity level of the MBE grown chamber.

Changes in the growth parameters can change the impurity levels in the MBE chamber, which changes the mobility of the undoped devices. Undoped devices, therefore, can be used to track the condition of the MBE chamber over time. From the iHEMT mobility-density curves, comparing wafers grown with As_2 and As_4 the As_4 wafers had a lower background impurity density, perhaps due to the lower temperature of the cracker, when using As_4 , causing less outgassing within the chamber. Comparing the effect of keeping the silicon cell hot but closed during the growth of material showed no detectable change in the impurity level in the material, opening the possibility of keeping the silicon cell hot during the growth of doped

structures avoiding having to pause the growth to heat the silicon cell.

The background impurities limit the mobility of the induced device. Strategies to reduce the impurities are needed to improve the maximum mobility of the GaAs heterostructure. Due to the shape of the confinement of carrier in the growth direction and different growth rates and materials in the AlGaAs and GaAs, impurities in each contribute a different amount to the impurity scattering. By doping the AlGaAs spacer within an undoped device with $1 \times 10^{15} \text{ cm}^{-3}$, the mobility was reduced by $\sim 10\%$. A reduction of this size shows that the mobility of the device can be changed significantly by the impurity level in the AlGaAs. Growth strategies that focus on reducing the impurity level in the AlGaAs, such as reducing the aluminium fraction may give a small but notable increase in mobility.

Undoped structures with a 300nm, 225nm and 150nm AlGaAs spacer showed no significant change in mobility, above levels of variation seen in devices from different cool-downs. The lack of change in mobility shows that, once carrier gases are deeper than 100nm, so that surface charge effects aren't significant, the AlGaAs spacer thickness does not affect the mobility, as impurities in the AlGaAs spacer are not the dominant source of scattering in these structures.

By growing deep 100nm structure throughout the growth campaign, the mobility-density curves allow the condition of the chamber to be monitored over time, providing useful feedback about the condition of the chamber. The variation between devices from the same wafer fabricated on the same chip showed a variation of $\sim 4\%$. By cooling down the same device multiple times, it was found that the mobility of the same device could vary by $\sim 5\%$ between cool-downs. It is essential to keep this level of variation in mind when comparing the effects of MBE growth parameter changes to avoid drawing false conclusions. Changing the cool-down rate did not affect the amount of variation between cool-downs, but the ability to change the cooling power was limited. In a system where the sample is more thermally isolated from the cooling source, better control of the cooling rate might be achievable.

Finally, the carrier density has a maximum and minimum value due to either the ohmic contacts or carrier gas itself no longer conducting for the minimum value, and the carrier density saturating once the gate voltage increased above a critical value due to charge trapping.

OPTIMISATION OF FABRICATION

For the undoped heterostructure Hall bar devices in chapters 3 the yield of functioning and measurable devices was between 50% and 60%. This yield could be worked with for looking at carrier density and mobility curves in Hall bars as the probability of not being able to make a measurement from a set of four Hall bars between 6.25% and 13%. However, when looking to make nanostructures, like quantum point contacts and quantum dots, which involves e-beam lithography introducing additional fabrication challenges, a yield of 50% is too low.

Therefore, before attempting to make nanostructures an optimisation of the fabrication steps for undoped devices took place in an attempt to increase the yield of functioning 2D devices.

For an induced 2D device, the main cause for the failure of a device a leakage current between the ohmic contacts and the top gate used to induce carriers, caused by a failure of the insulating layer. Failure of the insulating layer manifests in two ways. The first is a simple shorting of the top gate to the contacts when no bias is applied, due to an insufficient covering of the rough ohmic contact surface. The second is either a slow or sudden increase in the leakage current from the top gate to the contacts when applying a bias. The onset of leakage is often very sudden, around the expected threshold voltage.

The precise cause of leakage is difficult to determine as the testing of a device only shows that a leakage path exists with only very limited information about the path itself. However, this behaviour of leakage around the expected threshold voltage is suspected to be due to pinholes in the film itself, as the sudden onset of leakage near the threshold voltage is highly suggestive that the leakage path requires the presence of the 2DES. A leakage path through the 2DES will

most likely pass from the top gate through the film, GaAs and AlGaAs spacer into the 2DES and then to the ohmic contacts. As the MBE grown GaAs surface should be much easier to cover with a dielectric film than the rough ohmic contacts, and there is no direct leakage path to the ohmic contact before the onset of leakage, this type of leakage path, if correct, suggests pinholes in the film itself. Assuming the density of pinholes is constant in the film, it is far more likely that a pin hole will cause a leakage path via the 2DES due to the much larger area where the topgate covers the GaAs surface, rather than the ohmic contacts.

The problems with leakage to the ohmic contacts can be addressed by optimising the ohmic surface and insulator deposition for better coverage of the contact. The pinholes can only be removed by optimising the insulator so that pinholes in the film are not the limiting cause of leakage.

In this chapter the changes to previous fabrication methods and the reason for these changes is discussed. Details about the new ALD system installed at the Cavendish Laboratory including the setup and optimisation of two types of Al_2O_3 depositions at 150°C to be compatible with existing fabrication processes. The new ALD process for depositing Al_2O_3 over the ohmic metal used for ohmic contacts was imaged for any obvious difficulties in covering the rough contact surface. To measure not only the yield of functioning ohmic contacts but also the average resistance of the contacts to the undoped device a intrinsic transmission line measurement (iTLM)^a device compatible with undoped material was designed and fabricated with contact resistances for n-type and p-type ohmic contacts measured at 4 K. As seen in section 3.5 the upper carrier density limit, and therefore carrier mobility, is set by the saturation of the carrier density in the 2DES. This saturation is measured directly as a continuous function of topgate voltage with discussion about potential causes and methods to improve this saturation in future work.

4.1 Changes to previous fabrication methods

4.1.1 Atomic layer deposition (ALD) of Al_2O_3

During previous work on induced devices [10, 68], the insulating layer used on induced devices changed from spin-coated polyimide to alumina deposited by Atomic layer deposition (ALD). Alumina has two main advantages over the polyimide as the ALD process deposits the material monolayer by monolayer resulting in a uniform and conformal film[106, 107].

The increased uniformity is vital for induced devices as the thickness of the insulator controls the local capacitance of the device, which in turn controls the electric field and there-

^aThe intrinsic (undoped) nature of the TLM is stated explicitly here to highlight that the ohmic contacts must overlap with the topgate to function, and means subtle differences in the contacts compared to doped contacts

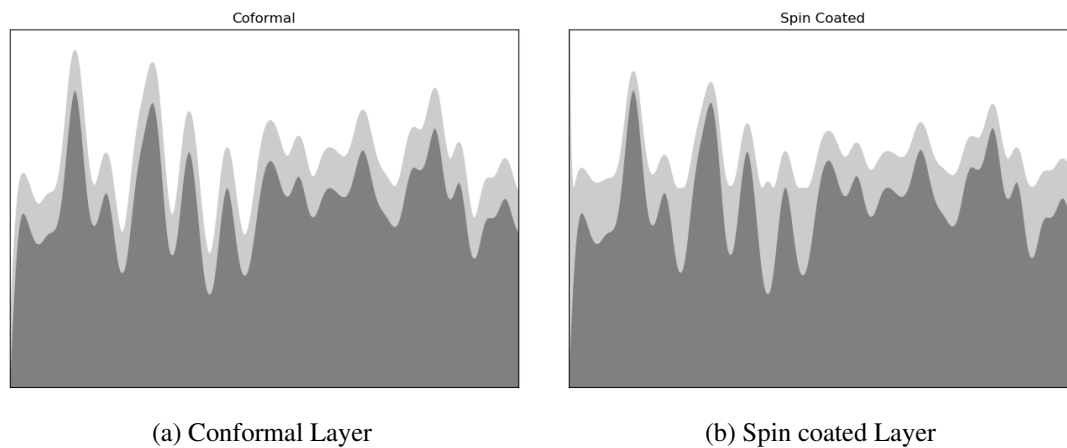


Figure 4.1: Semantic diagram of a rough surface cover by a conformal and spin coated layer, where length scales have been exaggerated to show how the spin coated layer can become thinner at the top of spikes in the surface.

fore the carrier density. Therefore any non-uniformity in the insulator thickness causes non-uniformity in the carrier density in the induced device.

The polyimide has two shortcomings. The polyimide is spin-coated onto the chip, resulting in a thick layer, $\approx 1 \mu\text{m}$, which varies across the device. The thickness of the polyimide film has two impacts on the functioning of an induced device. The thickness of the film means that, to form the conducting channel requires higher voltages of $\approx 10 \text{ V}$. The thickness of the film also prevents polyimide being used to insulate external gates used to form nanostructure, as the gates would be too far from the conducting channel to give a good definition of such fine features.

The non-uniformity of the polyimide layer means that the top gate distance from the surface will vary, therefore varying the electric field strength applied by the top gate. As the electric field strength is proportional to the carrier density, any non-uniformities in the polyimide thickness cause non-uniformities in the carrier density. Depending on the device applications, this can have a varying impact.

When attempting to insulate ohmic contacts, where the surface is significantly rougher than the wafer surface, the conformal nature of the ALD film is beneficial. For an ohmic metal surface with low aspect ratio spikes in height, the spin-coated polyimide has a thinner profile over the spikes. The thinning of the insulator, combined with the increased electric field from the spike makes insulating the ohmic challenging. In contrast, a conformal ALD film follows the surface profile with a constant thickness of insulating material, as shown in figure 4.1.

Two improvements to the ALD process, discussed in the following sections, resulted in an increased yield of functional ohmic contacts compared to previous work.

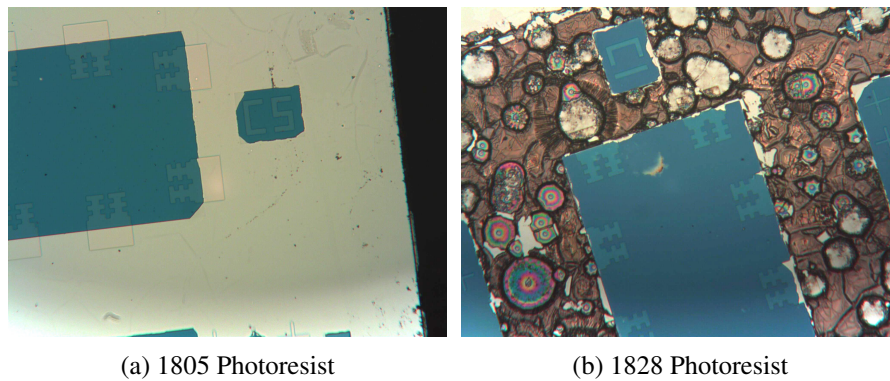


Figure 4.2: Optical images of alumina ALD layers, deposited into photoresist defined windows, after cleaning with Acetone and IPA showing the damage to the alumina caused by the removal of the photoresist.

4.1.1.1 Photo-lithography definition of Insulating Windows

The previous designs of the induced device created a photoresist window into which alumina was deposited by ALD. The alumina was deposited over the electrical contact points of the ohmic contacts, and the rest of the device is removed by normal liftoff with acetone and IPA. However, the liftoff was often very difficult and time-consuming, requiring agitation to remove hard-baked resist. During the ALD process, the substrate was held at 80 °C to 120 °C for up to 8 hours, depending on the precise ALD processes used and the desired film thickness. This resulted in a change to the photoresist that made liftoff very difficult, and the amount of agitation and time needed causing damage to the insulating layer of alumina.

Figure 4.2 shows optical images of two devices after liftoff when using the thinnest and thickest photoresists (S1805 and S1828) commonly used in the cleanroom at the Cavendish Laboratory. The S1828 resist could not be removed despite a combination of acetone and IPA with agitation and an additional 48 hours in acetone over a weekend. The thinner S1805 resist was removed using the same combination of acetone and IPA with agitation but the alumina film edges have been damaged and there is still resist residue remaining.

It is unknown precisely what causes the change in the resist due to the number of uncontrollable parameters: age of the resist, device preparation, deposition time and the state of the ALD chamber. Even if the resist were easy to remove with acetone, because the ALD processes completely encapsulates the chip^b it is difficult for the acetone to reach the resist to start the liftoff process.

Due to the problems using ALD on the device with photoresist windows, the process was changed to pattern with photoresist after the ALD stage. This meant fully encapsulating the

^bThe deposition on the back side of chip is significantly thinner, 20-40nm, for a 60 nm deposition

chip in alumina followed by opening windows above the regions of ohmic contacts used for electric contact and using buffered HF to etch away the unwanted alumina. For alumina the etch rate is $\sim 3 \text{ nms}^{-1}$. For a 60nm alumina film, an etch of 20 seconds in buffered HF is sufficient to remove the alumina. As the HF does not affect the GaAs surface or ohmic contacts significantly, an etch of 30-60s is used to ensure that the rough ohmic surfaces are completely clear of alumina.

Using this etch-back method to define windows for contacts to the region below the ALD layer does require a few alterations to the existing photomask set to account for the removal of excess alumina by etching rather than liftoff. The etch-back pattern is restricted to small windows only directly over contact points, meaning the minimal amount of material is etched away. The use of smaller windows means the etch time is relatively short, as only small areas are etched. Only removing a small amount of material also avoids potential problems with the HF etchant becoming saturated with alumina, changing the etch rate. The additional unnecessary alumina that remains does not affect the function of the device.

The second consideration when using HF and this etch-back method comes when making contact with the Ti/Au contacts below the insulating layer. Because HF will remove the titanium but not the gold, there is a small risk that if the HF will get around the gold cap of the Ti/Au, contact stripping the titanium and lifting off the gold. To reduce the risk the etching removing contacts, the new photomasks were designed so that the Ti/Au contacts are larger than the windows in the insulation layer. The larger window size ensured that the HF only comes into contact with the Au surface. Having smaller windows in the insulator than the contact pads also improves the connection to the contacts below the insulator as the entire perimeter of the insulator window is covered by metal, increasing the chance of metal climbing the insulator edge at some point.

4.1.1.2 Optimisation of ALD Process

The ALD process uses two precursor gases with the first precursor containing the material, in this case, aluminium, and necessary reactive groups so that the second precursor containing the oxygen, in this case, H_2O , reacts with the first precursor depositing Al_2O_3 on the surface. By cycling between pulses of precursors, a layer of alumina is built up monolayer by monolayer. Fundamentally the ALD process is not dissimilar from Chemical vapour deposition (CVD); however, what distinguishes ALD from CVD is that between the pulses of precursors the ALD chamber is fully purged. After the purge of the ALD chamber, precursor covers all of the surfaces of the ALD chamber. When the second precursor enters the chamber, the ALD reaction takes place on all of the surfaces creating a monolayer of the alumina on the surfaces.

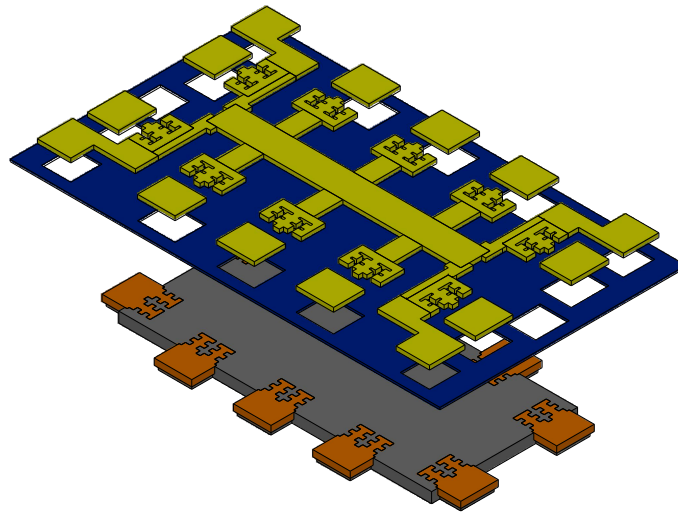


Figure 4.3: 3D Render of the layer of the newly designed photomask for undoped Hall bars.

4.1.1.3 Setup of ALD in Anric 400 System

In 2018 a new Anric 400 ALD system was installed in the semiconductor physics cleanroom at the Cavendish Laboratory. After installation, the system required optimising for depositing alumina on GaAs, AuGeNi and AuBe surfaces to act as the insulating layer for induced devices with either N-type or P-type ohmic contacts. The Anric system, figure 4.4 has positions for three material precursors and two reactive precursors connected to the ALD chamber by a common heated manifold line, with a constant flow of N_2 (99.9999% purity) throughout the system. The material precursors connect to the manifold via a 3ml dose volume. A typical ALD cycle consists of n dose pulses of a material precursor followed by a purge with N_2 then m doses of a reactive precursor followed by a purge with N_2 . While many variables can affect the ALD process, for simplicity only the precursor doses, temperature and purge efficiency were considered. The number of precursor doses in a single cycle increases the amount of material delivered to the chamber. Increasing the number of doses of a material precursor is useful when covering particularly rough material with low aspect ratio spikes where covering the bottom of the valleys created by the surface roughness is difficult. Increasing material precursor dose is also useful when covering materials to which the precursor struggles to adhere, such as single crystal gold. Increasing the temperature of the deposition can reduce hydrogen inclusion in the film, which forms charge traps and can increase the purge efficiency of the chamber, reducing purge times. The impact of purge efficiency is less evident than the dose number and temperature. In order for ALD to take place instead of CVD, the ALD chamber is purged of

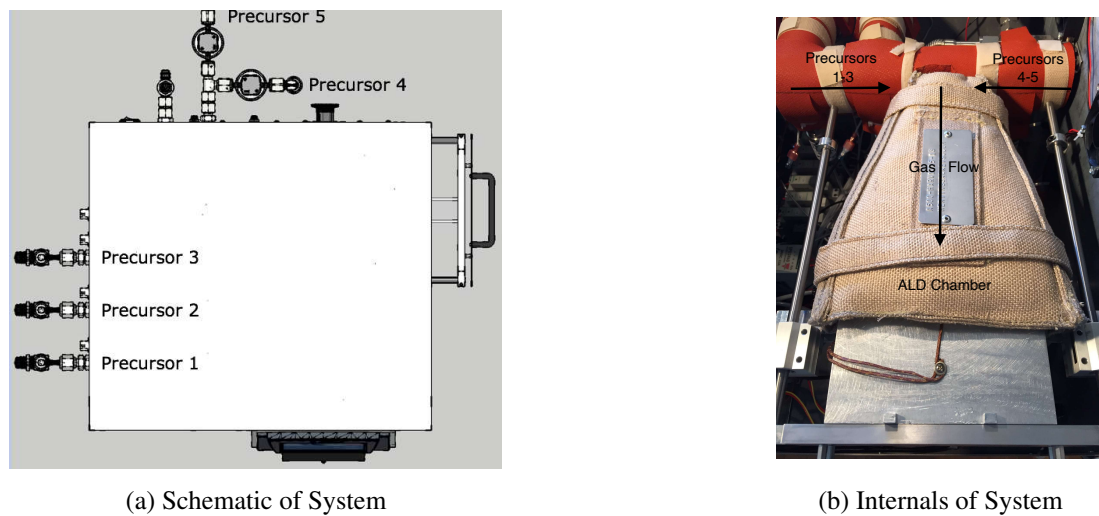


Figure 4.4: Schematic of Anric 400 and image of internals showing the direction of gas flow through the system.

precursors between doses so that the two types of precursors only combine on the surface of the device (and chamber). Purging of the chamber is done by flowing nitrogen gas through the system and pumping on the chamber. The primary controls on the purging efficiency are the flow of nitrogen gas through the system and the length of time pumping during a purge. The pump used on the system and the impedance of the pumping lines also impacts the pumping efficiency, but there is less control over these factors.

Typically for ALD with H_2O as the reactive precursor the temperature of the deposition is between 150°C and 250°C in order to make the purging of the H_2O easy. Undoped quantum well devices are sometimes fabricated with insulated gates on the front and back side of the chip [108]. Fabrication of these devices requires thinning the back of the device and mounting it with epoxy to a host substrate before further thinning and deposition of the insulator and gates on the back side of the chip. The choice of epoxy used for this process is critical and may degrade at prolonged temperatures above 150°C . While this back-gating process was not used in this with the devices in this work, the ALD process was developed at 150°C to enable future work with back-gated devices.

Therefore the parameters available for optimising the ALD are precursor dose number, nitrogen flow and purge times. Initially, the ALD precursor was set up with two doses of material precursor and a single dose of the reactive precursor with 10s purge time and N_2 flow set to 228-241mTorr as base pressure. With these settings, alumina was deposited with a growth rate of 0.11nm per cycle but with a large CVD streak in the centre of the chamber, figure 4.5. To prevent CVD from taking place, the purging of the chamber needed to be improved. Removal of the foreline trap placed on the pump of the system and increasing the purge time to 18s



Figure 4.5: Optical Image of 4" Si wafer after 600 cycles of Alumina ALD showing a clear CVD white streak on one side of the wafer due to insufficient purging of the chamber between precursor cycles.

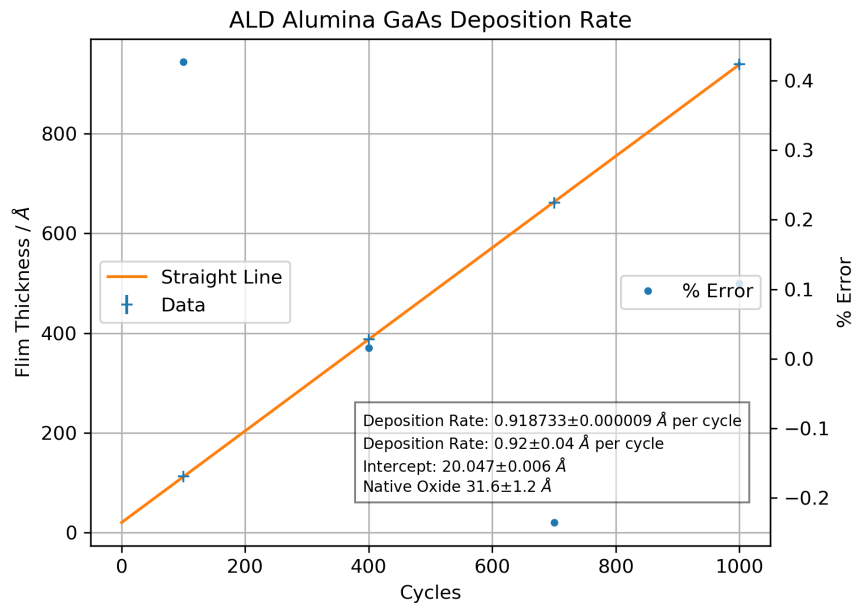
resulted in a deposition rate of 0.13nm per cycle with uniformity of 99.8% across a 4" silicon wafer with an average of 102.47 ± 0.018 nm of alumina from a 800 cycles deposition.

Another property of ALD is the linear dependence of film thickness of the number of ALD cycles as each ALD cycle should deposit one monolayer of material. From a series of four depositions with 100, 400, 700, and 1000 cycles, an ellipsometry measurement of the film thickness allows the deposition rate to be determined. Figure 4.6 shows a plot of the measured thicknesses as a function of the number of cycles. The deposition rate is linear with the number of cycles, further confirming that ALD rather than CVD is taking place in the chamber. It's worth noting that a linear fit of the thickness as a function of cycle does not have a zero intercept value, however the intercept value is comparable to the measured thickness of the native oxide on the GaAs surface, which is not accounted for in the ellipsometer measurement and was concluded to be the reason for the non-zero intercept value.

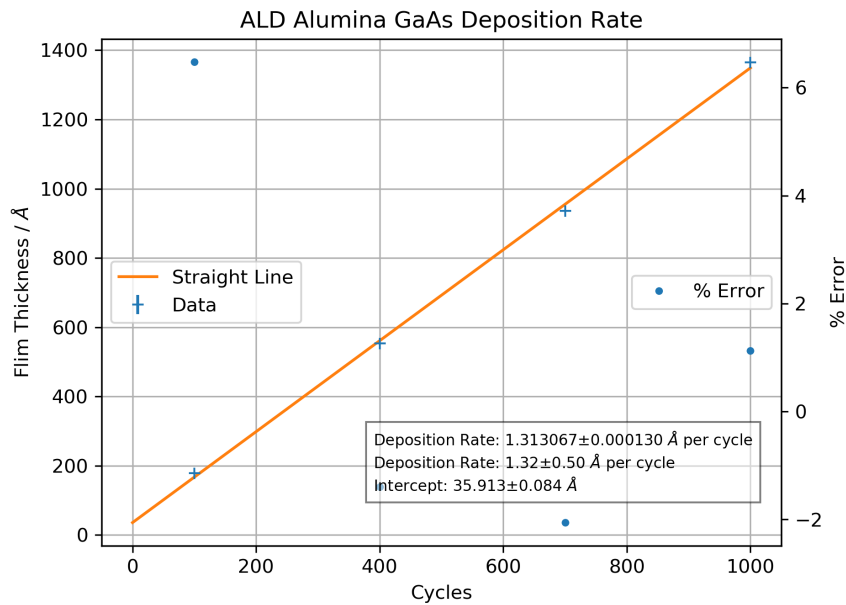
4.1.1.4 ALD Covering of Ohmic contacts

The leading cause for failure of an undoped device is the top gate leaking to an ohmic contact usually without a voltage applied on the top contact, but sometimes at the gate voltage where a 2DES is induced. The leakage is due to the ALD insulating layer failing. There are two main ways that the ALD layer can fail: pin holes in the film, or difficulties in covering the surface, particularly for the rougher annealed ohmic metal surfaces. If pinholes were the reason for the ALD layer failing, the devices would be equally likely to fail at the point of inducing when a 2DEG forms under the pinholes, providing a shorting path. As the devices fail more often with no voltage on the top contact, the main problem with the ALD appears to be covering the annealed ohmic metal.

In order to improve the yield of ohmic contacts, the 'dynamic' ALD process changed to a 'static' process in the Anric AT-400 system. The 'dynamic' ALD process continually pumps on the ALD chamber with nitrogen gas passing through the system. Therefore the precursor



(a) Dynamic ALD



(b) Static ALD

Figure 4.6: Alumina ALD layer thickness on GaAs wafers as a function of number of ALD cycles. Both dynamic and static processes show a good linear dependence on number of cycles to within a few percent error. Respectively the dynamic and static process have a deposition rate of $0.92 \pm 0.04 \text{ \AA}$ and $1.32 \pm 0.50 \text{ \AA}$ per cycle.

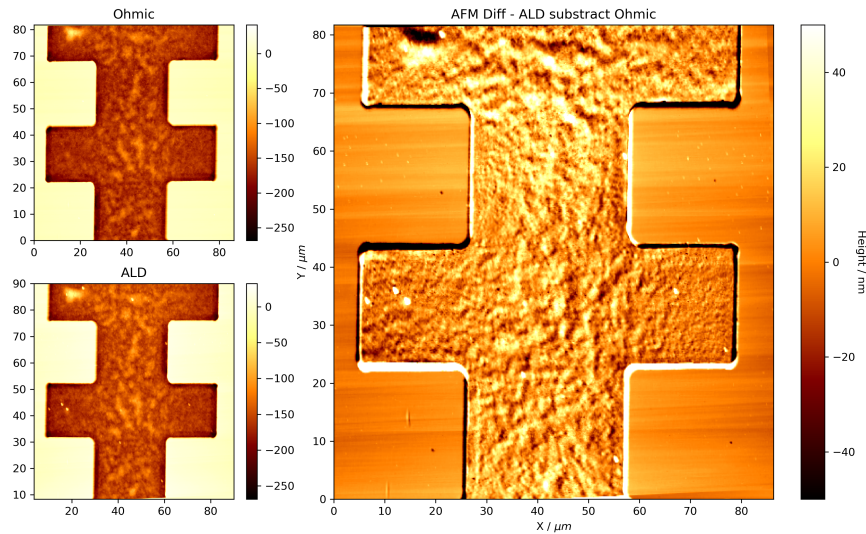


Figure 4.7: AFM Image of ohmic contact before and after annealing. As the ALD produces a co-formal layer the AFM images should appear identical. Therefore subtracting the ALD image from the Ohmic image allows variation in the covering to be viewed. Lighter regions correspond to thicker regions. AFM image taken by A. Lowe.

gas doses flow continually over and pass the sample. A ‘static’ process introduces an exposure time, set to 1s for this process, sealing the chamber from the pump with the gases pushed into the chamber by the nitrogen gas pressure. The exposure time gives the precursor gases more time to settle onto the surface, increasing the coverage from a single dose and allowing the precursor to cover the low aspect ratio valleys on rough surfaces. The ‘static’ process has a slightly higher deposition per cycle at 0.13nm per cycle compared to the ‘dynamic’ process at 0.9nm per cycle, figure 4.6.

Atomic Force Microscope (AFM) images of the ohmic contacts before and after ALD are shown in figure 4.7. As the ALD produces a conformal layer, the two AFM images should be identical. Thus, by looking at the difference in the images, any variation in the ALD coverage can be viewed.

Ideally the ALD film is conformal with a thickness of 60 nm and therefore is too thin for the AFM to image the film on the side walls of the ohmic pits. This means the surface profile that the AFM will image will ideally be identical as the AFM cannot image a global increase in height, instead measuring relative changes in height. Therefore subtracting the two AFM images from before the ALD should be a type of null measurement where deviation from zero correspond to either a thickened or thinner region of the ALD film.

This ideal situation is complicated by the reality of the AFM measurement and imaging of

a rough ohmic metal surface. As the data in figure 4.7 show the ohmic surface varies over a range of approximately 100 nm. This means that in order for the null measurement of the ALD film thickness to work, the AFM data from before and after ALD must be both aligned and imaged with sufficient resolution when subtracting the two images it is variations in the ALD film and the ohmic roughness that is measured by the null measurement.

Aligning the AFM images was done using a combination of Hough transform[109] to find the edges of the ohmic contact and match the rotation of the images followed by cross-correlation to correct for any translation of the two images. The wafer surface, which is atomically smooth from MBE growth and is assumed to be uniformly covered by the ALD, is used as the reference point for the height; correcting the raw AFM data for distortion using a planar fit of this region. An example of the output of these process is shown in figure 4.7. The two source images in figure 4.7 look very similar with only variation in the ohmic surface visible. The difference between this two images shows no systematic difference but there are artefacts from the AFM scanning visible at the edges of the image from scanning the atomically smooth surface and large differences at the edge of the ohmic. These artefacts and difference are probably due to limitation in the aligning the two source images and limitations in the image resolution of the ohmic surface introducing a type of noise to the null measurement.

In an attempt to understand and qualify the sources of noise introduced to the null measurement by the alignment of the images an idealised image was generated to test the null measurement method. This generated idealised image is the AFM image of a real ohmic before ALD, with a surface roughness, which is then processed adding globally a height of 60 nm to all points in the image. In this way the generated image is now what would be measured if the ALD was perfectly conformal and the AFM was able to measure the same exact positions on the sample before and after ALD. Therefore using the original ohmic image and the generated ideal image as inputs for the null measurement will indicate how much noise is added to the null measurement due to limitations in aligning the images. The output is shown in figure 4.8 (right). This output shows that the misalignment of the two images results in the large difference at the edge of the ohmic and also causes the ohmic surface to appear <10 nm higher than expected. This is important to keep in mind when examining a real AFM null measurement image as seen in figure 4.8 (left).

Looking at the real AFM difference image in figure 4.8 and comparing the the idealised image, the large difference in the perimeter of the ohmic can be ignored as these are clearly visible in the idealised image and therefore are artefacts from the aligning of the two source images. Similarly the real difference image indicates that the ALD is thicker on the central track of the ohmic material by 10 nm-30 nm but because the idealised image also shows a thicker film in the same region this is partly an artefact of the alignment. Considering the

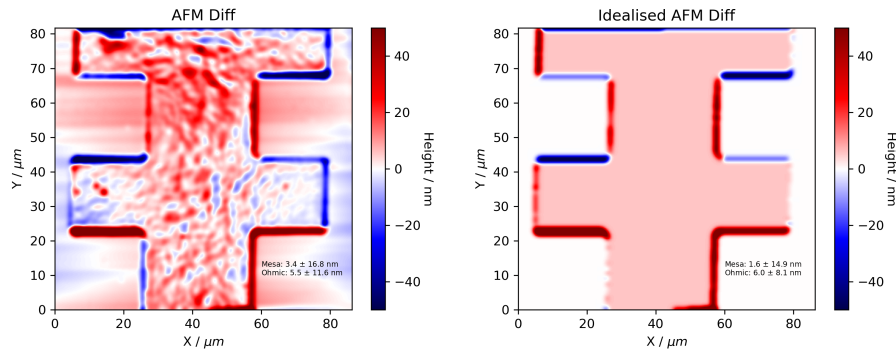


Figure 4.8: AFM difference images for real data and the idealised case. Red regions correspond to thicker ALD covering. AFM image taken by A. Lowe.

artefacts introduced by the alignment process, the real AFM difference images is very similar to the idealised image overall. This indicates that general the ALD covers the ohmic material well. A closer look at the difference image does show some small regions particularly in the corners of the ohmic that are thinner (blue). However these regions are <10 nm therefore even in the worse case accounting for errors from the alignment these regions are <20 nm thinner than the 60 nm deposited so are still well covered by the ALD film.

Based on these AFM images, the ALD seems to be performing very well at covering the ohmic contacts, with the difference images suggesting that the Alumina may be thicker on the contact itself compared to the GaAs surface. The thicker film on the ohmic surface may be due to the rougher ohmic metal surface being easier for the ALD precursors to adhere to than the atomically smooth GaAs surface. Therefore optimising ALD processing on atomically smooth GaAs surface seems a logical approach to set up working processes for covering ohmic material.

4.1.2 Improving Ohmic Contacts Smoothness

The main focus of improvements to the ohmic contacts is to improve the yield of functional ohmic contacts that do not leak to the top gate and have a low enough resistance for measurement[110]. In the case of n-type contacts, made from a Ni/AuGe/Ni layered contact, the surface roughness of the contact was improved by using a ceramic boat to evaporate the Ni layers. Due to the shape of the ceramic boat, which is an approximately hollow cone, by careful loading of the boat to produce a tightly packed Ni charge at the bottom of the boat, heating of the charge was more efficient, allowing a shorted evaporation with a deposition rate of >0.1 nms⁻¹, figure 4.9. With a 470 °C anneal 4.10 this procedure resulted in a visibly smoother contact surface.

In addition to looking at the yield of non-leaking ohmic contacts, a Transmission line measurement (TLM) of the induced contacts gave values for the resistance of the contacts, details

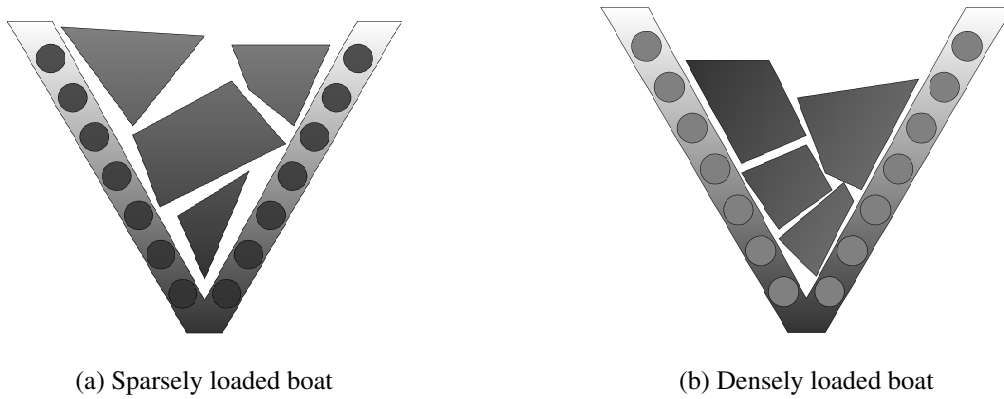


Figure 4.9: Diagram of Ni boat loading. 4.9a shows an example of a sparsely packed boat, which results in less efficient heating of the Ni charge causing lower deposition rates and longer evaporation times. 4.9b shows an example of a tightly packed boat which resulted in visibly smoother ohmics contacts. The circles in the walls of the boat represent the heat coil of the boat.

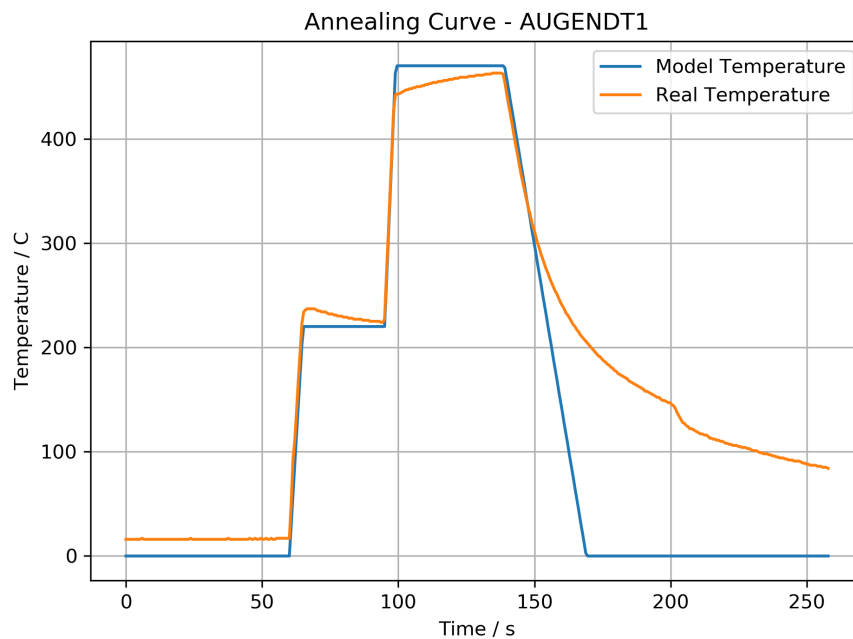


Figure 4.10: Output from RTS annealer showing target temperature curve and the achieved temperature as a function of time. The initial offset in the real data is due to the annealing chamber being warm from a previous test run.

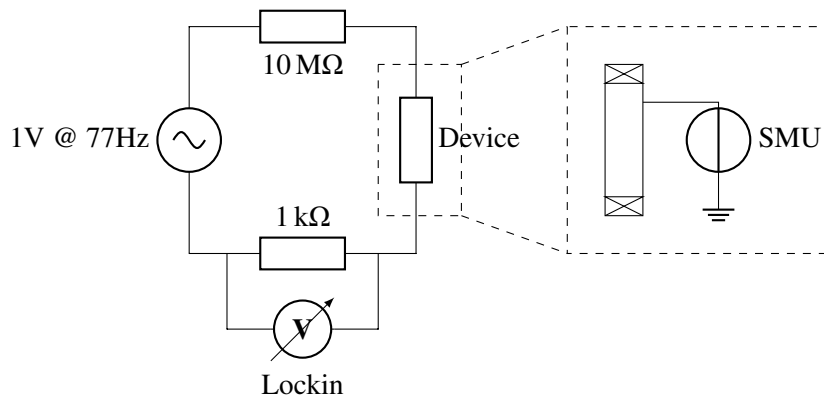


Figure 4.11: Circuit diagram for the TLM measurement circuit.

of which are in the next section.

4.2 Contact Resistance Measurement Using iTLM

A transmission line measurement (TLM) is a standard method for determining the contact resistance [111, 112]. A TLM works by measuring the resistance of different lengths of conducting channels. As the conducting channel's resistivity is constant, the resistance of the channel is proportional to the length of the transmission line. Therefore the resistance as a function of length will be a straight line, where the intercept value is the resistance for a channel of length zero, e.g. twice the contact resistance. This method assumes that the contact resistance is the same for all contacts. In reality there can be contact-to-contact variation, however the TLM value for contact resistance will be the average value of resistance and provides an uncertainty and visual measure of the variation in the contacts from the spread in the resistance values.

To perform a TLM on induced contacts, a new mask for intrinsic transmission line measurement (iTLM) with five conducting channels of lengths 300 μm , 600 μm , 940 μm , 1240 μm , and 1860 μm , with a width of 140 μm was made. The five conducting channels all have separate top gates so that one leaking contact does not prevent all bars from being measured. The resistance measurements were performed at 4K using an AC four-terminal measurement with a 10M Ω limiting resistor to give a 100nA current, figure 4.11. In addition to the resistance of the conducting channel, this set up allows the inducing voltage to be measured across five separate regions on a single chip, building up statistics that would be time consuming to obtain on their own.

Figure 4.12 shows a typical inducing curve for a single iTLM bar with the measurement circuit shown in figure 4.11. There are two inducing points to consider, the first at ~ 0.5 V and

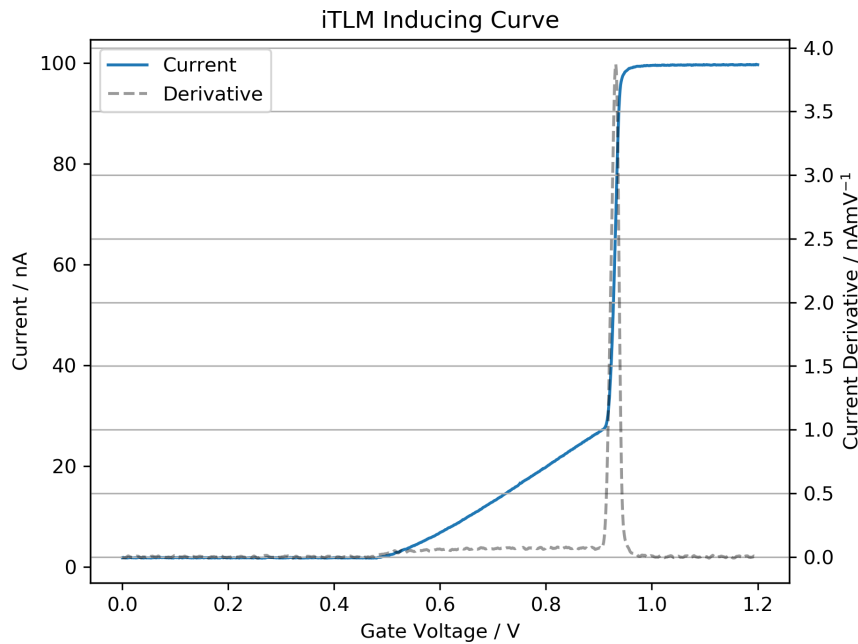


Figure 4.12: Typical inducing curve for an iTLM. Threshold voltage is taken to be the second step in the current, corresponding to the peak in the derivative shown.

the second at ~ 0.9 V. The lower inducing point corresponds to the formation of a conducting channel but one with a very high resistance > 10 M Ω , while the higher one is the value taken as the inducing voltage as the bar reaches full conductance, so the resistance drops below 10M Ω . The threshold voltage is taken to be the peak in the derivative of the inducing curve seen in figure 4.12. Figure 4.13 contains a summary of the threshold voltages of the iTLM bars, which are very consistent.

The resistance measurements use a voltage range of 0.9 V to 1.975 V, to give a value of the contact resistance as a function of gate voltage. Figure 4.14 contains a typical set of linear fits for the bar resistances as a function of length, from which the intercept gives the contact resistance. Figure 4.14 shows that in some cases, there is a significant deviation from the straight line fit. This variation is due to variation between the ohmic contacts' resistances. In order to minimise the effect of highly resistant contacts and bars that do not conduct well, multiple linear fits of the data were performed removing data points such that all possible straight lines through the set and all sub sets (excepting the null set and sets with just a single data point) of the data were calculated. These values for the gradient and intercept from these straight line were then averaged towards to produce a 'best' linear fit which proved robust against outliers. Figure 4.15 contains a plot of the iTLM contact resistances as a function of top gate voltage.

The contact resistances in figure 4.15 vary from $O(1\text{k}\Omega)$ at the threshold voltage falling

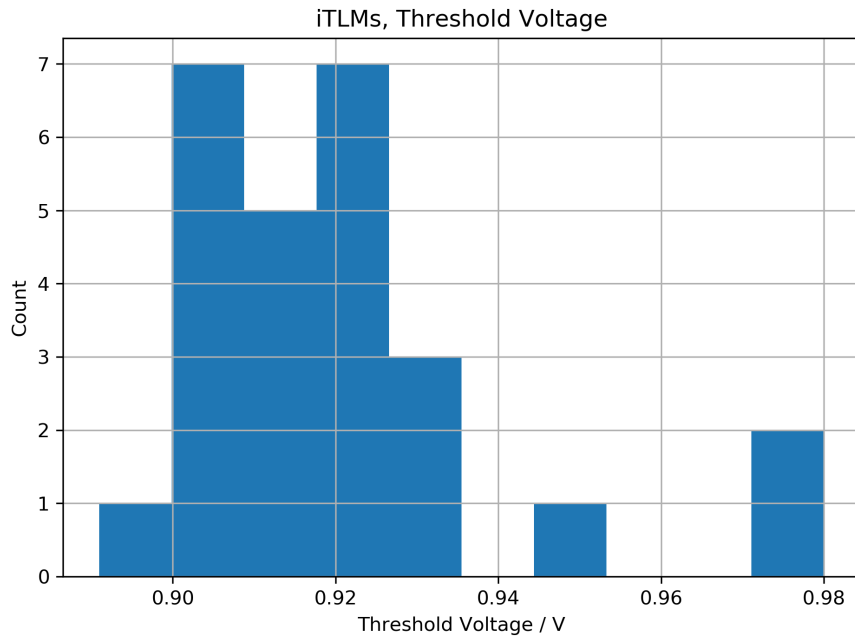


Figure 4.13: Histogram of threshold voltages from 26 iTLM bars, fabricated on W1170 a 100nm undoped heterostructure with a 60 nm alumina gate dielectric. Average threshold voltage is $0.92 \pm 0.02\text{V}$.

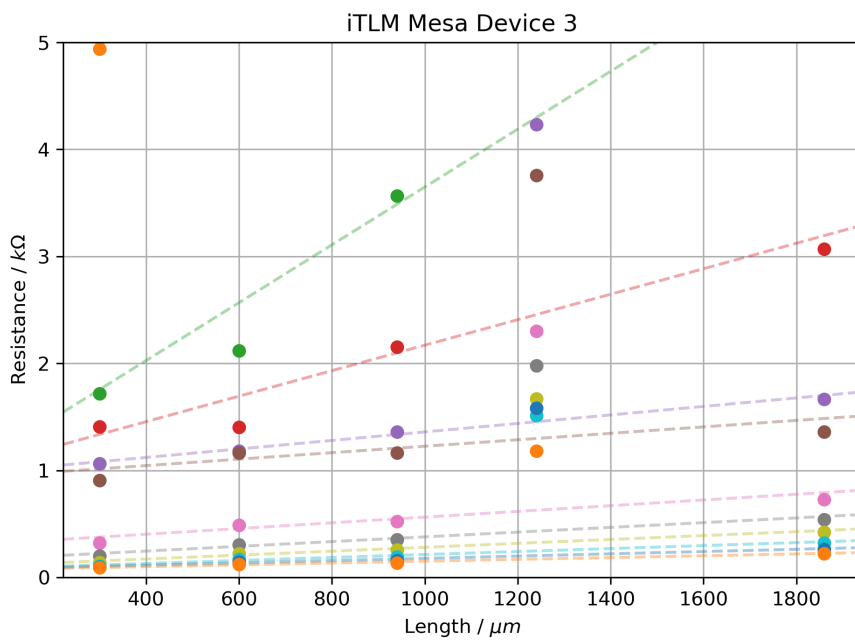


Figure 4.14: iTLM measurements with linear fits of resistance as a function of bar length. Each colour corresponds to a different voltage applied to the top gate on the device. For some TLM there is significant deviation from the straight line fit. For this iTLM device the bar of length $1240\mu\text{m}$ shows a systematic offset from the other bars, suggesting one or both of the contacts for that bar are much more resistive than the other contacts.

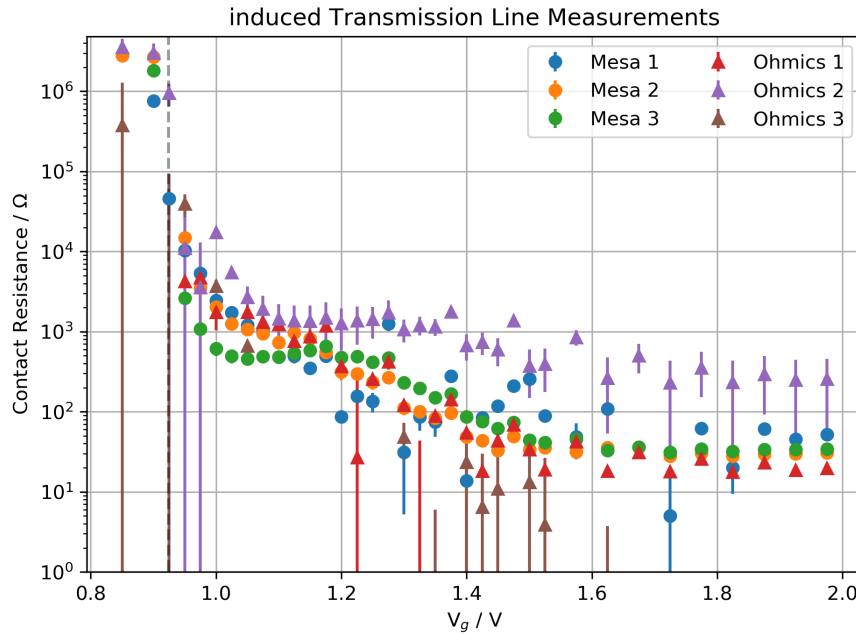


Figure 4.15: Contact resistance as a function of gate voltage from iTLMs. Contact resistance range from $O(1k\Omega)$ at the threshold voltage falling to $O(10\Omega)$ at the highest gate voltages used. Threshold voltage is marked by the dashed line. ‘Mesa’ devices had the mesa etched before the ohmic deposition. ‘Ohmic’ devices has the mesa etched after the ohmic deposition. The order of the mesa etch and ohmic deposition has no meaningful effect on the contact resistance.

to $O(10\Omega)$. This reduction in contact resistance as a function of gate voltage may be due to two factors. Firstly, the induced ohmic contacts are designed to have a $5\ \mu\text{m}$ overlap with the top gate, to ensure that there is a carrier gas as close to the ohmic contact as possible. A side effect of this is that the top gate cover will gate the ohmic metal causing the ohmic to screen the effect of the gate increasing the contact resistance. To reduce the screening of the top gate by the ohmic, a rotatilt at 60° to the sample’s normal is used to evaporate the ohmic metal at an angle. This produces a more cone like ohmic contact reducing the screening of the top gate, as shown in figure 4.16. Increasing the gate voltage may be important to overcome any screening from the ohmic. The second effect the top gate may have on the contact resistance may be due to the local carrier density around the ohmic contact. Increasing the gate voltage will also increase the local carrier density in the region surrounding the ohmic. The effect of this on the contact resistance may be two-fold, firstly at higher densities, the carrier gas will be more able to screen any charge traps limiting the conductance of the contact.

Secondly, it is well known that a Schottky barrier forms at a GaAs surface[113]. When recessing the ohmic contacts the Ni/AuGe/Ni will be deposited on a GaAs surface, therefore there is potentially a Schottky barrier and a corresponding depletion region around the ohmic

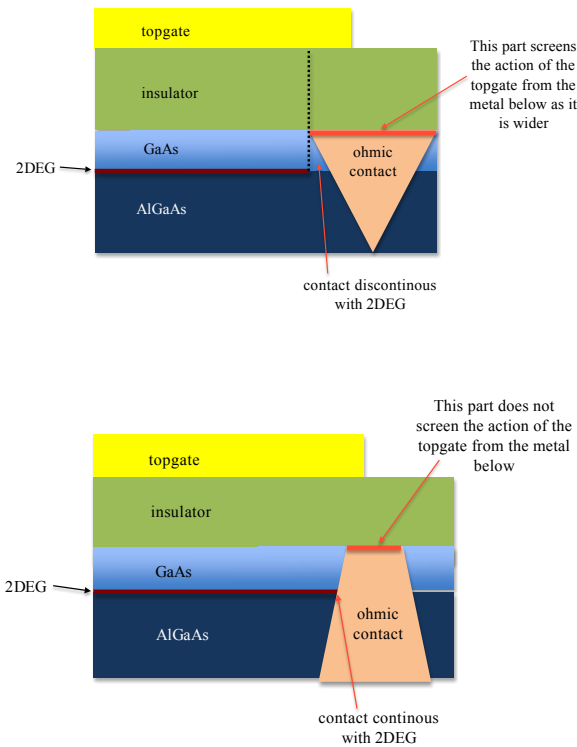


Figure 4.16: Diffusion profiles of ohmic metal deposited onto the surface of a wafer and deposited into a recessed ohmic pit using rotatilt. Images from [9].

contact. If such barrier and depletion regions exist, then increasing the carrier density and therefore Fermi energy would allow carrier to overcome the Schottky barrier, while the increased potential would narrow any depletion region. Both effects would result in a lower contact resistance at higher top gate voltages.

The iTLMs in figure 4.15 compare the effect of depositing the ohmic metal into recessed ohmic pits on an MBE clean surface (Ohmic Devices) or a surface where the Mesa had already been defined by photolithography and a wet etch. The fact that the contact resistances from the iTLM for both the Mesa and Ohmic devices agree with each other to within the spread on the data shows that there is no measurable difference between the two methods of processing ohmic contacts.

4.2.1 Yield of Ohmic Contacts

In order to contact electron gases and hole gases in an induced device, AuGeNi or AuBe ohmic contacts are deposited for n-type and p-type contacts respectively. For ambipolar devices, AuGeNi and AuBe metals are deposited close together so that a single ohmic bond pad connects

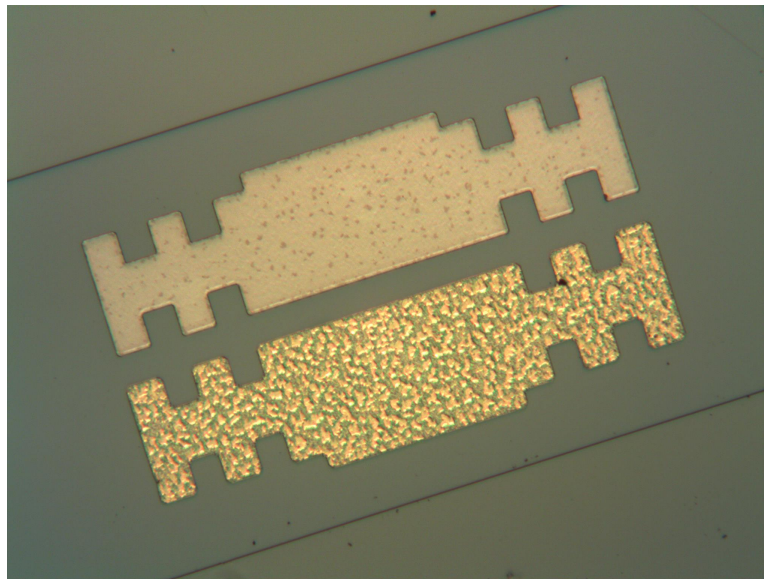


Figure 4.17: Optical micrograph of an ambipolar ohmic contact made from AuGeNi (Top) and AuBe (bottom). The contacts have been annealed at 430 °C and 470 °C respectively. The contacts are 320 μm long and 70 μm wide.

to both an n-type contact and p-type contact, see figure 4.17. As the ohmic contacts are the limiting factor in the yield of induced devices, from iTLMs of n-type, p-type, and ambipolar contacts, the yield for each type of contact was measured. The criteria for an ohmic failing was the bar either leaking with zero bias on the top gate or the bar leaking before reaching full conduction. The TLMs of the n-type, p-type and ambipolar contacts in figure 4.18 show that all types of contacts are in the range $O(1 - 10\text{k}\Omega)$ down to $O(10 - 100\Omega)$. While these contact resistances are good they are an order of magnitude higher than the state of the art contact which have contact resistances of a few Ohms[114, 115]

Table 4.1 summarises the yield of the three types of ohmic contacts. All types of ohmic have $\geq 90\%$ yield with the additional processing for the ambipolar ohmic not causing any change to the ohmic yield. Taking the yields in table 4.1, the binomial distribution can be used to calculate the probability of having at least one fully working device for a device from a batch of n devices with 4, 6, and 10 ohmic contacts, see figure 4.19. In order to have a 90% of at least one functional device from the batch, the yields from table 4.1 give the number of devices per fabrication run as 2, 3 and 5 respectively. These are manageable numbers of devices for a single fabrication run.

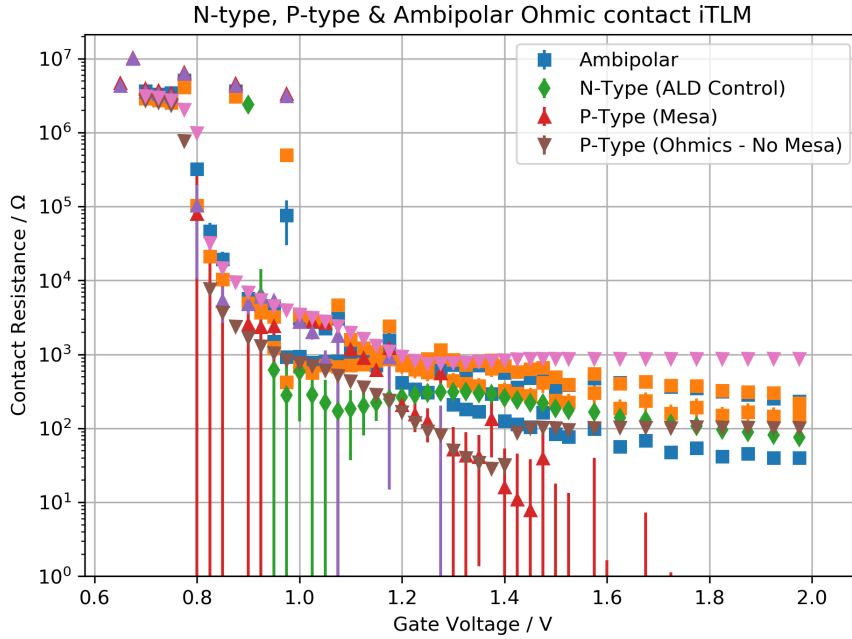


Figure 4.18: iTLMs for N-type (diamonds), P-type (triangles) and Ambipolar (squares) ohmic contacts showing contact resistances in the range $O(1 - 10\text{k}\Omega)$ at point of inducing and $O(10 - 100\Omega)$ for the highest gate voltages used. Each colour represents a single iTLM.

Ohmic Type	Leaking Contacts	Total Measured	Probability of Failure
N-type	2	20	0.1
P-type	4	40	0.1
Ambipolar	1	20	0.05
N-Type and Ambipolar	3	40	0.075
P-type and Ambipolar	5	60	0.083

Table 4.1: Ohmic yields for n-type, p-type and ambipolar devices tested using iTLM mask.

4.3 Surface Charge Passivation

In an induced device, charge trapping sets the upper limit on carrier density [78]. At sufficiently high gate voltage, typically $\geq 1.8\text{ V}$, increasing the gate voltage no longer increases the carrier density in the carrier gas; instead the carrier density saturates. The mobility-density curves shown in figure 4.20 are from before and after pushing the top gate past the critical voltage at which charge trapping occurs.

For both the 50nm and 100nm iHEMT device, after passing the critical voltage, the carrier density saturates but the mobility is increased by a small amount. From linear fits of the carrier density as a function of top gate voltage, the capacitance of the 100nm device is unchanged, but the 50nm device's capacitance increased by 1.75%. The threshold voltages for both the 50nm and 100nm device increased.

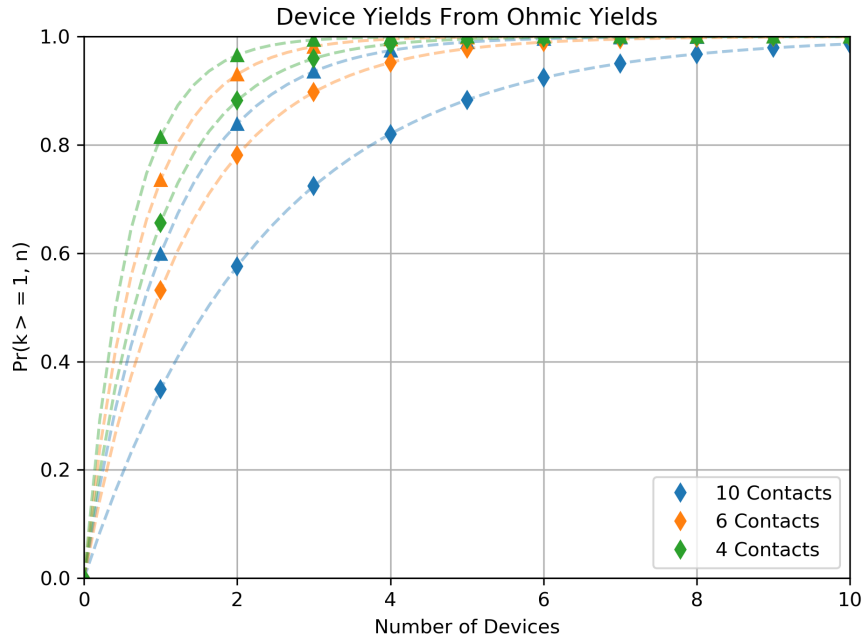


Figure 4.19: Graph of device yields based on ohmic yields from table 4.1. Yields for devices with 4, 6, and 10 ohmic contacts have been plotted. The diamonds are the yields for unipolar devices, the triangles are ambipolar.

W1160 - 50nm AlGaAs Spacer		
	$V_{threshold} / V$	Capacitance per units area / $\mu F \mu m^{-2}$
Non-hysteretic	0.810 ± 0.004	0.0687 ± 0.0002
Hysteretic	0.857 ± 0.007	0.0698 ± 0.0003
W1171 - 100nm AlGaAs Spacer		
	$V_{threshold} / V$	Capacitance per units area / $\mu F \mu m^{-2}$
Non-hysteretic	0.789 ± 0.002	0.0514 ± 0.0001
Hysteretic	0.886 ± 0.003	0.0515 ± 0.0001

Table 4.2: Threshold voltages and capacitance per units area for W1171 and W1160 before and after the critical voltage where the density mobility becomes hysteretic.

The offset in carrier density indicates that charge has been trapped somewhere in the device structure other than the AlGaAs/GaAs heterointerface. The most likely place for charge traps is the GaAs surface/Alumina interface. Once the gate voltage passes a critical value, additional carriers are no longer pushed into the carrier gas at the AlGaAs/GaAs heterointerface, setting an upper limit on the working range of the device.

In order to improve the maximum carrier density that the induced devices can achieve, the cause of this saturation needs to be understood. Assuming that the cause of this saturation is the GaAs surface/Alumina interface due to charge traps at this interface, a method to reduce

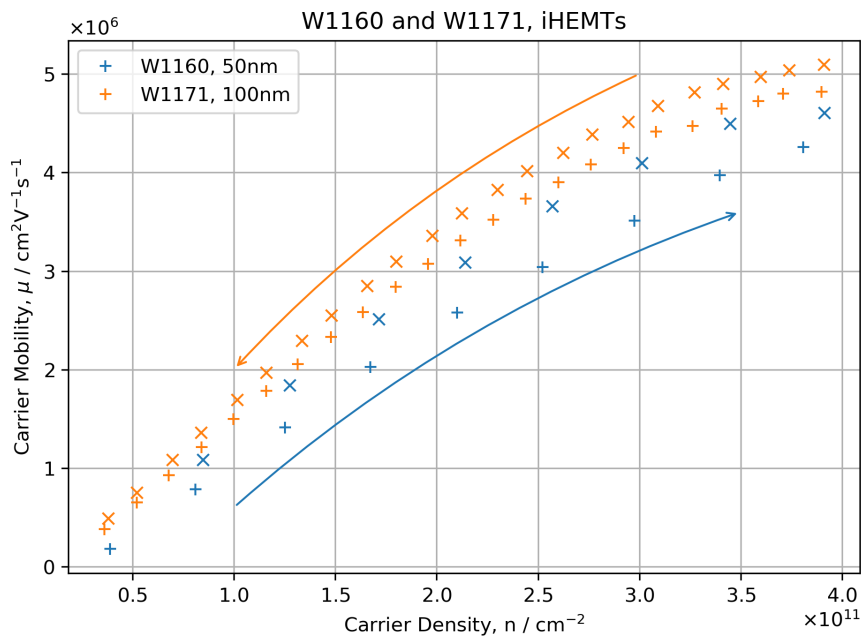
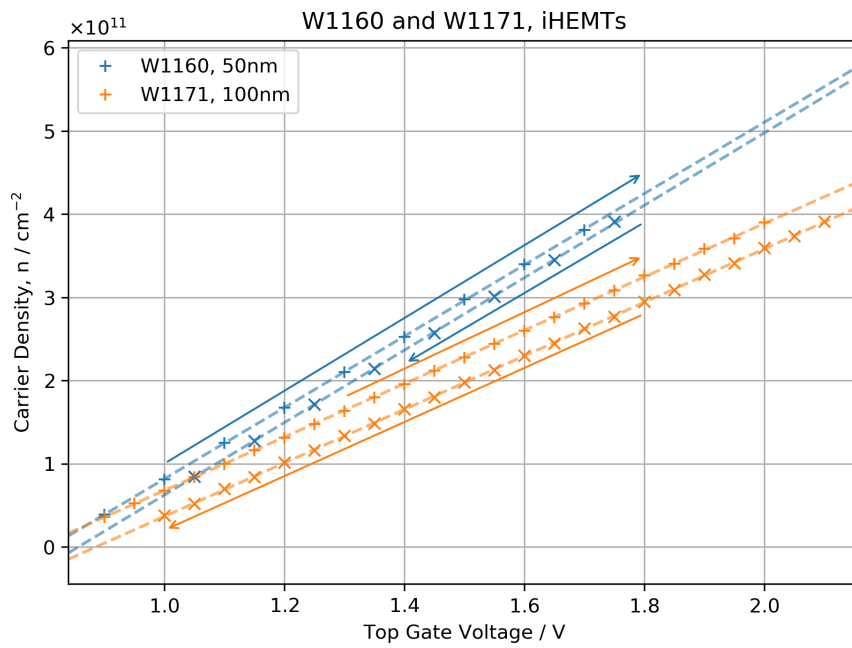


Figure 4.20: Carrier mobility and carrier density curves for W1171 and W1160, a 100nm and 50nm AlGaAs spacer iHEMT respectively. In both devices the gate voltage has been increased past the critical point where the carrier density saturates. Table 4.2 details the linear fits of carrier density as a function of top gate voltage.

the charge trapping is needed. In literature it is a standard method to anneal ALD Alumina at high temperatures, $> 700^\circ\text{C}$ in forming gas[116–118]. However, these methods are not suitable for GaAs based devices as the As dissociates at such temperatures. Additionally for the ohmic contacts, which have to be deposited and annealed at 430°C and 470°C , are unlikely to function as expected if annealed at $> 700^\circ\text{C}$. Therefore a lower temperature treatment was attempted to see if this had any effect on the charge trapping.

4.3.0.1 Continuous Measurement of Carrier Density

In order to continuously measure the carrier density as a function of gate voltage, the gate voltage was swept slowly while measuring the Hall voltage V_{xy} at a fixed magnetic field. As the Hall resistance is inversely related to the carrier density, given the Hall coefficient, R_h , at the start of the gate voltage sweep, the carrier density is given simply by,

$$n_c = \frac{1}{eR_h(V_0)} \frac{\rho_{xy}(V_0)}{\rho_{xy}(V)} \quad (4.1)$$

Careful consideration of the time constants of the lock-in amplifiers and the sweep rate of the gate voltage is needed to avoid measuring the effects from the lock-in time constants rather than the change in the device. A simple check for these effects is to measure the Hall coefficient using a small magnetic field sweep before and after the gate voltage sweep and use both values to convert the Hall voltage to carrier density. At low gate voltages well below the critical value for charging any difference between the carrier densities calculated using the two Hall coefficient indicates a problem with the setup. Figure 4.21 contains a plot comparing the continuous measurement of the Hall resistance with the standard method of measuring the Hall coefficient as a function of gate voltage. The continuous voltage sweep methods agreed with the measured Hall coefficient. Therefore this method can be used to measure the carrier density as a continuous function of gate voltage to look at the saturation of the carrier density.

4.3.0.2 Results of Post Deposition Annealing

As illustrated in figure 4.22 using the method described in section 4.3.0.1 the carrier density of W1093 a 50nm AlGaAs spacer iHEMT was measured while continuously varying the gate voltage showing the carrier density increased linearly as expected from the capacitive model, until $\approx 1.9\text{V}$ when the carrier density saturates at $4 \times 10^{11}\text{cm}^{-2}$.

As a first attempt at treating the alumina insulating layer annealed chips from W1089 and W1093 at 400°C for 150 s, the temperature curve is shown in figure 4.23, to see if that had any effect on the carrier density curve. Both these wafers are 50nm heterostructures so have mobilities limited by surface charges. From the carrier density curves, figure 4.22, from W1089

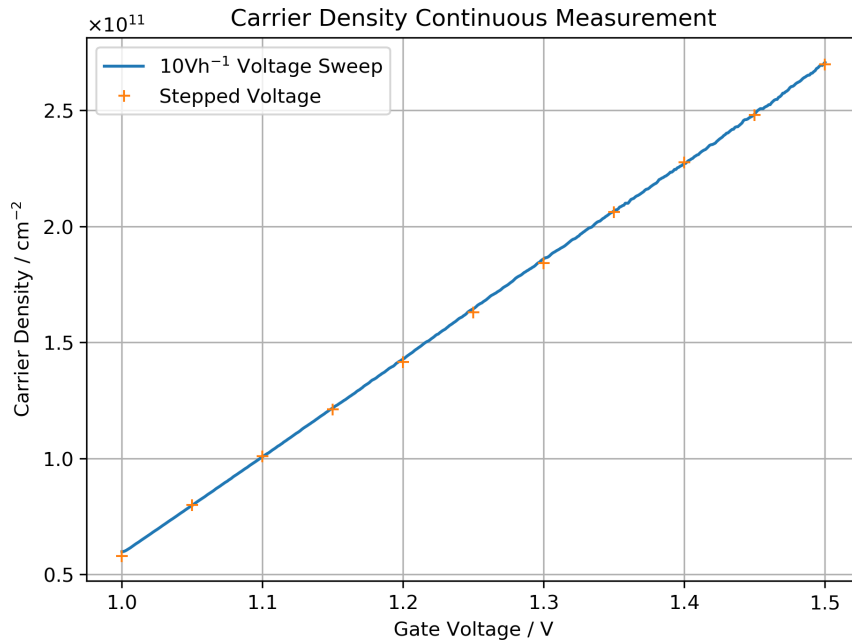


Figure 4.21: Comparison of continuous voltage sweep and Hall coefficient measurement to measure the carrier density as a function of gate voltage. The continuous voltage sweep agrees with the measured values of the Hall coefficient at certain gate voltages.

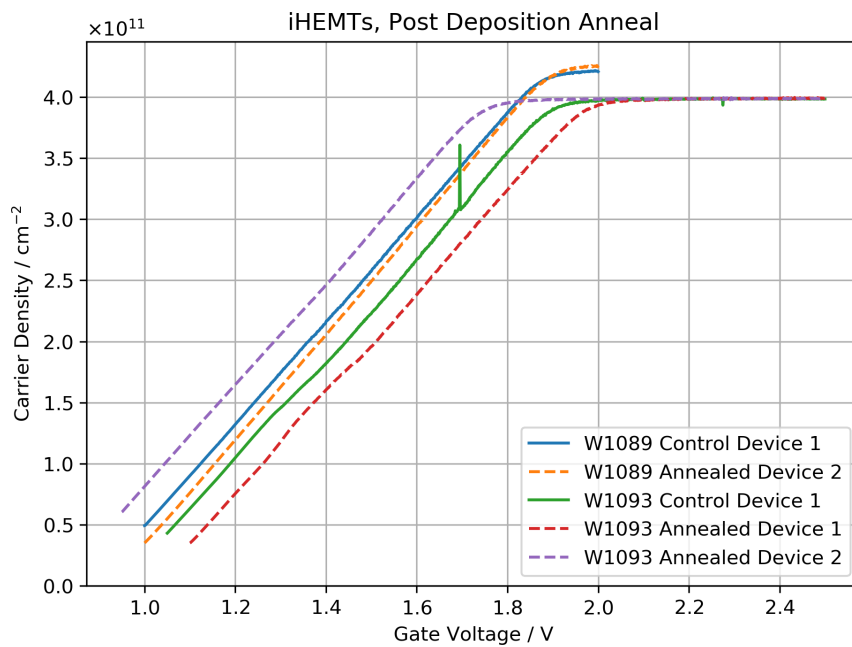


Figure 4.22: Carrier density against gate voltage curves for W1089 and W1093 with and without annealing at 300°C after Alumina insulating layer has been deposited.

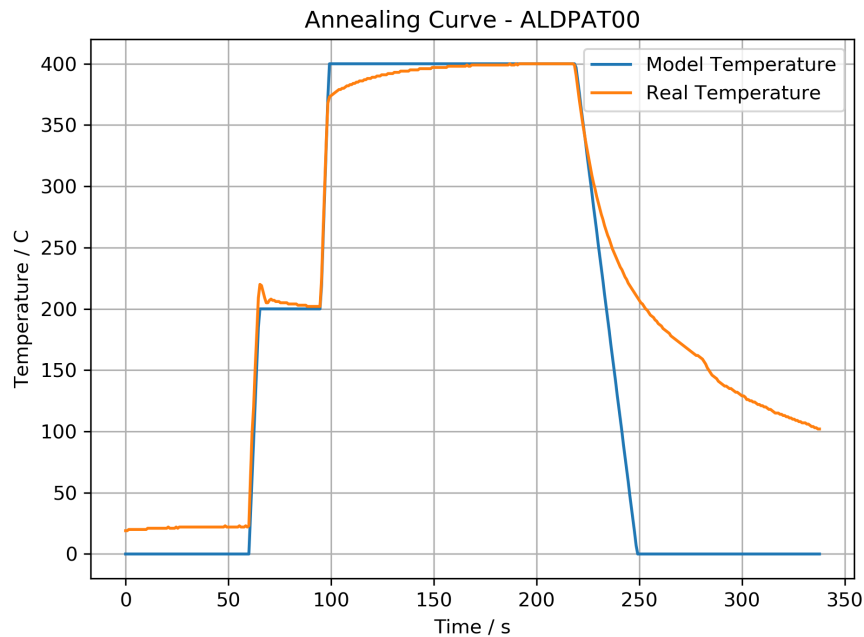


Figure 4.23: Output from RTS annealer for the post deposition annealing of the ALD alumina.

and W1093, there is no change in the maximum carrier density due to the treatment. The threshold voltage of the W1093 device does vary for the annealed devices, but as the two annealed devices have threshold voltages shifted up and down this variation does not appear to be due to the annealing.

While this particular attempt at annealing the alumina after deposition did not result in changing the carrier density curve, it also did not affect the ohmic contacts as a second anneal was feared to do. Therefore there is merit in continuing with a study of the effect of annealing the alumina to try and clean the interface and potentially improve the undoped devices working range.

4.4 Further Work and Conclusions

A 60nm thick ALD film is very thick compared to other insulating films used in industry[119–121]. It is possible to reduce the thickness of the ALD film and still have an insulating film. The ability to deposit thinner films opens up the possibility of using a few nm of ALD insulating material to insulate inducing gates used to define nanostructures. Insulating inducing gates removes problems with leakage in such devices. In this work the standard 60nm was used as there was not the time nor requirement to reduce the thickness of the alumina layer, but this would be an interesting area of study for future work.

The possible post deposition annealing to improve the alumina/GaAs interface and the

performance of the undoped device is of particular interest for the possibility of improving the mobility of shallow undoped devices. In shallow devices the mobility is limited by surface charge and therefore any improvement to the alumina/GaAs interface, thought to be a likely source of surface charge traps, would be beneficial. Such shallow devices are of particular interest for use in the fabrication of nano-structures due to the closer proximity of the carrier gas to the surface gates defining the nano-structure. This work is only in the very first stages of such research but the results from a post deposition anneal have at least shown that such treatment is not detrimental to function of the device.

In this chapter, work on the optimisation of the fabrication methods used to make undoped devices has been presented. The main improvements to the fabrication methods involved altering the photo-mask patterns for the insulating alumina layer moving away from a liftoff based processing to an etch back processing due to difficult liftoff. While ALD deposited alumina had been used in previous work on undoped devices, a new ALD system and processing was set up and optimised for use with existing fabrication methods for undoped devices. Two ALD processes, a 'dynamic' and 'static' process, were set up with deposition rates of $0.92 \pm 0.04 \text{ \AA}$ and $1.32 \pm 0.50 \text{ \AA}$ per cycle respectively with a film uniformity of $> 99.8\%$ across a 4" silicon wafer.

Analysis of AFM data of the ALD alumina coverage of AuGeNi contacts, showed no indication that the ALD was failing to cover the rough ohmic surfaces and through the careful handling of the Ni charge for the AuGeNi layer contacts the surface roughness of the contact was improved.

To quantify the yield of the ohmic contacts, an intrinsic transmission line measurement (iTLM) photo-mask set was designed and made with the results from the resistance measurements showing that the ambipolar, n-type and p-type contacts used for undoped device had a contact resistance $< 10 \text{ k}\Omega$ when the carrier gas had been induced. The contact resistance showed a dependence on the applied top gate voltage with the lowest contact resistance being between $10 \text{ }\Omega$ and $1 \text{ k}\Omega$. Based on the measurement of 20 - 40 ohmic contacts, yields of $\geq 90\%$ for all types of ohmics were achieved.

MODELLING OF 2D TRANSPORT

In chapter 3, characterisation data at 1.5K was presented and qualitatively analysed to compare the growth conditions within the MBE system. The difficulty with the analysis in chapter 3 is separating out the different contributions to the mobility of the device. From the shape of the mobility density curve, it is possible to look at the different contributions to the scattering from background impurities and the interface roughness, as these two scattering mechanisms dominate at the extrema of the carrier densities ranges measured in chapter 3. In order to examine the contributions from other sources of scattering, as such surface charge or considering different background impurities contributions from AlGaAs and GaAs regions a more detailed analysis is required.

In this chapter, the scattering rates from point-charges, interface roughness and alloy scattering modelled using the Boltzmann formalism are calculated and used to analyse the carrier mobility density curves from the devices in chapter 3. In addition to determining numerical values for the relevant growth parameters from chapter 3, the analysis is extended to numerically compare the effects of the different scattering sources in induced heterostructures and different sources of the same scattering type e.g. AlGaAs and GaAs background impurity density.

5.1 Background

For 2D transport of electrons at 1.5K, the Boltzmann formalism is sufficient to model the carrier mobility [6, 17, 122, 123]. From the Boltzmann transport equation, the carrier mobility

is defined as:

$$\mu \equiv \frac{e}{m^*} \tau \quad (5.1)$$

where the total scattering time, τ , defined as the sum of the scattering rates:

$$\frac{1}{\tau} \equiv \sum_i \frac{1}{\tau_i} \quad (5.2)$$

For the 2D transport measurement in AlGaAs/GaAs heterostructures at 1.5K, there are three sources of scattering to consider: point-charges, interface roughness, and alloy scattering. This chapter covers the calculation of the scattering rates from these three sources within the Boltzmann formalism, with the derivation based on an equivalent derivation from [17, 123].

The Boltzmann formalism describes transport using a distribution function $f(t; \mathbf{r}, \mathbf{k})$, which generally is a function of time, t , position, \mathbf{r} , and wave-vector, \mathbf{k} . The effect of any source of scattering is to cause a change to this distribution function. Assuming that within a 2DES the carrier density is uniform meaning there is no positional dependence, the distribution function is expressed as,

$$\left. \frac{\partial f_{\mathbf{k}}}{\partial t} \right|_{\text{scattering}} = - \int \frac{d^2 \mathbf{k}'}{(2\pi)^2} [\Gamma_{\mathbf{k}, \mathbf{k}'} f_{\mathbf{k}} (1 - f_{\mathbf{k}'}) - \Gamma_{\mathbf{k}', \mathbf{k}} f_{\mathbf{k}'} (1 - f_{\mathbf{k}})] \quad (5.3)$$

where the scattering event results in a change in k-state from \mathbf{k}' to \mathbf{k} with $\Gamma_{\mathbf{k}, \mathbf{k}'}$ as the probability of scattering from the k-state \mathbf{k}' to \mathbf{k} per unit time. The factors $f_{\mathbf{k}}(1 - f_{\mathbf{k}'})$ account of the probability of the initial and final k-states being occupied and vacant.

The scattering probability rates $\Gamma_{\mathbf{k}, \mathbf{k}'}$ are given by Fermi's golden rule [124],

$$\Gamma_{\mathbf{k}, \mathbf{k}'} = \frac{2\pi}{\hbar} |\langle \mathbf{k} | H' | \mathbf{k}' \rangle|^2 \delta(\epsilon_{\mathbf{k}} - \epsilon_{\mathbf{k}'}) \quad (5.4)$$

where H' is the scattering potential and the delta function, $\delta(\epsilon_{\mathbf{k}} - \epsilon_{\mathbf{k}'})$ explicitly conserves energy. Assuming that the scattering potential is time-independent and that the scattering event can only redistribute momentum, the energy within the 2DES is conserved. For the AlGaAs/GaAs heterostructures, this assumption treats the remote ionised impurities as static and requires that Phonons are negligible, both of which are true for low temperatures.

Conservation of energy within the 2DES leads to conservation of k-state magnitude as,

$$E = \epsilon_0 + \frac{\hbar^2 |\mathbf{k}|^2}{2m^*} = \epsilon_0 + \frac{\hbar^2 |\mathbf{k}'|^2}{2m^*} \rightarrow |\mathbf{k}| = |\mathbf{k}'| \quad (5.5)$$

With a conserved k-state magnitude and assuming that the scattering mechanism is symmetric e.g. $\Gamma_{\mathbf{k}, \mathbf{k}'} = \Gamma_{\mathbf{k}', \mathbf{k}}$ then equation (5.3) reduces to,

$$\left. \frac{\partial f_{\mathbf{k}}}{\partial t} \right|_{\text{scattering}} = - \frac{1}{2\pi\hbar} \int d^2 \mathbf{k}' |\langle \mathbf{k}' | H' | \mathbf{k} \rangle|^2 (f_{\mathbf{k}} - f_{\mathbf{k}'}) \delta(\epsilon_{\mathbf{k}} - \epsilon_{\mathbf{k}'}) \quad (5.6)$$

$$= - \frac{m^*}{2\pi\hbar^3} \int d\theta d\epsilon |\langle \mathbf{k}' | H' | \mathbf{k} \rangle|^2 (f_{\mathbf{k}} - f_{\mathbf{k}'}) \delta(\epsilon_{\mathbf{k}} - \epsilon_{\mathbf{k}'}) \quad (5.7)$$

where the second integral has been converted the 2D integral in \mathbf{k} -space to polar coordinates, $d^2\mathbf{k} = |k|dkd\theta$, introducing θ as the scattering angle between the \mathbf{k} -states \mathbf{k} and \mathbf{k}' and converting the integral in \mathbf{k} -state magnitude to the integral in energy.

From the linear Boltzmann transport equation, the distribution function $f_{\mathbf{k}}$ is approximated as:

$$f_{\mathbf{k}} \approx f_0 + \nabla_{\mathbf{k}} f_{\mathbf{k}} \cdot \mathbf{k} \quad (5.8)$$

where $\nabla_{\mathbf{k}} f_{\mathbf{k}}$ is a function of energy. Introducing this expression for $f_{\mathbf{k}}$ and the scattering time $\tau_{\mathbf{k}}$ defined as:

$$\frac{\partial}{\partial t} \rightarrow -\frac{1}{\tau_{\mathbf{k}}} \quad (5.9)$$

(5.6) can be further reduced to:

$$\frac{\nabla_{\mathbf{k}} f_{\mathbf{k}}}{\tau_{\mathbf{k}}} = \frac{m^*}{2\pi\hbar^3} \int d\theta d\epsilon |\langle \mathbf{k}' | H' | \mathbf{k} \rangle|^2 \nabla_{\mathbf{k}} f_{\mathbf{k}} \cdot (\mathbf{k} - \mathbf{k}') \delta(\epsilon_{\mathbf{k}} - \epsilon_{\mathbf{k}'}) \quad (5.10)$$

Equation (5.10) can be further reduced by expressing \mathbf{k}' in the basis of \mathbf{k} and noting that only the symmetric part $|k| \cos \theta$ is non zero. This gives the final expression for the scattering rate $1/\tau_{\mathbf{k}}$ as:

$$\frac{1}{\tau_{\mathbf{k}}} = \frac{m^*}{2\pi\hbar^3} \int_{-\pi}^{\pi} d\theta |\langle \mathbf{k}' | H' | \mathbf{k} \rangle|^2 (1 - \cos \theta) \quad (5.11)$$

$$= \frac{m^*}{\pi\hbar^3} \int_0^{\pi} d\theta |\langle \mathbf{k}' | H' | \mathbf{k} \rangle|^2 (1 - \cos \theta) \quad (5.12)$$

5.1.1 Scattering Mechanism

Equation (5.12) shows that the scattering rate depends on the matrix elements $|\langle \mathbf{k}' | H' | \mathbf{k} \rangle|$, which in turn depends on the scattering potential H' . Assuming that the state of the carrier, $|\mathbf{k}\rangle$, is a free state in the x-y plane, $|k_{xy}\rangle$, and a bound state, $|\psi\rangle$, then the matrix element simplifies to,

$$\langle \mathbf{k}' | H' | \mathbf{k} \rangle = \int dz |\psi(z)|^2 \tilde{V}_q(z) \quad (5.13)$$

where $\tilde{V}_q(z)$ is the 2D Fourier transform of the perturbation potential H' . The calculation of this term for each of the scattering mechanisms modelled are detailed in the following sections.

To describe the 2D transport of electrons in an AlGaAs-GaAs structure, we will consider three sources of scattering: point-charge scattering, interface roughness at the AlGaAs-GaAs interface, and alloy scattering.

5.1.1.1 Point-Charge Scattering

Within the semiconductor structure, charge-traps can form such as the well known DX centres in AlGaAs[125]. These charge-traps cause scattering due to the Coulomb interaction between

the trapped charge and the carriers in the 2DES. Using the Coulomb interaction to model the scattering from any charge causing scattering within the device, the perturbation potential, H' , for a fully ionized charge at a position z_d interacting with a charge e at position z in the 2DES is given by:

$$H' = \frac{e^2}{4\pi\epsilon_0\epsilon_r|\mathbf{r} - \mathbf{r}'|} \quad (5.14)$$

Calculating the Fourier transform of the Coulomb potential is most easily done using the translation theorem [126] so that,

$$\int dx dy \frac{e^2}{4\pi\epsilon_0\epsilon_r \sqrt{x^2 + y^2 + (z - z_d)^2}} \exp[-i(k_x x + k_y y)] = \frac{e^2}{2\epsilon_0\epsilon_r q} \exp[-q|z - z_d|] \quad (5.15)$$

by using $\mathbf{r} - \mathbf{r}' = \mathbf{r}_{xy} - i(z - z_d)$ where \mathbf{r}_{xy} is 2D vector in the x-y plane. Using the result that $\mathcal{FT}(1/|\mathbf{r}_{xy}|) = 2\pi/q$

Therefore the matrix element for point-charge scattering is given by,

$$\langle \mathbf{k}' | H' | \mathbf{k} \rangle = \frac{e^2}{2\epsilon_0\epsilon_r} \int \frac{dz}{q\epsilon_q} |\psi(z)|^2 \exp[-q|z - z_d|] \equiv \frac{e^2}{2\epsilon_0\epsilon_r} F(q) \quad (5.16)$$

introducing $\epsilon_r \rightarrow \epsilon_r\epsilon_q$ where ϵ_q accounts for carrier-carrier interactions[127–129] within the random phase approximation (RPA)[130–132] and $F(q)$ is a form-factor that accounts for the shape of the wave function due to the confining potential.

Therefore the scattering rate due to a single point charge is given by:

$$\frac{1}{\tau_{point\text{-}charge}} = \frac{m^*}{2\pi\hbar^3} \left| \frac{e^2}{2\epsilon_0\epsilon_r} \right|^2 \int_{-\pi}^{\pi} d\theta \left| \frac{F[z_d, q(\theta)]}{q(\theta)\epsilon_q(\theta)} \right|^2 (1 - \cos \theta) \quad (5.17)$$

Scattering from point charges comes in two general forms within semiconductor structures: either a 3D region with a charge density per unit volume such as background impurities, or modulation dopants, or a 2D sheet at fixed position z_d and a charge density per unit area for delta dopants or surface charges. To model these two types of scattering from point-charge the expression (5.17) is integrated with the relevant charge density, $N_{3D}(x, y, z) = N$ or $N_{2D}(x, y, z) = N\delta(z - z_d)$. These give the two following expressions for scattering due to 3D and 2D region of point charges,

$$\begin{aligned} \frac{1}{\tau_{impurity}} &= N_{impurity} \int_{-\pi}^{\pi} d\theta \int_V dz_d \nu(z_d, \theta) \\ \frac{1}{\tau_{surface}} &= \sigma \int_{-\pi}^{\pi} d\theta \nu(z_{surface}, \theta) \\ \nu(z, \theta) &= \frac{m^*}{2\pi\hbar^3} \left| \frac{e^2}{2\epsilon_0\epsilon_r} \right|^2 \left| \frac{F[z_d, q(\theta)]}{q(\theta)\epsilon_q(\theta)} \right|^2 (1 - \cos \theta) \end{aligned} \quad (5.18)$$

5.1.1.2 Interface Roughness Scattering

The interface between the GaAs and AlGaAs is not a perfect, as the AlGaAs construction on the GaAs surface forms elliptical islands with the semi-major axis aligned parallel to the major flat of the wafer [103]. The model for the interface roughness is a small random variation in the position of the interface at $z = 0$ with displacement Δ_r which is assumed to follow a Gaussian autocorrelation[127, 133, 134],

$$\Delta_r * \Delta_{r'} = \Delta^2 \exp[-(\mathbf{r} - \mathbf{r}')^2 / \Lambda^2] \quad (5.19)$$

where the parameters Δ and Λ describe the roughness amplitude and the roughness correlation length. While the interface correlation length varies with crystal direction in the wafer, a single parameter Λ is used here because the Hall bars used to measure the carrier mobility constraint the carriers to move along a single direction. Therefore the more complex dependence of the correlation length of the crystal direction can be ignored and replaced with a single parameter to describe the interface roughness in a particular direction.

As the roughness of the interface is assumed to be small, a Taylor expansion of the confinement potential gives the approximate perturbation potential H' ,

$$U(z + \Delta_r) \approx U(z) + \frac{dU}{dz} \Delta_r + O(\Delta_r^2) \quad (5.20)$$

hence $H' \approx dU(z)/dz \Delta_r$. Calculating the matrix element from this perturbation potential

$$\langle \mathbf{k} | H' | \mathbf{k} \rangle = \Delta_q \int dz |\psi(z)|^2 \frac{dU}{dz} \quad (5.21)$$

In order to calculate the gradient of the confinement potential we use the fact that the state must be a bound state, and therefore have no net force acting on the state. Hence the following integral must be zero[135],

$$\int dz |\psi(z)|^2 \left(\frac{dU}{dz} + \frac{dV_H}{dz} + \frac{dV_d}{dz} \right) = 0 \quad (5.22)$$

Here $U(z)$ is just a step function due to the step in the conduction band at the GaAs/AlGaAs interface and therefore the derivative involves a delta function. V_H and V_d are the Hartree potential and depletion field potential, discussed in more detail in section 5.5. Using the bound state property above, the required integral for the matrix element can be calculated from the Hartree and depletion field potentials.

From the Gaussian autocorrelation definition of the interface roughness, the interface roughness Δ_q is,

$$\begin{aligned} \Delta_q &= \mathcal{FT}(\Delta_r) = \sqrt{\mathcal{FT}(\Delta_r * \Delta_{r'})} \\ &= \Delta \exp[-\Lambda^2 q^2 / 4] \end{aligned} \quad (5.23)$$

therefore the scattering rate due to interface roughness is given by,

$$\frac{1}{\tau_{IR}} = \frac{m^*}{2\pi\hbar^3} (\Delta\Lambda)^2 \int_{-\pi}^{\pi} \frac{d\theta}{\varepsilon_q} \exp[-\Lambda^2 q(\theta)^2/2] (1 - \cos\theta) \left[\int dz - |\psi(z)|^2 \left(\frac{dV_H}{dz} + \frac{dV_d}{dz} \right) \right]^2 \quad (5.24)$$

5.1.1.3 Alloy Scattering

Alloy scattering occurs due to the random replacement of some atoms in a material with different atoms that form the alloy, for example Al atoms replace Ga atoms in AlGaAs. This random replacement of some atoms in the structure introduces a disorder potential which causes the scattering. From the Harrison and Hauser model [127, 136] for Ga and Al atoms, the scattering rate for alloy scattering is given by[127]:

$$\frac{1}{\tau_{Al}} = \frac{2\pi x(1-x)\Delta E_c^2 a^3}{\hbar} \frac{1}{4} \int_{-\pi}^{\pi} \frac{d\theta}{\varepsilon_q} (1 - \cos\theta) \int dz |\psi(z)|^4 \quad (5.25)$$

where x is the Al fraction, ΔE_c the difference in the carrier band between AlAs and GaAs, in this case 1.58 eV[65] and a is the lattice constant of GaAs.

5.1.1.4 Form-Factors

The scattering rates detailed in the previous sections all have a dependence on the confinement wave function. If an analytic wave function is used then the wave function dependence can be calculated. The form-factors defined in this section summaries the wave function dependence of the scattering rates.

$$\begin{aligned} F_{PC} &= \int dz |\psi(z)|^2 \exp[-q|z - z_d|] \\ F_{IR} &= \exp[-\Lambda^2 q(\theta)^2/4] \int dz - |\psi(z)|^2 \left(\frac{dV_H}{dz} + \frac{dV_d}{dz} \right) \\ F_{AL} &= \int dz |\psi(z)|^4 \end{aligned} \quad (5.26)$$

For a genuinely 2D conducting gas, the wave function is a delta function at $z = 0$. For a real 2DES, the carriers are confined in the z -direction, leading to 2D transport, but the confinement has an extension in the z -direction. Therefore, the wave function of the sub-band of the confining potential must be used to calculate these form-factors. While it is possible to use numerical Poisson-Schrodinger solvers such as nextnano [64], the use of variational wave functions to approximate the sub-band wave function allows the form-factors to be computed by hand, saving computational time when modelling the scattering rates.

5.1.2 Fang-Howard Wave Function

One of the simplest and most commonly used variational wave function is the Fang-Howard function [137]. The wave function is defined as,

$$\psi_{FH}(z) = \begin{cases} \sqrt{\frac{b}{2}}z \exp[-bz/2] & \text{if } z > 0 \\ 0 & \text{otherwise} \end{cases} \quad (5.27)$$

where the parameter b is a variational parameter determined by minimising the total energy of the system. A more detailed calculation is presented in section 5.5 but by minimising the total energy of the system using the Hartree and depletion field potentials, the Fang-Howard b parameter is found to have a dependency on the carrier density, n_c and depletion field areal density, N_d , given by,

$$b^3 = \frac{12m^*e^2}{\epsilon_0\epsilon_r\hbar^2} \left(\frac{11}{32}n + N_d \right) \quad (5.28)$$

The form-factors for the Fang-Howard wavefunction are summarised in (5.29).

$$\begin{aligned} F_{PC}(q) &= \frac{8 + 9\frac{q}{b} + 3\left(\frac{q}{b}\right)^2}{8\left(1 + \frac{q}{b}\right)^3} \\ F_{IR}(q) &= \frac{ne^2}{2\epsilon_0\epsilon_r\epsilon_q} \exp\left[-\frac{q^2\Lambda^2}{2}\right] \\ F_{AL}(q) &= 0 \end{aligned} \quad (5.29)$$

The Fang-Howard wave function captures the key behaviour of the approximately triangular potential well that the GaAs/AlGaAs interface forms, with the peak of the wave function near the interface and pushed closer as the carrier density increases, but with a long tail that goes $\approx 50 - 100\text{nm}$ into the GaAs buffer. While the simplicity of the Fang-Howard wave function makes scattering rate calculation straight forward, there are two major shortcomings. Firstly, the Fang-Howard wave function by definition is terminated at $z = 0$, so there is no penetration into the AlGaAs spacer. The lack of penetration into the AlGaAs has two small effects on the calculated scattering rates: the scattering rate due to impurities in the AlGaAs region will be lower than in reality, and there is no alloy scattering as there is no wave function in the AlGaAs region. Secondly, the Fang-Howard function does not decay as quickly as the true wavefunction. This means that the average position of the carrier is further away from the interface than in reality, once again reducing the effect of the impurities in the AlGaAs region as well as reducing the effect of interface roughness. These shortcomings and potential solutions are discussed in detail in section 5.5, but the Fang-Howard wave function is still useful for characterising samples to understand the dominant scattering mechanisms from point-charges in the form of background impurities and surface charge and interface roughness.

5.2 Motivation for Fitting Experimental Data via Non-Linear Optimisation

In previous work [6] the Boltzmann scattering rate model described in the previous section has been used to fit for the relevant growth parameters, using a range of 50nm and 100nm induced heterostructures. In that work, the method for determining the fit parameters did not give an estimate of the uncertainty of the fitted values. This left the open questions, to what level the numerical values of the parameter could be trusted, and more generally, did the fitted parameter correspond to the global minima of the ‘goodness of fit’ metric?

To extend the analysis using the scattering rate model, use of non-linear optimisation algorithms to fit the scattering rate model by the minimisation of χ^2 . The optimisation algorithms and other standard mathematical functions were provided by the scientific Python (scipy) library[138]. The methods from the scipy library force the scattering rate model analysis to be framed as a non-linear optimisation problem. This allows the problem of the uniqueness of a solution / set of fit parameters to be more directly addressed. For example, the background impurity densities in the AlGaAs and GaAs regions are the dominant sources of scattering within the undoped structure, as seen from the shape of the mobility-density curves in chapter 3. Both background densities are calculated using the scattering rate, due to point charges assumed to have a uniform density within a region of the structure, and therefore have very similar mobility-density curves. It is unclear how easy it is to uniquely separate the contributions from the AlGaAs and GaAs contributions when they have such similar curves. By using non-linear optimisation, not only can the fitting on the parameters be done without input from a user, but estimates of the uncertainty in the fitted parameters can be estimated to attempt to determine if difference between the AlGaAs and GaAs can be seen in the mobility-density curves.

5.2.1 Fitting Procedure

In order to fit the mobility density curves obtained from standard assessment in section 3.2.2, the mobility as a function of carrier density was calculated, and then the residuals to the experimental mobility examined to calculate parameters from the model. The free parameters in the model are the point charge densities for background impurities and surface charge and the two interface roughness parameters Δ and Λ , as these are the parameters of the model set by the conditions in the growth chamber.

The ‘goodness of fit’ metric used for fitting a model, $y(\mathbf{p}, x)$, with parameters \mathbf{p} , to a dataset, (x_i, y_i) , was the standard least-squares metric $\chi^2 \equiv \sum_i [(y_i - y(\mathbf{p}, x_i))/\sigma_i]^2$. However, to improve the speed and accuracy of the fitting routines used, the reciprocal of the mobility was fitted as a function of carrier density. From the definition of the mobility, the reciprocal of the

mobility is given by,

$$\frac{e}{m^*\mu} \equiv \sum_i \frac{1}{\tau_i(n_c)} \quad (5.30)$$

In this form the scattering rates, $1/\tau(n_c)$ are calculated using (5.12). Because the scattering rates are proportional to the free parameters, this form of the model is as close as possible to a linear model. The one exception is the interface roughness correlation length, Λ , which causes the interface roughness scattering rate to be non-linear in Λ .

5.2.1.1 Optimisations from Previous Scattering Rate Model Computations

The improvements to the model focus on computation efficiency, expanding the functionality of the model, and allowing for further expansion to the model in the future. The main computation improvement makes use of standard integration libraries to replaced fixed-step trapezium rule integration. Use of integration libraries increases the accuracy of the integration, as tolerances can be defined, and adaptive step size integration routines reduce the computation time notably. The functionality of the model has been expanded by creating a form-factor object to handle the form-factor calculation. The form-factor object means new wave functions, such as for a quantum well wafer structure, can be added to the model by the creation of a new form factor object, instead of writing a new model.

In order to avoid unnecessary computations during the fitting, which require many function evaluations, for point-charge scattering, the integral (5.18) can be precomputed and stored before running the fitting routine. Storing the integrals avoids computing these integrals each time a scattering rate is required, allowing fitting of the data in a few minutes rather than hours. The Python library, *scipy* [138], handles the fitting of the data set, as multiple optimisation algorithms are implemented in the library. These algorithms are well documented and allow for constrained optimisation of an objective function, in this case, χ^2 .

5.2.1.2 Use of Atomic Units

The expected size of the parameters is $O(10^{20})$ for background impurities but $O(10^{-9})$ for the interface roughness parameters in SI units. In order to reduce the difference in order of magnitude, the scattering rate model was calculated in atomic units where the units of energy, time, charge, and mass are scaled such that the electron mass, $m_0 = 1$, electron charge, $e = 1$, reduced Planck constant, $\hbar = 1$ and the Coulomb constants, $1/4\pi\epsilon_0 = 1$ are all one by definition. This unit system is particularly useful for atomic physics as the length scale and energy scale are the Bohr length $a_0 = 0.0529\dots\text{nm}$ and Hartree energy $E_h = 27.2\dots\text{eV}$. In practice, this unit system halves the difference in the order of magnitude between parameters from 29 in SI units to around 12 in atomic units and the reciprocal mobility is of the order

$O(10^{-7})$, which helps the minimisation routines converge more efficiently than using SI units. For the remainder of this chapter, all modelling uses atomic units unless stated otherwise.

5.2.1.3 Error Estimation in Fit Parameters and Over Fitting

As part of using the scattering rate model to fit growth parameters, an estimate of the uncertainty in the fitted parameter is needed to avoid giving undue importance to the value of the fitted parameters. Two methods were used to obtain estimates of the uncertainty in the fit parameters. The first uses the scipy function ‘curve_fit’ which provides a numerical estimate of the covariance of the fitted parameters. The square root of the diagonal terms in the covariance matrix give estimates of the uncertainties in the parameters. Other optimisation routines in the scipy library, only provide the values of the free parameters at the found minimum. The second method approximates the Hessian matrix of the objective function, χ^2 , at the found minimum. Based on the degrees of freedom in the data an acceptable change in χ^2 for a set confidence interval is calculated. From this change in χ^2 and the Hessian matrix bounds on the free parameters can be determined, given an uncertainty value for each parameter. Details of this calculation are given in appendix C. This method can be used with any optimisation method that finds a minimum in the objective function. These two methods result in very small estimated uncertainties, particularly for the interface roughness parameters, which often have uncertainties less than 1pm. Uncertainties this small are not physical and raise the questions of over-fitting.

Over-fitting is a problem in fitting real data, where minimisation routines such those implemented in the scipy library can adjust the free parameters to match the experimental data, including any noise or anomalous points in the data. Over-fitting results in the model function only matching the given data points, and has limited use as a predictive model for values that were not used to calculate the free parameters. The fitting routine has an option to use K-fold cross-validation to reduce the problem of overfitting experimental data.

K-fold cross-validation [139] is a resampling method which can limit the potential of over-fitting and provide a more robust fitting routine. The core idea of the method is to break the dataset into k subgroups by random sampling without replacement and then removing each subgroup in turn ‘training’ the model on the remaining data from all $k - 1$ subgroups. Here, ‘training’ of the model means minimisation of the χ^2 with respect to the free parameters of the model. After ‘training’ the removed subgroup is used as a test dataset. Calculating the residuals of the model using the test dataset and the ‘goodness of fit’ metric, χ^2 in this model, provides a ‘goodness of fit’ value based on the predictive value of the model. At the end of K-fold cross-validation, there are k sets of fitted parameters, each with a predictive χ^2 value. The χ^2 values allow the fitted parameters to be compared based on their predictive accuracy to

data that was not used to ‘train’ the model. These values of χ^2 can be used to reduce the effect of anomalous data points and noise within the dataset. K-fold cross-validation also provides a set of fitted parameters which can be used to look at the variation of the fitted parameters values, used here to estimate the uncertainty in the parameters.

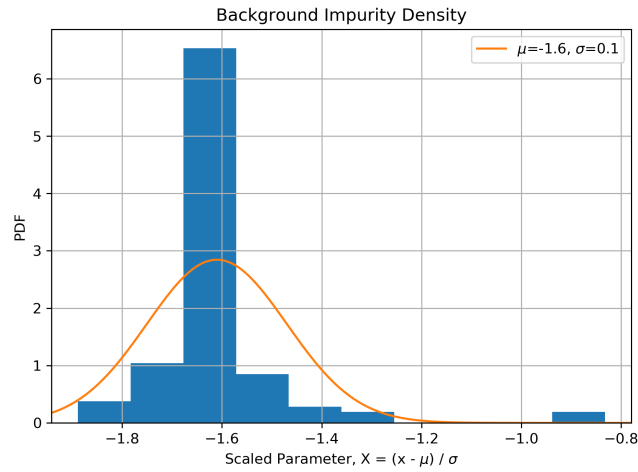
The disadvantage of using K-fold cross-validation is that it requires k objective function minimisation and residual evaluation, and therefore can have a significant time penalty when used. With the optimisations of the model calculations, from 5.2.1.1 K-fold cross-validation with five folds in a dataset of 20 points takes 5-20 minutes when using the simplest models for the confinement.

The range of parameter values that K-fold cross-validation produces showed a much larger spread than the uncertainty estimates from the covariance matrix would have suggested, indicating that over-fitting is an issue for modelling mobility.

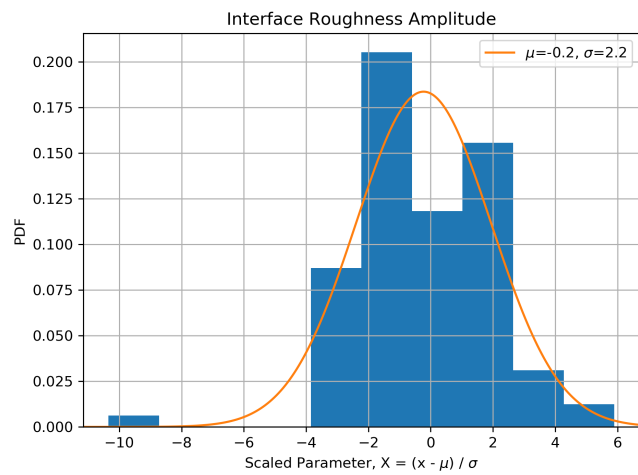
5.2.2 Testing of Fitting Procedure

Validation of the fitting procedure generated mobility-density from known parameters to use as test data sets. After the addition of a small amount of Gaussian noise to each dataset, the fitting routine was run with the test data set with the resulting parameters and uncertainty estimates checked against the known original parameters. Testing started with the simplest scattering rate model, a 100nm heterostructure with a uniform background impurity density in the AlGaAs and GaAs and interface roughness. Figure 5.1 shows the results of testing the non-linear optimisation of the full data set. The histograms in figure 5.1 are of the scaled parameter $X = (x - \mu)/\sigma$ for the 100 sets of parameter. If the fitted routine works perfectly, this scaled parameter X should be described by a Gaussian distribution, with a mean and standard deviation of zero and one respectively. The histograms for the interface parameters show that the fitting routine is working well, finding the parameters within the estimated uncertainties. The histogram for the background impurity density illustrates the problem of over fitting, as the histogram is not centred between ± 1 , which indicates that the fitted values are not correct within the estimated uncertainties due to over-fitting of the data causing the size of the uncertainties in the parameters to be under-estimated, while also causing the fitting routine to find values smaller than the true values. K-fold cross-validation should help with this problem.

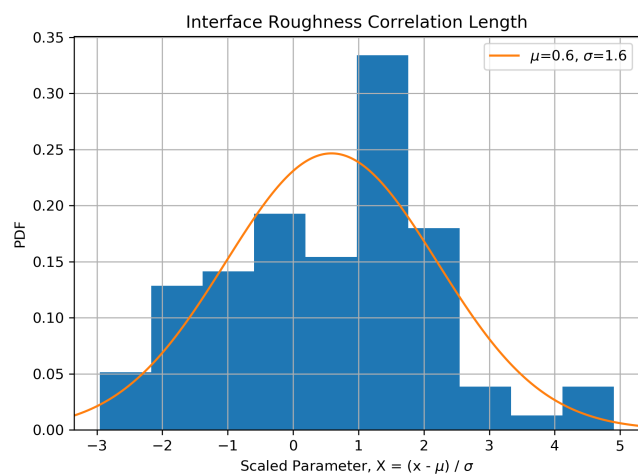
Running the same series of tests with the K-folding enable with 20 data points and 5 folds, gave the fitting results in figure 5.2 with a total of 100 parameter sets generated and tested. The fitted Gaussian in figure 5.2 all have a mean of between ± 1 but with a standard deviation greater than 1. This shows that the fitting routine is working, as the fitted parameters are, on average correct, to within the estimated uncertainty, but the larger standard deviation indicates that the estimated uncertainty still under-estimate the error in the fitting routine.



(a) Background Impurity Density

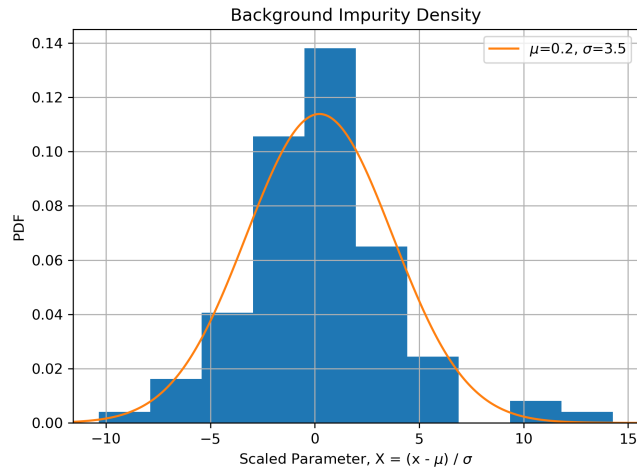


(b) Interface Roughness Amplitude

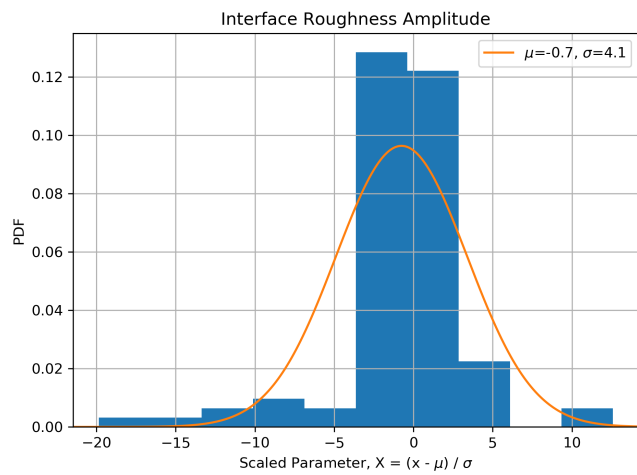


(c) Interface Roughness Correlation Length

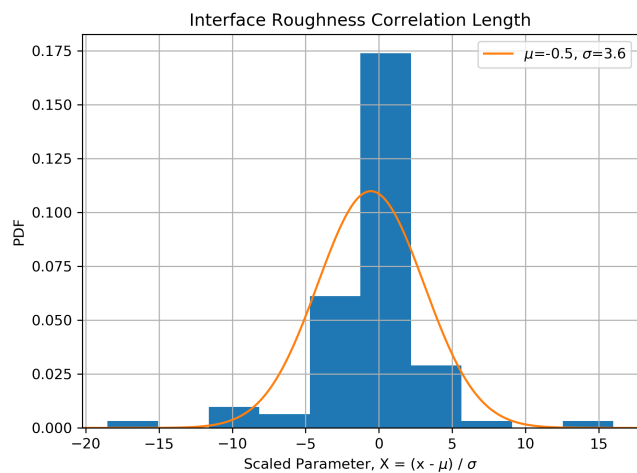
Figure 5.1: Fitting results from 100 generated dataset for a 100nm heterostructure with a uniform background impurity density in the AlGaAs and GaAs and interface roughness. The results of the fitting have been scaled $X = (x - \mu) / \sigma$ to compare to the expected Gaussian curves. The background impurity density shows the problem of over fitting, as the fits have a very small uncertainty but are not centred at zero, showing that the fitting routine is not finding the correct value due to the added noise.



(a) Background Impurity Density



(b) Interface Roughness Amplitude



(c) Interface Roughness Correlation Length

Figure 5.2: Results from test fitting of a 100nm Heterostructure with a uniform background density and interface roughness. The results of the fitting routine have been converted to the scaled parameter $X = (x - \mu) / \sigma$ which would ideally be following a Gaussian distribution, centred at zero, with a standard derivation of one. The fitted Gaussian (solid lines) show that the parameters X are centred near zero with a standard derivation greater than one. This indicates that the fitting routine is working, but the estimated errors can be smaller than the true error.

One of aims in introducing an automatic fitting routine was to explore the possibility of distinguishing different levels of background impurities in different regions of the structure. For a heterostructure, the two regions of interest are the AlGaAs spacer and the GaAs buffer. It is suspected that the AlGaAs spacer has a higher level of impurities than the GaAs, but the carriers themselves are further away from the AlGaAs compared to the GaAs buffer. Scattering from point charges has an exponential dependence on the distance from the point charge with the Fermi wave-vector giving the length scale of the dependence. Because of these two factors is difficult to determine the extent to which the two different regions impact the mobility. By using the fitting routine development, not only can the mobility-density curves be fitted for without human bias, but the estimated uncertainties in the fitting parameters will help to determine the fitted values for the different background impurity densities can distinguish for each other, given the uncertainties.

The histograms in figure 5.3 contain histograms of the scale fitted parameter $X = (x - \mu)/\sigma$ from a set of 100 test fits to 100nm heterostructure with AlGaAs and GaAs backgrounds and interface roughness. The results in figure 5.3 are very similar to the results in figure 5.2, showing the fitting routine is working, but the estimated errors can still be smaller estimates of the true error. This result shows that, in principle, the fitting routine used can distinguish between AlGaAs and GaAs backgrounds.

5.3 Characterisation with the Fang-Howard Wave Function

With the form-factors for the Fang-Howard wave function, it is possible to calculate mobility-density curves like those experimentally determined in section 3.2.2. For a 100nm AlGaAs spacer with $1 \times 10^{15} \text{cm}^{-3}$ background impurity density and an interface roughness amplitude of $A = 0.3 \text{nm}$ and interface roughness correlation length $\Lambda = 10 \text{nm}$, the mobility-density curve using the Fang-Howard wave function is shown in figure 5.4. These parameters were chosen to approximate a very lightly doped HEMT structure with an interface roughness on the order of a monolayer of GaAs over 20 units cells. The mobility-density curve in figure 5.4 shows the same general behaviour seen in the experimental mobility-density curves from section 3.2.2, with the background impurities dominating at carrier densities below $1 \times 10^{11} \text{cm}^{-2}$ but the interface roughness becoming comparable and exceeding the background impurities at carrier densities higher than $1 \times 10^{11} \text{cm}^{-2}$. An increase in interface roughness scattering gives rise to the turning over of the mobility curve seen in the experimental curves.

As the Fang-Howard wave function can produce curves that are similar to the measurement curves, the possibility of fitting the model to the experimental curves to give characteristic values for impurities in the structure and the roughness of the AlGaAs/GaAs interface, thereby

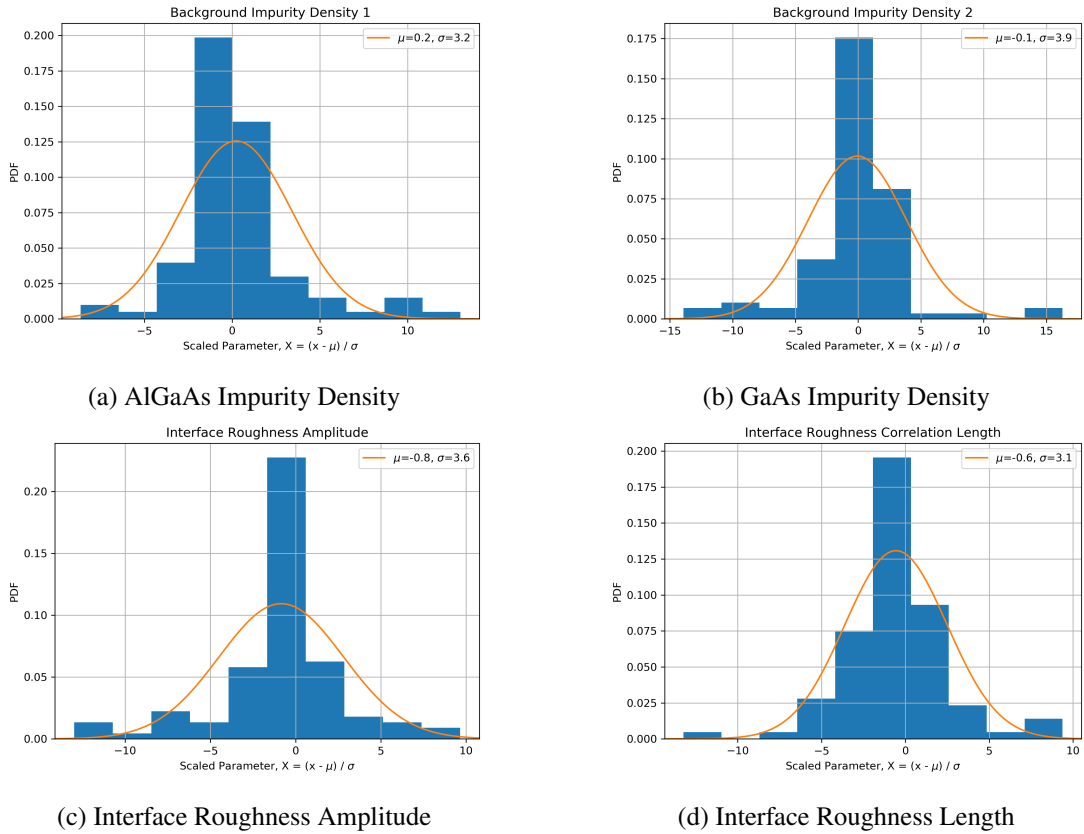


Figure 5.3: Test fitting results for 100 test fits of data from a 100nm heterostructure with AlGaAs and GaAs backgrounds and interface roughness. The histogram of the scaled result from the fits $X = (x - \mu)/\sigma$ have been fitted with a Gaussian distribution showing that the fitting routine obtains the correct parameters as all distributions have a mean of between ± 1 .

giving quantitative information about the state of the growth chamber, is worth exploring.

5.4 Analysis of iHEMT Mobility-Density Curves

The mobility density curves from section 3.2.2 were analysed using the Fang-Howard wave function for the confinement wave function. This allows a more detailed and quantitative analysis of the effect of variations of the conditions within the growth chamber. For the 50nm and 100nm iHEMTs, the model used a global background impurity density in both the AlGaAs and GaAs regions with interface roughness, and for the 50nm devices a surface charge density.

Before running the fitting routine on real experimental data, providing bounds on the background impurity densities, surface charge density, and interface parameters based on physically meaningful values is important to avoid unphysical results. For the background impurity and surface charge, the densities can be bound by looking at modulation-doped HEMTs and the

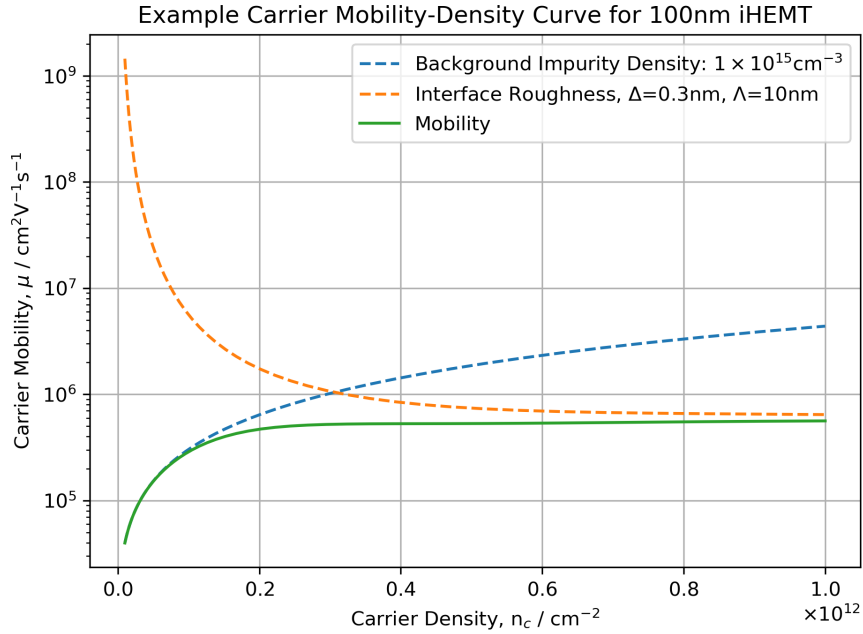


Figure 5.4: Carrier mobility-density curve for a 100nm AlGaAs spacer iHEMT with a background impurity density of $1 \times 10^{15} \text{cm}^{-3}$ and an interface roughness amplitude of $\Delta = 0.3 \text{nm}$ and interface roughness correlation length $\Lambda = 10 \text{nm}$ using the Fang-Howard wave function.

carrier densities in the iHEMTs. Doped HEMTs are grown with dopant densities of the order $\mathcal{O}(10^{18} \text{cm}^{-3})$. While there is not a simple one-to-one mapping of physical dopant density and the charge centres caused by the dopants, as the iHEMT have no intentional dopants the dopant density for the doped structures can be taken as an upper bound. Similarly, for the surface charge density, considering the iHEMT device as a capacitor, the charge on present on the top contact will be of the same order of the carrier density in the conducting gas, as the device starts as being charge-neutral. An upper bound of $\mathcal{O}(10^{12} \text{cm}^{-2})$ is used for the surface charge density.

The interface roughness parameters are harder to estimate, as the interface by its nature is difficult to image directly. For bounds on the interface parameters, the surface roughness of the wafer is used as an approximation for the AlGaAs/GaAs interface. The surfaces of W1088, W1089, W1091, and W1093 were measured with an AFM, scanning a $10 \mu\text{m}^2$ area. The AFM data for W1088 and W1091 are shown in figure 5.5. The y-axis of the images is parallel to the major axis, and the length scale of the roughness in these directions is significantly longer than in the direction parallel to the minor direction. The amplitude of the roughness is $\pm 1 \text{nm}$, which corresponds to 1-2 lattice constants for GaAs.

The interface roughness within the scattering rate model is characterised by the parameters Δ and Λ , which are defined by the autocorrelation of the interface roughness, $\Delta r(\mathbf{x}) * \Delta r(\mathbf{x}') \equiv$

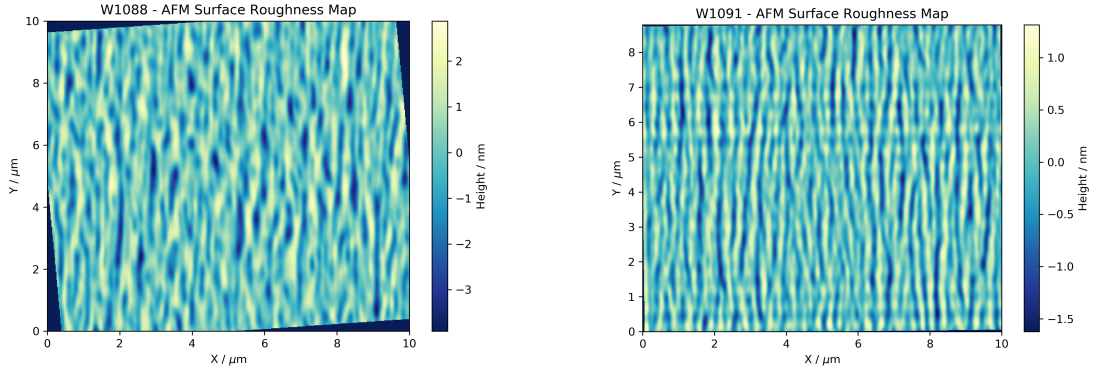


Figure 5.5: AFM Images of the surfaces of W1088 and W1091. The y-axis of the images is aligned parallel to the major of the wafers. Both images have been rotated to correct for misalignments.

Wafer	Δ /nm	Λ_X /nm	Λ_Y /nm
W1088	1.139 ± 0.006	75.47 ± 0.11	483 ± 4
W1089	1.060 ± 0.006	60.09 ± 0.25	509 ± 5
W1091	0.435 ± 0.003	48.1 ± 0.6	558 ± 3
W1093	0.540 ± 0.004	48.6 ± 0.6	613 ± 2

Table 5.1: Summary of surface roughness Gaussian fits of the autocorrelation in the Y direction parallel to the major flat and the X direction parameter to the minor flat.

$\Delta^2 e^{-\frac{(x-x')^2}{\lambda^2}}$. Here, the correlation length is shown as a vector, as it varies with crystal direction as can be seen in figure 5.5. In order to gain an estimate of the order of magnitude for Δ and Λ , the autocorrelation of the AFM data in figure 5.5 was calculated, shown in figure 5.6.

The autocorrelations of the surface roughness are shown in figure 5.6: both show a peak at the centre which decays to approximately zero within 1-2 μ m, with two different length scales in the X and Y directions. Assuming a Gaussian peak shape of the form in the scattering model the peak was fitted for the general linear model of a conic section $aX^2 + bX \times Y + cY^2 + dX + eY + F = \ln \Delta r * \Delta r$. The fitted conic was found to be an ellipsoid, centred at the centre of the autocorrelation, with minor and major axis closely aligned with the X and Y axes. The major and minor axes of the fitted ellipsoid are marked in figure 5.6. Cuts of the interface roughness autocorrelation along the major and minor axes are shown in 5.6. The roughness parameters Δ , Λ_X , and Λ_Y were calculated from the fitted ellipsoid and the resulting Gaussians have been plotted in 5.6. A summary of the fitted parameters is given in table 5.1. The surface roughness amplitude is of the order of 1-2 units cells for GaAs, and the correlations lengths range from ≈ 50 nm parallel to the minor flat up to ≈ 600 nm parallel to the major flat.

The values of Δ obtained are comparable to other measurements of MBE grown (001)

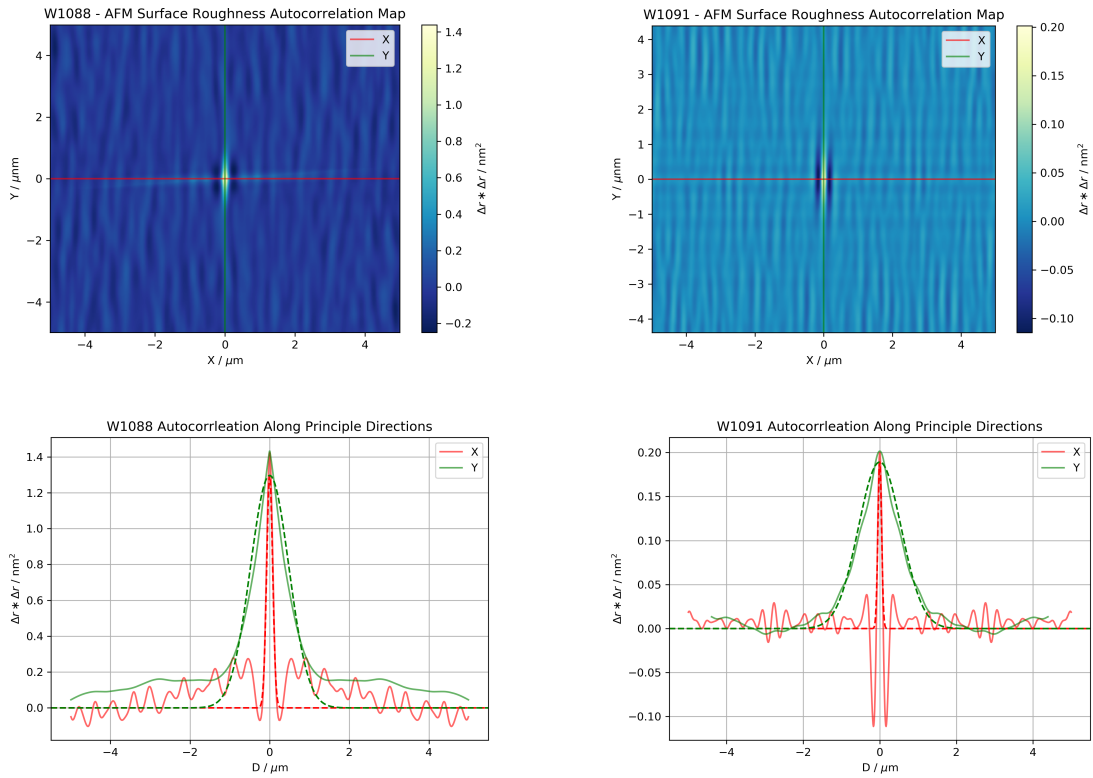


Figure 5.6: Autocorrelation of surface roughness data taken using an AFM. The principle axis of the surface roughness has been calculated from a linear fit of a conic section and has been marked. The autocorrelation in these two directions has been plotted and fitted with a Gaussian (dashed) with the parameter Δ and Λ from the scattering rate model. A summary of the Gaussian fit parameters for W1088, W1089, W1091, and W1093 is given in table 5.1.

GaAs surfaces [140–142], however measurements of the $\text{Al}_x\text{Ga}_{1-x}\text{As}/\text{GaAs}$ interface during growth [143, 144] show that the interface can be an order of magnitude lower. The values for Λ are comparable to reported values for GaAs/AlAs quantum wells[145].

While the relation of the surface roughness to the interface roughness is not clear as the GaAs/AlGaAs interface and the GaAs cap surface have some significant differences, the surface roughness parameters give an idea of the order of magnitude of the interface roughness parameter and provide a useful upper bound for the interface roughness parameters.

5.4.1 Cool Down

Figure 5.7 contains the carrier mobility-density curves for a 100nm AlGaAs spacer iHEMT from W1171. A single device from this wafer was cooled down multiple times to see how much of an effect the cooldown of an induced device had on the mobility-density curve. As the mobility-density curves are from the same device, the variation in the fitted parameters in

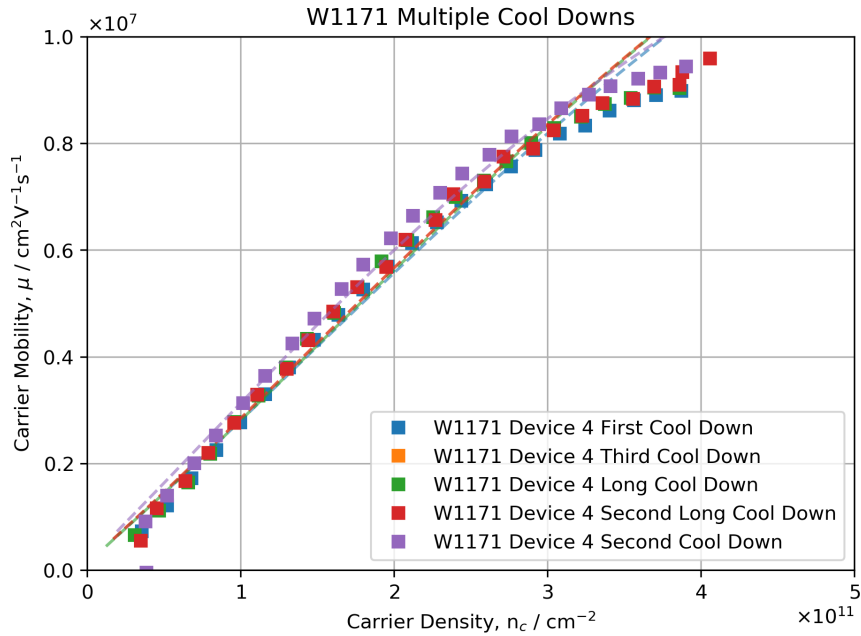


Figure 5.7: Carrier mobility-density curves for a 100nm AlGaAs spacer iHEMT cool down multiple times, with fitted mobility curves.

Cool Down	$N_i/10^{14}\text{cm}^{-3}$	Δ/nm	Λ/nm
First Cool Down	2.06 ± 0.03	0.24 ± 0.02	41 ± 1
Second Cool Down	1.82 ± 0.005	0.7 ± 0.3	80 ± 30
Third Cool Down	2.04 ± 0.03	0.28 ± 0.02	47 ± 1
Long Cool Down	2.08 ± 0.03	0.6 ± 0.3	80 ± 30
Second Long Cool Down	2.04 ± 0.03	0.28 ± 0.02	47 ± 1

Table 5.2: Summary of fitted parameter for a 100nm AlGaAs spacer iHEMTs cool down multiple times.

table 5.2 will be representative of uncertainty in the fitted parameters, as the physical growth parameter will be identical.

The values in 5.2 show excellent agreement in the fitted background impurity density, except second cool-down which is significantly lower than the other cool-downs. Looking at the mobility curves in figure 5.7, the second cool-down mobility curve is the highest mobility curve, which would correspond to a lower background impurity density. The interface parameters for the second cool-down and long cool-down are much larger than the other fits, but the uncertainties in the fitted parameters are much more considerable, and once these are considered the interface parameters are in agreement. Looking at the fitted curve themselves it's clear that no one the fits curve in the same way the data does at carrier densities $>3.5 \times 10^{11}\text{cm}^{-2}$. Therefore the fitting routine is not capturing the interface roughness contribution to the mobility-

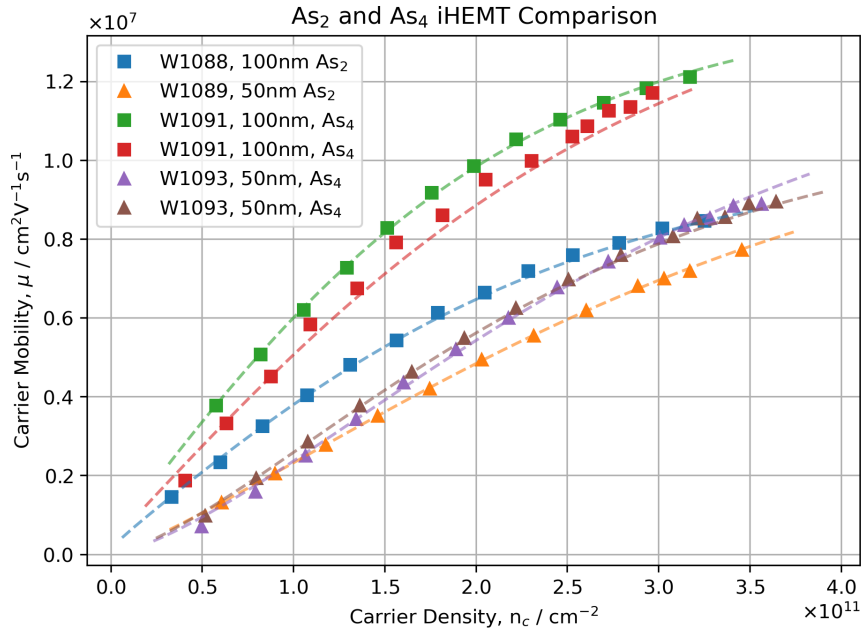


Figure 5.8: Carrier Mobility density curves for 100nm and 50nm, As₂ and As₄ iHEMTs measured at 1.5K. A mobility density curve has been fitted to the experimental data assuming a global background impurity density, interface roughness and for the 50nm device surface charge density, resulting curve plotted.

density curve due to the lack of data at higher carrier density where the interface roughness is more significant. Therefore the disagreement and wide ranges particular for the interface correlation length scale, Λ is understandable as these values do not correspond to the data.

The difficult in fitting for the interface roughness component of the mobility does leave open a question about the physical significance of the parameter introduced in equation 5.23. If these parameters are physical characteristics of the interface then they should not vary between cool down. However because of the difficulties in extracting these parameters it is not possible to see if these parameters vary with cool down indicating that they are not related to the physical interface.

In summary, the small variation in the mobility-density data due to cool-down effects lead to variation in the fitted parameters but the variations of these parameters is comparable to the uncertainty estimates for each parameter. Therefore the cool-down variation is not significant enough to change the conclusions from the mobility-density model analysis.

5.4.2 As₂ vs As₄

Figure 5.8 contains the mobility-density curves from section 3.2.2. Assuming a global background impurity density, interface roughness, and for the 50nm devices a surface charge, the

Wafer	$N_i/10^{14}\text{cm}^{-3}$	Δ/nm	Λ/nm	$\sigma/10^9\text{cm}^{-2}$
W1088	1.35 ± 0.01	0.7 ± 0.2	60 ± 15	-
W1089	1.7 ± 0.1	0.056 ± 0.003	10.7 ± 0.6	7.1 ± 0.8
W1091	0.832 ± 0.009	0.92 ± 0.15	80 ± 9	-
W1091	1.04 ± 0.02	0.47 ± 0.26	54 ± 19	-
W1093	< 0.01	0.056 ± 0.001	9.2 ± 0.5	20.77 ± 0.04
W1093	0.1 ± 0.2	0.074 ± 0.001	12.3 ± 0.2	17.3 ± 0.3
W1088 & W1089	1.08 ± 0.05	0.2 ± 0.1	27 ± 9	9.4 ± 0.2
W1091 & W1093	0.65 ± 0.4	0.39 ± 0.03	45 ± 3	12.3 ± 0.03

Table 5.3: Summary of fitted parameters for the mobility-density curves in figure 5.8 for 100nm and 50nm, As₂ and As₄ iHEMTs measured at 1.5K

mobility-curves were fitted for the background density N_i , interface roughness amplitude Δ , interface roughness correlation length Λ , and the surface charge σ . A summary of the fitted values is given in table 5.3.

The modelling results agree with the assessment of the mobility density curves from section 3.2.2 and can describe the small variations in the different devices and wafers very well. However, there is only a broad agreement between devices from the same wafer in the fitted parameters. The variation in the parameters is most likely due to cool down effects; the freezing on the background potential causes small changes between different cool-downs, as seen in section 3.2.2. These small variations in the background potential could be described by point charge scattering, so could explain the difference in the fitted values and the mobility density curves of different device from the same wafer.

Despite the disagreement in the fitted parameters; a general trend of the background impurity density being lower in the As₄ devices is clear. To average the variation between devices and compare the differences between As₂ devices and As₄ devices, fits for the As₂ wafers, W1088, and W1089, and the As₄ wafers, W1091, and W1093, with a common set of fits parameters for both sets were performed.

As a result of constraining the background impurity densities to be the same in the 100nm and 50nm devices, the background impurity densities for both the As₂ and As₄ wafers have reduced, with the surface charge density increasing to compensate. The As₄ wafers still have a lower background impurity density at $(0.65 \pm 0.4) \times 10^{14}\text{cm}^{-3}$ compared to $(1.08 \pm 0.05) \times 10^{14}\text{cm}^{-3}$ in the As₂ wafers. This 40% decrease in background impurity density shows the significant effect using the high mobility As cracker at a lower temperature can have on the background impurity level in the MBE chamber.

The interface roughness parameters show that the amplitude of the interface roughness between the As₂ and As₄ wafers is comparable with the As₂ potential having a slightly smaller

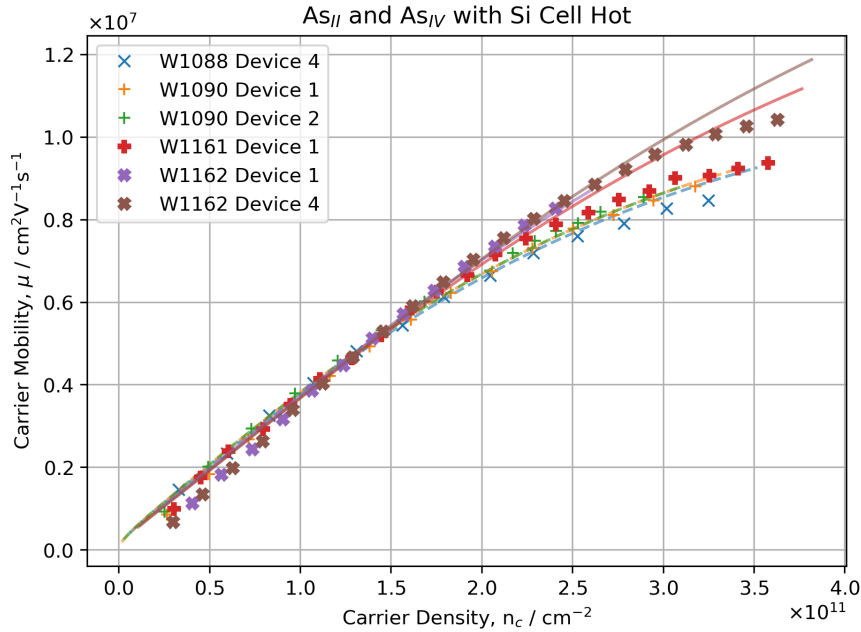


Figure 5.9: Carrier mobility-density curves for W1088, W1090, W1161 and W1162 comparing the effects of having the Si cell hot (plus) but closed during growth for As_2 and As_4 (bold).

Wafer	$N_i/10^{14}cm^{-3}$	Δ/nm	Λ/nm
W1088	1.40 ± 0.02	0.46 ± 0.06	48 ± 4
W1090	1.37 ± 0.03		
W1161	1.507 ± 0.004	0.32 ± 0.05	44 ± 5
W1162	1.48 ± 0.01		

Table 5.4: Carrier mobility-density curve fitted parameter for As_2 (W1088, W1090) and As_4 (W1161, W1162) 100nm AlGaAs spacer layer iHEMTs, comparing the effect of having the Si cell hot but closed during the growth of W1090 and W1161.

amplitude, but the uncertainty in this value makes it difficult to be sure of this. Notably, the correlation length of the As_4 wafers is longer than the As_2 . These two results suggest that the choice of As cracker may result in smaller AlGaAs island recombining on the surface of the GaAs when using As_2 compares to As_4 .

5.4.3 Si Cell

Figure 5.9 contains the carrier mobility-density curves from W1088, W1090, W1161, and W1162 with fitted curves. For 100nm AlGaAs spacer layers, the effects of surface charge are small and have been ignored in the modelling of the scattering rate to reduce the number of free parameters to fit. As the wafers were grown in pairs on the same day with identical growths apart from W1090 and W1161 having the Si cell hot but closed during growth, the scattering

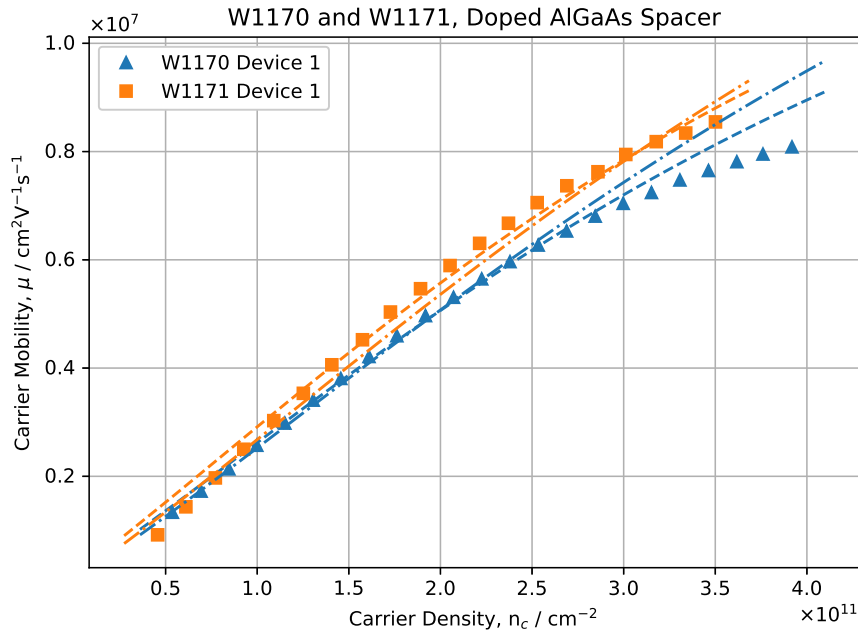


Figure 5.10: Carrier mobility-density curves from W1170 and W1171, both As_4 100nm AlGaAs Spacer layer iHEMTs, with silicon dopants added to the AlGaAs spacer layer of W1170. Mobility curve have been fitted with a common background in the GaAs buffer and separate AlGaAs backgrounds and interface roughness parameters.

rate model has different background impurity densities but common interface parameters for the As_2 and As_4 wafer pairs.

The results of the fitting, shown in table 5.4, show that for the As_2 wafers, there is no measurable difference in the background impurity level. While the As_4 wafers indicated a small increase in background impurities when the Si cell is hot, but only by 2%, this would be consistent with a small additional heat load on the chamber causing a slight increase in outgassing, but could also be due to the 'self cleaning' of the MBE chamber as newly deposited material can trap impurities, lowering the background levels in the chamber. As W1161 was grown first, a 2% drop could be the result of 'self-cleaning' during the growth, particularly as the increase in background levels between the As_2 wafers and the As_4 wafers shows that the growths in between the growth of those wafers have increased the background levels in the MBE chamber.

5.4.4 Doped AlGaAs Spacer

Figure 5.10 contains the carrier mobility-density from W1170 and W1171, both with 100nm AlGaAs spacer layers grown with As_4 . The AlGaAs spacer layer in W1170 is deliberately doped with $1 \times 10^{15} \text{cm}^{-3}$ to allow the effects of a higher background density in the AlGaAs

Wafer	$N_{AlGaAs}/10^{14}\text{cm}^{-3}$	$N_{GaAs}/10^{14}\text{cm}^{-3}$	Δ/nm	Λ/nm
W1170	2.15 ± 0.03		0.29 ± 0.02	39 ± 1
W1171	1.92 ± 0.05			
W1170	27.086 ± 0.003	0.9111 ± 0.0002	0.220145 ± 0.00001	36.6987 ± 0.0007
W1171	24.439 ± 0.003			

Table 5.5: Summary of the fitted parameters for W1170 and W1171, both 100 nm iHEMTs with W1170 growth with the Si cell hot but closed to examine the effect of the additional heat load from the hot Si cell.

spacer compared to the GaAs buffer to be examined.

With a global background and common interface parameters, fits of W1170 and W1171 show a 12% increase in the background impurity density in W1170. However, with a global background, the background impurity density parameter is an averaged value of the AlGaAs spacer and the GaAs buffer. In this particular sample, the AlGaAs impurity level is higher than the GaAs buffer. Therefore W1170 and W1171 were fitted with a free background density in the AlGaAs spacer layer and a common GaAs buffer background and interface parameters. This is possible with the Fang-Howard wave function as even through the Fang-Howard has no penetration into the AlGaAs region the carriers in the GaAs still experience an interaction with the remote AlGaAs impurities. Therefore a value for the AlGaAs impurities can be fitted for with the Fang-Howard function but as discussed in the follow section the limitation of the Fang-Howard wave function has implications for the fitted value for AlGaAs impurities.

Fitting for separate AlGaAs and GaAs backgrounds makes the fitting significantly more difficult as the scattering from the AlGaAs and GaAs region are both modelled as point-charge scattering. Therefore the mobility density curve of scattering from an AlGaAs background and a GaAs background are very similar. The similarity of the AlGaAs and GaAs backgrounds means that the fitting routines used can struggle to find a physically plausible set of parameters. Using the trust-region reflective algorithm [146], a type of gradient descent method, often results in a set of fit parameters with either the AlGaAs or GaAs too small to be physical ($< 10^{10}\text{cm}^{-3}$) and the other background parameter at a value the order of 10^{14}cm^{-3} for a GaAs background and 10^{15}cm^{-3} for an AlGaAs background. Using the global optimisation routine, dual annealing from the scipy optimisation library may help in this case. Dual annealing [147] is a stochastic approach which combines simulated annealing approaches with local optimisation with the result of faster convergence to a fit, with the ability for local minima to be avoided. The fitted parameter from dual annealing, shown in table 5.5, shows that the AlGaAs background parameter is an order of magnitude larger than the value for the global background previously fitted. The GaAs background level has reduced by a small amount, to $9 \times 10^{13}\text{cm}^{-3}$. Comparing W1170, the doped AlGaAs device, the AlGaAs background is

$(2.647 \pm 0.004) \times 10^{14} \text{cm}^{-3}$ higher than W1171, the ‘clean’ AlGaAs device. The doped AlGaAs spacer was doped with $1 \times 10^{15} \text{cm}^{-3}$ Si, however there is not a 1:1 mapping of silicon atoms to an equivalent number of fully ionised point charges. The fitted value gives a physically plausible approximate 4:1 mapping of Si atoms to fully ionised point charges.

From the results of the fitting, the scattering rate models show that, despite the significantly higher background level in the AlGaAs spacer layer, it is the scattering in the GaAs that is the dominant source of scattering. The scattering from the AlGaAs is the second most significant source of scattering. Therefore, growth strategies which reduce the Al content and thus the background level may be worth exploring to achieve the highest mobilities possible.

5.5 Extension to Transport Model

While the Fang-Howard captures the general behaviour of the wave function of the lowest sub-band in a heterostructure, it has two significant shortcomings due to its simplicity. Firstly, the Fang-Howard wave function by definition terminates at the AlGaAs/GaAs interface, so there is no penetration into the AlGaAs spacer layer. The lack of penetration into the AlGaAs underestimates the scattering from the AlGaAs region’s impurity background and means there is no alloy scattering. Secondly, the tail of the Fang-Howard wave function is too long, making the average distance from the interface too large, again changing the calculated scattering rates.

In this section, other options for the wave function are explored to see if the choice of the wave function has a significant effect when modelling the scattering rates.

5.5.1 Variational Wave Function

A clear option for the wave function used in modelling the scattering rates would be a numerical solution to the Poisson and Schrödinger equations for the heterostructure system. Such solves are common place and well established. However, the main aim of this numerical modelling of the mobility is to use experimental data to calculate characteristic values for growth parameters like the background impurity density to inform MBE growth optimisation. The calculation of the scattering rate required the computation of the form factors defined in section 5.1.1.4. While these integrals can be computed numerically, to introduce a numerical wave function raises complications of numerical mesh size, making sure to get the numerical wave function on a fine enough grid to calculate the integral accurately, while keeping the mesh sparse enough to keep the computation time to a minimum.

The need for computation efficiency is driven by the scattering rate integrals, which, at worst, for a 3D doped region is a 2D integral where the integrand depends on the form-factors taking the full integral to 3D. Due to the exponential growth of the number of points required

to compute an N dimensional integral, the use of integration library with good performance is important to allow the scattering rates to be computed on modest desktop machines. Therefore, adding in the additional complication of a numerical wave function, while very possible, is a significant investment of effort.

As an alternative, a more general variational wave function, similar to ones used by Takada and Uemura[148] and Ando[127], is explored as an option, giving the wave function more degrees of freedom to address the specific shortcomings of the Fang-Howard wave function. Comparison of this wave function to numerical solutions will be used to determine the suitability of the final variational wave function.

Variational Method

The variational method allows an approximate solution for the ground state of a system to be determined by introducing free parameters and minimising the total energy of the system in the usual way.

For our system the energy has four components:

- \hat{T} - Kinetic energy
- $\hat{\phi}_h$ - Hartree potential energy
- $\hat{\phi}_d$ - Depletion field potential energy
- $\hat{\phi}_b$ - Conduction band potential energy

such that the total energy of the system is given by $\hat{H} = \hat{T} + 1/2 \hat{\phi}_h + \hat{\phi}_d + \hat{\phi}_b$.

Kinetic Energy The standard kinetic energy operator is $\hat{T} = \frac{\hat{p}^2}{2m^*} = \frac{1}{2m^*} \frac{\partial^2}{\partial z^2}$, however this is for the cases where the effective mass is constant. The effective mass in an $\text{Al}_x\text{Ga}_{1-x}\text{As}$ system varies as a function of the Al content. Therefore the kinetic energy operator needs to account for the varying mass. Allowing for a varying effective mass the kinetic energy is given by

$$\langle T \rangle = \langle \psi | \hat{p} \frac{1}{2m^*} \hat{p} | \psi \rangle = \frac{1}{2} \int \frac{dx}{m^*(x)} \left| \frac{\partial \psi}{\partial x} \right|^2 \quad (5.31)$$

Hartree Approximation The Hartree approximation accounts for electron-electron interactions by introducing a potential ϕ_h which satisfies the equation

$$\nabla \cdot (\epsilon \nabla \phi_h) = -4\pi n_c |\psi|^2 \quad (5.32)$$

Applying the boundary conditions $\phi_h(0) = 0$ and $\nabla \phi_h(z \rightarrow \infty) = 0$, the second of which corresponds to no electric field in the substrate, allows the potential to be written as,

$$\begin{aligned} \phi_h(z) &= \frac{4\pi n_c}{\epsilon} \int_0^z dx \int_x^\infty dy |\psi(y)|^2 \\ &= \frac{4\pi n_c}{\epsilon} \left[\int_0^z dy y |\psi(y)|^2 + z \int_z^\infty dy |\psi(y)|^2 \right] \end{aligned} \quad (5.33)$$

therefore the Hartree potential energy is,

$$\begin{aligned}
\langle \phi_h \rangle &= \frac{4\pi n_c}{\epsilon} \int dz |\psi(z)|^2 \phi_d(z) \\
&= \frac{8\pi n_c}{\epsilon} \left[\int_0^\infty dx x |\psi(x)|^2 \int_x^\infty dy |\psi(y)|^2 \right. \\
&\quad \left. - \int_{-\infty}^0 dx x |\psi(x)|^2 \int_{-\infty}^x dy |\psi(y)|^2 + \frac{1}{2} \int_{-\infty}^0 dx x |\psi(x)|^2 \right]
\end{aligned} \tag{5.34}$$

Depletion Field Potential Energy Generally, the formation of a 2DES can result in the formation of a depletion region in the structure. Assuming a uniform charge density of N_a in this depletion region $0 < z < L$, the potential due to these charges, ϕ_d , is given by:

$$\nabla \cdot (\epsilon \nabla \phi_d) = -4\pi N_a \tag{5.35}$$

defining the areal depletion density as $N_{depl} \equiv N_a L$ the potential is simply:

$$\phi_d(z) = \frac{4\pi N_{depl}}{\epsilon} z \left(1 - \frac{z^2}{2L} \right) \tag{5.36}$$

The width of the depletion region is typically much wider than the width of the electron wave function, therefore the potential for the depletion region can be simplified by approximating $L \gg 1$ such that,

$$\phi_d(z) \approx \frac{4\pi N_{depl}}{\epsilon} z \tag{5.37}$$

With this simplified expression the depletion field potential energy is given by:

$$\langle \phi_d \rangle = \frac{4\pi N_{depl}}{\epsilon} \int dz z |\psi(z)|^2 = \frac{4\pi N_{depl}}{\epsilon} \langle z \rangle \tag{5.38}$$

Conduction Band Potential Energy At the AlGaAs-GaAs interface there is a band offset; $0.79x$ eV for the conduction band in an $\text{Al}_x\text{Ga}_{1-x}\text{As}/\text{GaAs}$ heterointerface. To account for this band offset, we introduce a left-sided step function potential of the form:

$$\phi_b(z) = \Delta E H(-z) \tag{5.39}$$

where $H(z)$ is the Heaviside step function and ΔE is the band offset. The potential energy is therefore simply:

$$\langle \phi_b \rangle = \Delta E \int_{-\infty}^0 dz |\psi(z)|^2 \tag{5.40}$$

Wave Function Definition

To address the shortcomings of the Fang-Howard wave function the follow variational wave function is included, in terms of the free parameters b , n , and λ :

$$\begin{aligned}\psi(z \geq 0) &= \sqrt{\frac{nb}{\Gamma(3/n)\nu}}(bz + \lambda)e^{-(bz+\lambda)^n/2} \\ \psi(z < 0) &= \sqrt{\frac{nb}{\Gamma(3/n)\nu}}\lambda e^{-\lambda^n/2} e^{\kappa bz/2}\end{aligned}\quad (5.41)$$

The parameters ν and κ are determined from the normal boundary conditions requiring the probability and kinetic energy must be continuous at $z = 0$ and the wave function to be normalised. The expression for ν and κ are:

$$\begin{aligned}\nu &= Q(3/n, \lambda^n) + \frac{n\lambda^3 e^{-\lambda^n}}{\Gamma(3/n)\tilde{m}(2 - n\lambda^n)} \\ \kappa &= \frac{\tilde{m}(2 - n\lambda^n)}{\lambda}\end{aligned}\quad (5.42)$$

As the wave function must tend to zero at $z \rightarrow -\infty$, the value of λ is bound between $0 < \lambda < 2/n^{1/n}$.

Wave Function Kinetic Energy From (5.31) the kinetic energy for this wave function is

$$\langle T \rangle = \frac{b^2}{8m^+} F(n, \lambda) \quad (5.43)$$

where \tilde{m} is the mean effective mass and the function $F(n, \lambda)$ is defined as

$$F(n, \lambda) \equiv \frac{(n\lambda^n - 2) \left((n+1)e^{\lambda^n} \Gamma\left(\frac{1}{n}, \lambda^n\right) + \lambda(n-1)n \right)}{e^{\lambda^n} (n\lambda^n - 2) \Gamma\left(\frac{3}{n}, \lambda^n\right) - \lambda^3 n} \quad (5.44)$$

Wave Function Hartree Potential From (5.34) the Hartree potential for this wave function is given by,

$$\begin{aligned}\phi_h(z \geq 0) &= \frac{4\pi n_c}{\varepsilon} \left\{ \frac{\left(z + \frac{\lambda}{b}\right) Q(3/n, (bz + \lambda)^n)}{\nu} + \frac{\lambda}{\nu} Q(3/n, \lambda^n) \right. \\ &\quad \left. + \frac{\gamma(4/n, (bz + \lambda)^n) - \gamma(4/n, \lambda^n)}{\nu b \Gamma(3/n)} \right\} \\ \phi_h(z < 0) &= \frac{4\pi n_c}{\varepsilon} \left\{ z + \frac{n\lambda^2 e^{\lambda^n} (1 - e^{\kappa bz})}{\nu b \Gamma(3/n) \kappa^2} \right\}\end{aligned}\quad (5.45)$$

with the potential energy given by

$$\langle \phi_h \rangle = \frac{4\pi n_c}{\varepsilon b} G(n, \lambda) \quad (5.46)$$

where the function $G(n, \lambda)$ is defined as

$$G(n, \lambda) = \frac{\Gamma\left(\frac{3}{n}\right)}{\left[\Gamma\left(\frac{3}{n}, \lambda^n\right) + \frac{\lambda^3 n e^{-\lambda^n}}{2-n\lambda^n}\right]^2} \int_{\lambda^n}^{\infty} du (u^{1/n} - \lambda) u^{3/n-1} e^{-u} Q(3/n, u) \\ + \frac{\lambda n (n - 2e^{\lambda^n} \lambda^{-3} (n\lambda^n - 2) \Gamma\left(\frac{3}{n}, \lambda^n\right))}{4(n\lambda^n - 2) (n - e^{\lambda^n} \lambda^{-3} (n\lambda^n - 2) \Gamma\left(\frac{3}{n}, \lambda^n\right))^2} \quad (5.47)$$

Wave Function Depletion Field Potential Energy From (5.38) the depletion field potential energy is

$$\langle \phi_d \rangle = \frac{4\pi N_d}{\epsilon b} H(n, \lambda) \quad (5.48)$$

where the function $H(n, \lambda)$ is defined as

$$H(n, \lambda) = \frac{\Gamma(4/n, \lambda^n) - \lambda \Gamma(3/n, \lambda^n)}{\Gamma(3/n, \lambda^n) + \frac{n\lambda^3 e^{-\lambda^n}}{2-n\lambda^n}} \\ - \frac{\lambda n}{(n\lambda^n - 2) (e^{\lambda^n} \lambda^{-3} (n\lambda^n - 2) \Gamma\left(\frac{3}{n}, \lambda^n\right) - n)} \quad (5.49)$$

Wave Function Conduction Band Energy From (5.40) the conduction band potential energy is

$$\langle \phi_b \rangle = \Delta EI(n, \lambda) \quad (5.50)$$

where the function $I(n, \lambda)$ is

$$I(n, \lambda) = -\frac{n}{e^{\lambda^n} \lambda^{-3} (n\lambda^n - 2) \Gamma\left(\frac{3}{n}, \lambda^n\right) - n} \quad (5.51)$$

b Parameter With the above expression for the energies, the total energy of the system is

$$\langle E \rangle = \frac{b^2}{8\bar{m}} F(n, \lambda) + \frac{4\pi}{\epsilon b} [n_c G(n, \lambda) + N_d H(n, \lambda)] + \Delta EI(n, \lambda) \quad (5.52)$$

the parameter b can be found in terms of n and λ by minimising this expression with respect to b .

$$b^3 = \frac{16\pi\bar{m} n_c G(n, \lambda) + N_d H(n, \lambda)}{\epsilon F(n, \lambda)} \quad (5.53)$$

with the value of b the total energy of the system can be reduced to

$$\langle E \rangle = \frac{3b^2}{8\bar{m}} F(n, \lambda) + \Delta EI(n, \lambda) \quad (5.54)$$

To find the values of n and λ (5.54) must be minimised with respect to n and λ . A simple manipulation of (5.54) defines a minimisation problem of the form

$$\min \left\{ \left[G(n, \lambda) + \frac{N_d}{n_c} H(n, \lambda) \right]^{\frac{2}{3}} F(n, \lambda)^{\frac{1}{3}} + \left(\frac{\tilde{n}}{n_c} \right)^{\frac{2}{3}} I(n, \lambda) \right\} \\ \text{subject to } 0 \leq \lambda \leq \left(\frac{2}{n} \right)^{\frac{1}{n}} \text{ with } \tilde{n} \equiv \left(\frac{\Delta E_c}{3} \right)^{\frac{3}{2}} \frac{\sqrt{2m^* \epsilon_r}}{\pi} \quad (5.55)$$

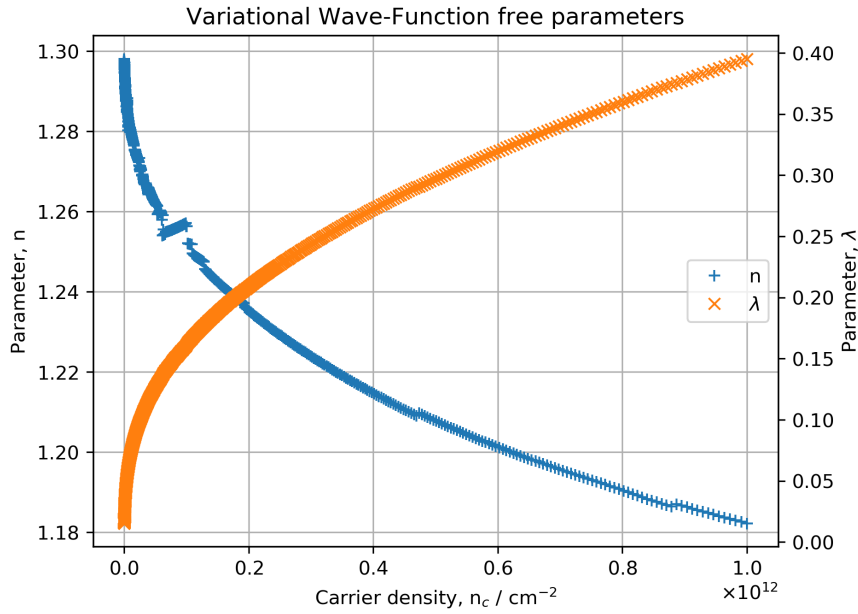


Figure 5.11: The values of variational parameters n and λ from minimising the objective function (5.55) varying the value of the carrier density. The value of n lies in between the Fang-Howard value of $n = 1$ and the Takada-Uemura value of $n = 3/2$. The value of λ is small but increases with carrier density showing more penetration into the AlGaAs spacer.

Solving this minimisation numerically using the scipy optimisation library, the value of n ranges between ≈ 1.3 and ≈ 1 and the value of λ ranges between ≈ 0 and ≈ 0.3 , figure 5.11.

5.5.2 Form-Factors

Modelling of the scattering rate depends on the wave functions through three form-factors defined in (5.26). With the variational wave function defined in terms of n and λ , the four form-factors for point-charge scattering, F_{PC} , carrier-carrier interactions, F_{CC} , interface roughness,

F_{IR} , and alloy scattering, F_{AL} are:

$$\begin{aligned}
F_{PC}(q, z > 0) &= \frac{n}{\Gamma(3/n, \lambda^n) + \frac{n\lambda^3 e^{-\lambda^n}}{2-n\lambda^n}} \left[\int_0^\infty dx (x + \lambda)^2 e^{-(x+\lambda)^n - \frac{q}{b}|x-bz|} + \frac{\lambda^3 e^{-\lambda^n - qz}}{2 - n\lambda^n + \frac{q}{b}\lambda} \right] \\
F_{PC}(q, z \leq 0) &= \frac{n}{\Gamma(3/n, \lambda^n) + \frac{n\lambda^3 e^{-\lambda^n}}{2-n\lambda^n}} \left[e^{qz} \int_0^\infty dx (x + \lambda)^2 e^{-(x+\lambda)^n - \frac{q}{b}x} \right. \\
&\quad \left. + \frac{\lambda \left[(2 - n\lambda^n) + \lambda \frac{q}{b} \left(1 - e^{-bz \left(\frac{n\lambda^n - 2}{\lambda} + \frac{q}{b} \right)} \right) \right]}{(n\lambda^n - 2) - \lambda^2 \frac{q^2}{b}} \right] \\
F_{CC}(q) &= \left(\frac{n}{\Gamma(3/n, \lambda^n) + \frac{n\lambda^3 e^{-\lambda^n}}{2-n\lambda^n}} \right)^2 \left[\int_0^\infty dx \int_0^\infty dy (x + \lambda)^2 (y + \lambda)^2 e^{-(x+\lambda)^n - (y+\lambda)^n - \frac{q}{b}|x-y|} \right. \\
&\quad \left. \frac{\lambda^3 e^{-\lambda^n}}{\alpha\lambda - n\lambda^n + 2} \left(\frac{\lambda^3 e^{-\lambda^n}}{2 - n\lambda^n} + \int_0^\infty dx (\lambda + x)^2 e^{-(\lambda+x)^n - \alpha x} \right) \right] \\
F_{IR} &= \frac{2\pi}{\varepsilon} (n_c + 2N_d) \\
F_{AL} &= \left(\frac{n}{\Gamma(3/n, \lambda^n) + \frac{n\lambda^3 e^{-\lambda^n}}{2-n\lambda^n}} \right)^2 \frac{b\lambda^5 e^{-2\lambda^n}}{2(2 - n\lambda^n)}
\end{aligned} \tag{5.56}$$

5.6 Comparison to Numerical Solutions

To compare the physical accuracy of the wave functions from variational methods, the fidelity of the wave functions to numerical solutions from nextnano provides a metric for comparison.

The solutions from nextnano solve the Poisson and Schrödinger equations self consistently. Details about the use of nextnano solutions follow in the next section.

5.6.1 Nextnano Solution

nextnano is a software package [64] that can solve the Poisson, Schrödinger, and current equations, self consistently if needed, for many semiconducting materials with a wide range of boundary conditions possible. An induced heterostructure was modelled in 1D along the growth direction.

Boundary conditions are required for nextnano to solve the Poisson, Schrödinger and current equations. The boundary conditions for the induced heterostructure set the electric field to zero at 1000nm below the AlGaAs/GaAs interface, while fixing the Fermi energy to 0eV at the AlGaAs/GaAs interface, and set the potential at the surface of the GaAs to V_g . The pinning of the Fermi energy due to GaAs surface states is simulated by fixing the Fermi energy to -0.7eV below the conduction band edge. The output from nextnano is shown in figure 5.12 with comparisons to the variational and Fang-Howard wave function. For high carrier densities, the

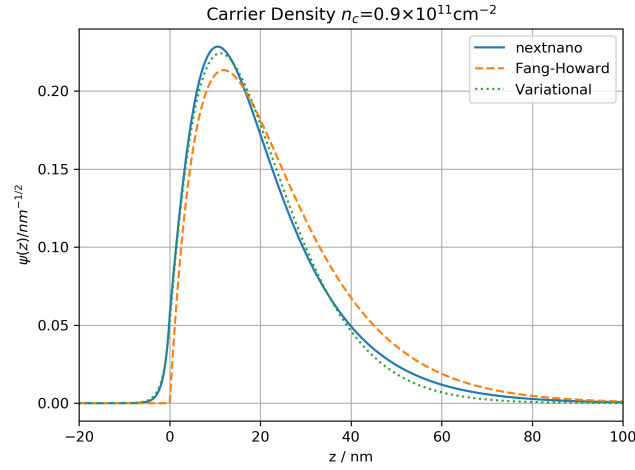
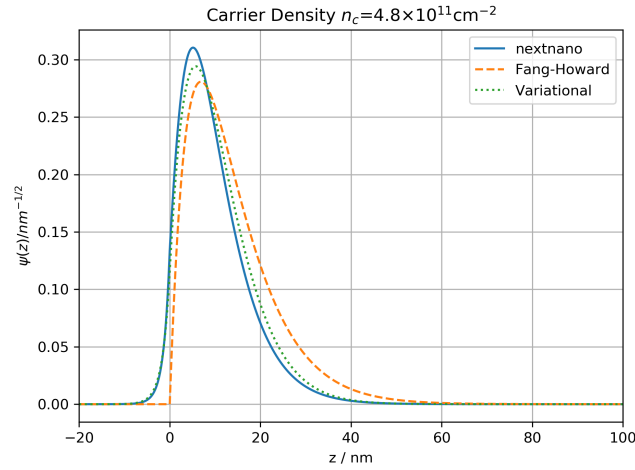
(a) $n_c = 0.9 \times 10^{11} \text{cm}^{-2}$ (b) $n_c = 4.8 \times 10^{11} \text{cm}^{-2}$

Figure 5.12: The confinement wave function in the growth direction calculated using nextnano [64], the Fang-Howard function [137] and the variational wave function introduced in this work. The variational wave function is a closer match to the nextnano function at both low and high carrier densities.

variational wave function agrees very well with the nextnano output near the interface. Away from the interface, the variational wave function has a tail that is longer than the nextnano solutions so like the Fang-Howard wave function. The variational wave function's average position from the interface is further away than in reality. The overestimate of the average position increases at lower carrier density, but for all densities, the variational wave function is a closer match to the nextnano output than the Fang-Howard wave function. The fidelity defined as $\mathcal{F} \equiv \left| \langle \psi_i | \psi_j \rangle \right|^2$, takes a value between zero, for two orthogonal states, and one for two identical states. Comparing the fidelity of the variational wave functions to nextnano, figure 5.13, shows

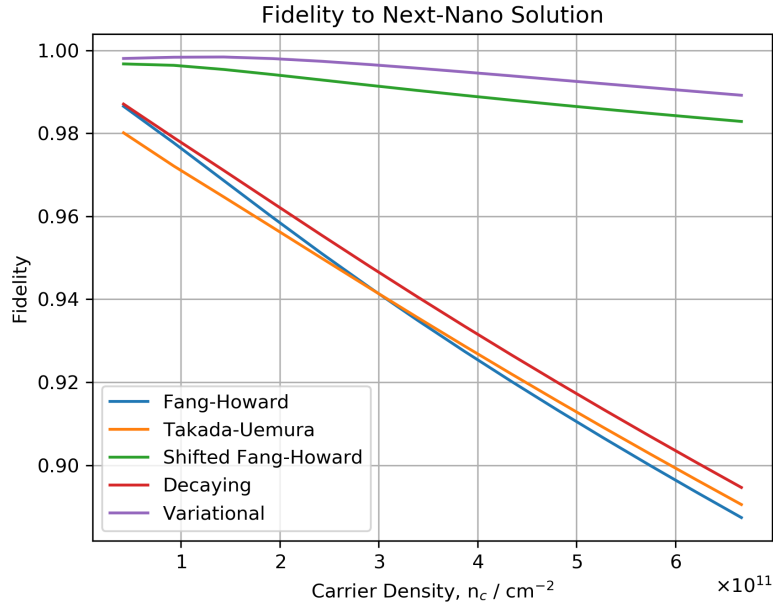


Figure 5.13: The fidelity of the wave functions to the Next-Nano Poisson-Schrödinger self consistent solution. Allowing penetration into the AlGaAs spacer increases the fidelity to $>98\%$ over all carrier densities.

that although the Fang-Howard wave function has a fidelity $> 90\%$, the variational wave function has a fidelity $> 98\%$. Figure 5.13 clearly shows that introducing some penetration into the AlGaAs spacer layer significantly increases the fidelity of the wave function to the Next-Nano solution from $>90\%$ for the Fang-Howard wave function up to $>98\%$ for the variational wave function at, all carrier densities.

Further improvement to the variational wave function's fidelity could be made by including the change in the effective mass between the AlGaAs spacer and GaAs spacer where the ratio of the confinement effective mass is $m_{z<0}/m_{z>0} \approx 1.44$ and the change in the dielectric constant $\epsilon_{z<0}/\epsilon_{z>0} \approx 0.93$. Accounting for the change in the effective mass is relatively straight forward through a change in the boundary condition at $z = 0$ for the variational wave function. The effect of account for the dielectric constants change more involved as the Hartree potential need calculating from a dielectric interface rather than point charges in a dielectric material, adding significant mathematical complication.

5.6.1.1 Alternative Wave Functions

The definition of the variational in terms of n and λ tends to the Fang-Howard wave function in the limit $n \rightarrow 1$ and $\lambda \rightarrow 0$. These two parameters primarily control the tail length in the GaAs and the penetration into the AlGaAs respectively. Setting either the value of n or λ controls the

tail or penetration. Here three new wavefunctions are introduced with fixed values of n or λ .

The shifted Fang-Howard, which has a fixed value of $n = 1$ to decay at the same rate of the Fang-Howard wave function, but λ is still a free parameter, to be determined from energy minimisation. The Takada-Uemura [148] wave function, with a fixed value of both $n = 1.5$ and $\lambda = 0$, which asymptotically decays at the same rate of the Airy function, which is the eigenstate of a triangular well. Finally, the ‘decay’ wave function has a fixed value of $\lambda = 0$ with n a free parameter. Between these three wavefunctions, the importance of the penetrations into the AlGaAs spacer compared to the decay rate can be studied.

$$\begin{aligned}\psi_{ShiftedFH}(z) &= \sqrt{\frac{b}{2}} \begin{cases} (bz + \lambda) \exp[-(bz + \lambda)/2] & \text{for } z > 0, \\ \lambda \exp[-\lambda/2 + (2 - \lambda)\frac{bz}{\lambda}] & \text{for } z \leq 0 \end{cases} \\ \psi_{TU}(z) &= \sqrt{\frac{3b}{2}} bz \exp\left[-(bz)^{\frac{3}{2}}/2\right] \\ \psi_{Decay}(z) &= \sqrt{\frac{nb}{\Gamma(3/n)}} bz \exp[-(bz)^n/2]\end{aligned}\tag{5.57}$$

Comparing the Fang-Howard, Takada-Uemura and decaying wave functions, figure 5.13, all of which have $\lambda = 0$ for no penetration into the spacer, the Fang-Howard ($n = 1$) and Takada-Uemura ($n = 3/2$) wave functions have a trade-off, with the Fang-Howard fidelity higher at lower carrier densities, and the Takada-Uemura higher at higher densities as the quantum well becomes more triangle-like. However, introducing a free parameter, $1 < n < 3/2$ with the decaying wave function give a higher fidelity than both the Fang-Howard and Takada-Uemura wave functions over the whole carrier density range.

Comparing the Fang-Howard ($\lambda = 0$ and shifted Fang-Howard ($\lambda < 2$) in figure 5.13, it is apparent that introducing penetration has a considerable improvement on the fidelity compared to improving the decay rate of the tail. Comparing the Shifted Fang-Howard and variational wave function fidelities, both of which are much higher than the Fang-Howard across the carrier density range, but improving the decay rate for the variational wave function gives only a small improvement over the shifted Fang-Howard compared to the improvement between Fang-Howard and Shifted Fang-Howard.

5.7 Scattering Rate Comparison

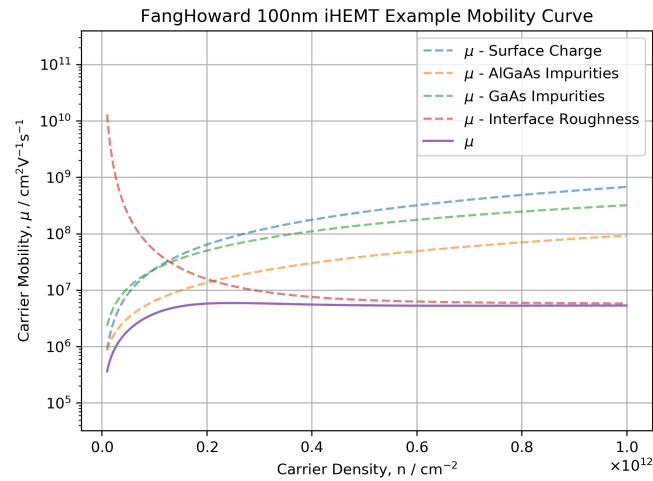
Equation (5.56) summarises the form-factors for the variational wave function needed for the scattering rate modelling. Taking limits on the values of n and λ recovers the form-factors for all the alternative wave functions discussed. Therefore (5.56) summaries all the form-factors for the wave functions.

To examine the effect of the scattering rates by using an improved wavefunction the scattering rates for the Fang-Howard, shifted Fang-Howard, and variational wave functions were calculated for 100nm and 50nm AlGaAs spacer thicknesses with a common set of scattering parameters, $\sigma = 1 \times 10^{10} \text{cm}^{-2}$, $N_{\text{AlGaAs}} = 5 \times 10^{14} \text{cm}^{-3}$, $N_{\text{GaAs}} = 1 \times 10^{14} \text{cm}^{-3}$, $\Delta = 0.1 \text{nm}$ and $\Lambda = 10 \text{nm}$, shown in figure 5.15.

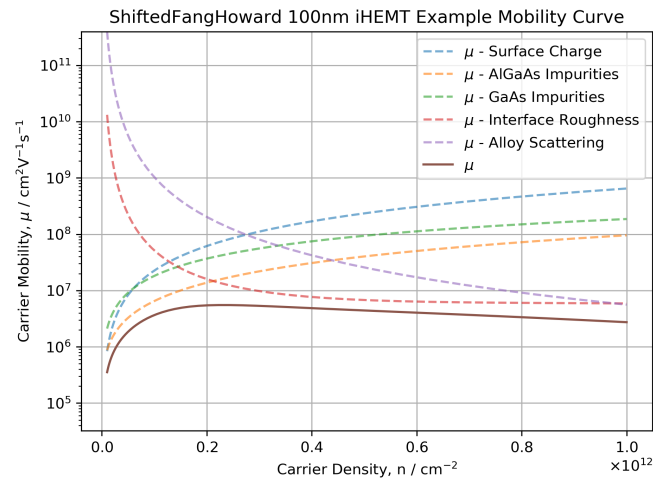
The mobility curves in figure 5.15 show that the choice of the wave function does change the scattering rate by a significant amount. Therefore, the parameters estimated using the Fang-Howard wave function are likely to be an overestimate, as the shifted Fang-Howard and variational wave functions show an increased scattering rate (causing lower mobility) for the same scattering rate parameters. This increased scattering is most significant for the point-charge scattering mechanisms, but the interface roughness is affected to a less extent. Due to the penetration of the wave function into the AlGaAs spacer for the Shifted Fang-Howard and variational wave function, alloy scattering is present with these wave functions. Alloy scattering, like interface roughness increases, with carrier density as the potential well tips towards the interface, moving the carriers into the spacer. For the shifted Fang-Howard and variational wave functions, there are two components to the mobility which causes the turning over at high carrier densities. As the Fang-Howard wave function does not have alloy scattering the interface roughness parameters are also likely to be overestimates as the Fang-Howard wave function will attempt to fit both the interface roughness component and the alloy scattering with just the interface roughness. Figure 5.16 shows a plot of the total mobility for the three wave functions from figure 5.15 demonstrating how changes in the shape of the wave function effect the mobility density curves. The lower mobility at $n_c > 5 \times 10^{11}$ of the Shifted Fang-Howard and the Variational wave function demonstrates how the lack of penetration into the AlGaAs in the Fang-Howard wave function results in a higher mobility. Therefore the Fang-Howard wave function is not the best choice particularly for understanding the effects of interface roughness and alloy scattering, as interface roughness scattering fitted with the Fang-Howard will be an over estimated to account for the absence of alloy scattering with the Fang-Howard wave function.

5.8 C-Shaped iHEMT Devices

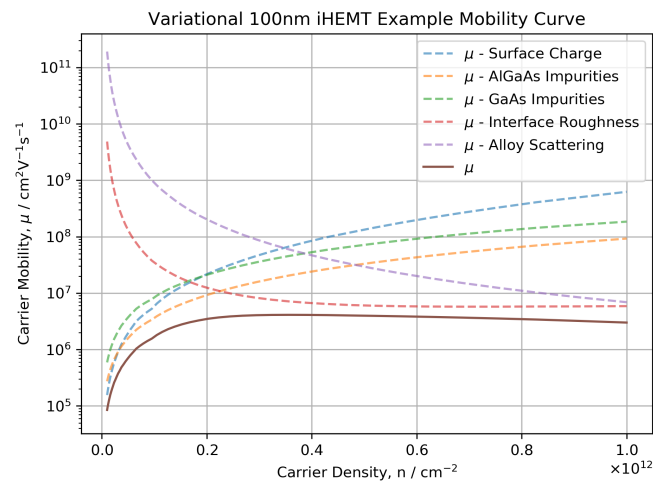
It is well known that the mobility of carriers in GaAs change as a function of angle to the major flat. The angular dependence of mobility is due to the interface roughness of the AlGaAs/GaAs interface [103]. The AlGaAs reconstruction on the GaAs surface forms small elliptical islands with the major axis of the ellipses parallel to the major flat of the wafer. Within the scattering rate model, the elliptical islands are characterised by the interface roughness correlation length,



(a) Fang-Howard 100nm

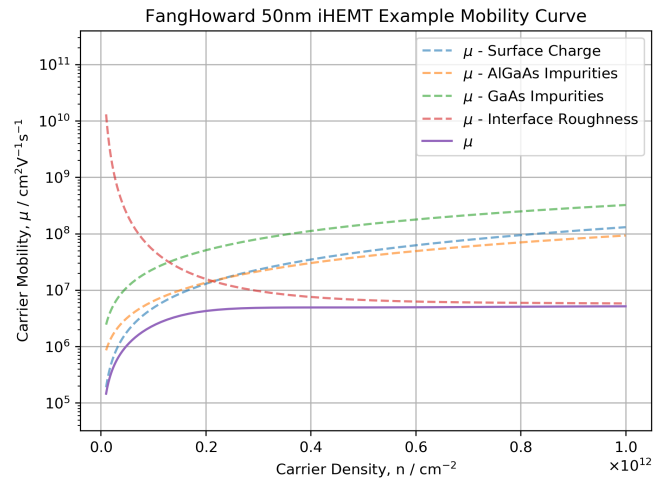


(b) Shifted Fang-Howard 100nm

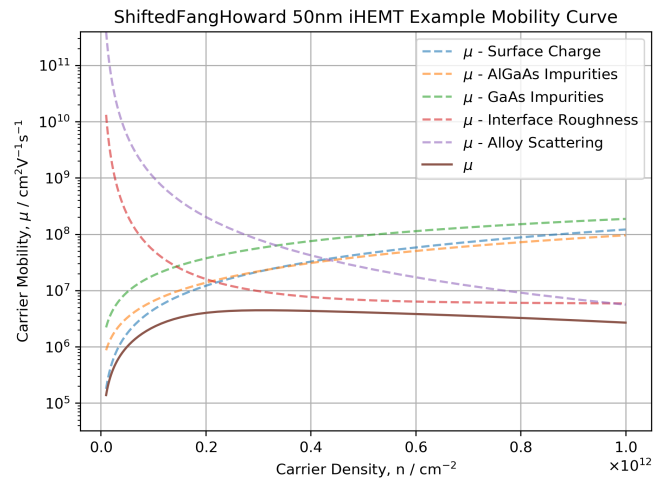


(c) Variational 100nm

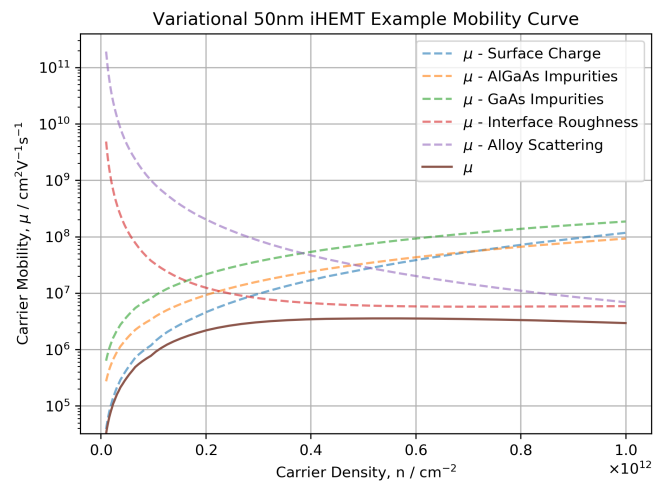
Figure 5.14: Example carrier mobility-density curve for 100nm AlGaAs spacer thickness iHEMTs, using the Fang-Howard, Shifted Fang-Howard, and variational wave functions.



(a) Fang-Howard 50nm



(b) Shifted Fang-Howard 50nm



(c) Variational 50nm

Figure 5.15: Example carrier mobility-density curve for 50nm AlGaAs spacer thickness iHEMTs, using the Fang-Howard, Shifted Fang-Howard, and variational wave functions.

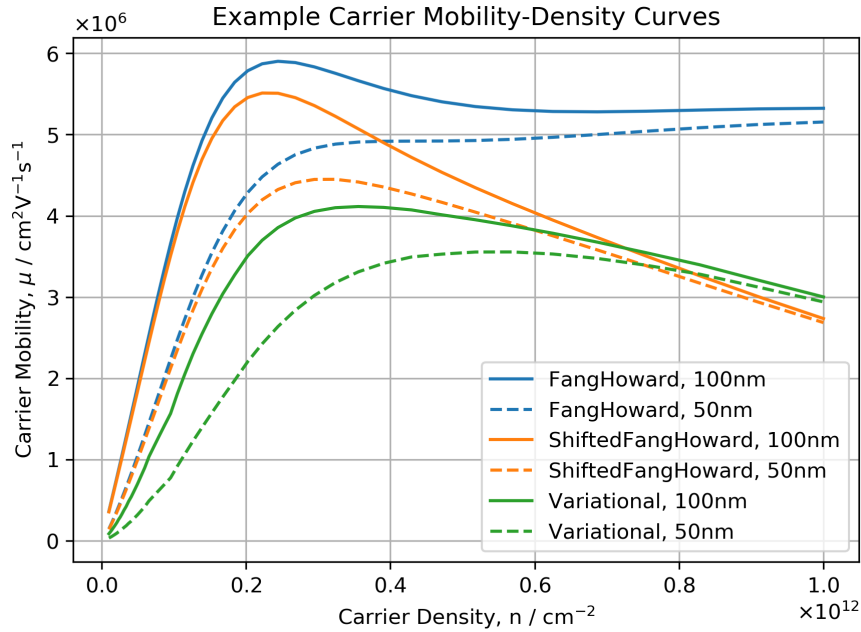


Figure 5.16: Example carrier mobility-density curves for 50nm and 100nm AlGaAs spacer thickness iHEMTs, using the Fang-Howard, Shifted Fang-Howard, and variational wave functions.

which will vary as a function of angle to the major flat; the longer correlation length parallels to the major flat.

Modelling of the scattering rate in GaAs heterostructure allows a value for the interface roughness parameter to be determined from carrier mobility-density curves. Therefore from a set of mobility density curves from Hall bars fabricated at different angles to the major flat of the wafer, information about the AlGaAs reconstruction on the GaAs surface can be determined.

5.8.1 The C-Shaped iHEMT Device

The photomask set for the C-shaped iHEMT device fabricated four Hall bars rotated by 45° with respect to each other, see figure 5.17. Aligning one of the Hall bars to the major flat the mobility-density curves for 0° , 45° , 90° , and 135° degrees to the major flat are measured in a similar major to standard assessment. For the 0° and 90° , the C-shaped iHEMT device has Hall voltage probes. Therefore, the carrier density can be determined from the Hall coefficient, R_h , but the 45° and 135° bars only have voltage probes for the longitudinal voltage, V_x . Therefore, to determine the carrier density along these bars, the frequency of the Shubnikov-de-Haas oscillations $f_{1/B} = R_k ne/2$ was used to estimate the carrier density in these directions. At 1.5K for electrons, the amplitude of the Shubnikov-de-Haas oscillations is small making the

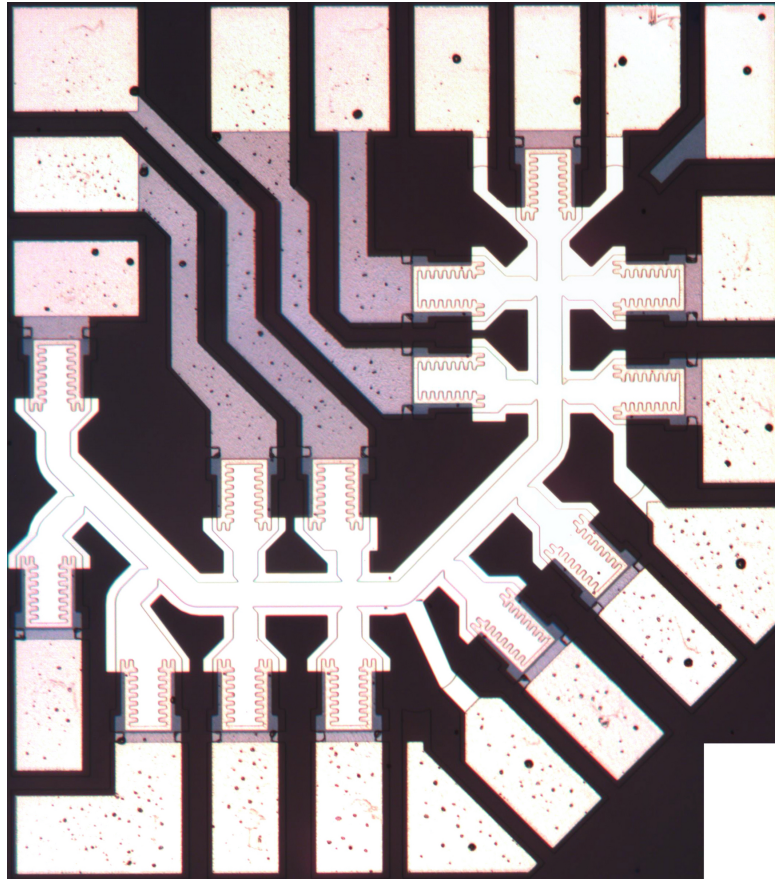


Figure 5.17: Optical image of the C-Shaped undoped Hall bar device.

low field oscillations, where the expression for the oscillations frequency is valid, challenging to measure over a broad enough field range to determine the frequency with low uncertainty. However, an approximate value can be determined and a mobility-density curve determined.

The mobility-density curves for the As_2 and As_4 50nm and 100nm AlGaAs spacer devices are shown in figure 5.18, separated in to 0° , 45° , 90° , and 135° devices. For each of the bar angles the same pattern for the As_2 , As_4 , 50nm and 100nm AlGaAs spacer layer is seen as from the major flat aligned Hall bar from section 5.3. Comparing the bars at different angles, the expected reduction of mobility as the bar's angle parallel to the minor flat increases can be seen for all devices. Looking carefully at the shape of the mobility curve at high carrier density, the 90° and 135° curves show a flattening / turning down compared to the 0° devices. This would be consistent with increased interface roughness scattering. The data from the 45° shows a particularly high amount of scattering due to the difficulties in measuring the low field Shubnikov-de-Haas oscillations and therefore is excluded from further analysis. The 135° data was used as an equivalent data set, as the symmetry of the zinc-blende structure means that the 45° and 135° bar should be equivalent.

The carrier mobility-density data from W1088, W1089, W1091, and W1093 was fitted with a common background impurity density, surface charge density and interface roughness amplitude but with an individual interface roughness correlation lengths. The mobility was modelled with three different wave functions: Zero-Thickness, Fang-Howard and variational, to examine the effect that the choice of confinement wave function makes to the fitted parameters.

Surface Charge Density, σ/cm^{-2}		
	As ₂ - W1088 & W1089	As ₄ - W1091 & W1093
Zero-Thickness	$(1.66 \pm 0.11) \times 10^{10}$	$(1.72 \pm 0.07) \times 10^{10}$
Fang-Howard	$(2.32 \pm 0.12) \times 10^{10}$	$(2.10 \pm 0.10) \times 10^{10}$
Shifted-Fang-Howard	$(7.1 \pm 0.4) \times 10^9$	$(1.82 \pm 0.09) \times 10^{10}$
Variational	$(6.9 \pm 0.3) \times 10^9$	$(4.8 \pm 0.3) \times 10^9$
Background Impurity Density, $N_{\text{background}}/\text{cm}^{-3}$		
	W1088 & W1089	W1091 & W1093
Zero-Thickness	$(5.18 \pm 0.06) \times 10^{14}$	$(3.21 \pm 0.17) \times 10^{14}$
Fang-Howard	$(3.12 \pm 0.03) \times 10^{14}$	$(2.40 \pm 0.12) \times 10^{14}$
Shifted-Fang-Howard	$(1.628 \pm 0.018) \times 10^{14}$	$(2.61 \pm 0.11) \times 10^{14}$
Variational	$(1.607 \pm 0.017) \times 10^{14}$	$(1.45 \pm 0.07) \times 10^{14}$
Interface Roughness Amplitude, Δ/nm		
	W1088 & W1089	W1091 & W1093
Zero-Thickness	0.135 ± 0.003	0.152 ± 0.003
Fang-Howard	0.1107 ± 0.0014	0.1130 ± 0.0018
Shifted-Fang-Howard	0.1294 ± 0.0008	0.176 ± 0.003
Variational	0.1361 ± 0.0009	0.1196 ± 0.0010

Table 5.6: Fitted parameters for W1088, W1089, W1091, and W1093. Values for surface charge density, σ/cm^{-2} , background impurity density, $N_{\text{background}}/\text{cm}^{-3}$, and interface roughness amplitude, Δ/nm .

The values for the surface charge density, background impurity density and interface roughness amplitude fitted to the C-shaped iHEMT data is summarised in table 5.6. Comparing the As₂ and As₄, devices the main trend between the two As types is the consistently lower background impurity density in the As₄ device with the fitted backgrounds between 40% and 10% lower in the As₄ devices compared to the As₂, depending on the wave function choice.

Looking at the surface charge density and interface roughness amplitude, there is no clear trend between As₂ and As₄ with the choice of wave function affecting which As type has more or less surface charge density or a rougher surface. From the nextnano simulations of the band structure of an induced iHEMT, the variational wave function gives the best approximation of the self-consistent solution. The surface charge density and interface roughness amplitude are both lower in the As₄ devices which is suggestive that the use of As₄, may have secondary

effects on the carrier mobility by reducing the scattering from the interface and the surface in addition to the main effect of reducing the background impurity density in the induced structure.

The interface roughness correlation length is expected to vary with the angle to the major flat due to the reconstruction of AlGaAs on a GaAs surface. GaAs is well known to have a ‘fast’ and ‘slow’ direction which corresponds to crystal directions, along with the interface roughness due to the AlGaAs reconstruction, resulting in a long length scale for a smoother interface along the ‘fast’ direction. Therefore, the interface roughness correlation length is best described by the two parameter Λ_X and Λ_Y the correlation lengths along the ‘fast’ and ‘slow’ directions, respectively.

To calculate the parameters Λ_X , and Λ_Y , from the interface correlation length determined from the C-shaped iHEMT devices, an ellipse was fitted to the values for interface roughness correlation length, assuming that the ellipse is centred at the origin. The fitted ellipses had three free parameters: the semi-major and semi-minor axes Λ_X and Λ_Y , and an offset angle $\Delta\theta$ to account for misalignment of the device pattern with respect to the major flat of the wafer and the ‘fast’ direction of the wafer. The fitted values of the interface correlation length, Λ , as a function of angle with the fitted ellipse and ellipse parameters are shown in figures 5.19 and 5.20.

5.8.2 Effect of Wave Function Choice

From the fitted parameters in table 5.6, the surface charge density and background impurity density fitted parameters demonstrate that the scattering due to point charges is over estimated when using wave functions that do not penetrate into the AlGaAs layer. Notably, with the background impurity density there is a clear trend of the fitted values reducing from $\sim 5 \times 10^{15} \text{cm}^{-2}$ down to $\sim 1.6 \times 10^{14} \text{cm}^{-2}$, with the change from a zero thickness wave function to the Fang-Howard wave function having as large an effect as introducing penetration into the AlGaAs spacer layer. While the background density still remains in the same order of magnitude, a change by a factor of ~ 3 is significant when looking at the more subtle secondary effects that changes in the grow parameters can have, as seen in the high mobility iHEMT structures. The surface charge density shows a similar trend to the background density, with the fitted values reducing as the wave function becomes closer to the ‘true’ wave function. Similarly the interface roughness amplitude only varies a small amount when changing the choice of wave function. As the mobility is more sensitive to small changes in the interface roughness than the background density, this is more an indication of how sensitive the mobility is to a small change in interface roughness than showing a dependence of wave function choice.

From the fitted elliptical parameters in figures 5.19 and 5.20, the interface roughness correlation length shows a general trend of a longer, and therefore smoother interface when using the more realistic wave functions.

Both the shifted Fang-Howard and variational wave functions penetrate into the AlGaAs spacer layer and therefore an alloy scattering component in the mobility. As the alloy scattering has the same dependence on the carrier density as the interface roughness, the presence of alloy scattering means that the needed scattering rate from alloy scattering and interface roughness combined can be achieved with a smoothed roughness. The range of values for the correlation length vary by $\sim 5 - 10\text{nm}$ with median values of $\sim 15\text{nm}$, therefore the varying due to the choice of wave function represents a fractional change of 30%–70%. If the modelled scattering rates are to be used to relate a physical length scale to the growth parameters, the choice of wave function is important to get the correct dependence on the interface roughness.

The results from fitting the same wafers with different wave function choices demonstrates the affect that the choice of wave function can have. Ultimately, the correct choice of wave function depends on the aims of the modelling. For all of the fitted parameters the fitted values remain the same order of magnitude for all of the wave functions used here. Therefore, if the aim of the modelling is to get a descriptive value for the relative strengths of the different scattering mechanisms it is arguable if the extra precision and numerical complexity of the new wave functions adds to the overall conclusion. The new wave functions show that the mobility of these wafers is limited by the background dopant density with the interface roughness becoming significant at the highest carrier densities measured. Therefore for ‘quick’ characterisation and comparison between wafers the Fang-Howard function still has some use.

5.8.3 As_2 vs As_4

Comparing the parameters in table 5.6 and figures 5.19 and 5.20, and comparing between the As_2 wafers (W1088 and W1089) and the As_4 wafers (W1091 and W1093) some of the fitted parameter show a definite difference between the two As types used. The surface charge density shows no clear dependence on the As type, which is understandable as the surface charge density will be dominated by processing conditions and cool-down dependent effects which control the trapping of charge in the interface of the GaAs and gate dielectric. The background impurity density shows a clear trend of lower impurity density in the As_4 wafers, which are lower on average when varying the wave functions used. Interestingly, the choice of wave functions changes the magnitudes of the fitted background impurities but also the difference between the As types. The zero-thickness wave function shows a $\sim 40\%$ decrease in background density in the As_4 wafers over the As_2 , but the variational only shows a $\sim 10\%$ drop in the As_4 material. This may be due to the finite thickness wave functions, Fang-

Howard, shifted Fang-Howard and variational, extending into the wave structure and thereby increasing the scattering from a uniform background density, showing that a smaller change in the background doping density is needed to achieve the measured improvement in mobility. The interface roughness amplitude for the As₂ and As₄ wafers both show a range of values between 0.15nm and 0.11nm, once again showing that the interface roughness is difficult to fit for when the mobility is dominated by other mechanisms, like the background scattering. Comparing the values for the interface roughness amplitude across all the wave functions the As₂ wafers have, on average, a smaller roughness amplitude, suggesting that the interface for the As₄ wafers has a greater variation in the interface position. The trend for the interface roughness correlation lengths is the same as the interface roughness amplitude with the As₄ wafer having a longer correlation length. Therefore the fitted parameters indicate that the interface which forms from elliptical islands of AlGaAs reconstructing on the GaAs surface, forms from larger islands when using As₄ compared to As₂, resulting in a smoother interface overall.

5.9 Conclusions

In conclusion, the carrier mobility carrier density curve can be modelled using the Boltzmann formalism, with the four major scattering mechanisms for an electron gas at 1.5K, surface charge, background impurities, interface roughness, and alloy scattering described using a series of integrals which depend on the wave function through four form-factors. Using the Fang-Howard wave function to approximate the confinement wave function within a heterostructure allows for the mobility density curves to be fitted to the experimental data from chapter 3. The mobility density curves were fitted using a uniform background impurities density, surface charge for the 50nm AlGaAs spacer devices, and interface roughness. The numerical results for these fitted parameters agreed with the conclusions from chapter 3.

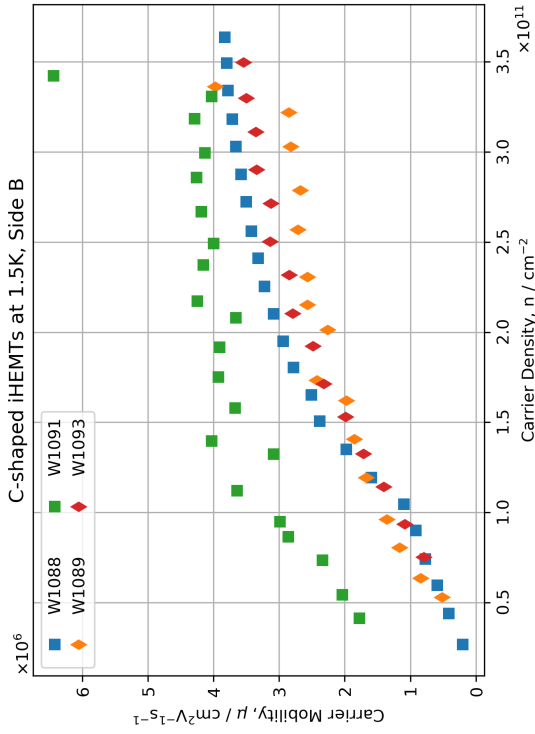
Comparing the As₂ and As₄ wafers using the Fang-Howard wave function, the numerical results from the fitted data curves showed that the increased carrier mobility in the As₄ wafer is due to a lower background impurity of $(0.64 \pm 0.01) \times 10^{14} \text{cm}^{-3}$ compared to $(1.05 \pm 0.07) \times 10^{14} \text{cm}^{-3}$, a reduction of $\sim 40\%$. The modelling showed that the background impurities are the dominant scattering mechanism for the measured wafers, but also indicated that the interface of the As₄ had a large roughness amplitude and correlation length describing a smoother interface compared to the As₂ wafer. From the fits of the Si cell wafers, W1088, W1090, W1161 and W1162, the model shows no measurable difference between the wafers with As₂, but with the reduced background of the As₄ the reduced mobility with W1161 compared to W1162 is due to an increase in background impurities of $\sim 2\%$. Such a small increase would be consistent with the additional heat load that the hot Si cell adds to the chamber, increasing the

impurities added to the wafer during growth. Given the size of the increase due to the Si cell, the lack of difference between the As₂ wafers can be understood as the modelling shows that the background impurities may be $\sim 40\%$ higher in the As₂ wafers, making a $\sim 2\%$ increase difficult to see and fit for.

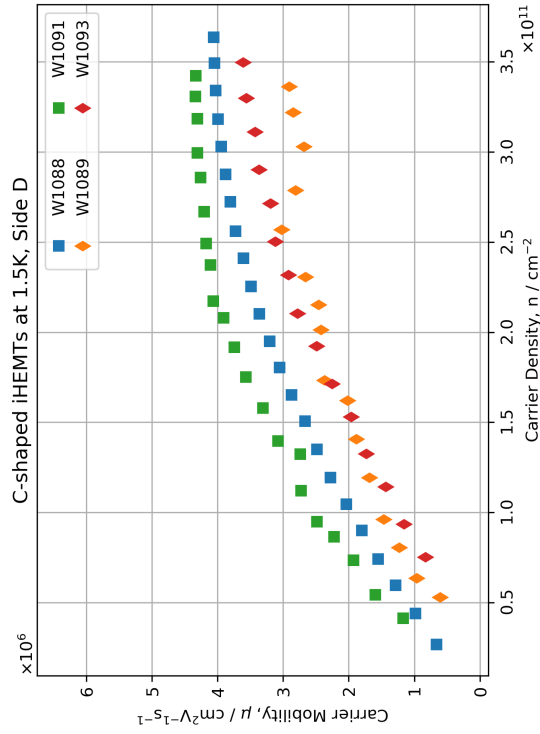
The results from fitting of W1170 and W1171 heterostructures grown with deliberate dopants added to the AlGaAs spacer, showed an increased background impurity in W1170, the deliberately doped wafer. The increase in background was $\sim 0.3 \times 10^{14} \text{cm}^{-3}$ and could be modelled as only an increase in the AlGaAs spacer layer background density. The increase of $\sim 0.3 \times 10^{14} \text{cm}^{-3}$, was plausible with a $1 \times 10^{15} \text{cm}^{-3}$ doping with Si. This adds weight to the results being linked to physical changes in the wafer structure.

Finally, extensions to the model were suggested and explored by introducing a new variational wave function which addressed the short-comings of the Fang-Howard wave function and could produce a > 0.98 fidelity to a self-consistent solution from nextnano. The variational wave function showed a distinctly different carrier mobility-density curve for a common set of parameters and from the fitting of ‘C-shaped’ Hall bar device to give values of the interface roughness as a function of angle. The effect of the different wave function showed that the fitted parameters from the Fang-Howard wave function had over-estimated the parameter by factors of order unity. While the differences between the parameters are notable, the conclusion drawn from the Fang-Howard fits are still valid however the numerical values may change if a different wave function has been used. The use of the variational wave function allows the effect of alloy scattering to be included in the mobility model, which had most effect on the numerical values for the interface roughness, which had been over-estimated due to the lack of alloy scattering. The results from comparing the different wave functions showed that the use of more complex wave functions, only add value to the analysis when trying to model and understand the more subtle secondary differences between growths, such as the difference between the Si wafers, which could only be seen in the highest mobility material. From the ‘C-shaped’ devices, the interface correlation length was fitted as a function of angle to the major flat. These lengths were then fitted and found to be described by the expected elliptical curve due to the elliptical reconstruction of AlGaAs islands on a GaAs surface. These fitted curves showed a difference of $\sim 5 - 10 \text{nm}$ between the major and minor lengths, with a misalignment of $< 10^\circ$ on average, mostly due to misalignment of the optical pattern to the crystal axes.

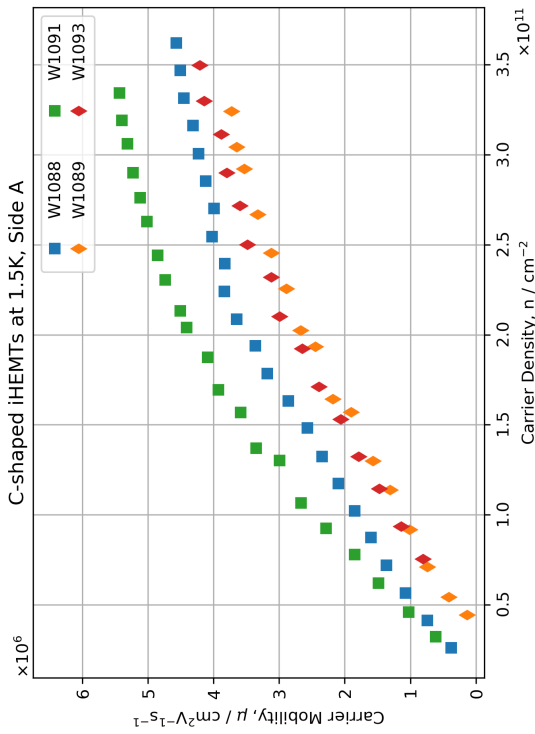
The results of the fitted curve have demonstrated that modelling of the mobility density curves can be a powerful addition to the analysis of mobility-density curves to understand the limiting factors of the mobility in a undoped structure.



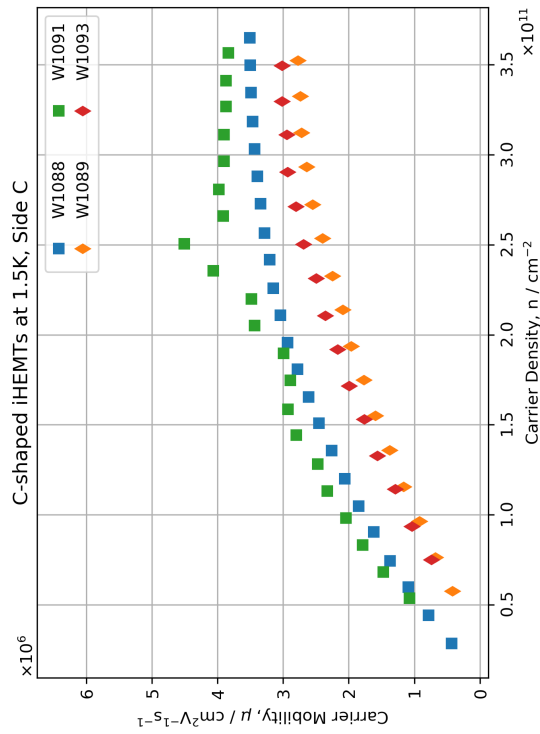
(b) Side B - 45° to the major flat



(d) Side D - 135° to the major flat



(a) Side A - 0° to the major flat



(c) Side C - 90° to the major flat

Figure 5.18: Carrier mobility-density curves for As₂ and As₄, 50nm and 100nm AlGaAs spacer layers separated by angle.

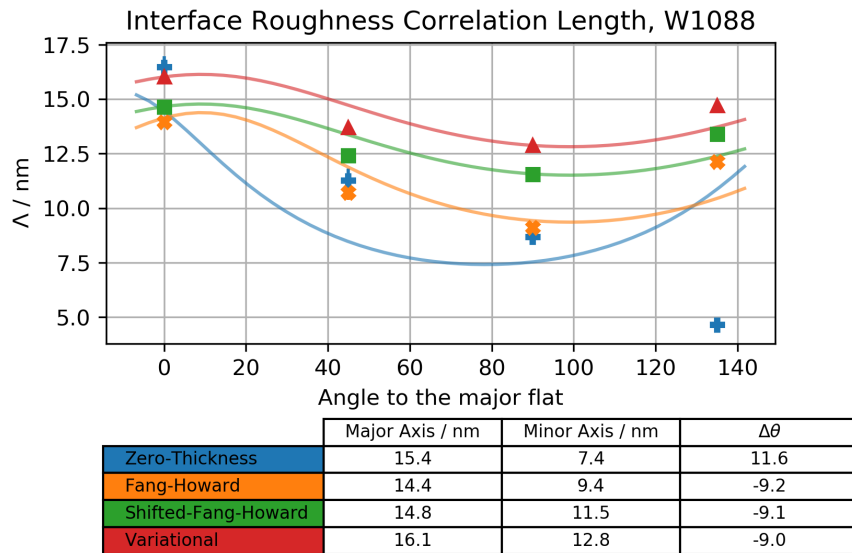
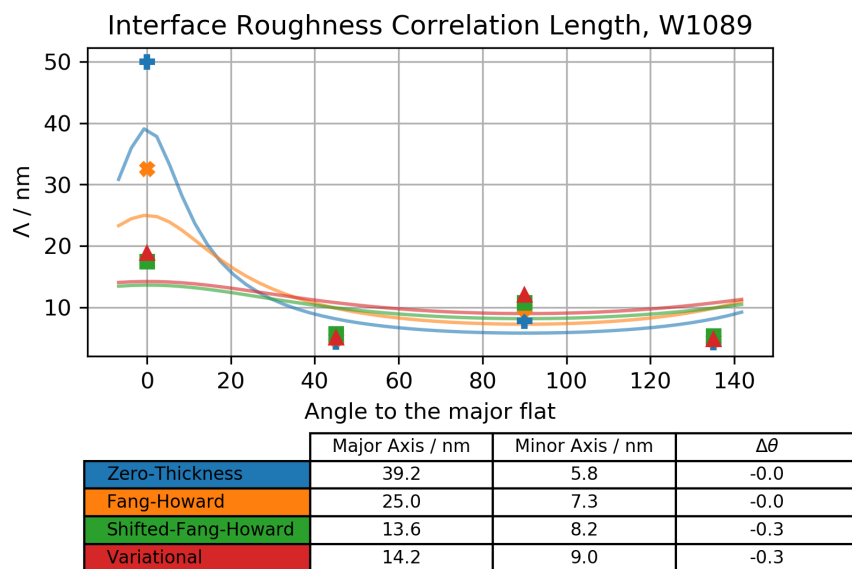
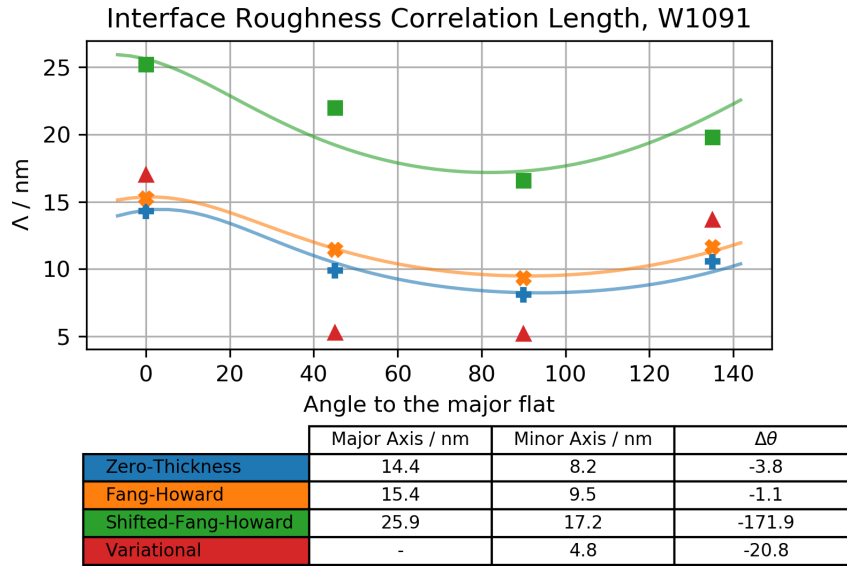
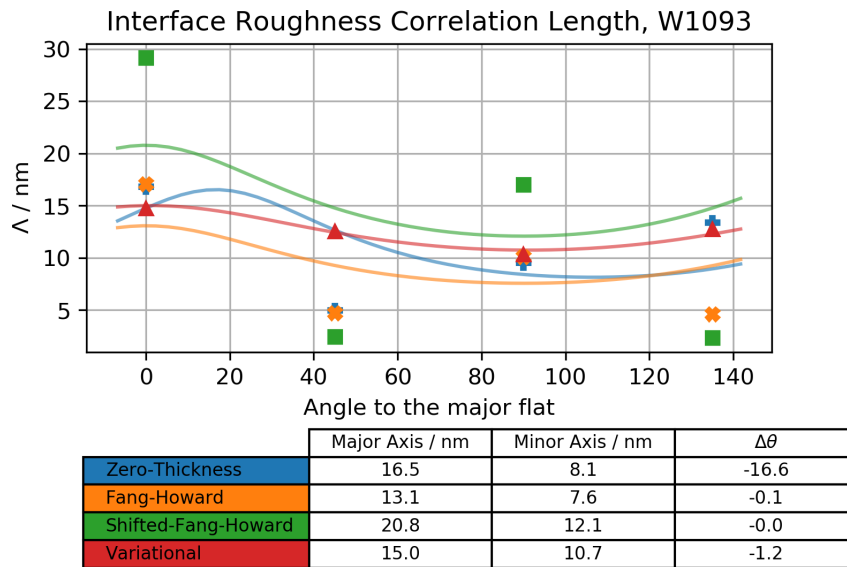
(a) W1088, As₂ 100nm AlGaAs Spacer(b) W1089, As₂ 50nm AlGaAs Spacer

Figure 5.19: Interface roughness correlation length, Λ , as a function of angle to the major flat of the wafer with fitted ellipses and parameters of ellipses for W1088 and W1089, As₂ 100nm and 50nm AlGaAs spacer thicknesses.



(a) W1091, As₄ 100nm AlGaAs Spacer



(b) W1093, As₄ 50nm AlGaAs Spacer

Figure 5.20: Interface roughness correlation length, Λ , as a function of angle to the major flat of the wafer with fitted ellipses and parameters of ellipses for W1091 and W1093, As₄, 100nm and 50nm AlGaAs spacer thicknesses.

LOW TEMPERATURE 2D TRANSPORT

A significant advantage of undoped material is not being limited to a single carrier type as either electron or holes can be induced by applying an external electric field, providing the field has the correct sign[149]. However, such ambipolar devices require two different ohmic contact metals to allow contact to the conduction band for electron and valence band for the holes. Depositing two different contact metals is relatively straight forward to achieve, although, as discussed in chapter 4, adds an extra step in the optimisation of the fabrication process.

Due to the much heavier effective mass of the holes compared to the electrons, the energy spacing between energy levels is much smaller. Practically this means that, to see the same sort of behaviour as electrons at 1.5K as in chapters 3 and 5 with holes, the temperature at which the hole gases are measured must be lower than 1.5K.

In this chapter, measurement of electron and holes gasses at temperatures down to 300mK in the presence of a magnetic field are presented and discussed. The data from measurement of GaAs heterostructures and quantum wells at these lower temperatures forms a useful control dataset for chapter 7 to separate the effects of the indium in a quantum well from the effects of a quantum well rather than heterostructure.

6.1 Shubnikov De Haas Oscillations

Shubnikov de Haas oscillations arise in 2D electron systems at sufficiently low temperatures due to the Landau level energy structure formed by the application of a perpendicular magnetic field, figure 6.1. The density of states at the Fermi level changes as a function of the magnetic

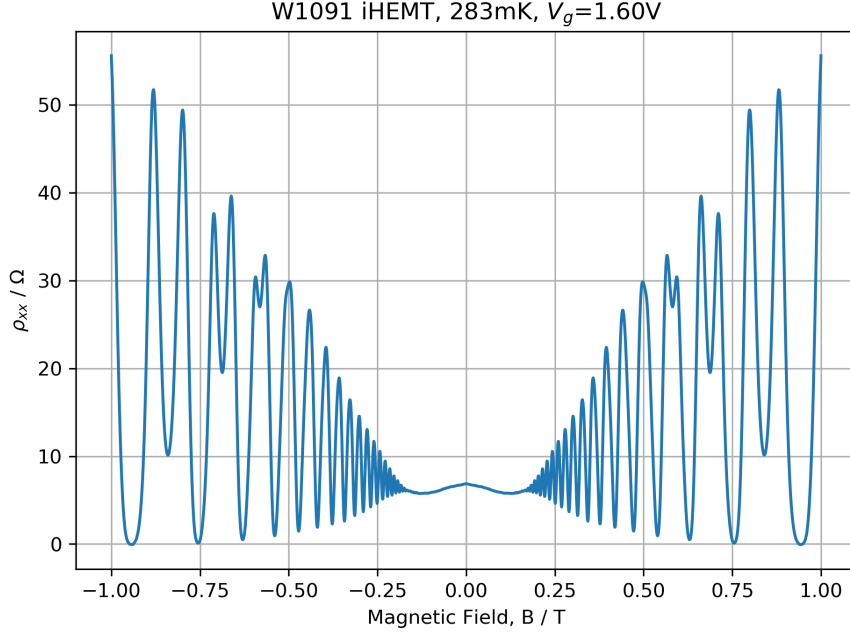


Figure 6.1: Typical Shubnikov Oscillations for a 2D electron gas in the GaAs/AlGaAs heterostructure. Data from W1091 taken at 283mK.

field, causing the conductivity of the sample to oscillate. These oscillations are periodic in the reciprocal magnetic field, $1/B$, with an expected form [150],

$$\begin{aligned}\rho_{xx} &= \rho_0 \left(1 + 2 \frac{\Delta g(T)}{g_0} \right) \\ \rho_{xy} &= R_h B \left(1 - \frac{1}{(\mu B)^2} \frac{\Delta g(T)}{g_0} \right)\end{aligned}\quad (6.1)$$

where, $R_h = 1/qn_c$, is the Hall coefficient and $\Delta g(T)/g_0$ is given by,

$$\begin{aligned}\frac{\Delta g(T)}{g_0} &= 2 \sum_{s=1}^{\infty} \exp \left[\frac{-\pi m^* s}{e \tau_q B} \right] \frac{X(s)}{\sinh(X(s))} \cos \left(\pi s \left[\frac{R_k}{R_h B} - 1 \right] \right) \\ X(s) &= s \frac{2\pi^2 k_b T m^*}{\hbar e B} \equiv s \alpha \frac{T m^*/m_e}{B} \sim 14.693 \dots \frac{T m^*/m_e}{B}\end{aligned}\quad (6.2)$$

with the von Klitzing constant $R_k = h/e^2 = 25.812 \dots \text{k}\Omega$.

Keeping only the $s = 1$ term, equivalent to assuming that $\mu B \gg 1$, the following expression for the difference in ρ_{xx} from ρ_0 given by $\Delta \rho_{xx} \equiv \rho_{xx} - \rho_0$, is,

$$\frac{\Delta \rho_{xx}}{\rho_0} = 4 \exp \left[\frac{-\pi m^*}{e \tau_q B} \right] \frac{X(1)}{\sinh(X(1))} \cos \left(\pi \left[\frac{R_k}{R_h B} - 1 \right] \right)\quad (6.3)$$

Therefore ρ_{xx} as a function of $1/B$ is expected to oscillate with a frequency of $f_{1/B} = \frac{R_k}{2R_h}$. Figure 6.2 show a plot of ρ_{xx}/ρ_0 as a function of $1/B$ and the power spectrum calculated using

the Fast-fourier transform (fft). The power spectrum shows only a single frequency with a small amount of the 2nd harmonic and a large DC component. The frequency matches the expected frequency from the Hall slope.

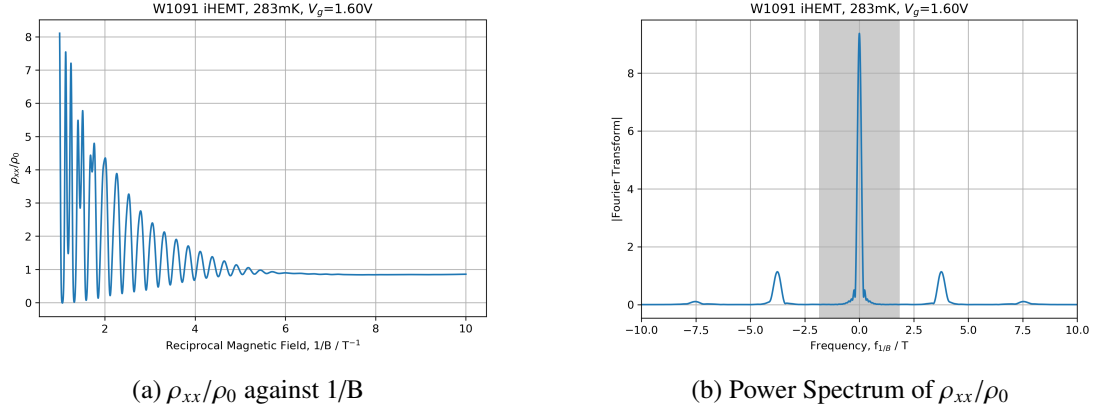


Figure 6.2: ρ_{xx}/ρ_0 as a function of $1/B$ for Electrons in W1091 at 283mK with power spectrum calculated from FFT showing only the expected frequency. The shaded area in 6.2b indicated the bandpass filter domain used to remove the background from the signal.

Calculation of $\Delta\rho_{xx} = \rho_{xx} - \rho_0$ was performed using a digital high pass filter with a cutoff frequency based on the expected frequency from the Hall slope, $f_{1/B}$, using 50% of this value for the cutoff as indicated in figure 6.2b. An example of $\Delta\rho_{xx}/\rho_0$ as a function of $1/B$ is shown in figure 6.3.

The Shubnikov De Haas Oscillations depend on three parameters of interest: the frequency of the oscillation ($f_{1/B} \propto n_c$) depends on the carrier density, the amplitude of the oscillation depends on the effective mass (m^*), and the quantum lifetime τ_q . The quantum lifetime is a measure of the total scattering rate within the electron system. Unlike the transport lifetime, which is weighed toward wide-angle scattering, which has a more significant effect on the transport of charge, the quantum lifetime has no such weighting. The defining equation for the transport lifetime and quantum lifetime are[151, 152],

$$\begin{aligned} \frac{1}{\tau_t} &= \int d\theta |V(q)|^2 (1 - \cos \theta) \\ \frac{1}{\tau_q} &= \int d\theta |V(q)|^2 \end{aligned} \quad (6.4)$$

The ratio of these lifetimes is often express as the Dingle ratio $\alpha_d = \tau_t/\tau_q$ [153]. Because of the weighting of the transport lifetime to wide angle-scattering, oppose to the quantum lifetime which has no weighting, the size of the Dingle ratio is a measure of the dominance of wide angle scattering in a structure. If the Dingle ratio $\alpha_d \gg 1$ then the transport lifetime is much longer than the quantum lifetime indicating that small angle scattering from long range

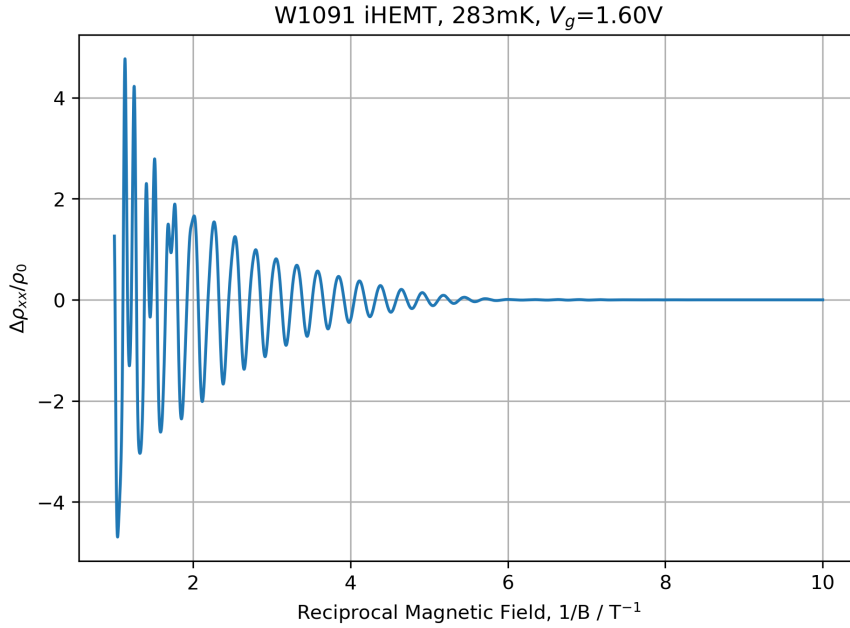


Figure 6.3: $\Delta\rho_{xx}/\rho_0$ as a function of $1/B$ for electrons in W1091 at 283mK. The background in ρ_{xx} was removed using a digital highpass with a cutoff frequency based on the expected frequency $f_{1/B} = R_k/2R_h$ calculated from the Hall slope.

scattering potentials is the dominate source of scattering. Therefore, determining the quantum lifetime from the Shubnikov-de-Haas oscillations gives extra information about the scattering in the electron system, that carrier density and carrier mobility does not give.

In order to extract the quantum lifetime from the oscillations, the effective mass of the carriers must be known. If the mass is known, then the temperature damping factor $\chi(X) \equiv X/\sinh(X)$ can be removed, leaving an oscillation with a decaying exponential envelope. Plotting the logarithm of the peak $\Delta\rho_{xx}/\rho_0\chi(X)$ against $1/B$ will give a linear plot from (6.3). Such a plot is called a Dingle plot, and the quantum lifetime can be extracted from a simple straight line fit.

6.1.1 Extracting Effective Mass from Shubnikov Oscillations

While the effective mass of electrons in GaAs is well known, it is useful to extract the effective mass from the Shubnikov oscillations to check the measurement set up and the data analysis method.

The typical method for extracting the effective mass from the Shubnikov oscillations is to look at the temperature dependence of the oscillations at a constant magnetic field [154, 155]. Assuming that the quantum lifetime has little/no temperature dependence then the ratio of the

peaks or troughs is given by,

$$\frac{\Delta\rho_{xx}(T_0, B)}{\Delta\rho_{xx}(T_1, B)} = \frac{T_0 \sinh(\gamma T_1 m^*/B)}{T_1 \sinh(\gamma T_0 m^*/B)} \quad (6.5)$$

where the parameter $\gamma = 2\pi^2 k_b m_e / \hbar e \sim 14.693 \dots$ if the effective mass is in units of the electron mass.

The peaks in $\Delta\rho_{xx}/\rho_0$ were found using a standard peak finding function from the scipy signal processing library [138], using the height of the oscillations in the semi-classic region where $1/B > 8T^{-1}$ as a threshold for noise in the signal, and using the peak frequency in the Fourier transform to determine the period of the oscillation to match peaks at the same filling factor. An example is shown in figure 6.4 from an electron gas in a GaAs heterostructure used for testing of this method. From the electron gas in a GaAs heterostructure measured at four gate voltages between 283mK and 1370mK the value of effective mass was $m^* = 0.068 \pm 0.001m_e$ which agrees with the literature value of $0.067m_e$ [65]. Likelihood curves for the effective mass are shown in figure 6.5, it is worth noting that the values from the higher carrier densities gave better values for the effective mass, due to more peaks in the oscillations being visible and higher mobility making the assumption in (6.3) more valid. Table 6.1 gives a summary of the values for m^* determined from the GaAs test sample.

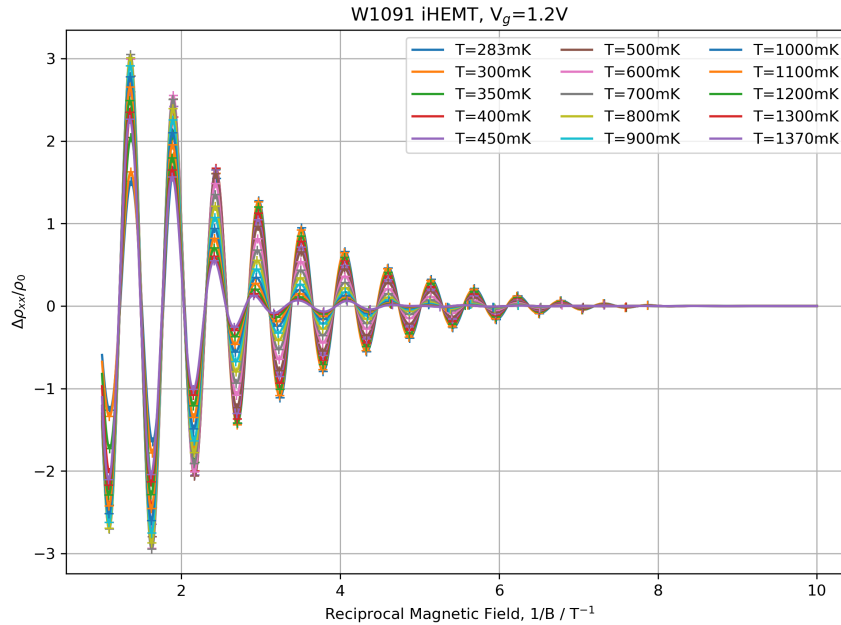


Figure 6.4: Shubnikov De Haas oscillations from an electron gas in a GaAs heterostructure, measured between 283mK and 1370mK. The peaks in the oscillations found using the method described have been marked.

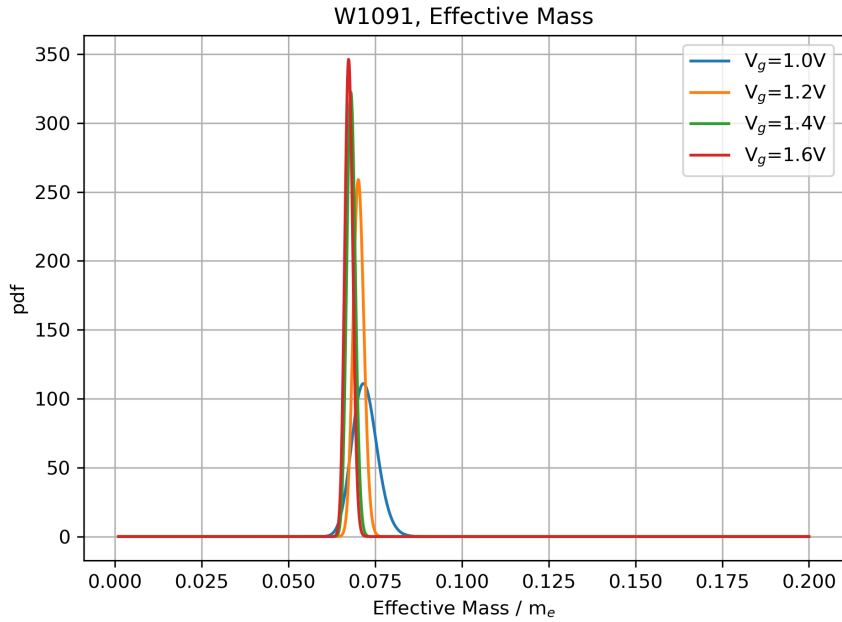


Figure 6.5: Likelihood curve for the effective mass in an electron gas in a GaAs heterostructure. Effective mass was determined from the temperature variation of the Shubnikov De Haas oscillations between 283mK and 1370mK for four gate voltages. The average value for the effective mass is $m^* = 0.067 \pm 0.001 m_e$ which agrees well with literature.

Gate Voltage / V	m^*/m_e	$\Delta m^*/m_e$	p-value using $m^* = 0.067 m_e$
1.0	0.072	0.004	0.04
1.2	0.070	0.002	0.01
1.4	0.068	0.001	0.10
1.6	0.067	0.001	0.18

Table 6.1: Effective Mass values determined from an electron gas in a GaAs heterostructure measure between 283mK and 1370mK. The higher carrier density measurements give better agreement with the literature value due to the increased number of visible peaks in the oscillations.

Looking at the temperature dependence works well if the oscillations are visible over a wide enough temperature range. However, in some cases, there is a limit on the range of temperatures that can be measured, or the temperature dependence is small. In cases like this, an alternative method for extracting the effective mass from the Shubnikov oscillations would be useful.

6.1.1.1 Extracting Effective Mass from Oscillation Spectrum

As stated previously, the effective mass and quantum lifetime change the shape of the envelope function of the Shubnikov oscillations. Being able to remove the oscillations and look only the

envelope function would allow a similar analysis of the temperature dependence, but at more magnetic field values than just the peaks and troughs of the oscillations.

In an attempt to remove the oscillations from the Shubnikov signal, the signal processing methods behind amplitude modulation were explored, as the Shubnikov oscillation can be viewed as the envelope function modulated on to a carrier frequency of $f_{1/B}$. Details of amplitude modulation are given in appendix A but the basic principle involve multiplying the signal by an oscillation with an equal frequency and phase. For the Shubnikov cosine oscillation this causes $\cos(2\pi f_{1/B}x) \rightarrow \cos(2\pi f_{1/B}x)^2 = [1 + \cos(4\pi f_{1/B}x)]/2$, therefore filtering out the oscillation at $2f_{1/B}$ will give just the envelope function. The frequency and phase of the Shubnikov oscillations were obtained from the Fourier transform of the signal, with the removal of frequencies $> f_{1/B}$ performed using a digital low-pass filter, using the signal frequency found from the Fourier transform as a cutoff.

Figure 6.6 shows the demodulated signals from Shubnikov oscillations for high and low carrier densities. For both densities, the demodulated signal matches the envelope of the oscillating signal very well, but at higher magnetic fields the demodulated signal still oscillates due to the spin splitting becoming large enough to make the odd minima visible.

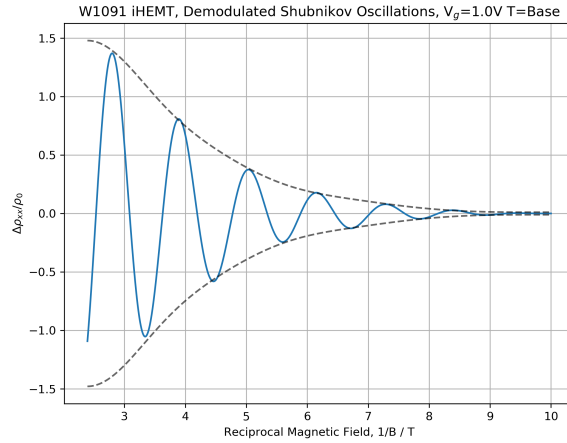
From (6.3) the envelope function is expected to have the form,

$$\left| \frac{\Delta\rho_{xx}}{\rho_0} \right| = 4 \exp[-\alpha\gamma x] \frac{\gamma x}{\sinh(\gamma x)} \quad (6.6)$$

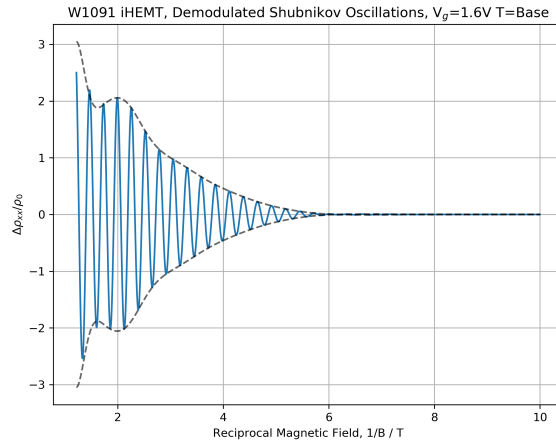
where $x \equiv 1/B$, $\alpha = \hbar/2\pi k_b T \tau_q$ and $\gamma = 2\pi^2 k_b T m^*/\hbar e$. To extract the parameters α and γ , the following non-linear curve is fitted as a function of x , figure 6.7.

$$y \equiv \ln \left| \frac{\Delta\rho_{xx}}{\rho_0} \right| = \ln \left[\frac{4\gamma x}{\sinh(\gamma x)} \right] - \alpha\gamma x \quad (6.7)$$

From the fits in figure 6.7b, the parameter $\gamma = 2\pi^2 k_b T m^*/\hbar e$ as a function of temperature plotted and fitted for the linear dependence expected from the definition of γ , figure 6.8. The values for γ in figure 6.8 follow a roughly linear trend, although the lower densities do deviate at the lower temperatures. The amplitude demodulation procedure described works best when the carrier frequency of the signal is much higher than the bandwidth of the signal being modulated. In the case of amplitude-modulated radio, the carrier frequencies are in the range 526.6kHz to 1606.5kHz (UK) with the bandwidth of the signal being modulated of the order 10-1000Hz based on human hearing, the key point being that the carrier frequency is at least an order of magnitude higher than the signal bandwidth. In the case of the Shubnikov oscillations, the bandwidth of the envelope function and the frequency of the oscillation are the same order of magnitude, as can be seen in figure 6.2. This can lead to the demodulation not removing all of the carrier frequency, causing distortion of the envelope function. At the lower carrier



(a) Low Carrier Density



(b) High Carrier Density

Figure 6.6: Example of demodulation of Shubnikov De Haas Oscillations using the method described in appendix A.

densities, the difference between the carrier frequency and the signal bandwidth is going to be less, explaining the deviation in the low-density high-temperature values of γ .

With the limitation of the demodulation accounted for, the gradients of the linear fits for γ give an average value for the effective mass of $0.067 \pm 0.006m_e$ which agrees with the literature value for electrons in GaAs, although the error is larger than the value from the temperature dependence of the peaks in the Shubnikov oscillations. Table 6.2 contains the values of the effective mass calculated from the linear fits of γ . Taking each gate voltage individually the values of the effective mass are not consistent with literature values, but averaging all the values together, there is an excellent agreement with literature. This suggests that this method of extracting the effective mass from Shubnikov oscillations is valid, but the method is susceptible

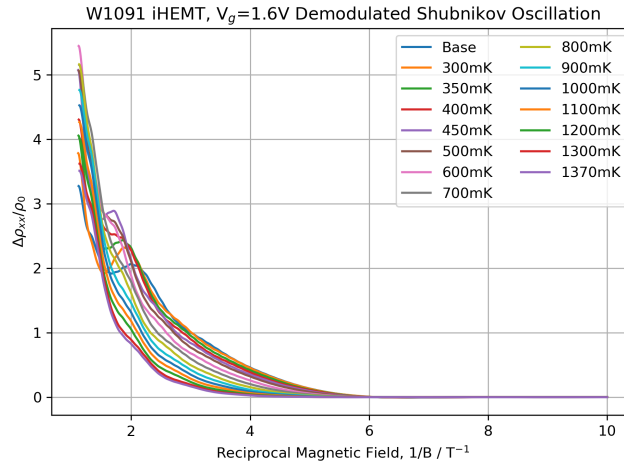
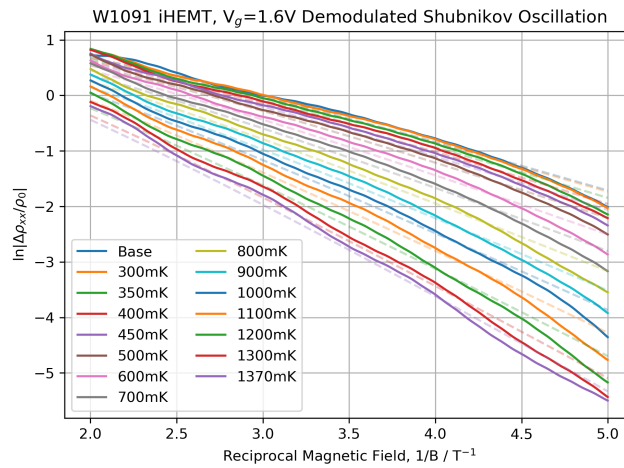
(a) $\Delta\rho_{xx}/\rho_0$ against $1/B$ as a function of temperature(b) $\ln|\Delta\rho_{xx}/\rho_0|$ against $1/B$ as a function of temperature

Figure 6.7: Demodulated Shubnikov De Haas Oscillations from an electron gas in GaAs as a function of temperature and fits of $\ln|\rho_{xx}/\rho_0|$ against $1/B$ as a function of temperature.

to either error in the measurement or distortion of the signal during demodulation. It is worth noting that, from the definition of γ , the intercept for the linear fits in figure 6.8 should be zero. All of the fits have a non-zero intercept, further suggesting that this method may be limited in application.

6.1.2 Quantum Lifetimes in Electron Gas

The quantum lifetime is a measure of the total amount of scattering in the 2DES and, unlike the transport lifetime, is not weighted towards wide angle scattering as can be seen from the definitions in (6.4). The ratio of the transport to quantum lifetime can be determined from the

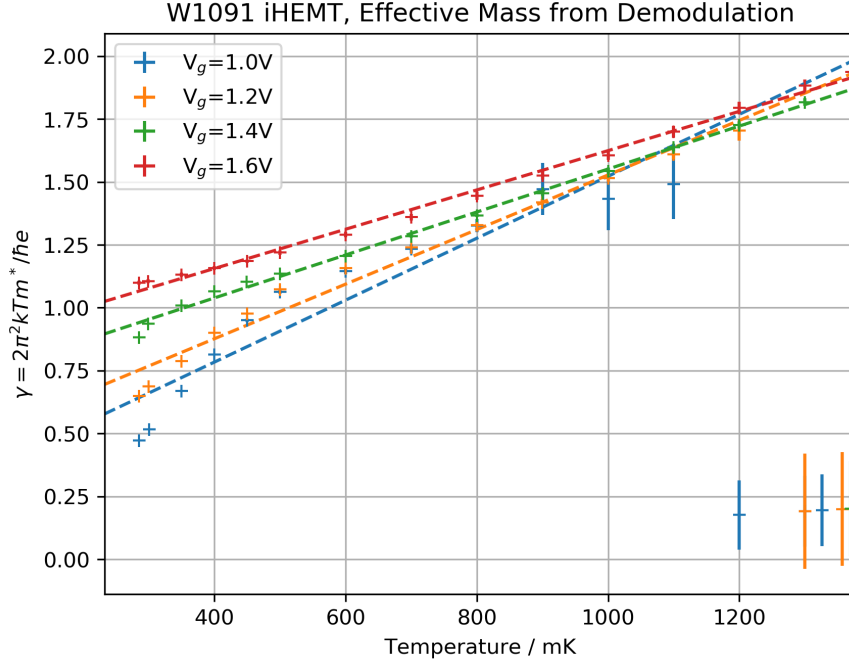


Figure 6.8: The fit parameter $\gamma = 2\pi^2 k_b T m^* / \hbar e$ as a function of temperature from $\ln \left| \frac{\Delta \rho_{xx}}{\rho_0} \right|$ as a function of $1/B$. The dashed lines are linear fits for γ , from which the effective mass of $0.067 \pm 0.006 m_0$ was calculated from the gradients.

Gate Voltage / V	m^*/m_e	$\Delta m^*/m_e$	p-value using $m^* = 0.067 m_e$
1.0	0.084	0.009	0.02
1.2	0.074	0.004	0.03
1.4	0.058	0.001	0.00
1.6	0.053	0.001	0.00
Avg	0.067	0.006	0.24

Table 6.2: Effective Mass values determined from an electron gas in a GaAs heterostructure measured between 283mK and 1370mK, using demodulation method on Shubnikov De Haas oscillations.

values of the positions and extrema in the Shubnikov De Haas oscillations. From (6.3) the extrema in the oscillations are expected to be described by the linear Dingle relation between the logarithm of the extrema as a function of B ,

$$\ln \left| \frac{\Delta \rho_{xx}}{4\chi(T, B)\rho_0} \right| = -\frac{\pi m^*}{e\tau_q B} = -\frac{\pi\tau_t}{\mu\tau_q B} \quad (6.8)$$

, with $\chi(T, B) \equiv X(1)/\sinh X(1)$ and $X(1) = 2\pi^2 k_b T m^* / \hbar e B$.

Therefore if the effective mass is known the temperature damping factor $\chi(T, B) \equiv X(1)/\sinh(X(1))$ can be calculated allowing the Dingle ratio, $\alpha = \tau_t/\tau_q$, to be calculated. The range of reported values for the Dingle ratio in GaAs structures varies depending on the qual-

ity of the material and the dominate source of scattering. In GaAs structures the Dingle ratio can be as low as 1-10[156–158] for structures limited by large angle scattering. For structures limited by small angle scattering the Dingle ratio can be an order of magnitude higher in the range $\gtrsim 50$ [159, 160].

The measured Shubnikov De Haas oscillations for W1088 and W1091, both 100nm iHEMT but grown with As₂ and As₄ respectively, are shown in figure 6.9. The resistivity in both along the Hall bar and across were measured between ± 1 T between 283 mK and ≈ 1370 mK. Only the positive magnetic field data as been plotted in figure 6.9 to better show the quantum Hall plateaus.

Using standard peak finding routines the extrema in the oscillations can be found and using the value of $m^* = 0.067m_0$ for the effective mass the Dingle plot for both W1088 and W1091 can be plotted, shown in figures 6.10 and 6.11.

The Dingle plots in figures 6.10 and 6.11 show an approximately linear dependence on $1/B$, expected from relation (6.8). At values of $1/B$ greater than $\sim 5\text{T}^{-1}$ the Dingle plots show a small amount of curvature, but as this is when the magnetic field is $\leq 0.2\text{T}$ this curvature is mostly like due to difficulties in resolving the Shubnikov De Haas oscillations which required $\mu B \gg 1$. This is consistent with the reduction of the curvature at higher temperatures as the amplitude of the oscillations reduces exponentially with temperature, meaning that the oscillations at 1300 mK can only be resolved at higher magnetic field than the oscillations at 283 mK.

From linear fit of the Dingle plot for $1/B \leq 5$ to exclude the curvature, and the carrier mobility calculated from the Hall coefficient R_h and $\rho_{xx}(B = 0)$ the ratio of the transport lifetime to quantum lifetime is plotted as a function of temperature in figure 6.12.

The ratio of the transport lifetime and quantum lifetime gives information about the dominant scattering mechanism, as the ratios from W1088 and W1091 are values $\gg 1$ this indicates that small angle scattering mechanisms are dominant over wide angle scattering and therefore suggest that long-range scattering potential may be the most important source of scattering in these GaAs heterostructures.

Figure 6.12 shows a temperature dependence of the lifetime ratio. In figure 6.13 the mobility and lifetime ratios have been converted to the transport and quantum lifetime in picoseconds. The transport lifetime show very little temperature dependence as to be expected from the temperature dependence of the mobility, but the quantum lifetime for W1088 (As₂) increases with temperature while the quantum lifetime for W1091 (As₄) reduces. The temperature dependence seen in figure 6.12, is therefore, due to the quantum lifetime. The analysis in section 6.1.1 was based on the quantum lifetime having no temperature dependence in order to extract the effective mass for electrons from the peak height of the Shubnikov de Haas

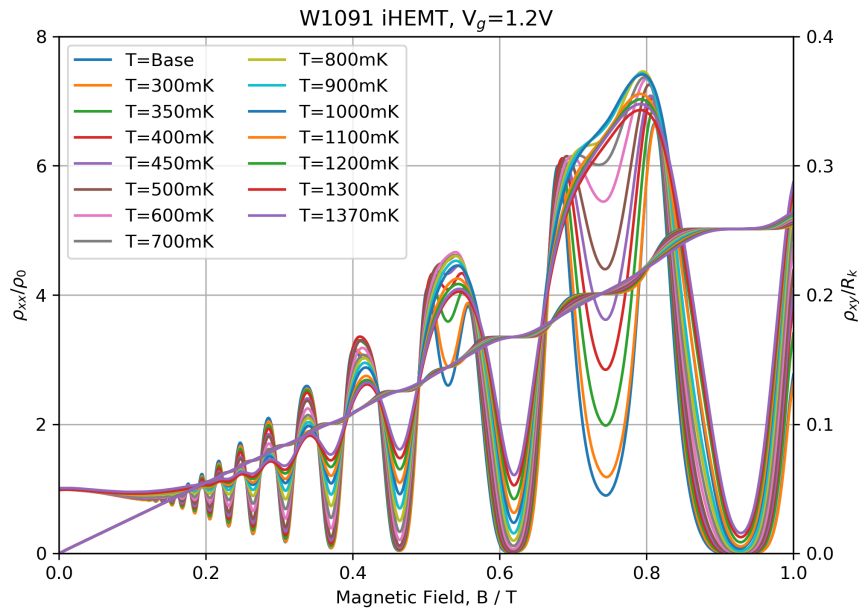
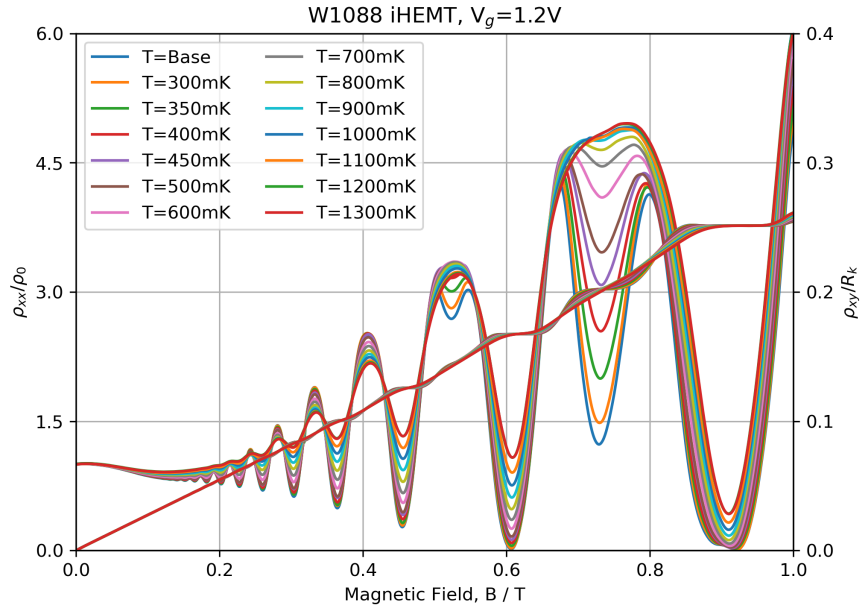


Figure 6.9: Shubnikov De Haas Oscillations measured between $\pm 1\text{T}$ between 283 mK and 1370 mK in W1088 and W1091, 100nm iHEMTs grown using As_2 and As_4 respectively. Both 2DEG have a carrier density of $0.88 \times 10^{11} \text{cm}^{-2}$.

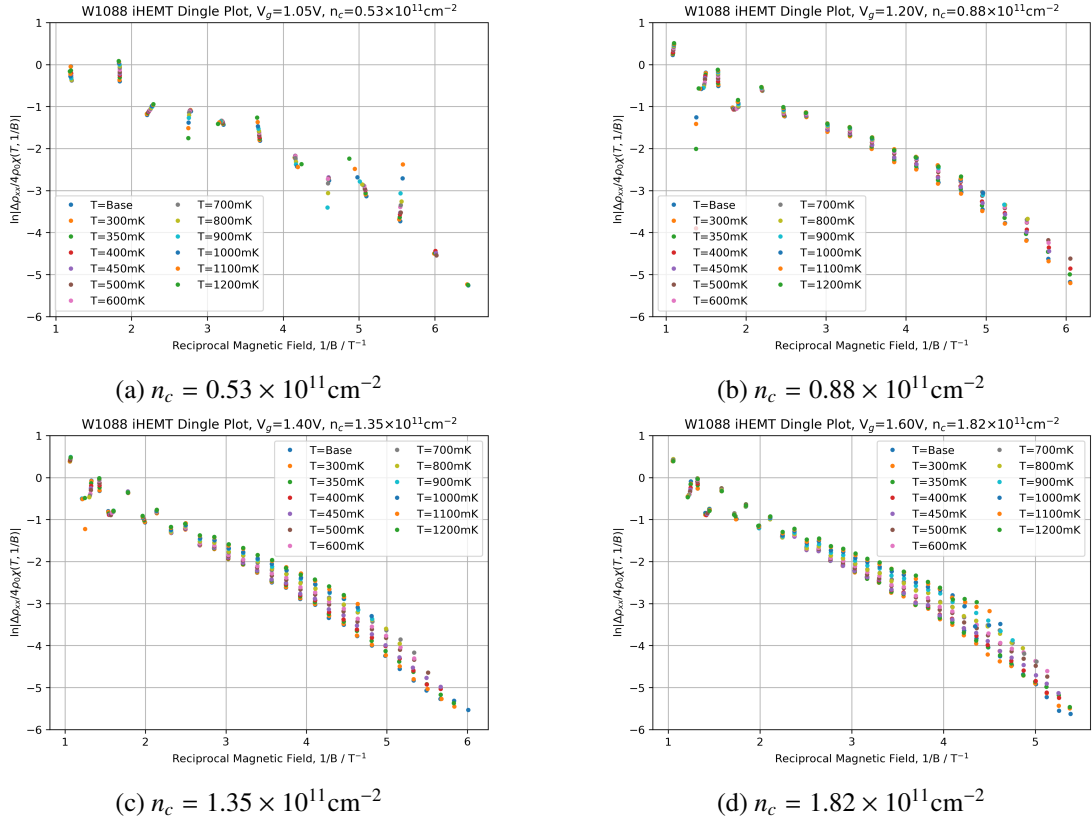


Figure 6.10: Dingle plots from Shubnikov De Haas oscillations in W1088 a 100nm iHEMT grown with As_2 .

oscillations. For the Dingle analysis the literature values of $0.067m_e$ has been used therefore this analysis only requires that the quantum lifetime is independence of magnetic field. The temperature dependence of the quantum lifetime seen in this data may be cause of the large range of effective mass values obtained in section 6.1.1. Interestingly the quantum lifetime values show that there is less overall scattering in the As_4 wafer (W1091). As the temperature dependence is only in the quantum lifetime this suggest that the cause of the temperature dependence is from small angle/long range interactions.

Plotting the Dingle ratio as a function of carrier density at base temperature, figure 6.14, shows that the Dingle ratio has a linear dependence on the carrier density. Because the Dingle ratio is > 20 at all carrier densities the conclusion above that small angle scattering is the dominate type of scattering is unchanged, however the increase of the Dingle ratio from ~ 20 to ~ 130 shows that the amount of small angle scattering is increasing with the carrier density, reducing the quantum lifetime more so than the transport lifetime. The interface roughness scattering rate is linearly dependent on the carrier density, (5.29). The matching dependence of the Dingle ratio on the carrier density suggestive that the Dingle ratio increase is a meas-

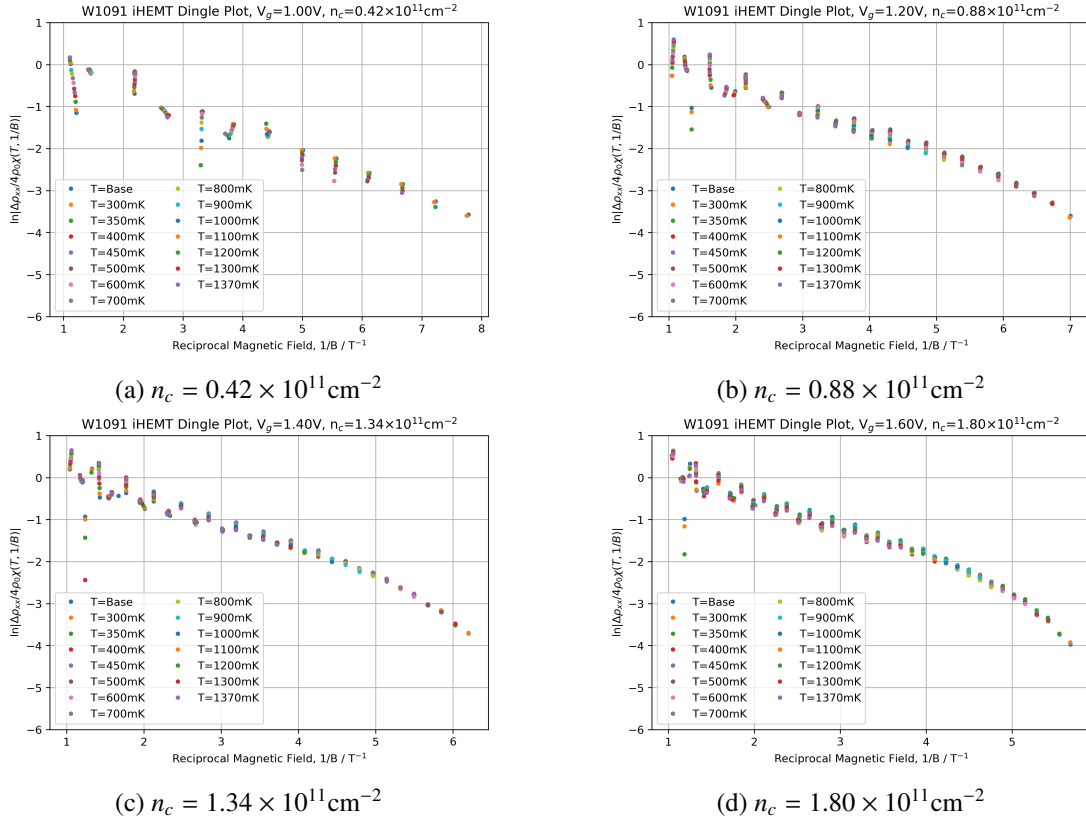


Figure 6.11: Dingle plots from Shubnikov De Haas oscillations in W1091 a 100nm iHEMT grown with As_4 .

ure of the increased scattering from the interface roughness. It has been reported that the quantum lifetime and transport lifetimes can be dominated by background impurities and interface roughness respectively[122], as similar dependence in this sample would lead to the measured linear dependence.

6.2 Dynamic Magneto-Resistance of Hole Gases

One of the major symmetries in the 2DES studied in a perpendicular magnetic field is $B \leftrightarrow -B$ for ρ_{xx} ; therefore a perfect device is symmetric about $B = 0$. When sweeping across zero fields in a hole gas, ρ_{xx} shows a distinctive asymmetry, figure 6.15.

The unusual behaviour of this asymmetry is that it depends on the direction of the magnetic field sweep. The resistivity increases as the field is swept away from zero, and therefore is not a simple mixing into the Hall voltage, which would add a linear dependence. The size of the asymmetry increases with the sweep rate of the magnetic field. To explore the sweep rate dependence a hole gas sample from W1091 was measured at 283 mK at the lowest pos-

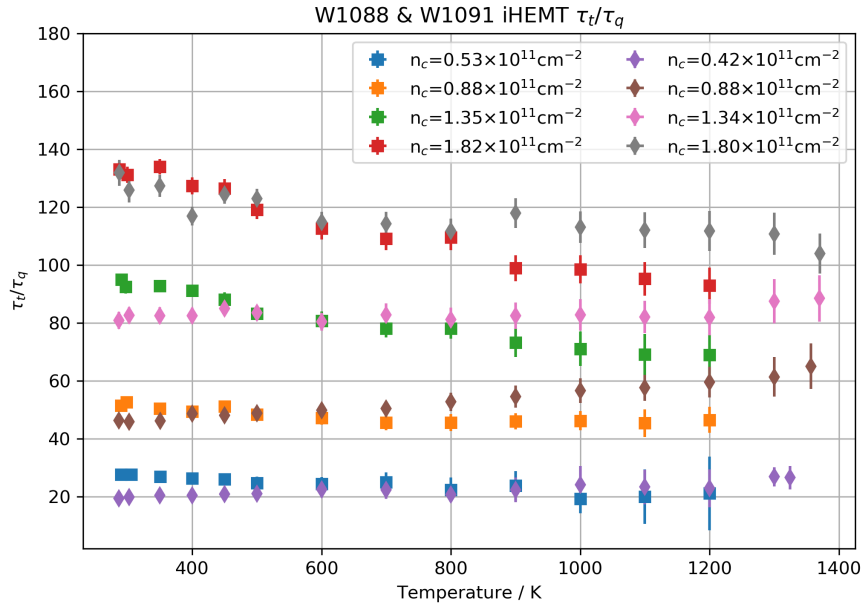


Figure 6.12: The ratio of the transport lifetime to the quantum lifetime for W1088 (squares) and W1091 (diamonds). The ratio has been calculated from the slope of a linear fit of the Dingle plots in figures 6.10 and 6.11.

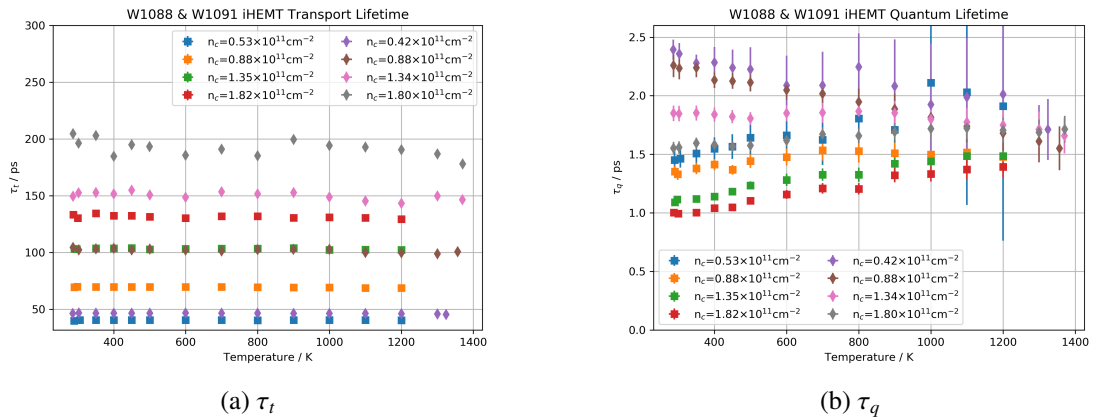


Figure 6.13: The transport and quantum lifetimes of W1088 (squares) and W1091 (diamonds). The transport lifetime shows little temperature dependence as expected but the quantum lifetimes show a small temperature dependence with W1088 (As_2) increasing with temperature and W1091 (As_4) reducing.

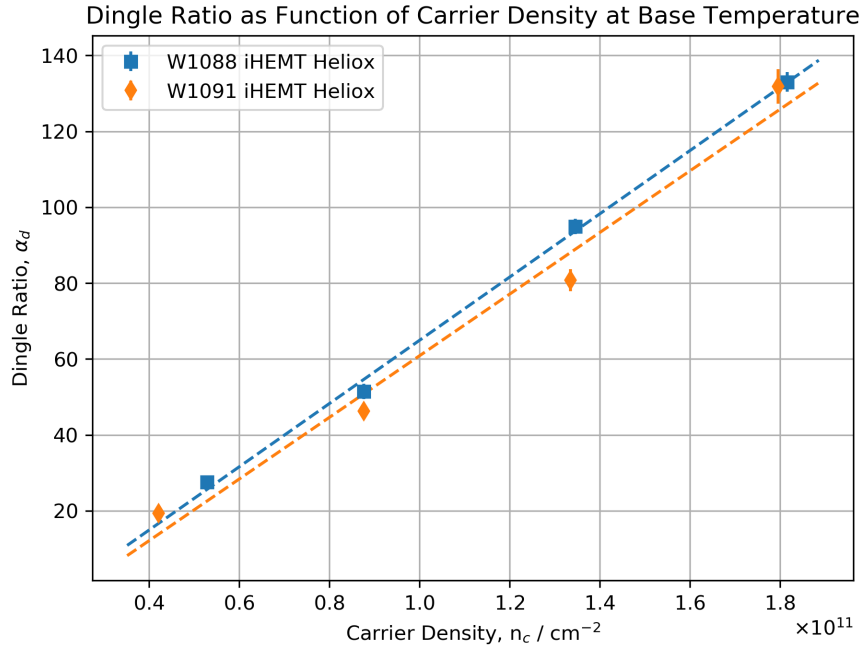


Figure 6.14: The ratio of the transport lifetime to the quantum lifetime for W1088 (squares) and W1091 (diamonds) as a function of carrier density. The ratio shows a linear dependence on the carrier density, which suggests that the ratio is dominated by the interface roughness scattering which is also linearly dependent on the carrier density.

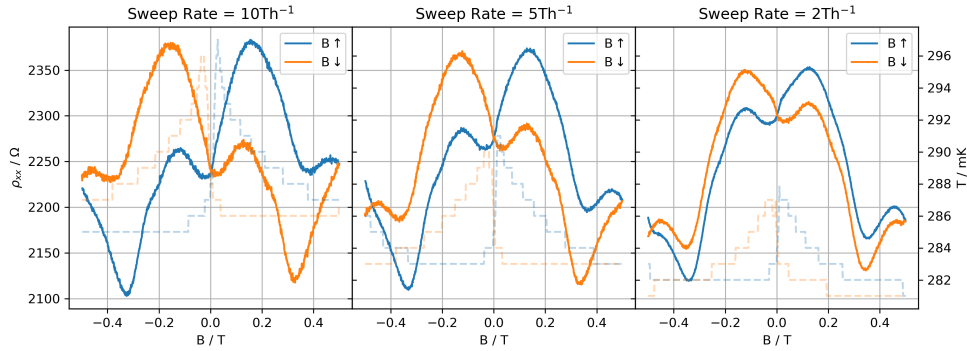


Figure 6.15: Sweeps of ρ_{xx} through zero field at 283mK with a range of sweep rates. The asymmetry has a dependence on sweep direction and cannot be explained by a simple mixing of the Hall voltage.

sible carrier density of $n_c = (3.6804 \pm 4) \times 10^{10} \text{cm}^{-2}$, that was achievable in that device. The resistivity was measured between $\pm 0.5 \text{T}$ at 5Th^{-1} , 10Th^{-1} , and 20Th^{-1} . In addition to the dynamic sweeps a quasi-static measurement of the resistivity was taken by stepping the magnetic field and waiting for 5 min to allow the system to approach static equilibrium. The results of these sweeps are shown in figure 6.16.

The measurement of W1091 at different sweep rates shows the same behaviour as the

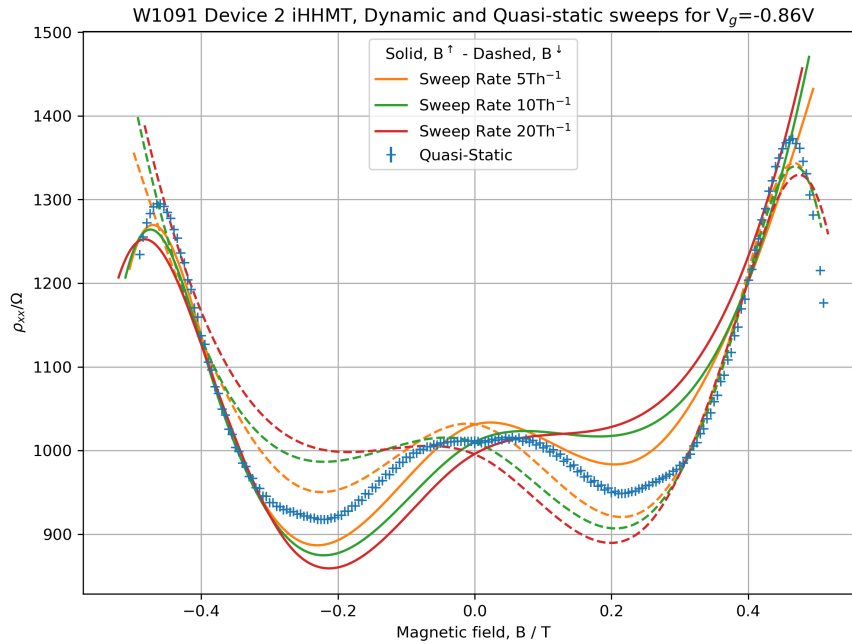


Figure 6.16: ρ_{xx} measured as a function of magnetic field with a magnetic field sweep rate of 5 Th^{-1} , 10 Th^{-1} , and 20 Th^{-1} . A quasi-static measurement of the resistivity was performed by stepping the magnetic field and waiting for 5 min before taking a measurement.

sample from W1170, however the quasi-static sweep shows no indication of the asymmetry in the dynamic sweeps, although there is a small amount of asymmetry consistent with mixing between the Hall and longitudinal voltages.

As the resistivity increases as the magnetic field sweeps away from zero, this is suggestive of a thermal effect similar to magnetocaloric effect [161], where applying a magnetic field results in magnetically active materials absorbing heat and cooling when the magnetic field reduces in magnitude. The temperature dependence of the resistivity was measured at higher carrier densities, figure 6.17. From this dataset the resistivity at zero magnetic field was extracted with a linear dependence on the temperature fitted, figure 6.18. This linear model gave a temperature dependence of the order of $20 \Omega \text{ K}^{-1}$. From figure 6.15 there is a change in resistivity of the order $10\text{-}100 \Omega$. This corresponds to a change in temperature of the order 1 K . The thermometry of the system measured a change in the temperature of the order 10 mK , and while the thermometry does not have a direct thermal connection to the sample, and is thermally connected to the ^3He pot which in turn connects to the sample, a change of the order 1 K in the sample would cause a measurable change in the temperature. Therefore, this change in resistivity is not consistent with the thermal temperature dependence of the sample.

Before disregarding temperature effects for the explanation of the asymmetry in the resistivity around zero fields, the potential effect of the Shubnikov de Haas oscillations, which

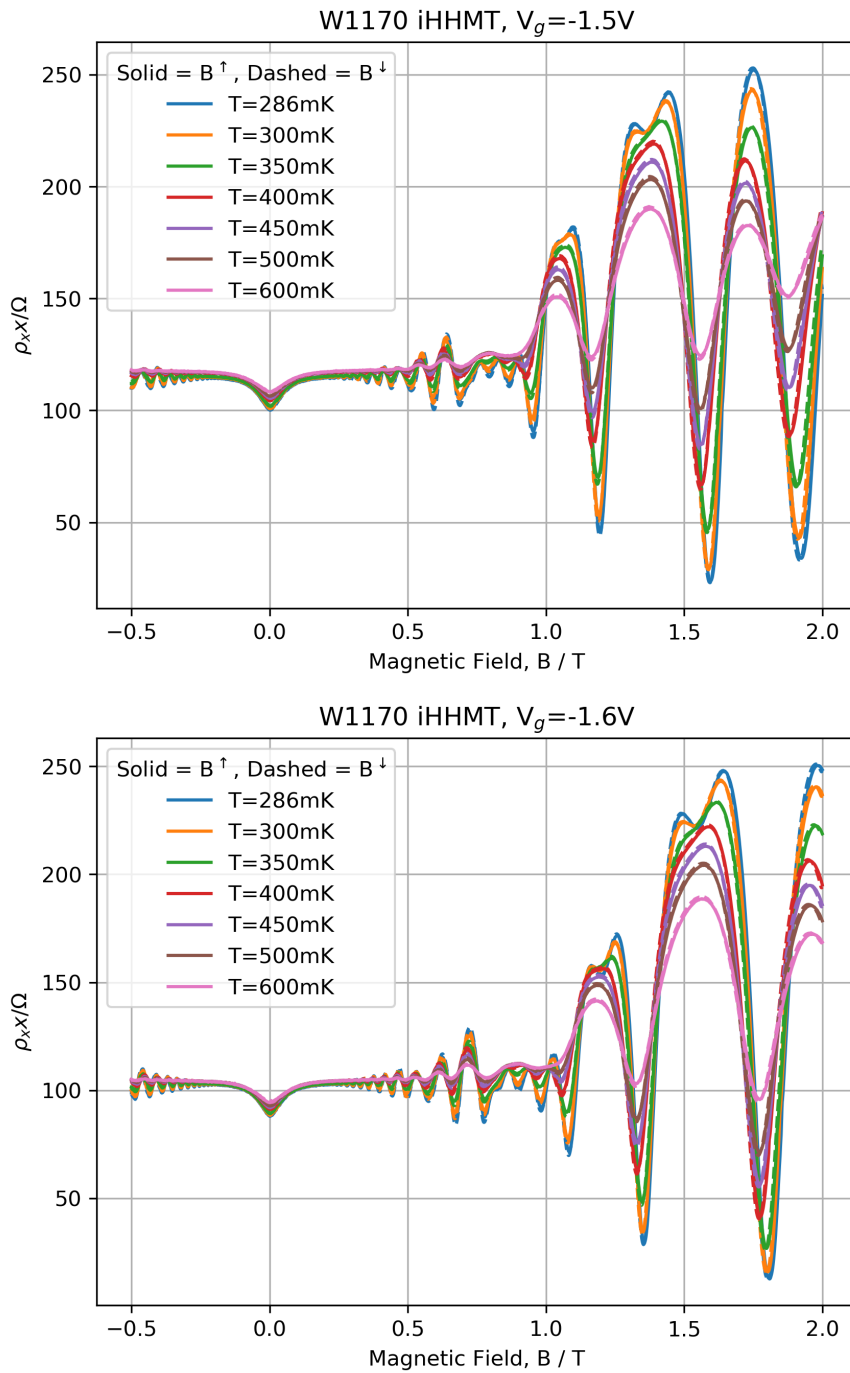


Figure 6.17: Temperature dependence of 2D Hole gas in W1170 between 283mK and 600mK.

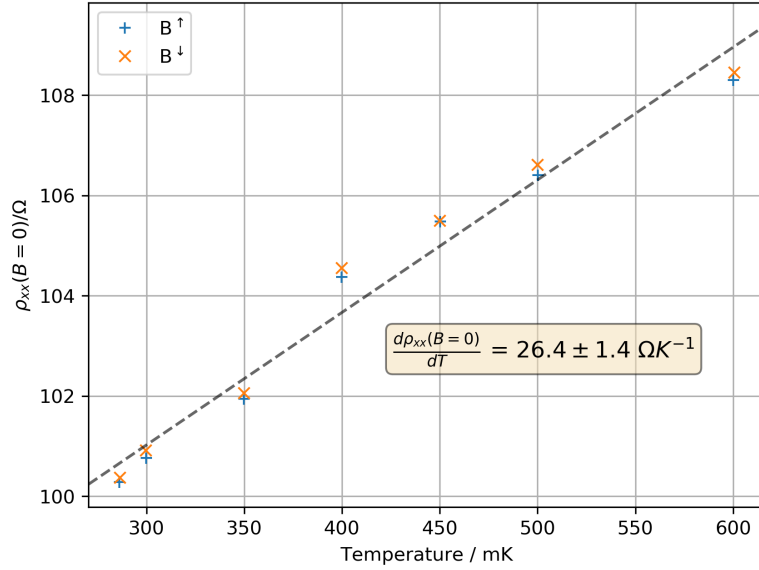
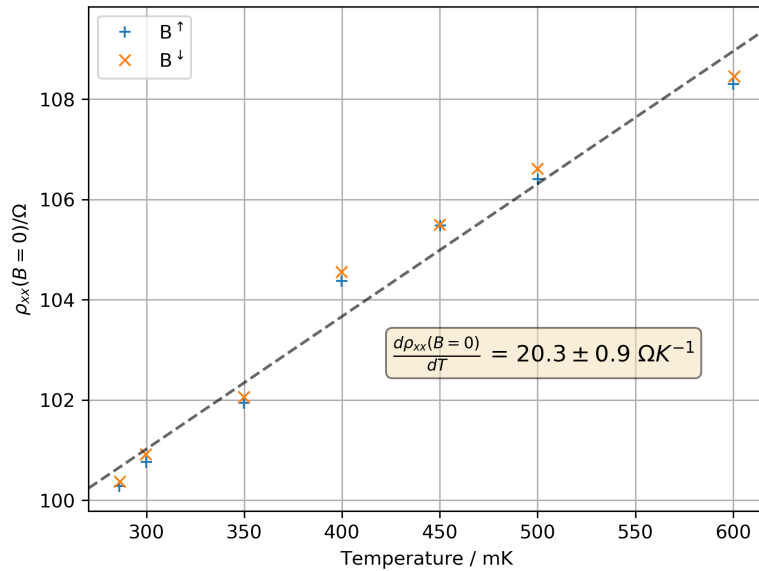
W1170 iHHMT, Zero Field Resistivity Temperature Dependence, $V_g = -1.5V$ W1170 iHHMT, Zero Field Resistivity Temperature Dependence, $V_g = -1.6V$ 

Figure 6.18: Temperature dependence of the resistivity at zero field for 2D Hole gas in W1170 between 283mK and 600mK.

also have a temperature dependence, should be considered. The temperature dependence of the Shubnikov de Haas oscillations is given by $\gamma x / \sinh \gamma x$, where $\gamma = 2\pi^2 k_b T m^* / \hbar e$ and $x = 1/B$. Therefore the amplitude of the Shubnikov is inversely related to the temperature. Figure 6.20 contains the sweeps in figure 6.15 converted to $\Delta\rho_{xx}/\rho_0$ as a function of $1/B$. The amplitude of the oscillation increases as the field sweeps away from zero. This is not consistent with an effect like the magneto-caloric [161] effect as the temperature would increase when the

field sweeps away from zero. Therefore the temperature dependence of the Shubnikov de Haas oscillations cannot explain the asymmetry seen in the hole gas.

Superconducting magnetics can have a small persistent field due to imperfections in the superconductor. Potentially this means that when the magnetic controller reports zero magnetic field there could be a magnetic field and therefore the magneto-resistance of the sample could be the cause of this asymmetry. Because the Hall resistance of the sample is linear in magnetic field at low field, $\rho_{xy} = R_H B$, the Hall resistance will be sensitive to any persistent field. The Hall resistance from the quasi-static sweep is shown in figure 6.19. The zero point crossing of the Hall resistance for all sweeps is within a few milli-Tesla of zero field. Therefore the persistent field is not large enough to explain the dynamic magneto-resistance.

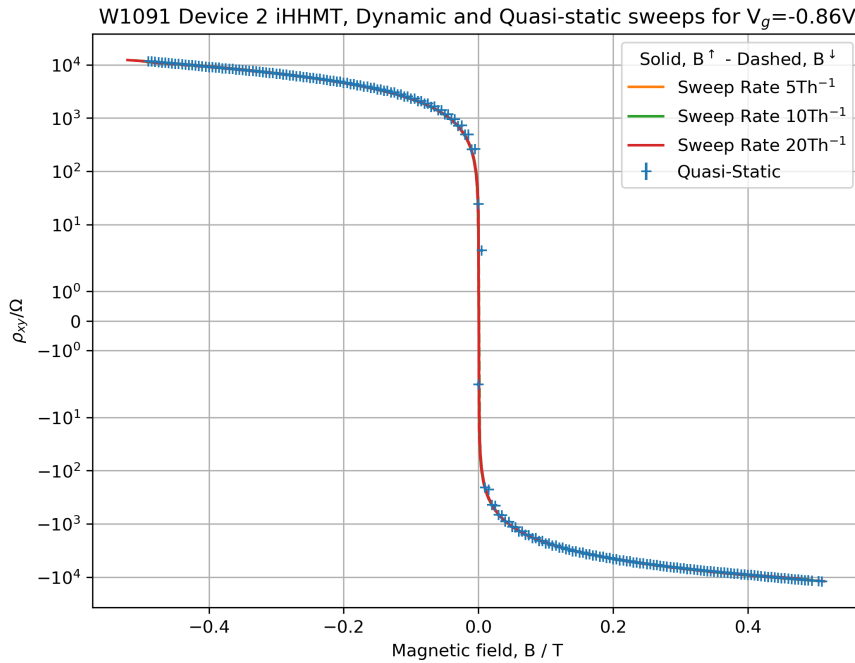


Figure 6.19: ρ_{xy} measured as a function of magnetic field with a magnetic field sweep rate of 5 Th^{-1} , 10 Th^{-1} , and 20 Th^{-1} . A quasi-static measurement of the resistivity was performed by stepping the magnetic field and waiting for 5 min before taking a measurement.

In figure 6.20, it is notable that the oscillations appear to have different frequencies depending on the sweep direction. To examine this further sweeps between $\pm 2T$ were taken and converted to functions of $1/B$, figure 6.21, showing Shubnikov De Haas oscillations with a beating pattern. From the spectrum in figure 6.21, the peak at the expected frequency from the Hall coefficient has split into two peaks at $f_{1/B}^- = 1.763 \pm 0.001T$ and $f_{1/B}^+ = 2.620 \pm 0.001$ corresponding to carrier densities $n^+ + n^- = 0.6335 \pm 0.0002 \times 10^{11} \text{ cm}^{-2}$ and $n^+ - n^- = 0.4263 \pm 0.0002 \times 10^{11} \text{ cm}^{-2}$ giving a higher carrier density of $n^+ = 0.5299 \pm 0.0001 \times 10^{11} \text{ cm}^{-2}$, consistent with the Hall coefficient and a lower carrier density of $n^- = 0.1036 \pm 0.0001 \times 10^{11} \text{ cm}^{-2}$

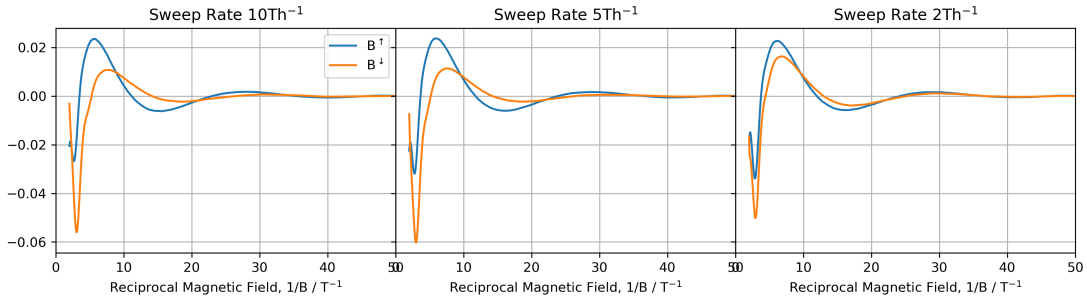


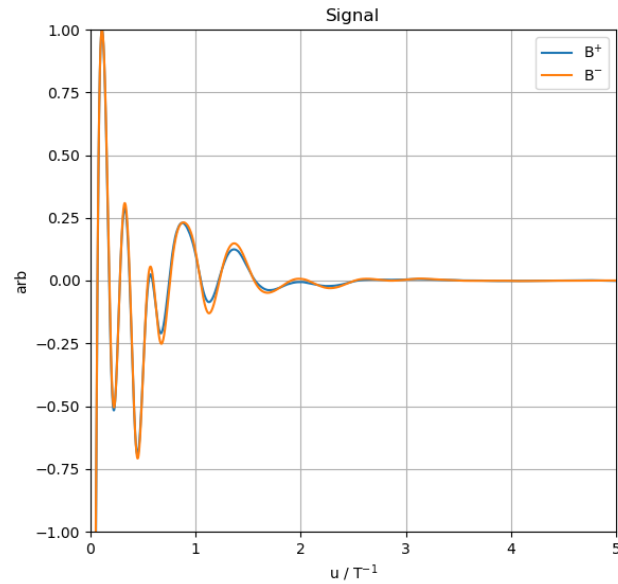
Figure 6.20: Sweeps of $\Delta\rho_{xx}/\rho_0$ against $1/B$ away and towards zero showing an increase in amplitude for sweeps away from zero and a change in frequency.

in the two holes gas populations present.

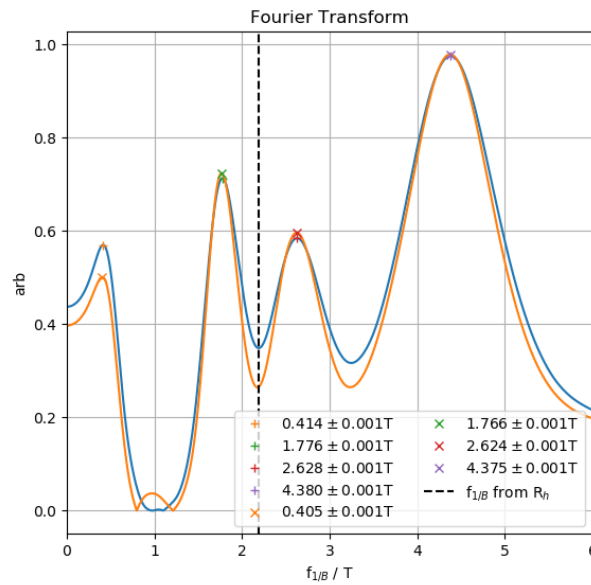
The amplitude of the sweep towards zero in figure 6.21 is slightly larger than the sweep away from zero. This is consistent with sweeps away from zero heating the sample via magnetically active elements in either the sample or cryostat. To estimate this increase in temperature, the ratio of the sweep towards zero to the sweep away from zero was taken, figure 6.22. From a linear trend line of the ratio of the sweep, the amplitude of the two sweep directions are approximately equal at high field but with the amplitude of the sweep towards zero increasing at low field by $0.16 \pm 0.01T^{-1}$. Using an effective mass value of $m^* = 0.47m_0$, this increase in the amplitude corresponds to a temperature ratio of between 101% and 107% depending on the field strength. Such a small change in temperature is consistent with the effect of magnetic heating and cooling.

The effect seen in figure 6.15 is largest at low field. Therefore, focusing only on the low field domain ($|B| < 0.5$), the Shubnikov oscillations, figure 6.23, most notably the peak at $f_{1/B}^+ = 2.620 \pm 0.001$ has reduced in amplitude so that it is only just resolvable and both peaks include the peak at $f_{1/B}^- = 1.763 \pm 0.001T$ have shifted down by $\Delta f = 0.2T$, which would correspond to a global decrease in carrier density of $0.05 \times 10^{11}\text{cm}^{-2}$. It also appears that the frequency of the visible peak at $f_{1/B}^- \approx 1.5T$ is slightly shifted depending on the sweep direction. For sweeps towards zero, the peak is higher at $f_{1/B}^- = 1.542 \pm 0.001T$ while for the sweep away from zero the peak is at $f_{1/B}^- = 1.505 \pm 0.001T$. While this change in frequency is small, corresponding to $\Delta n = 9.00 \pm 0.01 \times 10^8\text{cm}^{-2}$, there is no obvious reason for this apparent shift in the peak.

Similar asymmetries have been observed in other hole gas samples, figure 6.24. The data from A4022 in figure 6.24 was taken by J. Waldie measuring a doped hole gas sample on a different ^3He cryostat. This makes the asymmetries observed in the samples from W1170 and W1091 unlikely to be due to a cryostat specific effect, something that could not be excluded as all measurements were conducted on the same ^3He system.



(a) Modified Shubnikov Oscillation Signal



(b) Fourier Transform

Figure 6.21: $\Delta\rho_{xx}/\rho_0$ as a function of $1/B$ from a hole gas in W1170, showing Shubnikov De Haas oscillations for a positive magnetic field sweep from $-2T$ to $2T$. The oscillations show a small change in amplitude depending on sweep direction, consistent with magnetic heating and cooling.

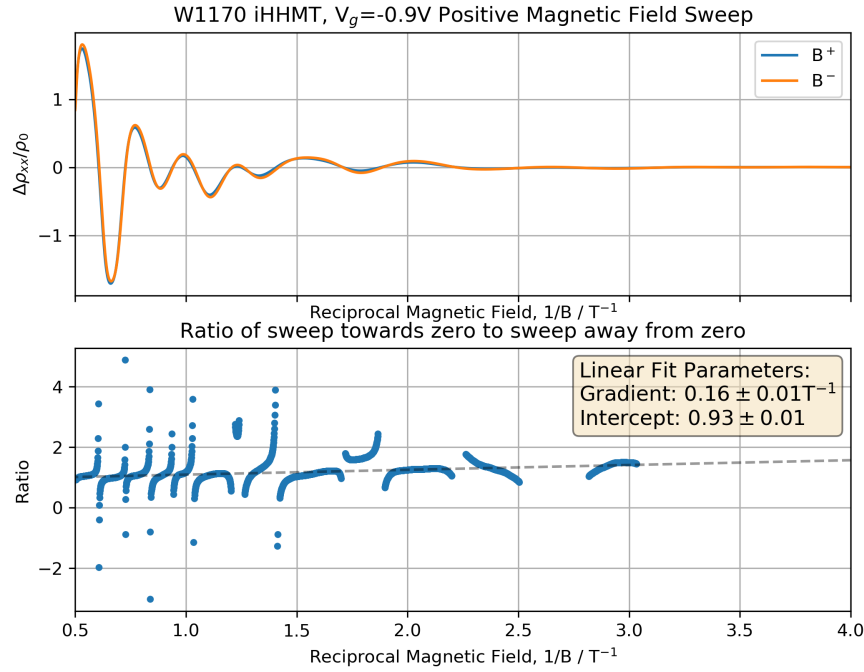


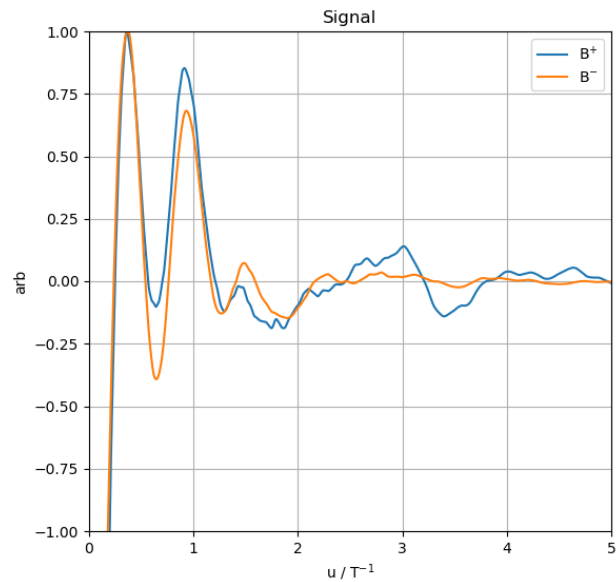
Figure 6.22: Ratio of the sweep towards zero to sweep away from zero expected to be given by $\gamma^- \sinh \gamma^+ x / \gamma^+ \sinh \gamma^- x$ where $\gamma^i = 2\pi^2 k_b T^i m^* / \hbar e$.

6.3 Further Work and Conclusion

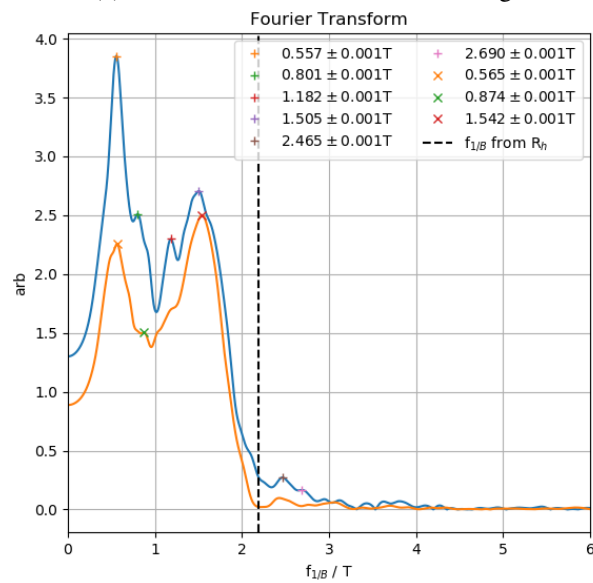
In this chapter, magneto-resistance measurements from Hall bar devices with electron and holes gases in GaAs heterostructures have been presented. Both the electron and hole gases show Shubnikov De Haas oscillations in the longitudinal resistivity, ρ_{xx} . For the electron gas samples, methods of calculating the effective mass from the Shubnikov oscillations were discussed, with an attempt to measure the effective mass from magneto-resistance data over a small temperature range. Averaging all the measurements of the effective mass, the literature value of $0.067m_0$ was calculated, with an error in the second significant figure.

The value of the effective mass for the electron is known, so-called Dingle analysis was performed to calculate the quantum lifetime from the Shubnikov De Haas oscillations in electron gas samples from W1088 and W1091, both of which are 100nm iHEMTs but grown with As_2 and As_4 respectively. The ratio of the transport lifetime and quantum lifetime ranged between ~ 20 to 100 depending on the carrier density, which typical of the range of values reported for GaAs[159, 160, 162–164]. The ratio of the transport lifetime and quantum lifetime is at the higher end of the range reported for heterostructures[159, 163, 164] due to the higher transport lifetime due to these samples' excellent mobilities.

The large value for the transport to quantum lifetimes ratio indicates that small angle



(a) Modified Shubnikov Oscillation Signal



(b) Fourier Transform

Figure 6.23: $\Delta\rho_{xx}/\rho_0$ as a function of $1/B$ from a hole gas in W1170, showing Shubnikov De Haas oscillations for a positive magnetic field sweep from -0.5T to 0.5T.

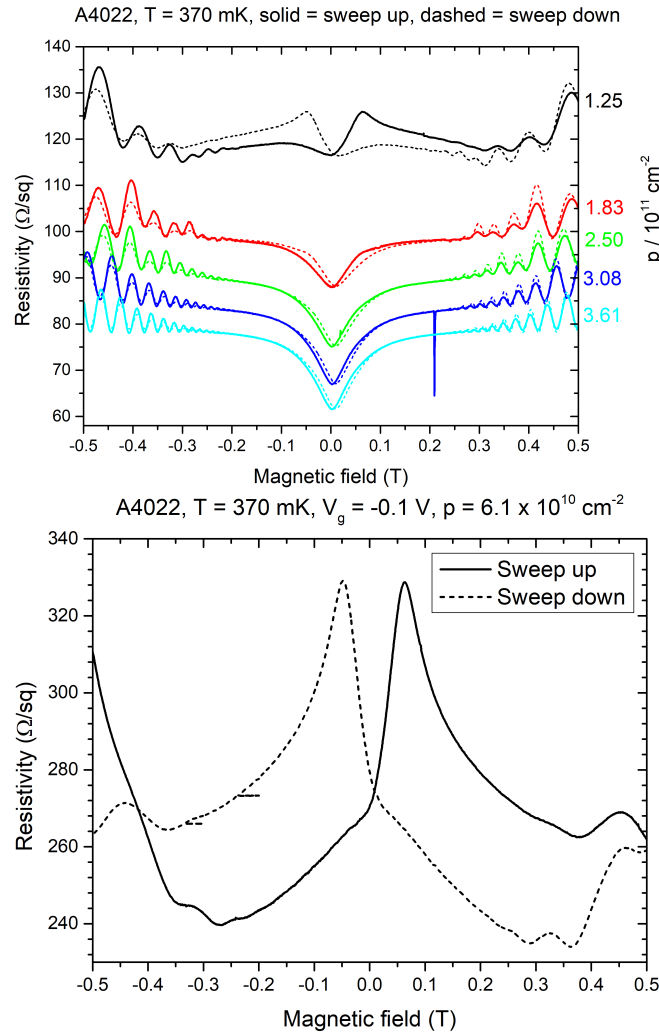


Figure 6.24: Magneto-resistance data, courtesy of J. Waldie, from A4022, a doped hole gas sample in a AlGaAs/GaAs heterostructure. Measurements were taken on a different ^3He system to the samples from W1170 and W1091 and show similar asymmetry in the magneto-resistance.

scattering from long-range interactions, which the transport lifetime is weighted towards, is the dominant type of scattering. The lifetime ratio showed a small temperature dependence between 283 mK and 1370 mK, with the As_2 ratio reducing with temperature but the As_4 increasing by $\sim 40 - 50\%$. This temperature dependence was present in the quantum lifetime only, with the transport lifetime remaining constant as expected. The quantum lifetime of the As_4 sample was $\sim 50 - 60\%$ higher than the As_2 sample at the carrier densities measured. The ratio of the transport lifetime to the quantum lifetime shows a linear dependence on the carrier density, which matches the dependence of the scattering from the interface roughness. The matching dependence suggests that the increase in interface roughness scattering, reduces the

quantum lifetime causing the linear increase in the ratio of transport and quantum lifetimes.

The magneto-resistance in the hole gas samples demonstrated an unexpected asymmetry in ρ_{xx} when crossing $B = 0$. The resistivity would increase or decrease depending on the magnetic field sweep direction, with the amplitude of the asymmetry increasing with the magnetic field sweep rate. The asymmetry disappeared in the quasis-static sweep, confirming that this is not an equilibrium effect. The cause of this asymmetry is unclear, but could not be related to possible heating effects such as magnetic heating of the sample. Similar behaviour has been observed independently in another hole gas sample measured in a different cryostat system.

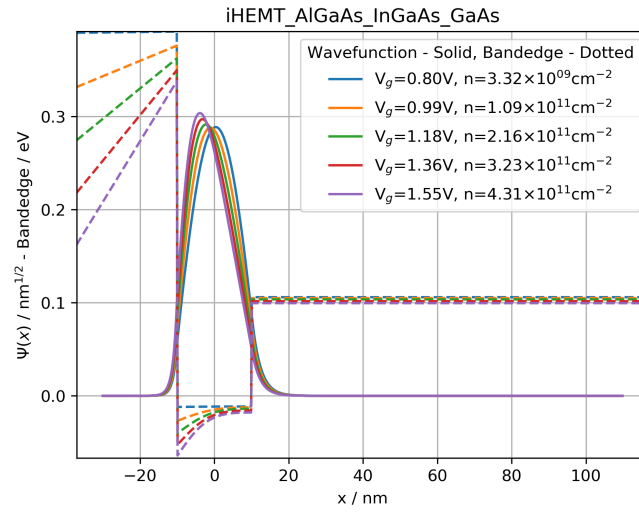
Further work on this anomalous dynamic magneto-resistance may wish to focus on a more complete study of this effect. As the asymmetry is not present in the quasis-static sweep, this suggests a relaxation of the dynamic magneto-resistance. Measuring this relaxation time as a function of carrier density, sweep rate, and temperature may provide more information. The study of an ambipolar device may be of particular interest, as there is no indication of a similar asymmetry in electron gases. One of the key differences between a hole gas and an electron gas is the orbit angular momentum of the holes due to the p-states of the valence band. An ambipolar device would allow the study of both electrons and holes within the same structure which may give insight to the cause of this magneto-resistance asymmetry.

UNDOPED INGaAs QUANTUM WELL

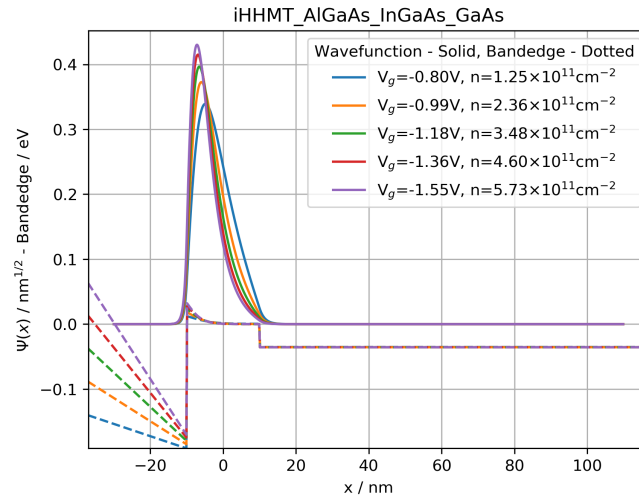
InGaAs is of particular interest due to the enhancement of spin-orbit coupling by the presence of Indium in the structure and the possibility of g-factor engineering through growth of thin layers to modify the effective g-factor. Much of research into the InGaAs material system is based around the $\text{In}_{0.53}\text{Ga}_{0.47}\text{As}$ [165–167] due to the lattice matching with InP, allowing growth on InP substrates. Growth of InGaAs on GaAs substrate is complicated by the lattice mismatching with growth layer of $> 20\%$ In, requiring careful management of the strain in the crystal[168–171]. The study of hole gases in InGaAs to look at spin-orbit effects is further complicated by the difficulty in growing high mobility doped hole gases[172]. In this chapter, measurement of a $\text{In}_{0.1}\text{Ga}_{0.9}\text{As}$ undoped quantum well is presented, with 2D transport measurement showing unexpected difference to holes gases in AlGaAs/GaAs/AlGaAs quantum wells. To understand the difference due to the InGaAs quantum well, ambipolar doubly gated devices were fabricated to allow the study of both electron and holes gases.

7.1 InGaAs Quantum Well

The wafer A4185 contains a 20nm $\text{In}_{0.1}\text{Ga}_{0.9}\text{As}$ quantum well in between a standard 100nm $\text{Al}_{0.33}\text{Ga}_{0.67}\text{As}$ spacer and a 1000nm GaAs buffer. In this way the wafer structure is similar to that of a 100nm undoped heterostructure with a 20nm $\text{In}_{0.1}\text{Ga}_{0.9}$ layer at the AlGaAs/GaAs interface. Work with a doped equivalent of this wafers has been reported[173]. Because of the band offsets, the potential well that forms, figure 7.1 in the InGaAs channel is more symmetric than the potential well in a heterostructure so is more like a quantum well wafer than a



(a) Electrons



(b) Holes

Figure 7.1: Conduction and valence band offset from nextnano for the wafer structure of A4185, showing the formation of a more symmetric potential well in the 20nm $\text{In}_{0.1}\text{Ga}_{0.9}\text{As}$ channel.

heterostructure.

7.2 Double Gated Ambipolar Device

A double-gated ambipolar device was fabricated to look at A4185. This device, previous used for electron-hole bilayer structures[108], has two sets of ohmic metals per contact, AuGeNi for n-type, and AuBe for p-type, and has two separate gates for inducing. The central gate, covering a Mesa etched defined Hall bar, is used to control the carrier density within the bar.

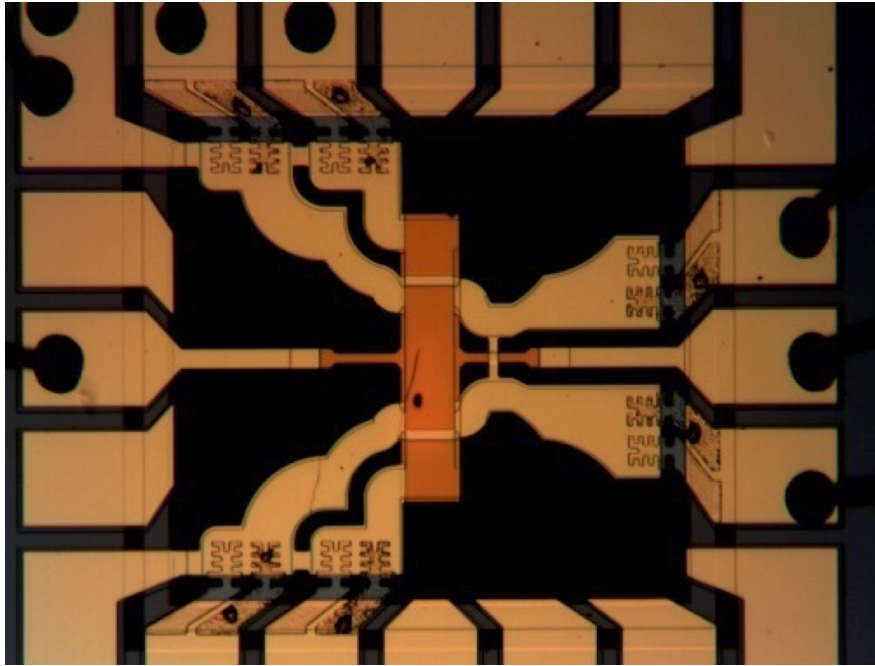


Figure 7.2: Optical image of Ambipolar Hall bar device

This gate is deposited on top of a 60nm Alumina layer so that it is the same distance from the carrier gas as the other induced devices studied. The second, ohmic, gate is deposited over the central gate with a 40nm Alumina layer between the two gates to keep them electrically isolated. This second, ohmic, gate covers the voltage probe arms and the ohmic contacts, setting the carrier density in these regions. The use of the central and ohmic gates together allows the carrier density surrounding the ohmic contact to be set independently of the carrier density in the bar, allowing the contacts to be held at a carrier density that ensures good contact with the carrier gas, while using the central gate to set the density in the Hall bar as low as possible before the carrier gas breaks down into small conducting islands. This allows the lowest possible carrier densities to be studied. An image of the double gated ambipolar device can be seen in figure 7.2.

The individual fabrication steps for this device are the same as those for the unipolar single gated devices, but with additional lithography, thermal evaporation, ALD and etching steps to deposit two sets of ohmic and two top gates.

7.3 Characterisation

As with the GaAs devices, measurement of the carrier density and carrier mobility was performed by measuring the voltage along and across a Hall bar while ramping magnetic field, figure 7.3.

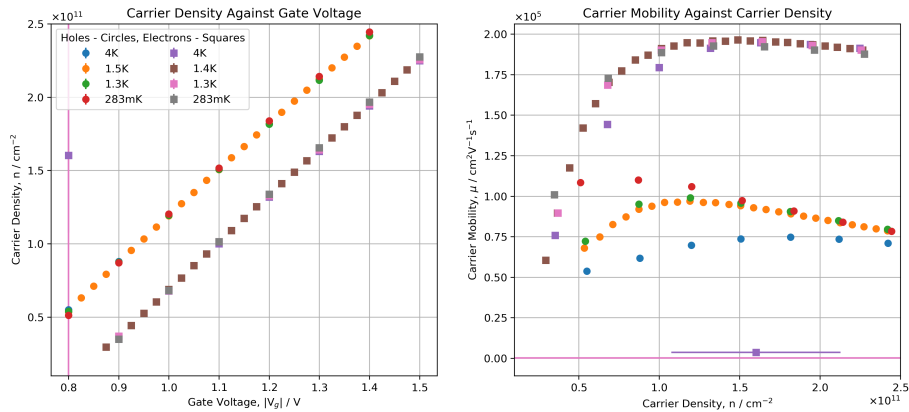


Figure 7.3: Carrier density and carrier mobility for A4185 InGaAs quantum well, determined from the Hall coefficient at 283mK

	Carrier Density / $\times 10^{11} \text{cm}^{-2}$	Carrier Mobility / $\times 10^5 \text{cm}^2 \text{V}^{-1} \text{s}^{-1}$
Electrons	0.3 - 2.3	0.55 - 1.95
Holes	0.5 - 2.45	0.7 - 1.1

Table 7.1: A4185 Carrier Densities and Carrier Mobilities

For a InGaAs quantum well with an equal amount of background dopant scattering and interface roughness as a GaAs quantum well the mobility of the InGaAs quantum well would be lower due to alloy scattering in the InGaAs[174], which is not significant in a GaAs device. Unlike the GaAs heterostructures the mobility of both the electrons and holes in the InGaAs falls for carrier densities greater than $1 \times 10^{11} \text{cm}^{-2}$. While alloy scattering with contribute to this reduction in mobility, interface roughness is also a factor. The characterisation data in figure 7.3 doesn't indicate the relative strength of the alloy scattering compared to interface roughness, however due to the known effect of Indium segregation[175, 176] the interface of the $\text{In}_{0.1}\text{Ga}_{0.9}\text{As}$ channel is likely to be rougher than a GaAs channel is a $\text{Al}_{0.33}\text{Ga}_{0.67}\text{As}/\text{GaAs}$ symmetric quantum well, examples structures are reported in[177, 178].

From figure 7.3 the mobility of the electrons does not change significantly below 1.5K, while the mobility of the holes increases by $\sim 50\%$ at the low carrier density between 1.5K and 283mK. Table 7.1 contains a summary of the range of densities and mobilities.

7.4 Shubnikov De Haas Oscillations

The inclusion of In into a GaAs structure may have an effect on the g^* factor and change the spin-orbit coupling for the holes, as spin-orbit coupling for holes in GaAs results in heavy, light, and split-off holes bands, which are not degenerate in a quantum well due to the confinement

of the carriers. The band structure can be modelled using Kane[179] or Luttinger[180] but the relevant result for understanding the transport in a hole gas is that the mix of states give rise to p-states in the hole bands, with an effective mass that is highest in the x-y plane. This state is therefore bound in the potential well with kinetic energy which rises with $|k|$ rapidly in the x-y plane. Other bands and states can be ignored at low temperatures. Additional effects like the Rashba effect[181, 182] can further split degeneracies resulting in different states being populated in the well. The presence of two quantum populations in a magnetic field causes a beating pattern in the Shubnikov de Haas oscillations as each population has a set of oscillations with a frequency $f_{1/B} = R_k/2R_h$, directly proportional to the carrier density. If the two states have different carrier densities, and therefore frequencies, the measured ρ_{xx} will be the superposition of these two sets of oscillations. Therefore, studying the Shubnikov De Haas oscillations can give information about any effects of the inclusion of In into the GaAs structure. A typical set of oscillations for electrons is shown in figure 7.4.

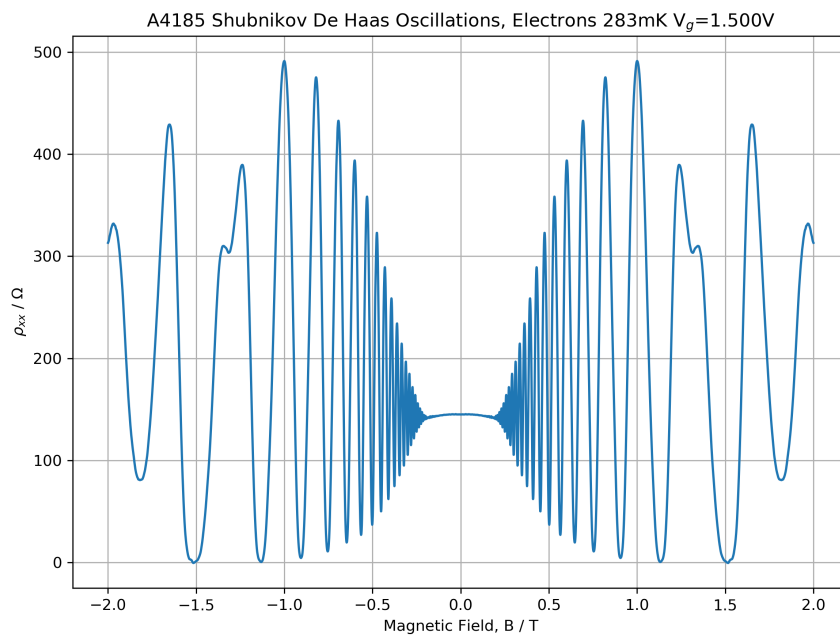


Figure 7.4: Shubnikov De Haas oscillations from electron gas in A4185, with carrier density $n=2.17 \times 10^{11} \text{cm}^{-2}$ and carrier mobility $\mu = 1.98 \times 10^5 \text{cm}^2 \text{V}^{-1} \text{s}^{-1}$.

As with the GaAs devices, the oscillations were converted to a function of $1/B$, figure 7.5, and the power spectrum calculated using the fast Fourier transform (FFT). The power spectrum shows only a single frequency, with a small amount of the 2nd harmonic and a large DC component. The frequency matches the expected frequency from the Hall slope.

Calculation of $\Delta\rho_{xx} = \rho_{xx} - \rho_0$ was performed using a digital band pass filter centred on the expected frequency from the Hall slope, $f_{1/B}$ with a bandwidth of 50% as indicated in

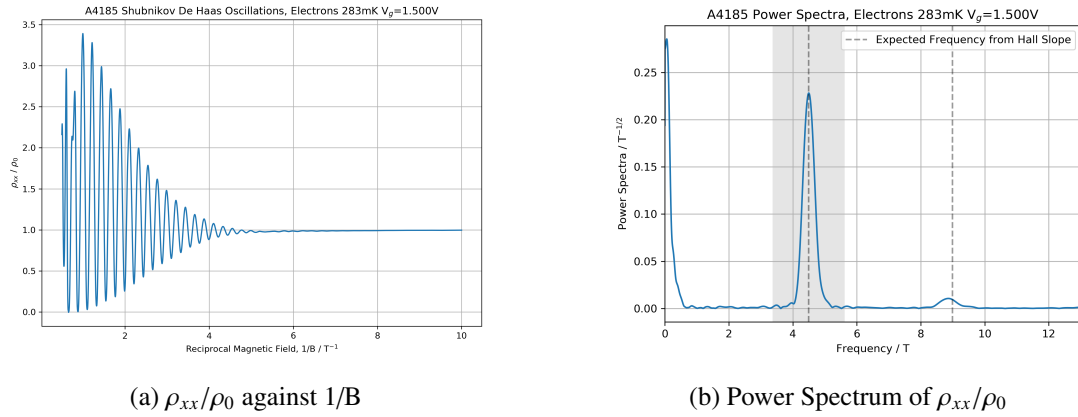


Figure 7.5: ρ_{xx}/ρ_0 as a function of $1/B$ for electrons in A4185 at 283mK with power spectrum calculated from FFT showing only the expected frequency. The shaded area in 7.5b indicates the bandpass filter domain used to remove the background from the signal.

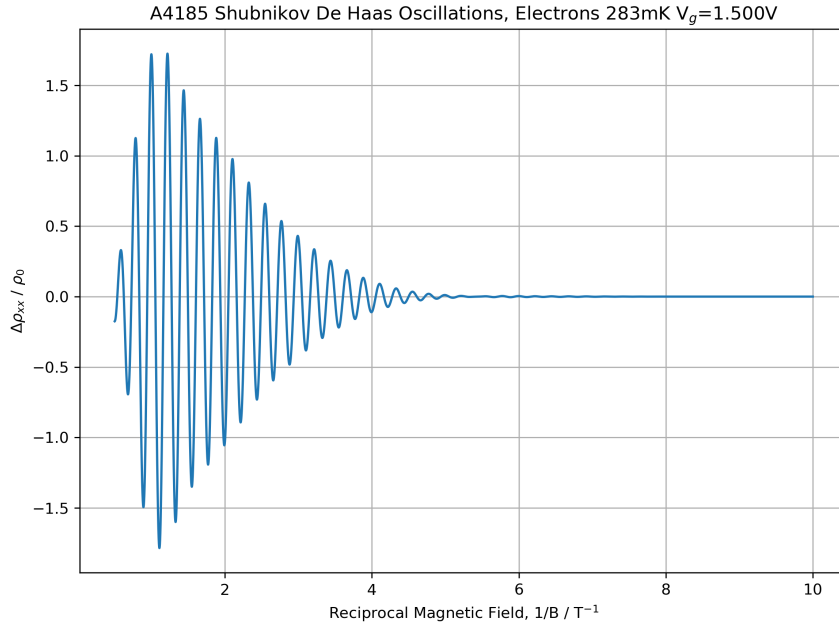


Figure 7.6: $\Delta\rho_{xx}/\rho_0$ as a function of $1/B$ for electrons in A4185 at 283mK. The background in ρ_{xx} was removed using a digital bandpass filter centred on the expected frequency $f_{1/B} = R_k/2R_h$ calculated from the Hall slope with a 50% bandwidth.

figure 7.5b. An example of $\Delta\rho_{xx}/\rho_0$ as a function of $1/B$ is shown in figure 7.6.

7.4.1 Dingle Analysis for Electrons

Figure 7.6 shows a typical set of Shubnikov De Haas oscillations for electrons in the InGaAs quantum well. The oscillations depend on two unknown parameters: the quantum lifetime τ_q

and the effective mass, m^* . The oscillations are expected to have the form:

$$\frac{\Delta\rho_{xx}}{\rho_0} = 4 \exp\left[\frac{-\pi m^*}{e\tau_q B}\right] \frac{X(1)}{\text{Sinh}(X(1))} \cos\left(\pi\left[\frac{R_k}{R_h B} - 1\right]\right) \quad (7.1)$$

where $X = 2\pi^2 k_b T m^* / \hbar e B$. If the effective mass is known then the quantum lifetime can be determined from a Dingle plot. The ratio of the transport lifetime, determined from the mobility μ , and the quantum lifetime holds information about the dominant scattering mechanism present. If the ratio is small, then small angle scattering from long range scattering potentials dominates.

To generate a Dingle plot, the effective mass is required. For the InGaAs quantum well with 10% In content, we expect the effective mass to be similar to the GaAs effective mass of $0.067m_e$ based on reported values for InGaAs at 300 K [183]. Several different methods were used to determine the effective mass in the InGaAs quantum well, detailed in the following section.

7.4.1.1 Determining Effective Mass from Transport Measurements

As with the GaAs transport devices, the effective mass is typically determined from the temperature dependence of the amplitude of the Shubnikov de Haas oscillations, given by:

$$\frac{\Delta\rho_{xx}(T_0, B)}{\Delta\rho_{xx}(T_1, B)} = \frac{T_0 \text{Sinh}(\alpha T_1 m^* / B)}{T_1 \text{Sinh}(\alpha T_0 m^* / B)} \quad (7.2)$$

where the constant $\alpha = 2\pi^2 k_b m_e / \hbar e \sim 14.693 \dots$. The peaks in $\Delta\rho_{xx}/\rho_0$ were found using a standard peak-finding function from the scipy signal processing library, using the height of the oscillations in the semi-classic region where $1/B > 8T^{-1}$ as a threshold for noise in the signal, and using the peak frequency in the Fourier transform to determine the period of the oscillation to match peaks at the same filling factor.

For the InGaAs quantum well, the temperature dependence was measured for six gate voltages from 283mK up to 500mK. Based on the temperature dependence, figure 7.7, of the oscillations, which is weaker than the GaAs heterostructure, the effective mass is expected to be lighter than the electron mass from GaAs.

The average value of the effective mass for electrons is $0.042 \pm 0.009m_e$, which is significantly lighter ($\sim 59\%$) than the GaAs electron, but the uncertainty in this value is an order of magnitude larger than the uncertainty in the GaAs electron mass due to the spread in values from different gate voltages. For a 95% confidence interval the effective mass, is bound between $0.016-0.074m_0$ corresponding to between 110% and 23% of the electron mass in GaAs.

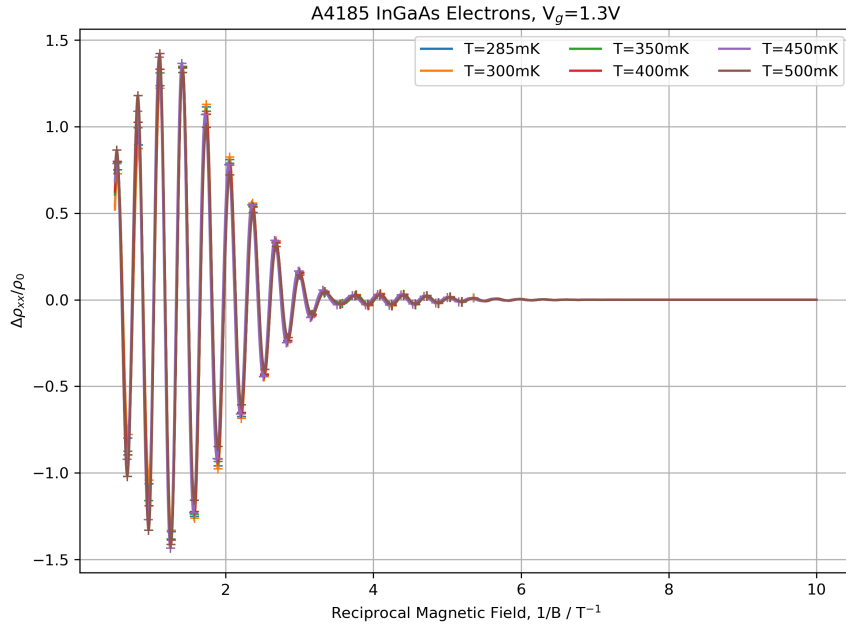


Figure 7.7: Temperature Dependence of Shubnikov De Haas oscillations for an electron gas in an InGaAs quantum well.

Gate Voltage / V	m^*/m_e	$\Delta m^*/m_e$
1.0	0.066	0.007
1.1	0.031	0.009
1.2	0.042	0.005
1.3	0.047	0.004
1.4	0.037	0.006
1.5	0.043	0.007

Table 7.2: Effective mass values for electrons in an InGaAs quantum well determined from likelihood curves in figure 7.8.

7.4.1.2 Possible Improvements for Effective Mass Measurement in InGaAs

Measurement of the effective mass in InGaAs is limited by the small temperature dependence of the Shubnikov de Haas oscillations between 283mK and 500mK; while it is possible to go to higher temperatures and still have large enough oscillations to measure for the electron, this is not possible for the holes. Also, completing a set of magnetic field sweeps over a range of temperatures takes a significant amount of time, so a method of determining the effective mass from a single temperature magnetic field sweep would be beneficial.

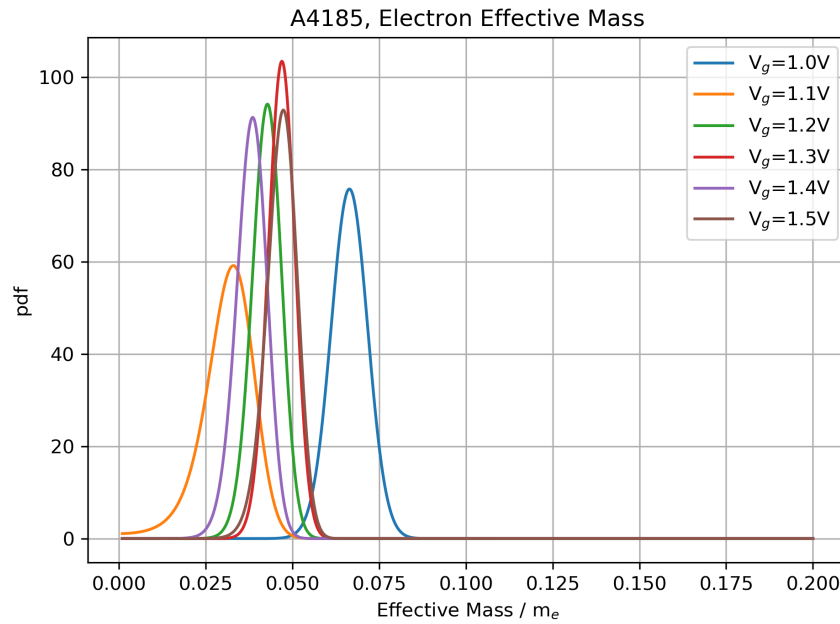


Figure 7.8: Likelihood curves of the effective mass of electron in an InGaAs quantum well, with a mean value of $0.042 \pm 0.009m_e$. Table 7.2 contains a summary of the values for all gate voltages.

7.4.1.3 Effective Mass Calculated by nextnano Using $k \cdot p$

In order to proceed with Dingle analysis to determine the quantum lifetime from the Shubnikov de Haas oscillations, the effective masses for electrons and holes were calculated from the band structure calculated with nextnano using a 6-band $k \cdot p$ theory for the valence band. The calculated band structure along the [001] direction from nextnano is in figure 7.9. At the gamma point, the effective masses for the electrons is $0.062m_0$.

7.4.1.4 Quantum Lifetime

The quantum lifetime is a measurement of the rate of scattering of the carrier in the 2D electron system. Unlike the transport lifetime, which is weighted towards wide-angle scattering, the quantum lifetime is a measurement of all scattering rates.

If the effective mass and temperature are known, then the temperature damping factor can be calculated. This allows for a Dingle plot to be made which is expected to have the functional form,

$$\ln \left| \frac{\Delta\rho_{xx}}{\rho_0\chi(T, B)} \right| = \ln(4) - \frac{\pi m^*}{e\tau_q} \frac{1}{B} \quad (7.3)$$

therefore a plot of $\ln|\Delta\rho_{xx}/\rho_0\chi(T, B)|$ against $1/B$ for the peaks in the Shubnikov De Haas oscillations should be a linear plot where the quantum lifetime can be determined from the

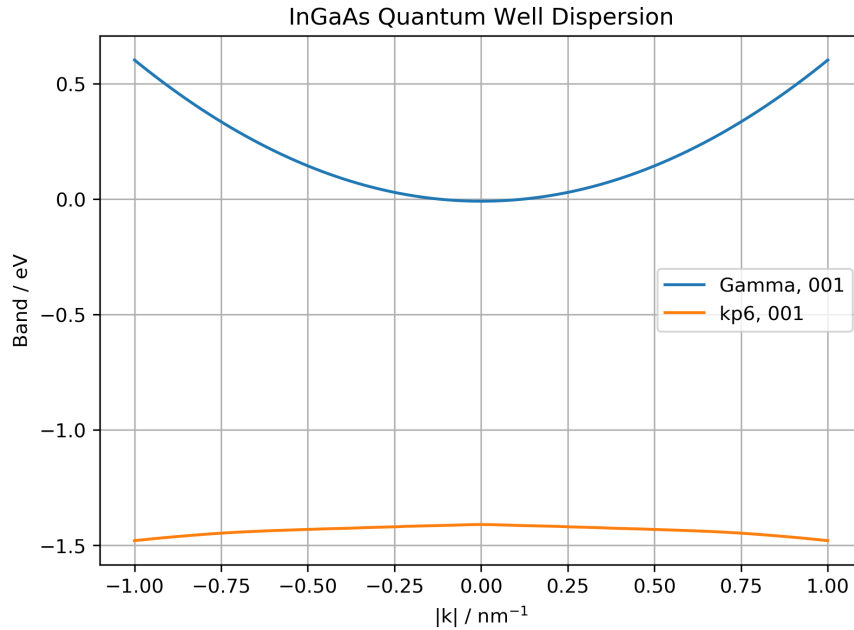
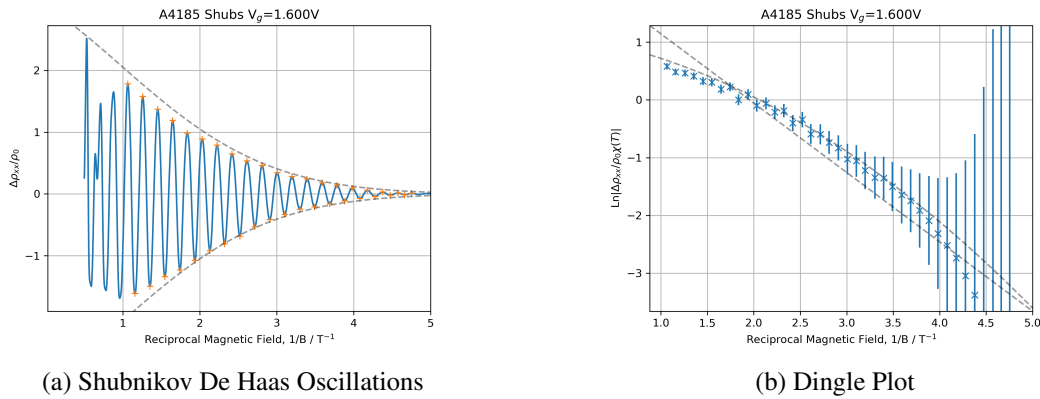


Figure 7.9: Dispersion along the [001] for for 20nm InGaAs quantum well



(a) Shubnikov De Haas Oscillations

(b) Dingle Plot

Figure 7.10: Shubnikov De Haas oscillation and Dingle plot for an electron gas in an InGaAs quantum well. A linear and quadratic fit of the Dingle data has been plotted in figure 7.10b, the quadratic fit has been used to plot the envelope functions in figure 7.10a.

gradient of the straight line.

The Dingle plot for the electron gas in A4185, figure 7.10, very clearly does not have a linear trend. Two potential explanations for this non-linear dependence are, firstly, that the effective mass value used here of $0.062m_e$ is not the correct value and the error introduced in the temperature damping factor $\chi(T, B)$, results in the non-linear dependence seen in figure 7.10. However, varying the value of the effective mass used between the InAs value of $0.023m_e$ and the GaAs value of $0.067m_e$ did not remove the non-linearity. The second explanation depends

on an inhomogeneity in the carrier density of the electron gas. From (6.3) the carrier density sets the frequency of the Shubnikov de Haas oscillations. If there is inhomogeneity in the carrier density, then the resulting measured oscillations would be the superposition of all the oscillations at different frequencies given by (7.1). Assuming that this inhomogeneity is small, such that the quantum lifetime does not change significantly, (7.1) can be modified to give,

$$\frac{\Delta\rho_{xx}}{\rho_0} = -4 \exp[-\alpha/B] \int dn P(n) \cos [2\pi f_{1/B}(n)/B] \quad (7.4)$$

where $\alpha \equiv \pi m^*/e\tau_q$, $f_{1/B}(n) \equiv R_k/2R_h$ and $P(n)$ describes the distribution of the carrier densities. Assuming that the carrier density distribution can be described by a normal distribution [184–186] centred on n_0 and with a standard deviation of Δn describing the homogeneity in the carrier gas and computing the integral in (7.4), the new expression for the Shubnikov De Haas oscillations is,

$$\frac{\Delta\rho_{xx}}{\rho_0} = -4 \frac{\exp[-\alpha/B - (\beta/B)^2/2]}{\sqrt{2\pi}\beta} \cos [2\pi f_{1/B}(n_0)/B] \quad (7.5)$$

where $\beta \equiv 2\pi f_{1/B}(n_0)\Delta n/n_0$ [152, 184, 185]. This relationship shows that a small inhomogeneity in the carrier density changes the Dingle plot from a linear relation to a quadratic relation given by,

$$\ln \left| \frac{\Delta\rho_{xx}}{\rho_0 \chi(T, B)} \right| = \ln \left(\frac{4}{(2\pi)^{3/2} f_{1/B}(n_0) \Delta n / n_0} \right) - \frac{\pi m^*}{e\tau_q} \frac{1}{B} - \frac{1}{2} \left(\frac{2\pi f_{1/B}(n_0) \Delta n}{n_0 B} \right)^2 \quad (7.6)$$

From figure 7.10 the quadratic fit clearly describes the Dingle plot better than the linear fit. The values for the quantum lifetime and carrier inhomogeneity are shown in figure 7.11; the quantum lifetime from the quadratic fit is growing with carrier density. This would be consistent with the increasing screening at higher densities reducing the scattering. The carrier inhomogeneity from the Dingle plot is small ($< 5\%$) as required by the assumptions in the expression (7.6). The inhomogeneity reduces with carrier density as expected, as at the lowest carrier densities the carrier gas is less able to screen charges and changes in the background potential, which in turn cause variation in the carrier density.

7.4.2 Spin Splitting in InGaAs

For a sufficiently high magnetic field, the spin splitting of the Landau levels becomes larger than the thermal energy, allowing odd filling factor minima to be resolved, figure 7.12. At a low field the spin splitting of the Landau levels is smaller than the thermal broadening around the Fermi level, causing suppression of the odd minima.

The electrons in InGaAs show the typical behaviour, with even minima present at a low magnetic field and odd minima appearing at a sufficiently high magnetic field. For $\pm 2T$, sweeps

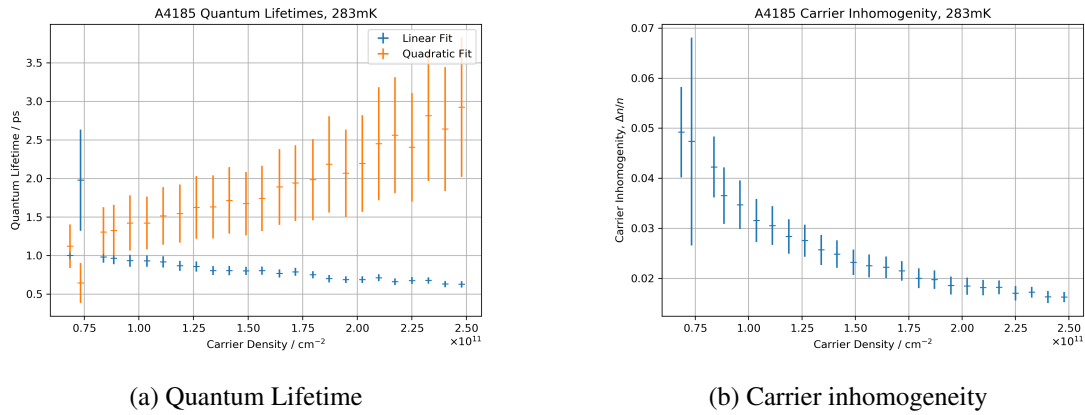


Figure 7.11: Quantum Lifetimes as a function of carrier density for an electron gas in an InGaAs quantum well at 283mK, calculated from a linear and quadratic fit of the Dingle plot, figure 7.10. The quadratic fit gives a value for the inhomogeneity in the electron gas shown in figure 7.11b.

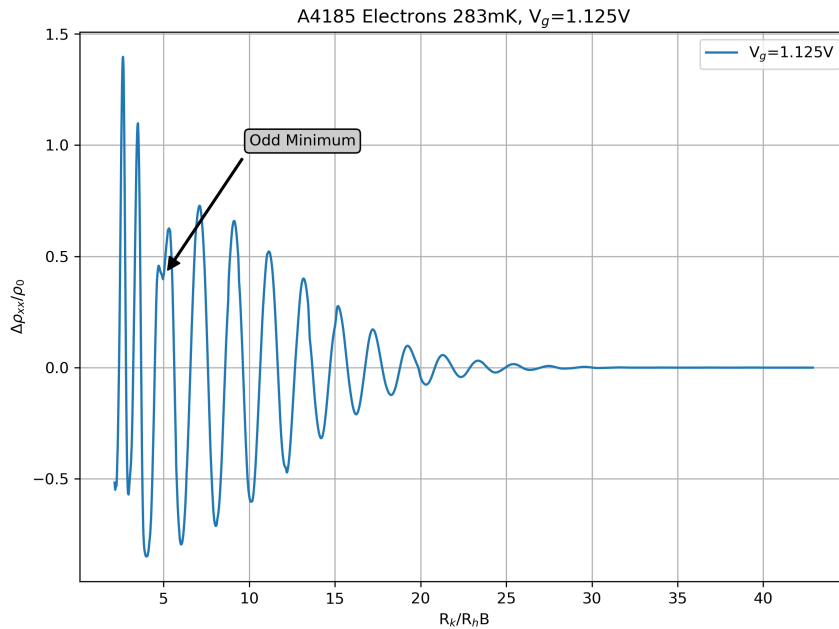


Figure 7.12: Shubnikov De Haas oscillation, $\Delta\rho_{xx}/\rho_0$ for electrons in an InGaAs quantum well, showing the appearance of odd filling factors 3 and 5 at high magnetic field.

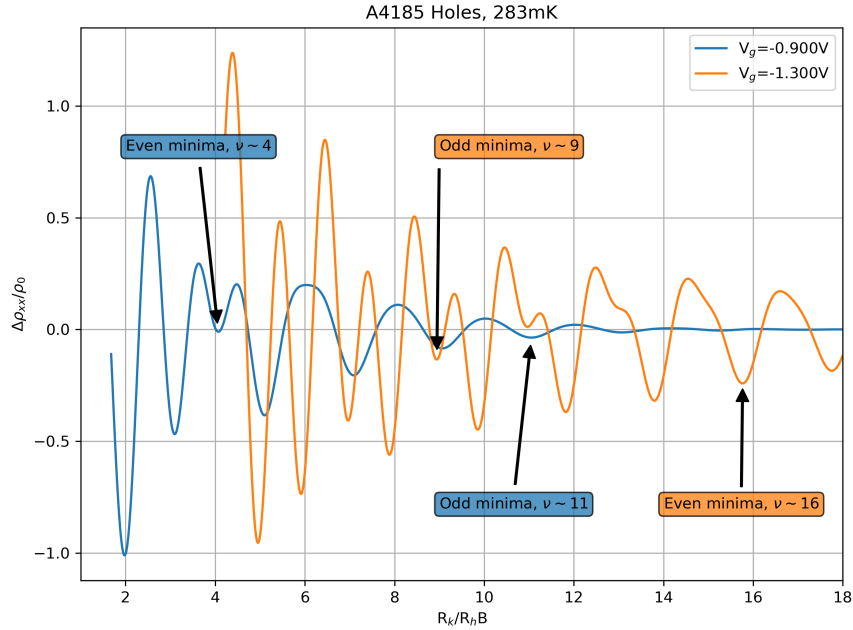


Figure 7.13: Shubnikov De Haas oscillation, $\Delta\rho_{xx}/\rho_0$ for holes in an InGaAs quantum well at 283mK. At low carrier densities the holes show suppressed even minima at high magnetic field and odd minima at low magnetic field.

the odd minima are most easily observed at the lower carrier densities as the field required for a particular filling factor scales with carrier density.

The holes in InGaAs show the opposite behaviour at low carrier density, figure 7.13, with even minima appearing at a high magnetic field and only odd minima observable at a low magnetic field. To examine this effect as a function of carrier density, figure 7.14 contains a plot of the depth of the minima in the Shubnikov De Haas oscillation for filling factors 9 and 10, which were the lowest filling factors present at most of the carrier densities measured. The turning point between odd minima being suppressed is shown in figure 7.14 by the crossing point of filling factors 9 and 10 at $n \sim 1.4 \times 10^{11} \text{cm}^{-2}$.

The usual energy structure, as shown in figure 7.15, has the Landau levels spaced by $\hbar\omega_c$ and the spin splitting of $g^*\mu_B B/2$. As in the case of electrons for high magnetic fields the spin splitting $g^*\mu_B B/2 \gtrsim k_b T$, therefore the Fermi level is in-between the spin split levels, leaving an odd number of energy levels populated with no states close enough to the Fermi level for scattering to occur. As the magnetic field decreases in strength, the spin splitting becomes smaller. At $g^*\mu_B B/2 \sim k_b T$, when the Fermi level is in between the spin split levels, there will be a small number of states populated due to the tail of the Fermi distribution. This results in scattering between states at the Fermi level, suppressing the odd minima. As the magnetic field continues to get weaker when $g^*\mu_B B/2 \lesssim k_b T$ the Fermi level can never lie in between the spin

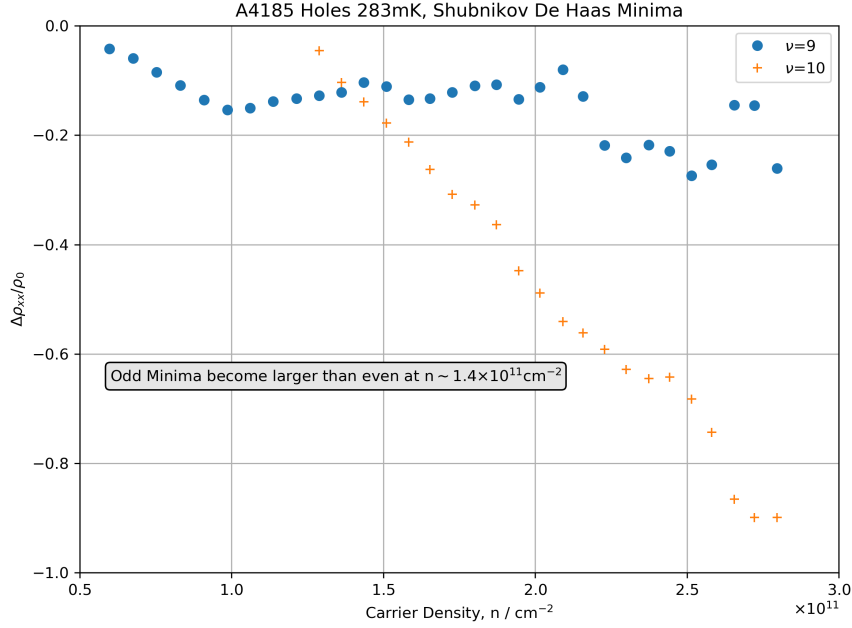


Figure 7.14: Height of Shubnikov De Haas oscillation, $\Delta\rho_{xx}/\rho_0$, for filling factors 9 and 10 for holes in an InGaAs quantum well at 283mK. At $n \sim 1.4 \times 10^{11} \text{ cm}^{-2}$, the filling factor 9 minima become larger than the filling factor 10 minima.

split levels without both the spin split levels being populated resulting, in the odd minima being completely suppressed. Similar suppression of the even minima has been reported in p-type Ge[187–190].

The size of the spin splitting depends on the value of g^* : if the size of g^* increases, it is possible for the lower energy level from the spin split Landau level at $E_{\nu+1}^{\downarrow} = \hbar\omega_c(\nu + 3/2) - g^*\mu_B B/2$ to be closer to the higher energy level from the Landau level at $E_{\nu}^{\uparrow} = \hbar\omega_c(\nu + 1/2) + g^*\mu_B B/2$ than the higher spin split level $E_{\nu+1}^{\downarrow} = \hbar\omega_c(\nu + 3/2) - g^*\mu_B B/2$. A simple rearrangement shows that this corresponds to $g^* > \hbar\omega_c/2m_b = m_e/2m^*$. As shown in figure 7.15, if g^* is large enough to cause the crossing of the E_{n+1}^{\downarrow} and E_n^{\uparrow} energy levels, when an even number of levels are filled the two levels are close together and when an odd number are filled the levels are far apart. This reordering of the energy levels would cause the Shubnikov odd and even minima to swap in character, with even minima being suppressed at low magnetic field.

One potential explanation for g^* increasing as a function of carrier densities is exchange enhancement[191, 192]. A simple model for this effect is,

$$g^*\mu_B B = g\mu_B B + E_{ex} \sum_{N'} (n_{N'}^{\uparrow} - n_{N'}^{\downarrow}) \quad (7.7)$$

where E_{ex} is the exchange energy parameter and $n_{N'}^{\uparrow}$ and $n_{N'}^{\downarrow}$ are the carrier densities of the spin levels. From this model it's possible for $m^*g^* > 2$ to increase if E_{ex} is large enough. This

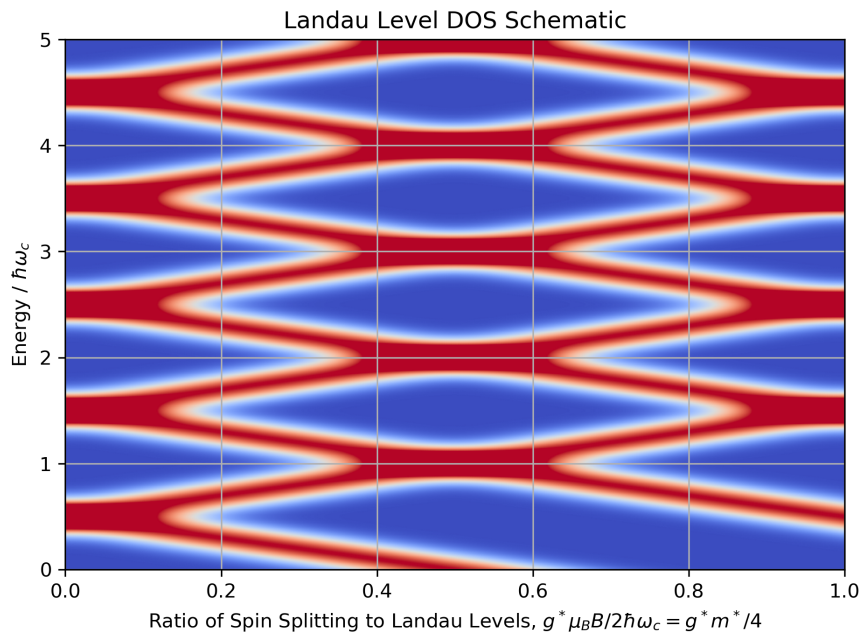


Figure 7.15: Schematic of the density of states of the Landau levels as the strength of the spin splitting increases along the x-axis.

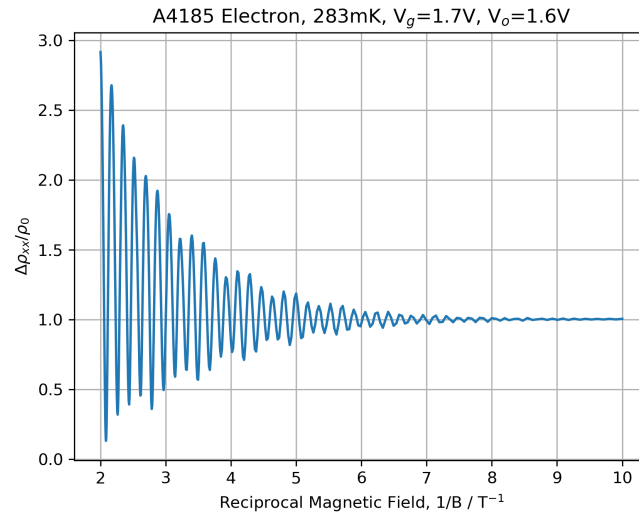
would be consistent with the data from A4184 which saw the reordering of the minima at lower carrier densities $n \lesssim 1.4 \times 10^{11} \text{cm}^{-2}$, where exchange effects which scale as $1/\sqrt{n}$ are larger.

7.4.3 Bridging Gates Population Mixing

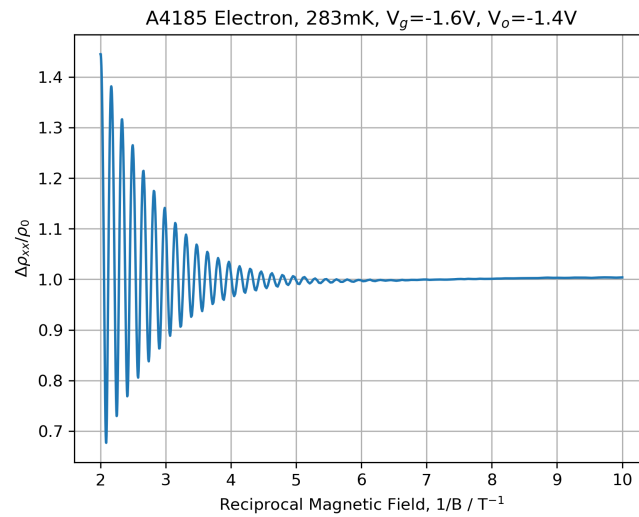
When looking at the low field Shubnikov de Haas oscillation sweeping slowly ($< 5 \text{Th}^{-1}$) to maximise the visibility of the oscillations, a beating pattern can be seen in both the electron and hole gases, figure 7.16. A beating pattern in Shubnikov De Haas oscillation suggests more than one quantum population is present [193, 194]. Looking at the Fourier spectra of the oscillations, two frequencies can be seen, figure 7.17. The first is at the expected frequency given the carrier population calculated from the Hall coefficient. The presence of a second population in the electrons rules spin-orbit coupling out as an explanation. In figure 7.18, the spectra for the electrons and holes are mapped with the central gate varying, changing the carrier density in the Hall bar.

In the spectral maps, the frequency of one of the populations varies linearly with the central gate voltage, matching the expected dependence based on the Hall coefficient. The second frequency remains fixed and independent of the central gate voltage, showing that this second population is independent of the central gate.

Within this device, there are two populations of carriers, one in the Hall bar control by the central gate, and one in the ohmic contacts and voltage probes arms, controlled by the



(a) Electrons



(b) Holes

Figure 7.16: Shubnikov De Haas oscillations in electron and holes gases at 283mK showing a beating pattern

ohmic gate. The ohmic gate sets the carrier density high enough that the contact resistance is low, giving a good signal. During measurement, the ohmic gate voltage is kept constant as the voltage probe arms and ohmic contact should not effect the four-terminal measurement. However, the presence of a second quantum population that is independent of the central gate in both the electron and hole gases is suggestive of the carrier population in the voltage probe arms being the source of this second frequency.

To test this, the second set of spectral maps were made, this time-varying the ohmic gate voltage with a fixed central gate voltage set to the highest voltages used to give the highest

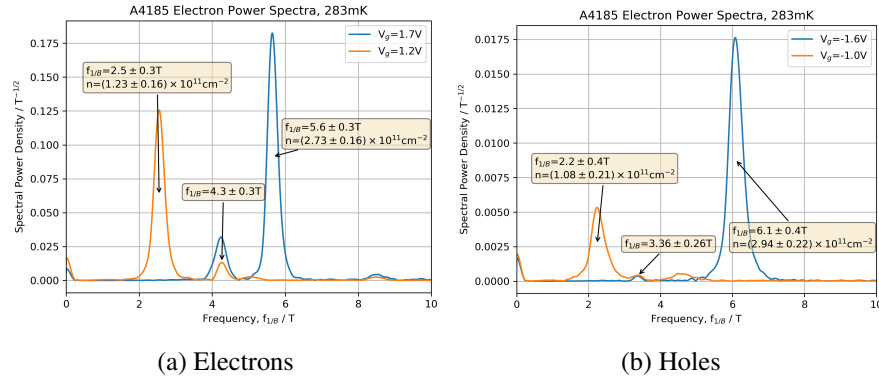


Figure 7.17: Power Spectra for electrons and holes at 283mK showing a common additional frequency, indicating the presence of a second quantum population in the InGaAs quantum well.

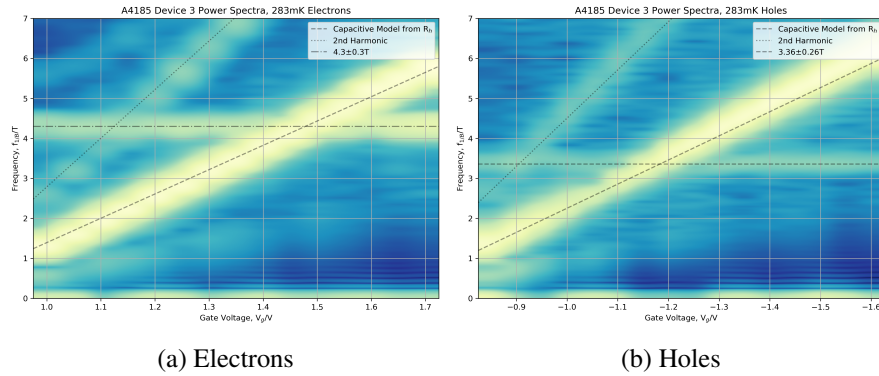


Figure 7.18: Spectral map of frequency against central gate voltage for electron and hole gases in A4185. The strongest peaks correspond to the carrier density in the capacitive model, determined from the hall coefficient and the second harmonic of the strongest peak can also be seen. There is a weak secondary peak for both the electrons and holes at $4.3 \pm 0.3T$ and $3.36 \pm 0.26T$ respectively.

frequency oscillations. As can be seen from figure 7.19, the second population frequency is linearly dependent on the ohmic gate voltage, as expected from the capacitive model, for both the holes and electrons, but the second population frequency is much weaker in the hole gas.

For the A4185 device the central gate is 60nm above the surface of the GaAs wafer, while the bridging gates are an additional 40nm above the central gate, giving 100nm total. From the linear dependence of the second population frequency in figure 7.19 and the capacitive model,

$$\frac{\epsilon_0}{e} \frac{\partial V}{\partial n} = \sum_i \frac{d_i}{\epsilon_r^i} \quad (7.8)$$

if the frequency has the expected dependence on carrier density, $f_{1/B} = R_k n e / 2$, the dielectric constant of the alumina dielectric is $\epsilon_r = 8.1 \pm 0.4$. From the linear dependence of the carrier density on the central gate voltage, the dielectric constant of the alumina is $\epsilon_r = 7.167 \pm 0.004$.

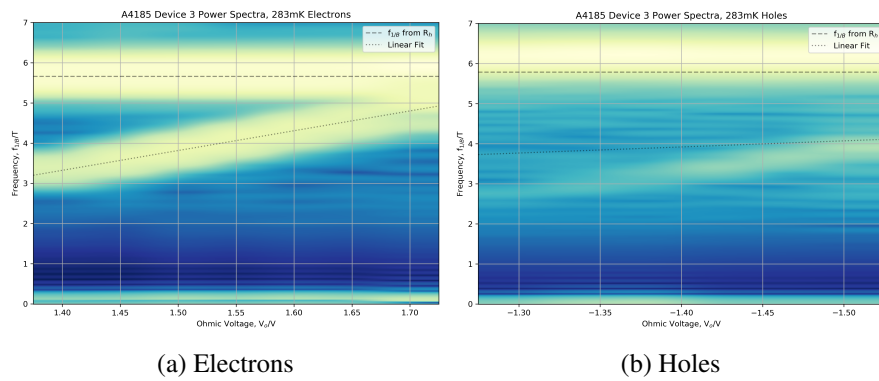


Figure 7.19: Spectral map of frequency against ohmic gate voltage for electron and hole gases in A4185. The strongest peaks correspond to the carrier density in the capacitive model, determined from the hall coefficient. There is a weak secondary peak for both the electrons and holes which varies linearly with the ohmic gate voltage.

Comparing the two values of the dielectric, there is a rough agreement with a p-value $p = 0.133$, showing that it is plausible that this second population is from the voltage probes. To understand how the population in the voltage probes could affect the four-terminal measurement of the Hall bar, nextnano[64] was used to simulate the current flow in the hall bar with a different carrier density in the voltage probes. The output from nextnano shown in figure 7.20

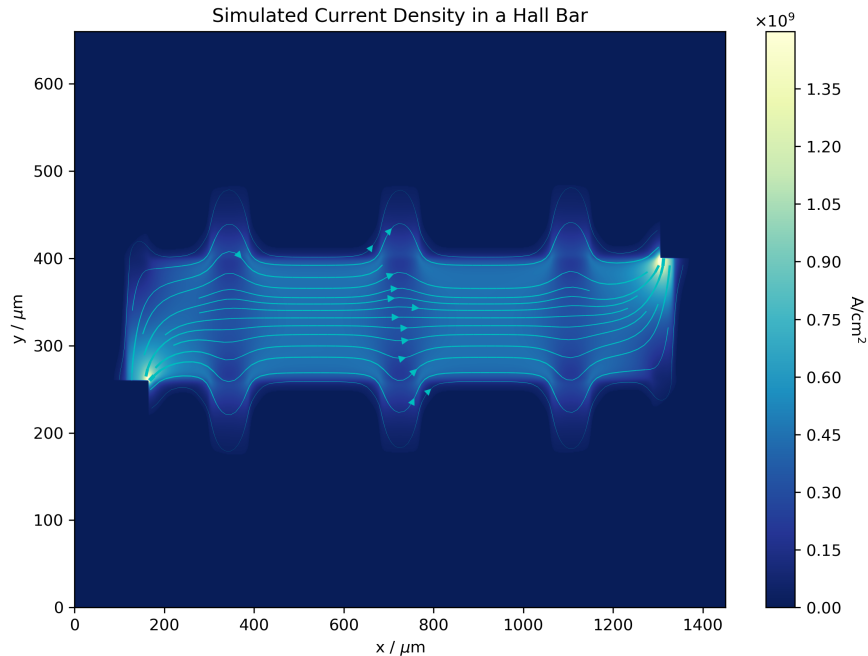


Figure 7.20: Current density map from nextnano simulation of Hall bar geometry with a carrier density in the voltage probes twice as high as the carrier density in the bar region. Current map shows that some current is present in the ohmic arms.

shows that there is some current flow in the voltage probe arms. As there is no net current flow in the voltage probe arms, the four-terminal measurement still gives valid measurements of V_{xx} and V_{xy} but looking at the region closest to the voltage probe it is clear that there is some mixing between the Hall bar carriers and the voltage probe carriers.

Based on the results of the next nano simulation and the approximate agreement between the dielectric constants, the second quantum population that causes the observed beating in the Shubnikov De Haas oscillations is, in all likelihood, a result of some mixing between the voltage probe and the Hall bar carrier populations.

This trend is consistent with the second peak being the voltage probe carriers, as when the carrier density in the hall bar is lower than the carrier density in the voltage probes the carrier will have a lower Fermi velocity so will not travel through as much of the voltage probe region. At higher gate voltages the opposite will be true, resulting in carrier travelling through a larger region of the voltage probe region, causing stronger oscillations.

7.5 Weak Localisation

Within the Drude model the equation of motion for charge is,

$$\frac{d\mathbf{p}}{dt} = q\left(\mathbf{E} + \frac{\mathbf{p} \times \mathbf{B}}{m^*}\right) - \frac{\mathbf{p}}{\tau} \quad (7.9)$$

solving this equation in the steady state with $\mathbf{B} = (0, 0, B)$, and recognising that the charge density $\mathbf{j} = nq\mathbf{p}/m^*$ gives the equation,

$$\mathbf{j} = \frac{qn\mu}{1 + (\mu B)^2} \begin{pmatrix} 1 & -\mu B \\ \mu B & 1 \end{pmatrix} \mathbf{E} \quad (7.10)$$

from which we recognise the conductivity matrix,

$$\boldsymbol{\sigma} = \frac{\sigma_0}{1 + (\mu B)^2} \begin{pmatrix} 1 & -\mu B \\ \mu B & 1 \end{pmatrix} \quad (7.11)$$

Weak localisation [195] adds a quantum correction, $\delta\sigma$, to the diagonal components of the conductivity matrix. With this quantum correction given by the expression[165, 196],

$$\delta\sigma(B) = -\frac{1}{R_k\pi} \left[\psi\left(\frac{1}{2} + \frac{B_\phi}{B}\right) - \psi\left(\frac{1}{2} + \frac{B_0}{B}\right) \right] \quad (7.12)$$

with the condition that $B_0 \gg B_\phi$.

Experimentally the resistivity, ρ , is more easily determined. Inverting the conductivity matrix gives the components of ρ as,

$$\begin{aligned}\rho_{xx} &= \frac{\sigma_{xx}}{\sigma_{xx}^2 + \sigma_{xy}^2} = \frac{1 + \frac{\delta\sigma}{\sigma_0}(1 + \mu^2 B^2)}{\sigma_0 \left(1 + \frac{2\delta\sigma}{\sigma_0}\right) \left(1 + \frac{\delta\sigma}{2\sigma_0}[1 + \mu^2 B^2]\right)} \\ \rho_{xy} &= \frac{\sigma_{xy}}{\sigma_{xx}^2 + \sigma_{xy}^2} = \frac{-R_h B}{\left(1 + \frac{2\delta\sigma}{\sigma_0}\right) \left(1 + \frac{\delta\sigma}{2\sigma_0}[1 + \mu^2 B^2]\right)}\end{aligned}\quad (7.13)$$

Hence the ratio of ρ_{xx} and ρ_{xy} gives an expression for $\delta\sigma$ of,

$$\delta\sigma(B) = \frac{\sigma_0}{1 + \mu^2 B^2} \left(\mu B \frac{\rho_{xx}}{\rho_{xy}} - 1 \right) \quad (7.14)$$

given the values of R_h , μ , $\sigma_0 = \mu/R_h$.

In the limit of $B \gg B_0 \gg B_\phi$, the quantum correction $\delta\sigma(B) \rightarrow 0$, therefore the expression for the components of ρ become,

$$\begin{aligned}\rho_{xx}(B \gg B_0) &= \frac{1}{\sigma_0} = \frac{R_h}{\mu} \\ \rho_{xy}(B \gg B_0) &= R_h B\end{aligned}\quad (7.15)$$

therefore the required values of μ and R_h can be obtained from the region of ρ_{xx} and ρ_{xy} where the gradient of ρ_{xy} is constant (R_h). In practice, this region was determined from the value of $\rho_{xy}/\rho_{xx}B$, as this value has the form,

$$\frac{\rho_{xy}}{\rho_{xx}B} = \mu - R_h \delta\sigma [1 + (\mu B)^2] \quad (7.16)$$

The derivative with respect to field (B) will be zero in the region where $\delta\sigma = 0$, this allows the values of R_h and σ_0 to be calculated from the values of ρ_{xx} and ρ_{xy} as above and the value of μ from a linear fit of ρ_{xy}/ρ_{xx} in this region.

7.5.1 Weak Localisation in a 2D Hole Gas

Figure 7.21 shows the quantum correction calculated from ρ_{xx} and ρ_{xy} for a hole gas in A4185. In order to extract the parameters B_0 and B_ϕ from this dataset, the function $\Delta\sigma(B)\pi R_k$ was fitted as a function of B . As the quantum correction is symmetric in field, only positive field values were used in the fitting.

The expected form for the quantum correction [165] is,

$$\Delta\sigma(B)\pi R_k = \psi\left(\frac{1}{2} + \frac{B_\phi}{B}\right) - \psi\left(\frac{1}{2} + \frac{B_0}{B}\right) - \ln\left(\frac{B_\phi}{B_0}\right) \quad (7.17)$$

however there is only one free parameter in this expression, B_0 , as the phase field, B_ϕ , can be determined from the value of the quantum correction at $B = 0$.

$$\delta\sigma(B=0)\pi R_k = \ln\left(\frac{B_\phi}{B_0}\right) \implies B_\phi = B_0 \exp\{\delta\sigma(B=0)\pi R_k\} \quad (7.18)$$

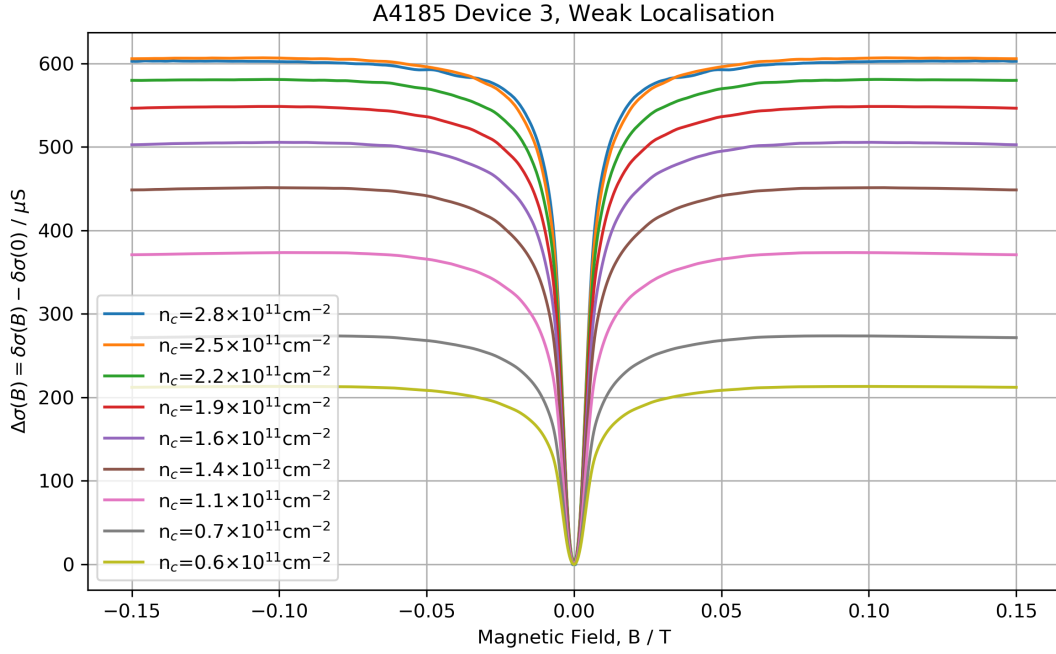


Figure 7.21: Quantum Correction $\Delta\sigma(B)$ measured in a hole gas in A4185. The height of the correction increases with carrier density.

Fitting the function in (7.17) with the relation in (7.18) gives a value for B_0 from which B_ϕ is obtained. Figure 7.22 shows one of the fits for a low carrier density hole gas in A4185.

The fitted model for the data in figure 7.22 gives a qualitative description of the quantum correction data, with the fitted parameters having a plausible order of magnitude. However, this model clearly does not fully describe the data and other models for weak localisation should be considered.

Figure 7.23 contains a plot of the fitted fields, B_0 and B_ϕ as a function of carrier density, showing the transport field B_0 increasing with carrier density and the phase field B_ϕ reducing.

7.5.1.1 Effective Mass from Weak Localisation

The model parameters B_0 and B_ϕ in (7.17) relate to the transport and phase coherence times τ_t and τ_ϕ via the Einstein relation,

$$B_i = \frac{\hbar}{4\mu k_b T \tau_i} \quad (7.19)$$

As B_0 is related to the transport lifetime which in turn is related to the mobility, μ , equation (7.19) provides an expression for the effective mass if the values of B_0 , μ and T are all known.

$$\frac{m^*}{m_e} = \frac{e\hbar}{4\mu^2 k_b T B_0 m_e} \quad (7.20)$$

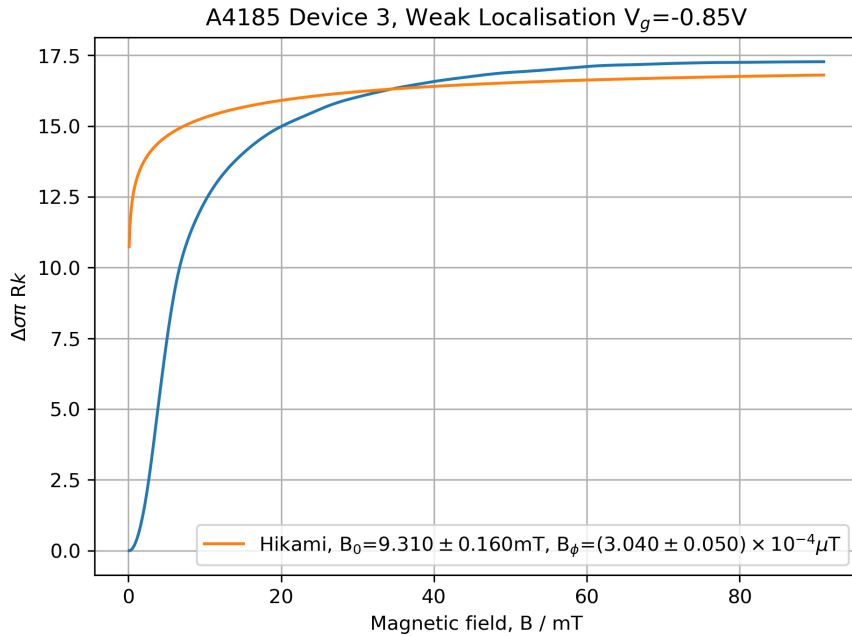


Figure 7.22: Fitting of weak localisation for low density holes gas in A4185, using the expression (7.17). The resulting fit gives a qualitative description of the data, with parameters for the transport and phase fields B_0 and B_ϕ which a plausible order of magnitude.

Taking the values of B_0 from figure 7.23, the effective mass of the holes in A4185 was found to be $0.78 \pm 0.01m_e$, which is significantly heavier than the GaAs heavy hole value of $0.51m_e$. As the fit of the experimental data is at best qualitative in nature, it can only be concluded that the mass of the heavy holes in A4185 is similar to that of GaAs.

Based on this value of the effective mass, the expected value of B_0 was calculated and plotted in figure 7.23. The plotted curve is consistent with the data, however the scattering in the data is too large to conclude that this curve is the best fit for the data. A linear fit is arguably just as good a fit for the values of B_0 .

7.6 Absence of Spin-Orbit Coupling in InGaAs

One of the major interests in InGaAs systems is potential spin-orbit coupling enhancement due to the presence of In. Control of the amount of spin-orbit coupling is one of the key requirements for applications like spintronics[197–199], which depend on g-factor engineering.

Spin-orbit coupling is known to be present in electron and hole gases in GaAs systems[194, 200, 201] and has been measured in InGaAs systems with higher Indium content[202]. The effect of spin-orbit coupling results in a splitting of the heavy hole band $m_j = \pm 3/2$ degenerate states into heavier and lighter carrier bands, due to the small difference in the curvature

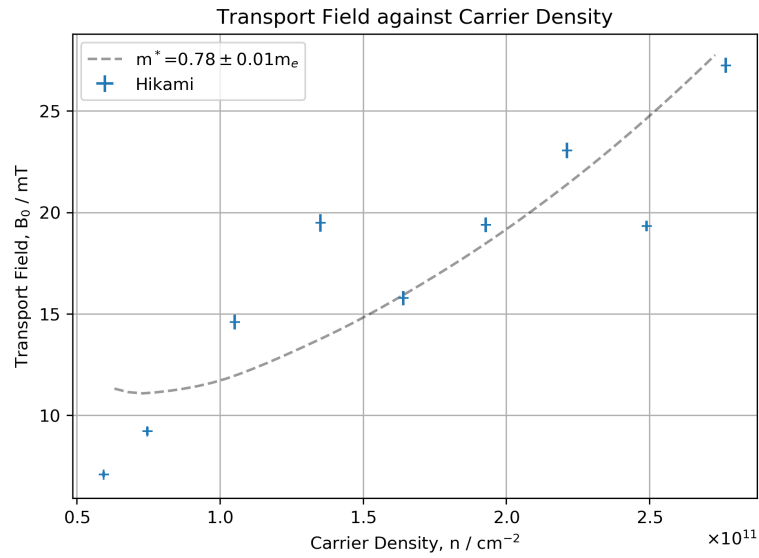
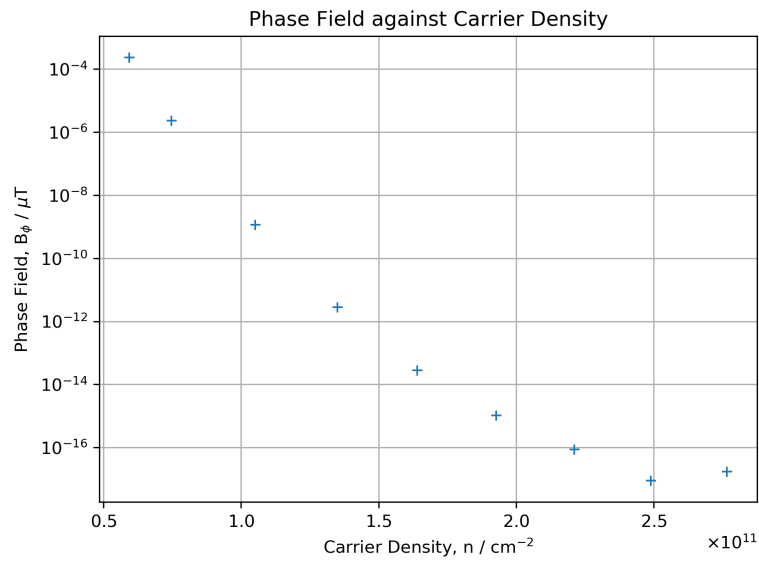
(a) Transport Field, B_0 (b) Phase Field, B_ϕ

Figure 7.23: Fitted parameters B_0 and B_ϕ as a function of carrier density. From the values of the transport field B_0 a value for the effective mass of the holes was calculated and the expected value of B_0 plotted giving a qualitative fit of the fitted parameters.

of the band structure. This results in two carrier populations being involved in the transport measurements which results in beating in the Shubnikov De Haas oscillations at high magnetic field.

In the InGaAs quantum well there is no measurable sign of beating that can be associated with spin-orbit coupling; in figure 7.5b there is only a single frequency peak corresponding to one carrier population. This lack of spin-orbit coupling is also confirmed by the weak localisation measurement rather than weak anti-localisation which would be expected in spin-orbit coupled systems.

A hole gas in a 15nm quantum well was measured at 283mK and beating was seen in the Shubnikov De Haas oscillation consistent with spin-orbit coupling, figure 7.24. As the quantum well in the GaAs device is 5nm narrower than the InGaAs quantum well, therefore causing a larger energy gap between the light and heavy hole band but beating can be measured in the GaAs device, we take this as conclusive evidence that the inclusion of the In in the GaAs structure has suppressed the spin-orbit coupling.

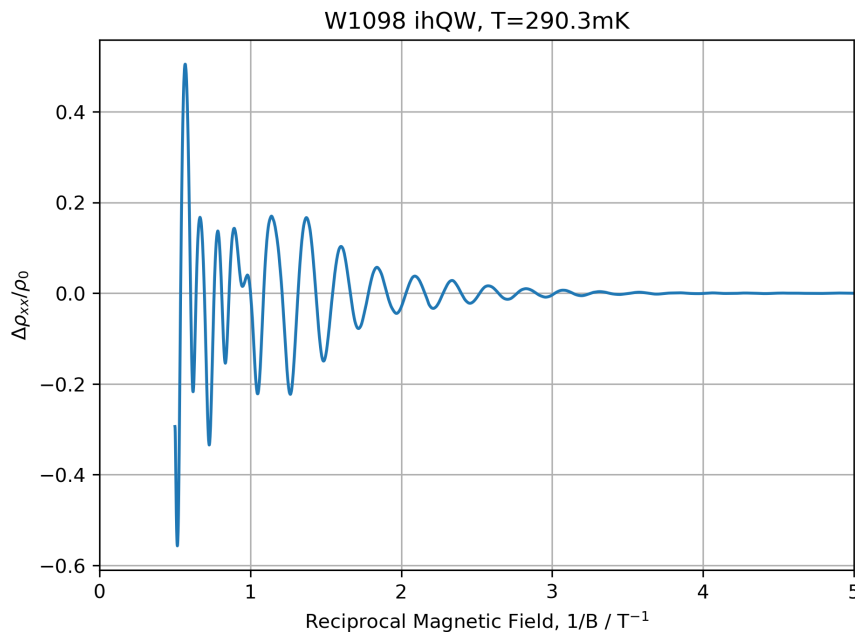


Figure 7.24: Shubnikov de Haas oscillations from a hole gas in a 15nm AlGaAs/GaAs/AlGaAs quantum well structure. Between 0.5T and 1.5T a beating occurs in the oscillations.

One key difference between the InGaAs and GaAs device is the strain in the InGaAs due to the lattice mismatch between InAs and GaAs. Calculation of the strain within nextnano give the value of 0.07 compared to 0.01 in GaAs. To explore the effect of strain on the spin-orbit coupling a set of InGaAs and GaAs devices have been fabricated with the aim to thin the samples down and attach a piezo element to the back of the device. The piezo element would

allow the substrate to be strained, in the case of the InGaAs removing the strain in the quantum well and in the case of GaAs straining the well. These devices have yet to be measured. Based on the work by Zduniak et al [203] it is suspected that the weak anti localisation peak that should be present due to spin orbit couple, may be visible at very low magnetic fields ($\sim 1 \times 10^{-4}$ T), which can be difficult to measure due to flux trapping and non-linearity in the magnetic power supply. Additional experiments with the yet to be measured samples may wish to replicate the approach of Zduniak et al.

7.7 Conclusions and Further Work

Fabrication of undoped Hall bars on a 20nm InGaAs quantum well wafer resulted in electron and hole gases with mobilities of the order $\mathcal{O}(\times 10^5)$ cm⁻² comparable with the low temperature mobility reported for a doped In_{0.1}Ga_{0.9}As structure[204] but higher than mobilities reported for higher indium content material[205–207]. Measurement of the magneto-resistance at 283 mK for both the electrons and holes shows the expected Shubnikov De Haas oscillations of a 2D system. The Shubnikov De Haas oscillations of the electrons showed very little temperature dependence below 500 mK. This small temperature dependence meant that attempts to determine the effective mass of the electrons could only bound the effective mass between 0.016m₀ and 0.074m₀, with an average value of 0.042±0.009m₀. Calculation of the band structure gave an effective mass value of 0.062m₀, slightly lighter than the effective mass in GaAs, but in line with expected values based values reported in other works[183, 204].

With the calculated value of the effective mass, Dingle plots were generated from the Shubnikov De Haas oscillations of the electrons. Unlike the Dingle plots from electrons in GaAs, the InGaAs Dingle plots were not linear, showing distinct curvature. Introducing a carrier density inhomogeneity assumed to follow a Gaussian distribution, as used in[152, 184, 185], about the mean n_c with a standard deviation of Δn resulted in a quadratic term in the expected Dingle plot relationship. Quadratic fits of the Dingle plot data give values for the quantum lifetime between 1ps and 2ps with a carrier inhomogeneity of less than 5%, reducing with carrier density. The extracted quantum lifetimes are lower than those reported for GaAs[152, 208, 209] and the carrier inhomogeneity larger than any measured in the GaAs heterostructures.

At the lowest carrier densities in the hole gas, the even minima in the Shubnikov De Haas oscillations are suppressed at low magnetic fields. A similar behaviour has been reported in p-type Ge[187–189]. This indicates a significant change in the energy structure, with the g^* factor being large enough that the spin-split levels from neighbouring Landau levels are closer in energy than levels from the same Landau level. This is consistent with an electron gas in an In_{0.76}Ga_{0.24}As 10nm quantum well which measured an 60% increase in g^* as the carrier density

was reduced from $3.9 \times 10^{11} \text{cm}^{-2}$ to 1.9^{11}cm^{-2} [210]. For carrier densities $\geq 1.4 \times 10^{11} \text{cm}^{-2}$ the suppression of the even minima changes to the odd minima, as is typical in Shubnikov De Haas. It is suspected that this change in the energy structure is due to exchange energy enhancement of the g^* factor. Further analysis of the data in order to calculate the g^* factor may provide more information on this effect.

During frequency analysis of the oscillations in the hole and electron gases, a second frequency was discovered, indicating the presence of a second quantum population. This second frequency caused beating in the Shubnikov De Haas oscillations for both electrons and holes, but was stronger in the electron gas. The second frequency was found to be linearly dependent on the voltage applied to the top gate above the ohmics and voltage probe arms. From linear fits of the frequency as a function of gate voltage, and the capacitive model of the top gate and carrier gas, the dielectric constant of the insulating layer was calculated and found to be a match for the dielectric constant of the Al_2O_3 used for this layer. This result, combined with next-nano current simulations showing current flow in the voltage probe arms, conclusively showed that this second population is the carrier density outside of the Hall bar. This is a useful result for future work with double top gates, as this frequency mixing was unexpected and can look similar to other physical effects causing beating in the Shubnikov De Haas oscillations.

One of the main interests in InGaAs is possible enhancement of spin-orbit coupling. Spin-orbit coupling can appear in the form of beating in Shubnikov De Haas oscillations but no such beating was observed. Spin-orbit coupling also causes weak anti-localisation, however measurements only showed weak localisation. The surprising lack of spin-orbit coupling in the InGaAs quantum well is thought to be due to strain within the quantum well, as beating due to spin-orbit couple was clearly measurable in a GaAs quantum well sample with a hole gas. Further work to explore the effect of strain, could include experiments with samples using a small piezo element to apply a strain to the sample. A comparison of a GaAs quantum well with an piezo element inducing strain to the structure and an InGaAs quantum well where the piezo element is used to match the strain in the structure would be of particular interest.

UNDOPED NANO-STRUCTURES

The Physics of 2D electron system (2DES) provides a wide range of phenomena such as quantum Hall, fractional quantum Hall, and carrier mobility modelling. However, 2D systems can be used as a starting point for further confinement of the carriers into 1D and 0D systems to study phenomena as the 0.7 anomaly [211, 212] in quantum point contacts and practical devices such as quantum dot system used for single electron pumps [58] to redefine the current standard.

From a 2D electron systems such as a heterostructure or quantum well, further confinement can be achieved by applying potentials to the surface via surface contacts which add an additional confining potential to the carrier gas. Depending on the geometry of these surface gates, 1D channels/quantum point contacts or 0D quantum dots can be defined. Because the potentials applied have to be on the same order as the wavelength of the electrons they confine, which for a 2D carrier gas at $1 \times 10^{11} \text{cm}^{-2}$ is $\approx 80 \text{nm}$, the surface gates must be of a similar dimension, $O(10 \text{ nm}-100 \text{ nm})$. This required the fabrication of a surface gate of the order of $\approx 100 \text{nm}$ therefore the fabrication of undoped nano-structures will be discussed in this chapter.

While many quantum point contacts and quantum dots have been fabricated in doped systems and undoped systems, although undoped is less common, [213–221] there is still much work to be done to fully understand 1D and 0D systems, particularly in other material systems such as InGaAs. It is here that undoped 1D and 0D devices may have an advantage over doped devices. The lack of dopants in undoped devices means there are fewer background charge centres which can disrupt 1D and 0D systems[7, 39]. Undoped systems also come with the advantage of being able to study electrons and holes in the same wafer, therefore presenting

an opportunity to study both types of carrier using a common set of fabrication procedures and material.

8.1 Fabrication of Low Dimensional Systems

In order to further confine a 2D electron system into a 1D or 0D system, an additional confinement potential needs to be applied to the plane of the 2D carrier gas. This is achieved by patterning nano-scale surface gates in geometries that result in the confinement desired when a bias is placed on the surface gates.

Because the surface gates have to be patterned into geometries on the order of $\approx 100\text{nm}$ optical lithography is insufficient as it lacks the resolution needed; instead, electron beam lithography is required.

8.2 Attempts to Replicate Previous Induced Quantum Dots

In work by a previous PhD students[10, 42], induced quantum dots were fabricated and Coulomb blockade was observed and measured. These induced quantum dots were fabricated using different insulating layers: polyimide and SiO_2 . Since that work, another PhD student [10] successfully fabricated single and double quantum dots, but with the aim of populating the dots with the last electron. In this work, the insulator used was Al_2O_3 but the thickness of the insulator was closer to 90nm rather than the current 60nm. Because of the multiple changes in the dot geometry and insulator used, it was unclear how each change affected the performance of the dot.

In an attempt to understand how the fabrication of induced dots may have changed, a set of dots using the dimensions from[42] dots were fabricated using the current ohmic contacts and 60nm ALD alumina. The dots consists of three pairs of surface gates: two outer barrier gates and a central plunger gate, figure 8.1.

To assess the dots performance they were cooled to 1.5K and then the plunger gate and barrier gates were swept to see if a channel through the dot opened and if the dot could be tuned to observe coulomb blockade. While the channel through the dots could be open and 1D conductance curve potentially seen, there was no sign of Coulomb blockade. While the parameter space of barrier gate, plunger gate and top gate were explored in a limited range, no signs of 1D conduction curve or Coulomb blockade were observed. It was concluded that the geometry of the current dot with 60nm Al_2O_3 was not correct to have the barrier gates high enough to isolate the dot from the 2DEG while being low enough to allow a bound state to exist in the dot. While it is possible that there is a region in the barrier, plunger and top gate

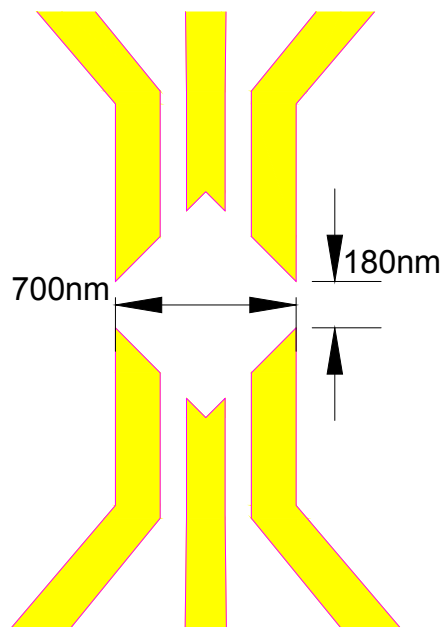


Figure 8.1: Schematic of the surface gates used to form the barriers and plungers for an undoped quantum dot. Copied from previous work [9].

parameter space where the dot functions, this parameter space is 3D before any asymmetry in the dot is considered.

To gain a better understanding of the geometry of nano-structure, fabrication was changed to a 1D system with a quantum point contact (QPC) due to an easier fabrication and the smaller parameter space to fully explore and understand.

8.3 P-type 1D Quantum Point Contacts

To explore the parameter space of geometry size of QPC, a range of devices were fabricated on 100nm and 50nm AlGaAs spacer undoped heter interfaces with a range of QPC widths and lengths. The lengths and widths of the QPCs ranged from 700nm down to 200nm to cover the parameter space of the widest quantum dots successfully fabricated down to the narrowest features on the quantum dot designs.

Because the quantum dots are p-type at 4K and 1.5K, it is only possible to measure that the QPC can be opened and closed with the side gates not shorted together. While the conductance curves through the QPC show a definition point which is compatible with the transition from 1D to 2D transport, there is no measurable Coulomb staircase in either the conductance trace or the derivative of the conductance. As the Coulomb staircase is the key characteristic of 1D transport, at 4K and 1.5K the 1D nature of the channel cannot be confirmed.

In an attempt to confirm the 1D nature of the channel, the iQPC devices were characterised

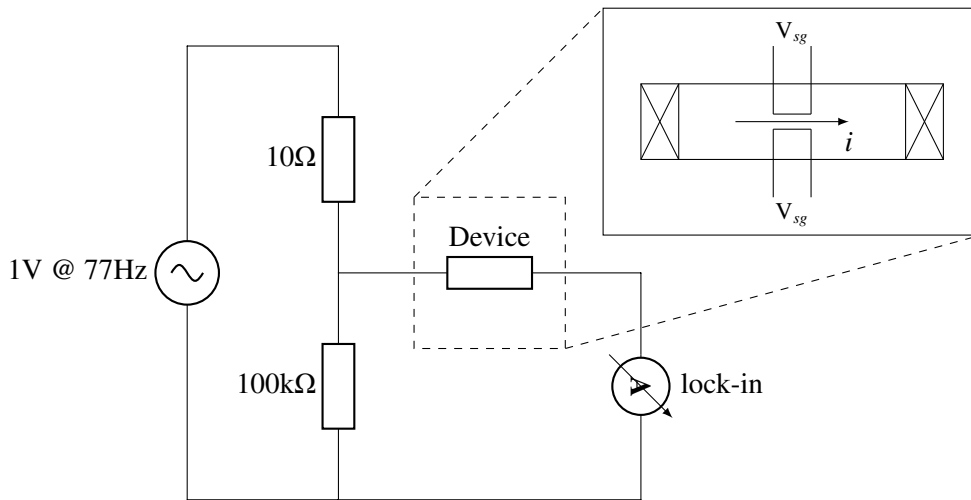


Figure 8.2: Schematic of the measurement circuit for the conductivity of the QPCs.

at 300mK, in the Heliox ^3He system as samples could be loaded and measured in just two days, rather than the week a dilution fridge would require per sample. This enabled a far more rapid characterisation of the different geometries to see how well they performed at lower temperatures.

8.3.1 Experimental Setup and Procedure

The two terminal conductance of the quantum point contacts was measured using a simple constant voltage circuit. An input AC signal 0.1mV in amplitude is applied to the QPC and the current is measured using a 10^7VA^{-1} amplifier and a lock-in amplifier, circuit diagram shown in figure 8.2. A SMU applies the voltage for the top gate of the device and measures any leakage current. A digital-to-analogue convert applies the voltage on the split gates that form the QPC. Due to the very sensitive nature of the fine split gates, precautions were taken to reduce the chance of electro static discharge which will very easily damage or destroy the device. Both the cryostat and user were grounded at all times when handling either the samples or when in contact with the cryostat. Before placing the sample in the cryostat, a set of six low pass filters were connected to the gate lines and grounded. The gate filters are wired up such that the device is on the output of the filter and the input can be held at ground by a toggle switch, figure 8.2. This ensures that the gates are held at a common ground until ready to have a voltage applied, and provides extra protection when adjusting circuit setup, although changes to the circuit are kept to a minimum when the device is cold.

The measurement procedure of the QPC has a few extra stages due to the split gates compared to 2D induced devices. Unless stated otherwise, all ohmics are grounded during the

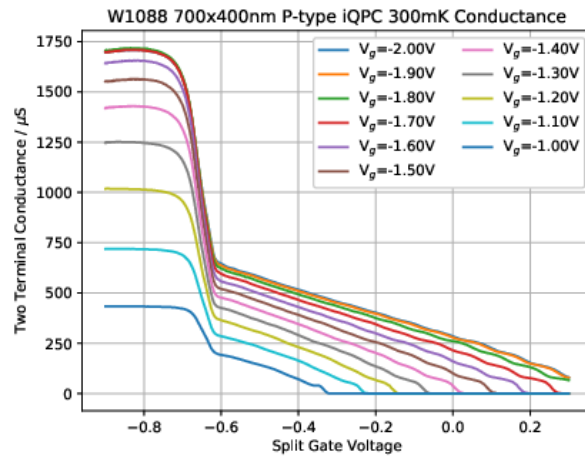
measurement. Once cold, the current measurement circuit is connected to the pair of ohmics on one side of the split gate. Voltage is then applied to the top gate and a typical inducing curve is measured. It is important that the maximum conductance measured at this state is $100 - 1000\mu\text{S}$, indicating that both ohmics work with an acceptable conductivity. If the conductivity is much lower than this, it can be an earlier indicator that the QPC channel is not closed when at 0V. Both sides of the QPC are checked in this way, ramping the top gate back to 0V in between changing the measured ohmic contacts, to protect the device. Once both pairs of ohmics have been confirmed functional, the current measurement circuit is connected across the QPC, again at 0V on the top gate. The voltage on the top gate is now increased until it is high enough that the holes gas is known to have formed. For these wafers and thickness of insulator, this is around -1.2V. With the holes gas induced, the two redundant ohmic contacts are floated, with the device's ground reference now from the measurement circuit. Until this point the split gates have been fixed at 0V through the gate filters. A voltage is now applied to the split gates with a negative voltage sweep to open the channel.

Once the channel has been opened, the split gates are put through a series of sweeps to check that the device is functioning as expected. The 'safe' working voltage range for the split gates is $\pm 1\text{V}$; thankfully very few devices were damaged so this may be a conservative range. Both split gates are swept to a voltage of -0.9V, to give the threshold voltage of the channel opening and the definition point when 2D transport occurs. The definition point for these devices was $\sim -0.6\text{V}$, while the threshold voltage range between the definition point and 0V depending on the device geometry, and carrier density. After measuring the channel with symmetric sweeps, the split gates are set to a mid-range voltage below the definition point. Both gates in turn are then taken to 0V, keeping the other gate voltage fixed. The two measured conductance curves are expected to be very similar but not identical. The more similar the curves the more symmetric the define QPC, but if the traces are identical the split gates are likely shorted together.

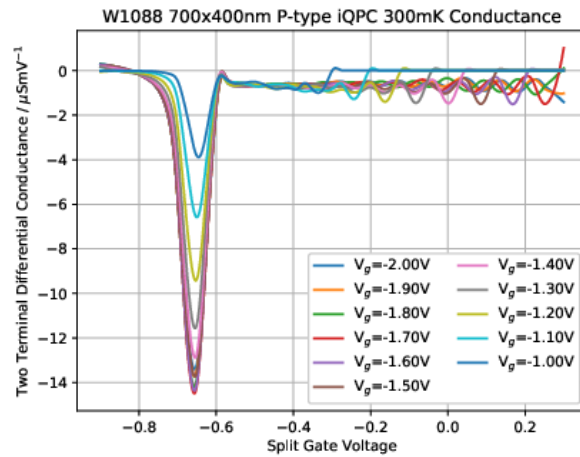
At the end of this process, the ohmics have been confirmed to function, the device has been safely induced and the channel has been opened. The definition point of the QPC is known and the split gates have been checked for obvious signs of damage.

8.4 iQPC Measurement at 300mK

The main aims of these measurements were to confirm that a 1D channel had been formed, by measuring a Coulomb staircase in conductance, and investigating the different geometries of QPC. These experiments were performed in a short amount of time and there was not enough to explore more complex measurements such as DC bias of the QPC or magnetic field variation.



(a) Two Terminal Conductance



(b) Two Terminal Differential Conductance

Figure 8.3: The two terminal conductance and differential conductance from a 700x400nm iQPC on W1088. The definition point is visible at $\sim -0.65\text{V}$ and the conductance above the definition point shows potential 1D conduction staircase.

To reduce the number of parameters that needed to be explored, the splits gate were assumed to be sufficiently symmetric, based on the checks performed when inducing the device. The conductance as a function of the joint split gate voltage was measured up to, and a little beyond, the definition point as a function of carrier density, example traces in figure 8.3.

The conductance traces in figure 8.3 are promising for 1D channel being defined by the split gates. The sharp increase in conduction at $\sim -0.65\text{V}$ given the size of the increase in conductance, looked likely to be the definition point as the channel defined by the QPC opened

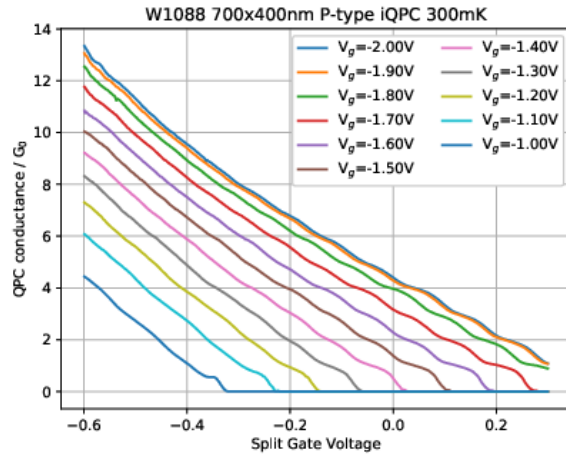
sufficiently for 2D transport. Above this point, the channel can be kept open with only one of the split gates with an applied voltage, therefore the definition point is due to the hole gas forming under the split gates so that the split gate with applied voltage no longer screens the action of the top gate on the hole gas below it. Below the definition point there is a definite structure of weak plateaus, as would be expected for 1D transport. This structure is more clearly visible in figure 8.5b, where the derivative of the two terminal conductance with respect to the split gate voltage is shown. There is a clear series of maxima in the differential conductance corresponding to the weak plateaus in the conductance. This is very promising for the formation of a true 1D channel, however further investigation is needed as the staircase is only weakly defined.

The conductance of a true 1D channel is the sum of the number of sub-bands occupied, with each sub-band contributing $G_0 = 2e^2/\hbar$ of conductance in series with the other sub-bands. Weak plateau observed in the conductances trace are from a true 1D channel, the conductance of the QPC at the plateau will be an integer multiple of G_0 . Because the conductance is measured from a two-terminal measurement, the conduction of the the QPC itself, is in parallel with the conductance from the resistance of the rest of the device, 2DHG, and ohmics, as well as the measurement circuit components. This series resistance is removed by measuring the two-terminal conduction above the definition point. Above the definition point the two terminal conductance is dominated by the series resistance of the circuit, therefore a value of the series conductance G_s can be obtained. Once the value for G_s has been measured, the conductance of the QPC is given by:

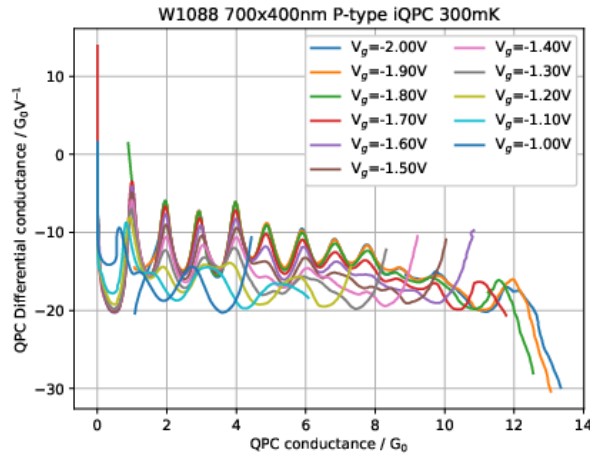
$$G_{QPC} = \frac{G}{1 - G/G_s} \quad (8.1)$$

where G is the two-terminal conductance. The QPC conductance and differential conductance from the 700x400nm QPC on W1088 are shown in figure 8.4. The conductance traces in 8.4a show a similar structure to the traces in 8.5a, but are scaled such the conductance in units of G_0 places the plateaus near integer values. The differential conductance in figure 8.4b is plotted as a function of the conductance of the QPC in units of G_0 , the series of maxima are visible and at the correct position for transport through a 1D channel.

The primary effect of changing the carrier density with the top gate voltage allows higher subbands to be populated, shown by the presences of peaks at 5-7 G_0 in figure 8.4. While the plateaus are definitely present in the conductance traces, the differential conductance peaks highlight that the derivative of the traces do not go to zero as seen in the ideal case. This is discussed further in section 8.5



(a) QPC Conductance



(b) QPC Differential Conductance

Figure 8.4: The conductance of the QPC, $G_{QPC} = G/(1 - G/G_s)$ calculated from the two terminal conductance, G and the series conductance, G_s .

8.4.1 Geometry Variation

Of the 100nm AlGaAs spacer wafers, W1088 and W1091, the 700x400nm, 400x400nm and 400x200nm geometries were measured at 300mK. A total of six QPCs had conductance traces that could be from a 1D channel. Two in particular showed weak conductance staircases, figure 8.5.

Both of these QPCs show, weakly, the expected conduction staircase with peaks in the differential conductance at integer value of the conductance quantum, with up to the eighth sub-band plateau visible. However, in both devices the plateaus do not fully reach zero, meaning further optimisation is required. The 400x200nm device, figure 8.6, did show similar traces

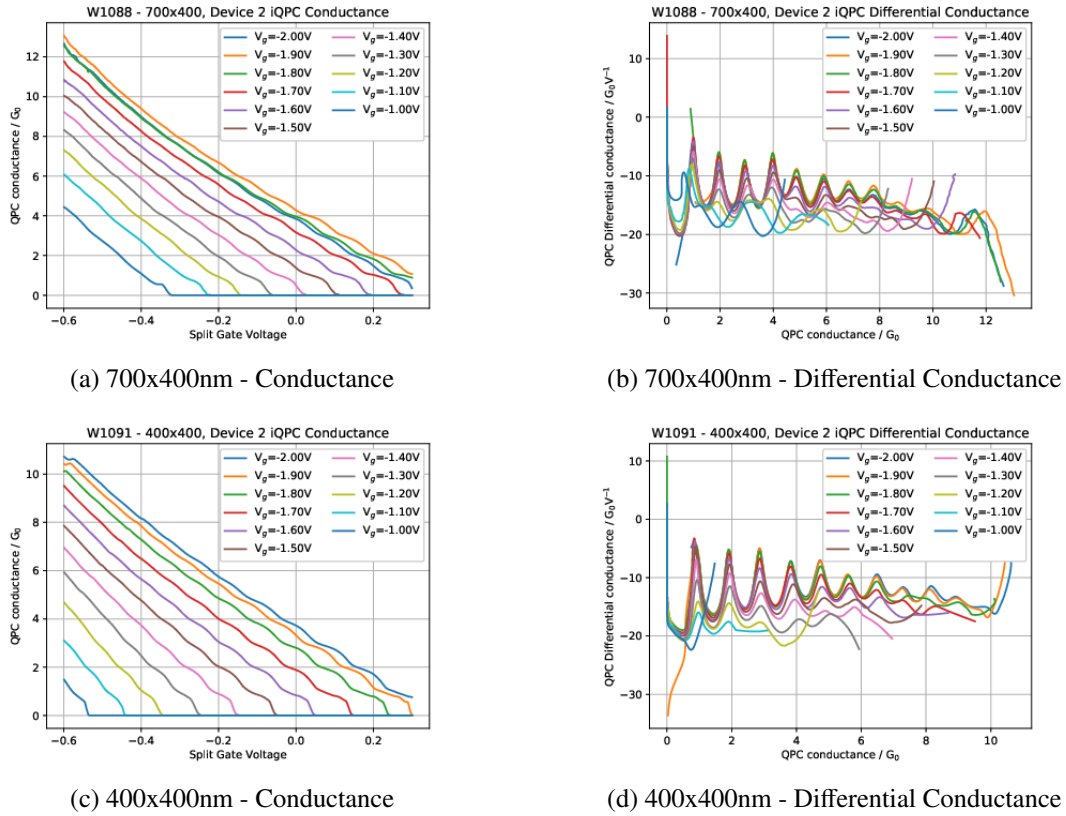


Figure 8.5: QPC conductance and differential conductance for 700x400nm and 400x400nm QPC geometries on W1088 and W1091, 100nm AlGaAs spacer undoped heterostructures. Both geometries show a weak conductance staircase, the ‘fingerprint’ of 1D transport.

to the 700x400 and 400x400 devices with a definition point at $\sim -0.65\text{V}$, however the region below the definition point does not show any sign of promising 1D behaviour, and there is only a small range of voltages where the channel is open. This, combined with the channel being highly resistive, leads to the conclusion that a 200nm spacing is too narrow, although more statistics from other test devices and checking a 200x200nm device would be useful further work.

The same QPC geometries were also fabricated on 50nm AlGaAs spacer heterostructures, W1089 and W1091. The results from the geometry variation were similar to the 100nm device, figure 8.7, with a weak conduction staircase visible, but less well defined than the 100nm AlGaAs spacer devices.

Two additional geometries were tested on the 50nm wafers, 700x700nm and 400x200nm, in an attempt to decrease and increase the confinement of the 1D channel. Changing the confinement in the 1D channel adjusts the sub-band spacing. The conductance trace for these two geometries, figure 8.8, shows that the 700nm wide channel is too wide, making the channel

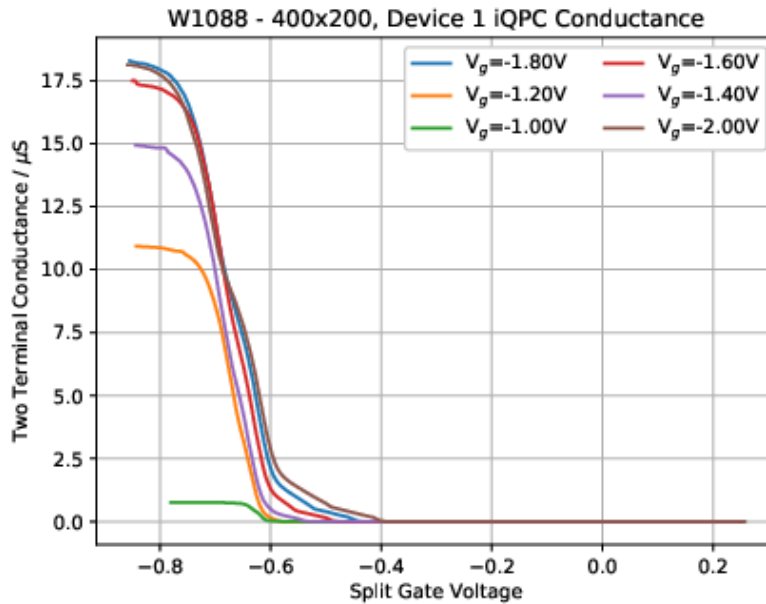
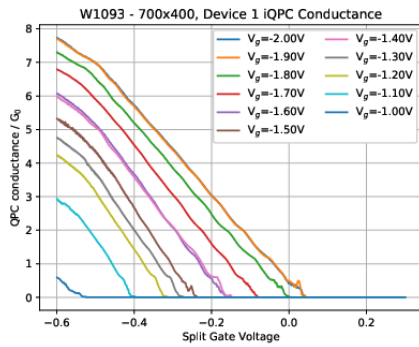


Figure 8.6: Two terminal conductance from a 400x200nm QPC on W1088 a 100nm AlGaAs Spacer HEMT.

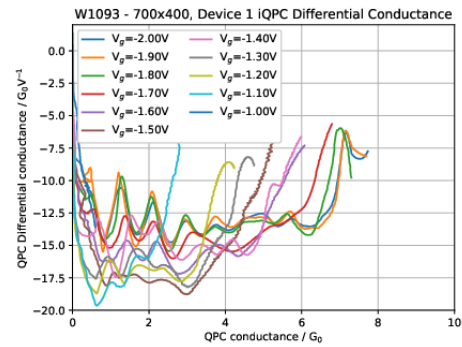
difficult to close without positive biasing of the split gates. It's worth noting that there is indication of weak plateaus for $V_g = -1.3V$ near sub-band 5. In contrast the 200nm-wide QPC is too narrow. There is a limited range of split gate voltages that keep the 1D channel open without opening a 2D channel under the split gate. Within this range, there are two weak plateaus near $0.7G_0$ and G_0 , but the channel becomes 2D before any other sub-bands are visible.

The results of the geometry variation show that a 1D channel has been formed in both the 100nm and 50nm wafers. But in all the devices, the conductance staircases are weak and only clearly visible when looking at the differential conductance. Between the 50nm and 100nm devices, the conductance staircases are better defined in the 100nm devices, with clearer plateaus sub-bands 1-6 easily seen in the differential conductance. The most successful geometries are the 400nm wide QPC. The 700nm and 200nm wide devices are too wide and too narrow respectively. Further work should focus on optimising the geometry around 400nm.

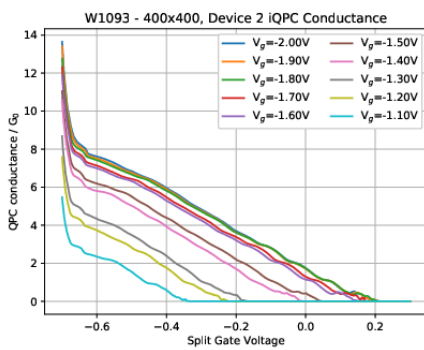
At the higher top gate voltages, the plateaus get closer to zero but it is unclear if this is due to the higher carrier density, and therefore a higher chemical potential in the holes gas, or an interaction between the top gate and surface gate changing the shape of the potential formed by the split gate. Another possibility for the plateaus not reaching zero is the temperature of the sample. While 300mK allows the conduction staircase to be seen, this is still a factor of 2-10 higher in temperature than a dilution fridge temperatures. It is unclear if going to lower



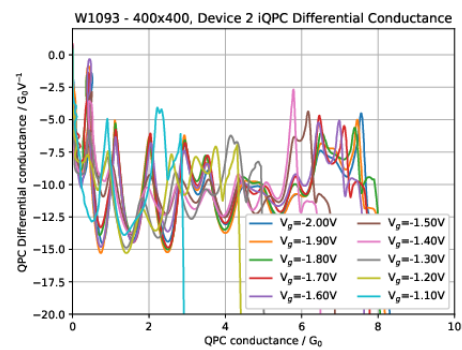
(a) 700x400nm - Conductance



(b) 700x400nm - Differential Conductance



(c) 400x400nm - Conductance



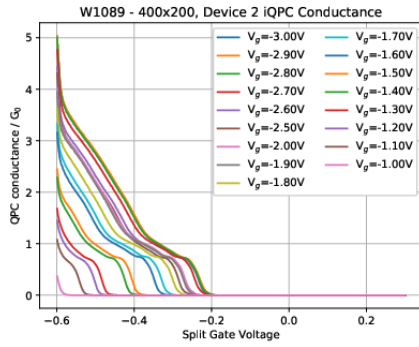
(d) 400x400nm - Differential Conductance

Figure 8.7: QPC conductance and differential conductance for 700x400nm and 400x400nm QPC geometries on W1089 and W1093, 50nm AlGaAs spacer undoped heterostructures. Again signs of Coulomb staircase can be seen but more weakly than the 100nm AlGaAs spacer devices.

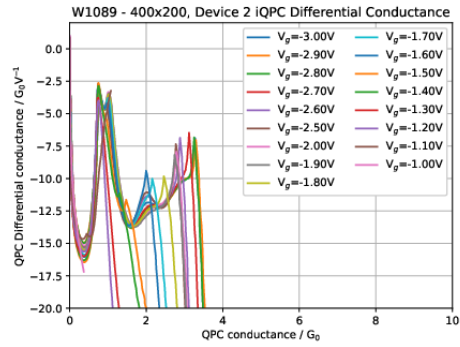
temperatures would improve the resolution of the staircases, or if changing the geometry of the QPC to increase the sub-band spacing is the best way forward.

8.4.2 1.5K, 300mK Comparison

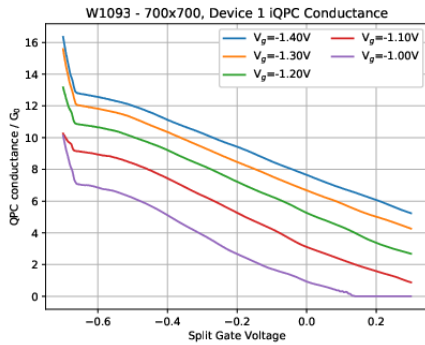
To get an idea of the effect temperature has on the definition of the conduction staircase, the 400x400nm device from W1091 was measured at 300mK and 1.5K in the same system. The differential conductance traces, figure 8.9, show that the reduction in temperature from 1500mK to 300mK increased the height of the peaks in the differential conductance by a factor of two. It is still difficult to say if reducing the temperature of the sample would result in a better definition of the conduction staircase but the data in figure 8.9 indicates that lowering the temperature will help, and any further experiments on these samples are worth doing in a



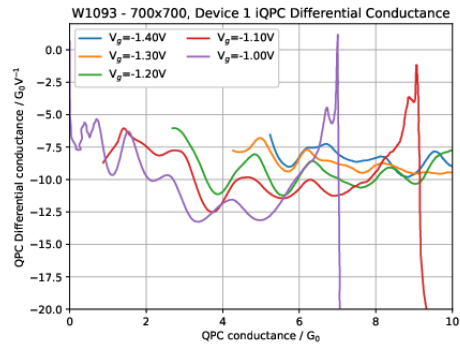
(a) 400x200nm - Conductance



(b) 400x200nm - Differential Conductance



(c) 700x700nm - Conductance



(d) 700x700nm - Differential Conductance

Figure 8.8: QPC conductance and differential conductance for 400x200nm and 700x700nm QPC geometries on W1089 and W1093, 50nm AlGaAs spacer undoped heterostructures. The 700nm wide channel is too wide preventing the channel being closed and the 200nm wide channel is too narrow.

dilution fridge.

8.5 Modelling with Nextnano

To further understand the effect of the geometry of the surface gates on the 1D channel formed in the 2DEG, a 2D simulation of the cross-section of the channel was created using nextnano. The use of periodic boundary conditions means that the simulated channel should be that of an infinite channel. A 2D rather than 3D simulation was used due to the limited computation power available with nextnano.

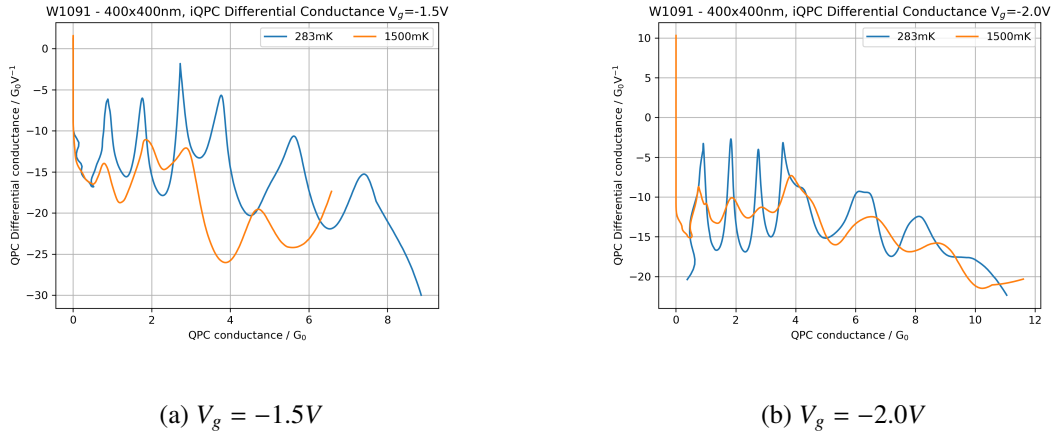


Figure 8.9: Differential conductance traces for W1091 400x400nm at 300mK and 1500mK. The peaks in the differential conductance increase by a factor of two due to the temperature reduction.

8.5.1 Nextnano Model

The nextnano simulation of the iQPC is an extension of the nextnano simulation of the conduction band of the induced devices in section 5. This simulation is extended into a second dimension to form a cross-section of the iQPC channel. The boundary conditions are the same as previously used, with the fermi level pinned mid band gap at the GaAs surface, and set to 0eV at the GaAs/AlGaAs interface where the 2DEG forms. To model the effect of the global top gate and the surface gates the surface of the GaAs is held at a potential V , relative to the GaAs/AlGaAs interface. Unlike the 1D conduction band modelling previous used, the 2D iQPC model has to reproduce the effects of both the global top gate and surface gates. To avoid the complexities of edge effects and interactions between the global top gate and the surface gate, the surface gates are assumed to completely screen the action of the global top gate. This translates to boundary conditions on the surface of the GaAs of V_{sg} everywhere except for the surface directly above the channel, to produce the effect of the surface gates. On the surface directly above the channel, the potential is set at V_g for the effect of the global top gate, see figure 8.10.

To compare the output from nextnano to the experimental data, the occupation of holes in the first 20 eigenstates as a function of the energy of the state was calculated. The bound ground states for a 200nm and 400nm QPC were plotted as a function of split gate voltage in figure 8.11. Figure 8.11 shows there are bound states for the 400nm between 0V and -0.4V and between -0.4V and -0.7V for the 200nm. This agrees with the measurements of the 200nm and 400nm devices at 300mK, which showed that the 200nm device formed a 1D channel at a higher split gate voltage of between -0.4V and -0.6V, compared to the 400nm

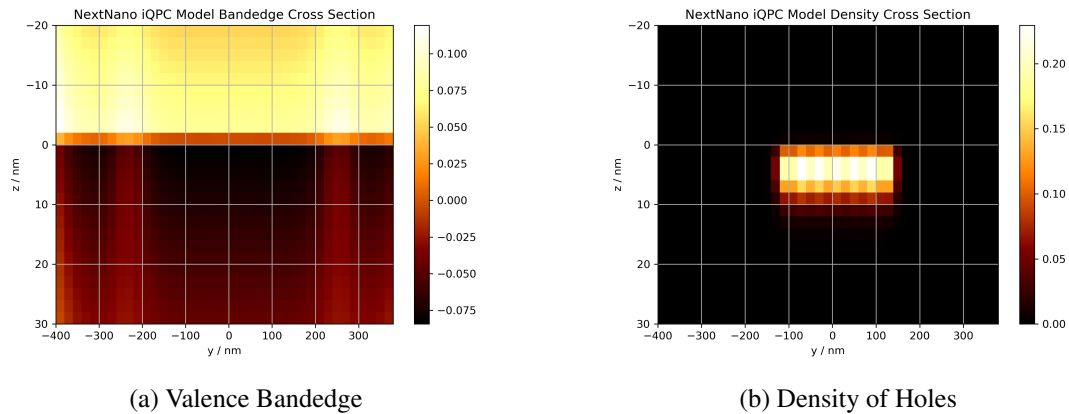


Figure 8.10: Cross-section of nextnano model looking down the channel with the Valence band edge and density of holes plotted showing the formation of a hole gas at the AlGaAs/GaAs interface, between the split gates at ± 200 nm.

device between 0.3V and -0.6V. While the nextnano model is only indicative of the behaviour of a real device due to the lack of gate dielectric to simplify the model, the general agreement between the model and the measured device adds confidence that the model can be used to at least qualitatively examine different gate geometries to inform the design and measurement of real devices. It is worth noting that the number of holes per nano-metre calculated by nextnano has no lower threshold, and some of the values are extremely low and would not be measurable in a real device due to experimental limitations from the measurement circuit. Figure 8.11 shows the output from nextnano for 200nm and 400nm devices, with a map of the hole density near the AlGaAs-GaAs interface with the band structure. Both simulations show the formation of a confined 1D channel in between the split gates from the surface. The output from similar simulations that show unbound states, taken to be an indication of a 2D channel forming, indicate the formation of a carrier gas under the split gates on the surface. This would match with the experimental measurements, which all showed a definition point near -0.6V due to a 2D channel forming by inducing a carrier gas under the split gates.

The Coulomb staircases, best seen in the 400nm device, are not as well-defined as other QPCs, with the differential conductances not reaching zero at the plateaus. It is unclear if this is due to the geometry of the device, wafer structure or temperature. From the output of the nextnano model, the energy spacing of the sub-bands can be calculated and used to infer the temperature below which the Coulomb staircases would be visible. For both the 200nm and 400nm, the lowest temperature corresponding to the energy difference between the levels was 1.4K, therefore measurement at 300mK should be sufficient to resolve the sub-band energies, as indicated by the experimental data. Therefore, the lack of resolution in the Coulomb staircase must be due to the geometry of the device.

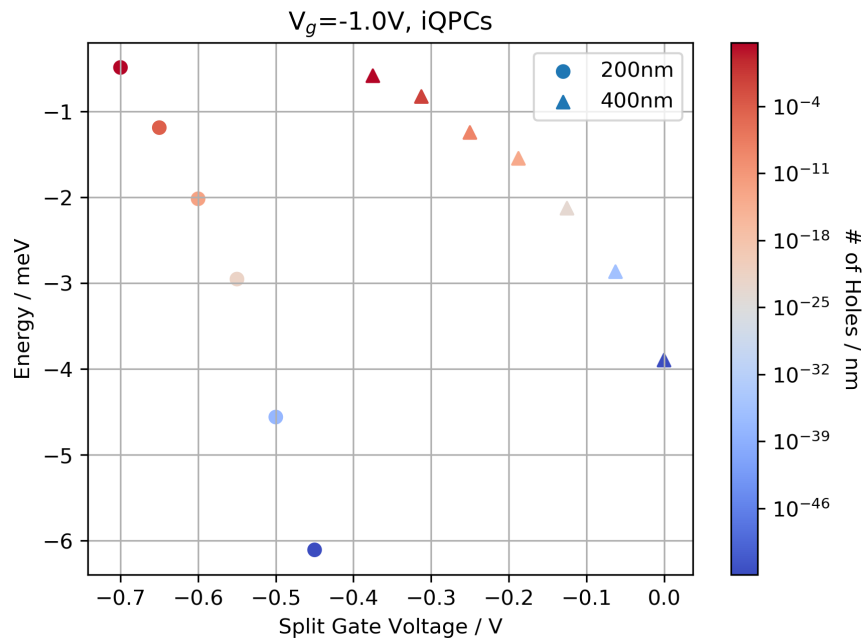
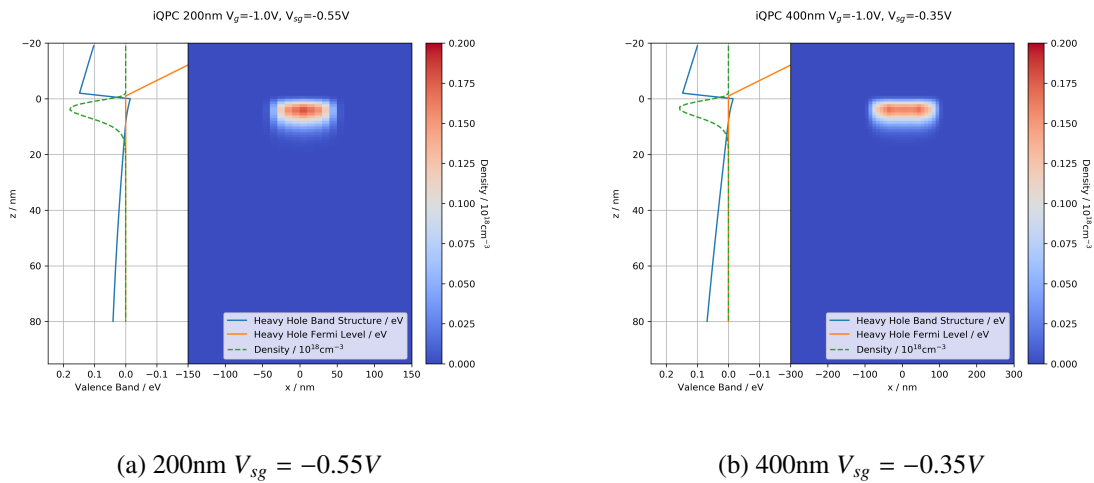


Figure 8.11: Output from Next-Nano, hole occupation in channel against energy for the bound ground states with $V_g = -1.0V$ and varying the split gate voltage between 0V and 1V.



(a) 200nm $V_{sg} = -0.55V$

(b) 400nm $V_{sg} = -0.35V$

Figure 8.12: Output from Next Nano showing the hole density at the AlGaAs-GaAs interface for a 200nm and 400nm iQPC. Both simulations show the formation of a channel in between the split gates, but with the 400nm device having a wider channel, as reflected in the energy of the ground states of figure 8.11

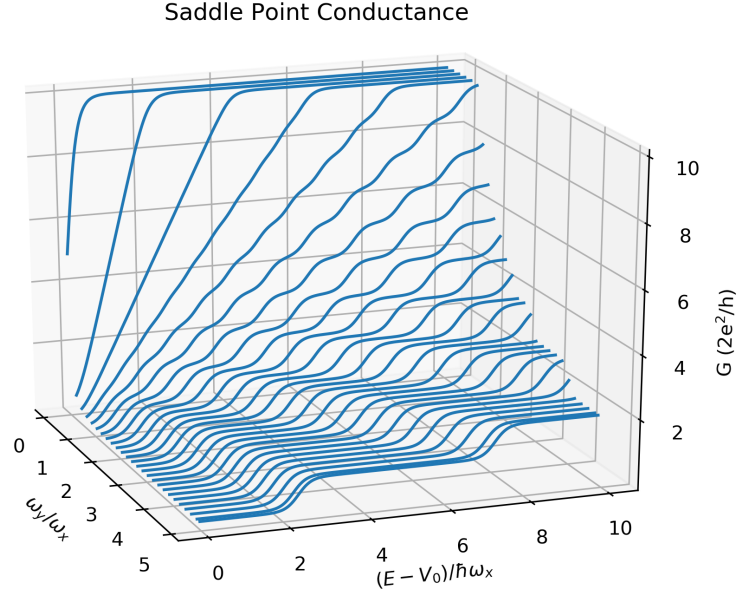


Figure 8.13: Conduction staircases for the saddle point potential as function of the ratio ω_y/ω_x .

To explore how the geometry of the QPC could be improved to resolve the Coulomb staircase, the saddle potential will be used to model the QPC potential. The saddle point potential is defined as:

$$V(x, y) = V_0 - \frac{1}{2}m^*\omega_x^2x^2 + \frac{1}{2}m^*\omega_y^2y^2 \quad (8.2)$$

with a natural length scale of $l_x = \sqrt{\hbar/m^*\omega_x}$ and similar for the y direction. Within the Landauer-Buttiker formalism[222] the conductance G is given by,

$$G = \frac{2e^2}{h} \sum_n \frac{1}{1 + \exp[-\pi\varepsilon_n]} \quad (8.3)$$

where the variable $\varepsilon_n \equiv 2[E - \hbar\omega_y(n + 1/2) - V_0]/\hbar\omega_x$. The ratio of $\omega_y/\omega_x = l_x^2/l_y^2$ controls the resolution of the conductance staircase as a function of $x = (E - V_0)/\hbar\omega_x$, shown in figure 8.13. The higher the value of $\omega_y/\omega_x = l_x^2/l_y^2$ the more well defined the conductance staircase becomes. This suggests that the 1D channel forming the measured devices needs to be elongated, to increase the ratio of $\omega_y/\omega_x = l_x^2/l_y^2$. The two geometries for the 400nm QPC of 700nm x 400nm and 400nm x 400nm have a ratio of approximately 3 and 1 respectively. Based on the saddle point potential, the 700x400nm device should have a better resolution of the individual energy levels in the conductance staircases, however this is not seen in the measured devices.

Using nextnano to solve the Poisson equation in 3D for the split gate geometry and wafer structure, but not solving the Schrödinger equation, provides a model for the potential that

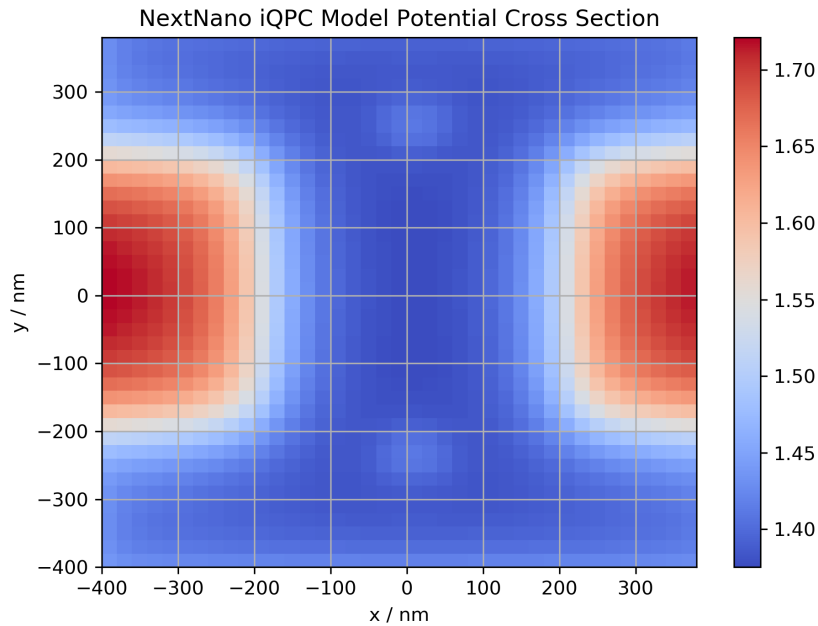


Figure 8.14: The potential at the AlGaAs/GaAs interface, showing the formation of a approximately parabolic potential in the y direction.

forms the the channel. For the 400nm x 400nm QPC which showed the best QPC behaviour, the potential from next nano is shown in figure 8.14.

8.6 Conclusions and Further Work

In this chapter, attempts to replicate previous induced quantum dots with current fabrication processes showed that the change in gate dielectric from polyimide to Al_2O_3 meant that previous surface gate geometries no longer produced functioning dot pattern. To simplify the process of optimising the surface gate geometry, a new quantum point contact mask set was designed so that devices with only two surface gates (rather the six needed for a quantum dot) could be fabricated. The reported geometry of quantum point contacts varies with some as large as $1\ \mu\text{m}$ [223] and others smaller at 100 nm-150 nm[224–226], with the state of nanostructures the art being smaller than 100 nm[227]. The geometry for a QPC fabricated on a similar wafer structure[228] to the wafers used in this work have a very similar dimension of 400 nm×400 nm[229]. Therefore the quantum point contacts with spacings between 700nm and 200nm fabricated on 50nm and 100nm heterostructures are comparable to other successful devices.

While all the QPC geometries showed indications of a 1D channel forming from the conductance staircases measured at 300mK, the 400nm QPC on 100nm wafer showed the clearest

conductance staircase. The 700nm device were too wide and prevented the channel from being closed, while the 200nm devices had a much smaller voltage range where the 1D channel opened before a carrier gas was induced under the surface gate, causing a 2D channel to form.

While the conductance staircases are clearly visible, particularly when looking at the differential conductance, the individual energy levels in the staircase were not individually resolved. From modelling using nextnano, the energy spacing of the sub-bands is wide enough that measurement below 1.4K should be sufficient to resolve the individual sub-bands, as has been done in other works[225, 226], notably with clear conductance plateaus at 4.2K reported in[230], therefore the limiting factor must be the QPC geometry. Using the saddle point potential within the Landauer formalism as a description of the channel potential, to improve the resolution of the conduction stair case in the QPC the channel must be elongated. From the saddle point potential the 700nm x 400nm QPC should be long enough to give a clear conductance staircase, but from the measurements at 300mK this is not the case. This suggests that edge effects from the finite size of the surface gates are reducing the length of the channel, and therefore longer surface gates are needed.

Further work on induced nano-structures could look at fabrication of 400nm wide QPCs but with longer channel lengths to see if the resolution of the staircases can be improved. If this is the case, then these devices could serve as the basis for a study of 1D conduction of holes within a structure that allows for a limited tuning of the Rashba parameter through the use of the top gate to change the shape of the potential well. This new round of devices would also allow ambipolar device to be fabricated, to explore the behaviour of electrons in a similar nano-structure.

For the induced quantum dots, the QPCs indicate that a surface gate separation of 400nm forms a functional 1D channel. The induced dot design used surface gates between 150nm and 500nm wide to form the barrier gates of the dots. The results from the QPC suggests that wider barrier gates are needed to allow the opening of a channel through the dot. However, this would still involve a significant amount of further optimisation to produce a fully functioning induced quantum dot using current fabrication processes.

An open question from the QPC data is: why did the 100nm wafer produce better 1D channel conduction? One obvious difference between the 50nm and 100nm wafer is the possible effect of surface charge, which is significant in the 50nm wafers' mobility in 2D Hall bars. Further investigation into the potential effect of surface charge on similar nano-structures would be interesting and useful if fabrication of shallow nano-structures is needed for projects where better definition of the confining potential from surface gates is needed.

CONCLUSIONS AND FURTHER WORK

The work presented in this thesis covers three general areas: optimisation of undoped fabrication, MBE optimisation, and 2D transport in InGaAs quantum well and GaAs heterostructure. The following sections summarise the key findings from the work in this thesis in each of these three areas, with some suggestions for further work.

9.1 Hole Gas in an $\text{In}_{0.1}\text{Ga}_{0.9}\text{As}$ Quantum Well

Magneto-transport measurements of 2D electron and hole gases in a 20 nm $\text{In}_{0.1}\text{Ga}_{0.9}\text{As}$ quantum well at 283 mK exhibited the characteristic Shubnikov de Haas oscillations of 2D transport. The hole gas carrier density ranged between $(0.5 - 2.45) \times 10^{11}\text{cm}^{-2}$ with a carrier mobility between $(0.7 - 1.1) \times 10^5\text{cm}^{-2}\text{V}^{-1}\text{s}^{-1}$ reaching a maximum at a carrier density of $1.2 \times 10^{11}\text{cm}^{-2}$. This range of mobilities is higher than reported mobilities for other $\text{In}_x\text{Ga}_{1-x}\text{As}$ structures[205–207].

The main finding from the measurement of the hole gas was the absence of any measurable spin-orbit coupling. Although a beating pattern was observed and two distinct frequencies measured from the spectra of the oscillations, the source of the second frequency was determined to be from the voltage probe arms of the device where the carrier density was controlled by a separate gate. The same behaviour was seen in the electron gas where there is no spin-orbit coupling and the linear dependence of the second frequency on the gate controlling the carrier density in the voltage probe arms conclusively showed that the beating pattern in the hole gas oscillation was not due to spin-orbit coupling.

The reason for the absence of spin-orbit coupling in the hole gas is unclear. Measurement of a 15 nm AlGaAs/GaAs/AlGaAs quantum well at 283 mK showed a clear beating pattern consistent with two quantum populations at different carrier densities as expected for the Rashba effect [181, 182]. As the $\text{In}_{0.1}\text{Ga}_{0.9}\text{As}$ quantum well is 5 nm wider the energy levels in the quantum well are lower than the AlGaAs/GaAs/AlGaAs quantum well, which should make any spin-orbit effects easier to resolve. Measurements of localisation effects from magnetic field sweeps near 0 T showed only weak localisation, once again with no indication of the expected weak anti-localisation caused by spin-orbit coupling. The measured weak localisation was poorly described by well-known theory and based on work by Zduniak et al [203], it is suspected that the weak anti-localisation peak was not resolved due to difficulties measured at very low magnetic field ($\sim 1 \times 10^{-4}\text{T}$).

At carrier densities lower than $1.4 \times 10^{11}\text{cm}^{-2}$ in the holes gas, the ordering of the observed minima in the Shubnikov de Haas oscillations, changed with even minima suppressed at low magnetic field and odd minima visible. Similar suppression of the even minima has been reported in p-type Ge [187–190] and is an indication that the Zeeman splitting energy is similar to the energy spacing of the Landau levels. Simple models for an exchange interaction enhancement of the g-factor have been suggested [191, 192] which may explain the measured reordering of the Shubnikov de Haas oscillations minima.

Further work on this $\text{In}_{0.1}\text{Ga}_{0.9}\text{As}$ quantum well may wish to focus on the absence of any measurable spin-orbit effects in the $\text{In}_{0.1}\text{Ga}_{0.9}\text{As}$ quantum well, as it is particularly interesting given the clear measurement of such effects in a narrower AlGaAs/GaAs/AlGaAs quantum well. One of the main differences between the AlGaAs/GaAs/AlGaAs and the $\text{In}_{0.1}\text{Ga}_{0.9}\text{As}$ quantum well is the estimated 7% strain in the $\text{In}_{0.1}\text{Ga}_{0.9}\text{As}$ due to the lattice mismatch between $\text{In}_{0.1}\text{Ga}_{0.9}\text{As}$ and GaAs. Further work focusing on the effects of strain in the $\text{In}_{0.1}\text{Ga}_{0.9}$ quantum well with the potential of changing the strain may reveal any suppressed spin-orbit effects.

9.2 Dynamic Magneto-Resistance of Hole Gases in GaAs Heterostructures

Measurement of a 2D hole gas in a $\text{Al}_{0.33}\text{Ga}_{0.64}\text{As}/\text{GaAs}$ heterostructure showed a distinctive asymmetry in the resistivity of the 2D hole gas, depending on the sweep direction of the magnetic field when sweeping across 0 T. Further investigation showed that this asymmetry could not be explained by a mixing between Hall voltage and the longitudinal voltage along the Hall bar, as the size of the asymmetry depended on the sweep rate of the magnetic field.

As a quasi-static magnetic field sweep showed that this asymmetry vanished in the static limit, heating effects such as the magneto-caloric [161] effect were considered as the cause

of the asymmetry in resistivity, as magnetic heating would have a dependence on the sweep rate of the magnetic field. However considering the temperature dependence of the resistivity at zero magnetic field and the temperature dependence of the Shubnikov de Haas oscillations; magnetic heating alone could not explain the measured change in resistivity without a change in sample temperature several orders of magnitude larger than the measured temperature change.

Measurement of the Hall voltage when sweeping the magnetic field showed the persistent field in the superconducting magnet was of the order of a few milli-Tesla and independent of the sweep rate of the magnetic field. This ruled out the persistent field as a cause of the resistivity asymmetry, which was visible over a range of 0.1 T. Any sample-specific or cryostat-specific causes were ruled out as a cause, as this effect has been measured in multiple wafers and cryostats.

Analysis of the Shubnikov de Haas oscillations, using Fourier transforms, showed the presence of two frequencies in the oscillations as expected for a hole gas where the Rashba effect breaks the degeneracy of the $m_j = \pm 3/2$ states. Comparison of the oscillation spectra for different sweep directions of magnetic field showed small changes in the amplitude and frequency of the $m_j = \pm 3/2$ states. These changes, combined with no observation of a similar asymmetry in electron gases, leads to the conclusion that the spin-orbit coupling present in a hole gas and the involvement of two $J = \pm 3/2$ states in the magneto-transport is the cause of the observed dynamic magneto-resistance, although the precise mechanism is not clear.

The sweep rate dependence of the dynamics-magneto resistance raises the possibility of a relaxation time between the dynamic and static magneto-resistances curves. A further study of any relaxation may provide information about the mechanism causing this asymmetry.

9.3 Scattering Rate Modelling - As₂ vs As₄

The carrier mobility of undoped Al_{0.33}Ga_{0.67}As/GaAs heterostructure is limited by scattering from remote charges, in the form of unintentional dopants, from impurities in the MBE grown chamber and surface charge at the Al₂O₃/GaAs interface and scattering due to the interface roughness of the Al_{0.33}Ga_{0.67}As/GaAs heterointerface. Because the mobility is limited by unintentional dopants the mobility can be used as a proxy measurement of the ‘cleanliness’ of the MBE growth chamber. Modelling of the scattering rates allows for a quantitative measurement of the impurity density and interface roughness parameters provide more detailed feedback on the MBE growth of material.

From the measured wafers in this work, the greatest improvement in carrier mobility was seen when grown using As₄ rather than As₂ as the arsenic species. For 100 nm deep structures, where the scattering from surface charge is reduced, the carrier mobility in the As₄ wafers

was 43% higher than the As₂ wafers at $3 \times 10^{11} \text{cm}^{-2}$. Calculating the scattering rates using the simple Fang-Howard wave function allowed numerical values for the background impurity density, interface roughness amplitude, interface roughness correlation length, and surface charge density to be obtained from a non-linear fit of the experimental data. This model confirmed that the carrier mobility was dominated by scattering from background impurities for the 100 nm deep structures, with the As₄ wafer having a 40% lower impurity density than the As₂. The 50 nm device showed the same reduction in impurity density with As₄ as the arsenic species but with scattering from surface charge dominating the mobility of these shallower structures.

The interface roughness is characterised by a roughness amplitude and correlation length. Modelling with the Fang-Howard[137] wave function produces values for the roughness parameters comparable with reported measurements of the amplitude and correlation length[140–145]. The roughness amplitude was approximately 1-2 monolayers in size with the correlation length approximately 5-10 units cells in length.

Extending the model through use of a more general variational wave function similar to ones used by Takada and Uemura[148] and Ando[127] addressed one of the short comings of the Fang-Howard and allowed for alloy scattering in the Al_{0.33}Ga_{0.67}As spacing to be added to the model. With alloy scattering the model still showed a 40% lower impurity density in the As₄, but now with less interface roughness as the Fang-Howard model overestimated the interface roughness scattering due to a lack of alloy scattering.

Finally, from carrier mobility-density data measured from a series of four Hall bars arranged at 45° to each other, the extended model allowed for the measurement of the interface roughness parameters as a function of angle to the major flat of the wafer. The model parameter showed that the As₄ wafers had a lower roughness amplitude and longer correlation length compared to the As₂ wafers, and that the correlation length followed an elliptical dependence on angle to the major flat.

Modelling of the scattering rates provides increased insight into the limits on the carrier mobility in these structures. As the structures used in this work were mainly Al_{0.33}Ga_{0.67}As/GaAs heterostructures the modelling focused on heterostructures. Extending the model quantum well structures and other materials systems such as InGaAs would allow similar insights into the limits of the carrier mobility for a wider range of structures and devices.

9.4 QPC in Induced Holes Gases

The setup of a new atomic layer deposition (ALD) system and process to deposit a Al₂O₃ at 150 °C on GaAs surfaces with AuGeNi and AuBe metal contacts compatible with existing

fabrication processes along with small optimisations of the processing flow in the fabrication of induced devices lead to an increased ohmic contact yield of $> 90\%$ for n-type, p-type, and ambipolar contacts, with a contact resistance between $1\text{ k}\Omega$ and $10\text{ }\Omega$ measured from a transmission line measurement (TLM).

With a yield this high, it was reasonable to attempt to replicate previous nano-structures with a reasonable probability of functional ohmic contacts. The thickness of the Al_2O_3 used in this work was 60 nm , which was thinner than the gate dielectric previously used for induced nano-structures. Attempts to replicate previous quantum dot patterns failed, due to the changes in the fabrication method, in particular the gate dielectric. This meant a re-optimisation of the surface gates used to define nextnano structures was needed. To simplify the nano-structure, a series of quantum point contacts for holes were fabricated with a variety of surface gate geometries. Measurement of the QPCs at 300 mK showed that, of the 700 nm , 400 nm , and 200 nm wide QPC, the 400 nm wide QPC showed the best 1D behaviour with conduction staircases up to 10 sub-band levels visible.

While these devices serve as a proof of concept for further work looking to fabrication induced nano structures, the plateaus of the conduction staircase were not fully resolved suggesting that the QPC are too narrow compared to the length of the QPC. Comparison with other QPC devices reported in literature[225, 226, 229] suggests that there are still improvements that can be made to these devices. The modelling of the potentials in the nano structures using nextnano may provide a starting point for further optimisations of the surface gate geometry of future devices, without the need to fabricate and measure a large number of surface gate geometry variations in the future.

BIBLIOGRAPHY

- [1] R. Willett, J. P. Eisenstein, H. L. Störmer, D. C. Tsui, A. C. Gossard, and J. H. English. Observation of an even-denominator quantum number in the fractional quantum Hall effect. *Physical Review Letters*, 59(15):1776–1779, oct 1987. ISSN 00319007. doi: 10.1103/PhysRevLett.59.1776. URL <https://link.aps.org/doi/10.1103/PhysRevLett.59.1776>.
- [2] K. J. Thomas, J. T. Nicholls, M. Y. Simmons, M. Pepper, D. R. Mace, and D. A. Ritchie. Possible spin polarization in a one-dimensional electron Gas. *Physical Review Letters*, 77(1):135–138, 1996. ISSN 10797114. doi: 10.1103/PhysRevLett.77.135.
- [3] S. M. Cronenwett, S. M. Cronenwett, H. J. Lynch, D. Goldhaber-Gordon, D. Goldhaber-Gordon, L. P. Kouwenhoven, C. M. Marcus, K. Hirose, N. S. Wingreen, and V. Umansky. Low-temperature fate of the 0.7 structure in a point contact: A Kondo-like correlated state in an open system. *Physical Review Letters*, 88(22):226805/1–226805/4, jun 2002. ISSN 00319007. doi: 10.1103/PhysRevLett.88.226805.
- [4] C. W.J. Beenakker. Theory of Coulomb-blockade oscillations in the conductance of a quantum dot. *Physical Review B*, 44(4):1646–1656, 1991. ISSN 01631829. doi: 10.1103/PhysRevB.44.1646.
- [5] M J Kane. Parallel conduction in GaAs/Al_xGa_{1-x} as modulation doped heterojunctions. *Journal of Physics C: Solid State Physics*, 18(29):5629–5636, 1985. ISSN 0022-3719. doi: 10.1088/0022-3719/18/29/013.
- [6] W Y Mak, K Das Gupta, H E Beere, I Farrer, F Sfigakis, and D A Ritchie. Distinguishing impurity concentrations in GaAs and AlGaAs using very shallow undoped heterostructures. *Applied Physics Letters*, 97(24), 2010. ISSN 0003-6951. doi: 10.1063/1.3522651.
- [7] D. H. Cobden, N. K. Patel, M. Pepper, D. A. Ritchie, J. E.F. Frost, and G. A.C. Jones. Noise and reproducible structure in a GaAs/Al_xGa_{1-x}As one-dimensional channel. *Physical Review B*, 44(4):1938–1941, 1991. ISSN 01631829. doi: 10.1103/PhysRevB.44.1938.
- [8] Carey, Stoddart, Bending, Harris, and Foxon. Investigation of deep metastable traps in Si delta -doped GaAs/Al_{0.33}Ga_{0.67}As quantum-well samples using noise spectroscopy.

- Physical review. B, Condensed matter*, 54(4):2813, 1996. ISSN 0163-1829. doi: 10.1103/PhysRevB.54.2813.
- [9] Wing Yee Mak. *Transport experiments in undoped GaAs/AlGaAs heterostructures*. PhD thesis, 2013.
- [10] Egle Tylaite. *Optimising undoped GaAs/AlGaAs quantum dots for radio frequency reflectometry measurements*. PhD thesis, 2016.
- [11] Victoria Helen Russell. *Towards G-factor engineering : electron transport in low dimensional InGaAs and AlGaAs devices*. PhD thesis, 2013.
- [12] William Shockley. The Path to the Conception of the Junction Transistor. *IEEE Transactions on Electron Devices*, 23(7):597–620, nov 1976. ISSN 15579646. doi: 10.1109/T-ED.1976.18463. URL <http://ieeexplore.ieee.org/document/1484034/>.
- [13] Yu B Bolkhovityanov. Gaas epitaxy on si substrates: modern status of research and engineering, 2008.
- [14] V Umansky, M Heiblum, Y Levinson, J Smet, J Nübler, and M Dolev. MBE growth of ultra-low disorder 2DEG with mobility exceeding $35 \times 10^6 \text{cm}^2/\text{Vs}$. *Journal of Crystal Growth*, 311(7):1658–1661, 2009. ISSN 0022-0248. doi: <https://doi.org/10.1016/j.jcrysgro.2008.09.151>. URL <http://www.sciencedirect.com/science/article/pii/S0022024808009901>.
- [15] C W J Beenakker and H Van Houten. Quantum transport in semiconductor nanostructures. *Solid State Physics*, pages 1–228, 1991.
- [16] David Tong. Lectures on the Quantum Hall Effect. *arXiv.org*, 2016.
- [17] J H (John H.) Davies. *The physics of low-dimensional semiconductors an introduction / John H. Davies*. Cambridge, U.K., Cambridge, U.K., 1998.
- [18] T Reker, H Im, L E Bremme, H Choi, Y Chung, P C Klipstein, and Hadas Shtrikman. Effective mass anisotropy of gamma electrons in GaAs/AlGaAs quantum wells. *Physical review letters*, 88(5):56403, 2002. ISSN 0031-9007. doi: 10.1103/PhysRevLett.88.056403.
- [19] Richard P Feynman, Robert B Leighton, Matthew Sands, and R Bruce Lindsay. The Feynman Lectures on Physics, Vol. 3: Quantum Mechanics. *Physics Today*, 19(11):80–83, 1966. ISSN 0031-9228.
- [20] R B Laughlin. Quantized Hall conductivity in two dimensions. *Phys. Rev. B*, 23(10):5632–5633, may 1981. ISSN 01631829. doi: 10.1103/PhysRevB.23.5632. URL <http://link.aps.org/doi/10.1103/PhysRevB.23.5632>.
- [21] K V Klitzing, G Dorda, and M Pepper. New method for high-accuracy determination of the fine-structure constant based on quantized hall resistance. *Phys. Rev. Lett.*, 45(6):494–497, aug 1980. ISSN 00319007. doi: 10.1103/PhysRevLett.45.494. URL <http://link.aps.org/doi/10.1103/PhysRevLett.45.494>.

- [22] B Jeckelmann and B Jeanneret. The quantum Hall effect as an electrical resistance standard. *Measurement Science and Technology*, 14(8):1229–1236, aug 2003. ISSN 0957-0233. doi: 10.1088/0957-0233/14/8/306. URL <https://iopscience.iop.org/article/10.1088/0957-0233/14/8/306>.
- [23] V Umansky, M Heiblum, Y Levinson, J Smet, J Nübler, and M Dolev. MBE growth of ultra-low disorder 2DEG with mobility exceeding 35×10^6 cm²/V s. *Journal of Crystal Growth*, 311(7):1658–1661, 2009. ISSN 0022-0248. doi: 10.1016/j.jcrysgro.2008.09.151.
- [24] Sir Isaac Newton. *Philosophiae Naturalis Principia Mathematica*. Dinslaken : anboco, 2016., Dinslaken, 2016.
- [25] B A Joyce. Molecular beam epitaxy. *Reports on Progress in Physics*, 48(12):1637–1697, dec 1985. ISSN 0034-4885. doi: 10.1088/0034-4885/48/12/002. URL <https://iopscience.iop.org/article/10.1088/0034-4885/48/12/002>.
- [26] K Adomi, J.-I. Chyi, S F Fang, T C Shen, S Strite, and H Morkoç. Molecular beam epitaxial growth of GaAs and other compound semiconductors. *Thin Solid Films*, 205(2):182–212, 1991. ISSN 0040-6090. doi: [https://doi.org/10.1016/0040-6090\(91\)90301-D](https://doi.org/10.1016/0040-6090(91)90301-D). URL <http://www.sciencedirect.com/science/article/pii/004060909190301D>.
- [27] R Bergamaschini, M Salvalaglio, R Backofen, A Voigt, and F Montalenti. Continuum modelling of semiconductor heteroepitaxy: an applied perspective, 2016.
- [28] Ju Wu and Peng Jin. Self-assembly of InAs quantum dots on GaAs(001) by molecular beam epitaxy. *Selected Publications from Chinese Universities*, 10(1):7–58, 2015. ISSN 2095-0462. doi: 10.1007/s11467-014-0422-4.
- [29] Paola Atkinson. *Growth and characterisation of low-dimensional semiconductor structures*. University of Cambridge : PhD. Dissertation., University of Cambridge, 2003.
- [30] Stefan Schmult, Samuel Taylor, and Werner Dietsche. Gallium beam analysis and implications for the growth of ultra-high-mobility GaAs/AlGaAs heterostructures. *Journal of Crystal Growth*, 311(7):1655–1657, 2009. ISSN 0022-0248. doi: <https://doi.org/10.1016/j.jcrysgro.2008.10.014>. URL <http://www.sciencedirect.com/science/article/pii/S0022024808010725>.
- [31] Geoffrey C Gardner, Saeed Fallahi, John D Watson, and Michael J Manfra. Modified MBE hardware and techniques and role of gallium purity for attainment of two dimensional electron gas mobility $>35 \times 10^6$ cm²/Vs in AlGaAs/GaAs quantum wells grown by MBE. *Journal of Crystal Growth*, 441:71–77, 2016. ISSN 0022-0248. doi: <https://doi.org/10.1016/j.jcrysgro.2016.02.010>. URL <http://www.sciencedirect.com/science/article/pii/S0022024816300367>.

- [32] Loren Pfeiffer and K W West. The role of MBE in recent quantum Hall effect physics discoveries. *Physica E: Low-dimensional Systems and Nanostructures*, 20(1):57–64, 2003. ISSN 1386-9477. doi: <https://doi.org/10.1016/j.physe.2003.09.035>. URL <http://www.sciencedirect.com/science/article/pii/S1386947703005174>.
- [33] H L Störmer, R Dingle, A C Gossard, W Wiegmann, and M D Sturge. Two-dimensional electron gas at a semiconductor-semiconductor interface. *Solid State Communications*, 88(11):933–937, 1993. ISSN 0038-1098. doi: 10.1016/0038-1098(93)90272-O.
- [34] R H Harrell, K S Pyskin, M Y Simmons, D a. Ritchie, C J B Ford, G a. C Jones, and M Pepper. Fabrication of high-quality one- and two-dimensional electron gases in undoped GaAs/AlGaAs heterostructures. *Applied Physics Letters*, 74(16):2328, 1999. ISSN 00036951. doi: 10.1063/1.123840. URL <http://scitation.aip.org/content/aip/journal/apl/74/16/10.1063/1.123840>.
- [35] Gregory Snider. Gregory Snider, 2009. URL <https://www3.nd.edu/~ggsnider/>.
- [36] Jian Huang, D. S. Novikov, D. C. Tsui, L. N. Pfeiffer, and K. W. West. Nonactivated transport of strongly interacting two-dimensional holes in GaAs. *Physical Review B - Condensed Matter and Materials Physics*, 74(20), 2006. ISSN 10980121. doi: 10.1103/PhysRevB.74.201302.
- [37] C. Dekker, A. J. Scholten, F. Liefrink, R. Eppenga, H. Van Houten, and C. T. Foxon. Spontaneous resistance switching and low-frequency noise in quantum point contacts. *Physical Review Letters*, 66(16):2148–2151, 1991. ISSN 00319007. doi: 10.1103/PhysRevLett.66.2148.
- [38] D. H. Cobden, A. Savchenko, M. Pepper, N. K. Patel, D. A. Ritchie, J. E.F. Frost, and G. A.C. Jones. Time-irreversible random telegraph signal due to current along a single hopping chain. *Physical Review Letters*, 69(3):502–505, 1992. ISSN 00319007. doi: 10.1103/PhysRevLett.69.502.
- [39] M. J. Testolin, J. H. Cole, and L. C.L. Hollenberg. Modeling two-spin dynamics in a noisy environment. *Physical Review A - Atomic, Molecular, and Optical Physics*, 80(4), oct 2009. ISSN 10502947. doi: 10.1103/PhysRevA.80.042326.
- [40] G. Kopnov, V. Y. Umansky, H. Cohen, D. Shahar, and R. Naaman. Effect of the surface on the electronic properties of a two-dimensional electron gas as measured by the quantum Hall effect. *Physical Review B*, 81(4):045316, jan 2010. ISSN 1098-0121. doi: 10.1103/PhysRevB.81.045316. URL <http://link.aps.org/doi/10.1103/PhysRevB.81.045316>.
- [41] D Laroche, S Das Sarma, G Gervais, M P Lilly, and J L Reno. Scattering mechanism in modulation-doped shallow two-dimensional electron gases. *Applied Physics Letters*, 96 (16), 2010. ISSN 0003-6951. doi: 10.1063/1.3402765.

- [42] W. Y. Mak, F. Sfigakis, K. Das Gupta, O. Klochan, H. E. Beere, I. Farrer, J. P. Griffiths, G. A C Jones, A. R. Hamilton, and D. A. Ritchie. Ultra-shallow quantum dots in an undoped GaAs/AlGaAs two-dimensional electron gas. *Applied Physics Letters*, 102(10):103507, 2013. ISSN 00036951. doi: 10.1063/1.4795613. URL <http://scitation.aip.org/content/aip/journal/apl/102/10/10.1063/1.4795613>.
- [43] R. Nemetudi, M. Kataoka, C. J B Ford, N. J. Appleyard, M. Pepper, D. A. Ritchie, and G. A C Jones. Noninvasive lateral detection of Coulomb blockade in a quantum dot fabricated using atomic force microscopy. *Journal of Applied Physics*, 95(5):2557–2559, 2004. ISSN 00218979. doi: 10.1063/1.1642287.
- [44] X Fu, Q Shi, M A Zudov, Y J Chung, K W Baldwin, L N Pfeiffer, and K W West. Quantum Hall stripes in high-density GaAs/AlGaAs quantum wells, 2019.
- [45] D. C. Tsui, H. L. Stormer, and A. C. Gossard. Two-dimensional magnetotransport in the extreme quantum limit. *Physical Review Letters*, 48(22):1559–1562, may 1982. ISSN 00319007. doi: 10.1103/PhysRevLett.48.1559. URL <http://link.aps.org/doi/10.1103/PhysRevLett.48.1559>.
- [46] W R Clarke, C E Yasin, A R Hamilton, A P Micolich, M Y Simmons, K Muraki, Y Hirayama, M Pepper, and D A Ritchie. Metallic behavior in low-disorder two-dimensional hole systems in the presence of long- and short-range disorder. *Physica E: Low-dimensional Systems and Nanostructures*, 40(5):1599–1601, 2008. ISSN 1386-9477. doi: 10.1016/j.physe.2007.09.179.
- [47] R. J. Nicholas, J. C. Portal, C. Houlbert, P. Perrier, and T. P. Pearsall. An experimental determination of the effective masses for Ga_xIn_{1-x}As_yP_{1-y} alloys grown on InP. *Applied Physics Letters*, 34(8):492–494, 1979. ISSN 00036951. doi: 10.1063/1.90860.
- [48] Andrew J Butterfield and John Szymanski. *spintronics*. Oxford University Press, 5 edition, 2018.
- [49] J W Matthews and A E Blakeslee. Defects in epitaxial multilayers. *Journal of Crystal Growth*, 27:118–125, 1974. ISSN 00220248.
- [50] A. C. Graham. *Many-body interactions in quantum wires*. PhD thesis, 2004. URL <https://doi.org/10.17863/CAM.31397>.
- [51] van Wees Bj, Kouwenhoven, Willems, Harmans, Mooij, van Houten H, Beenakker, Williamson, and Foxon. Quantum ballistic and adiabatic electron transport studied with quantum point contacts. *Physical review. B, Condensed matter*, 43(15):12431, 1991. ISSN 0163-1829. doi: 10.1103/PhysRevB.43.12431.
- [52] A. Douglas Stone and Aaron Szafer. WHAT IS MEASURED WHEN YOU MEASURE A RESISTANCE? - THE LANDAUER FORMULA REVISITED. *IBM Journal of Research and Development*, 32(3):384–413, 1988. ISSN 00188646. doi: 10.1147/rd.323.0384.

- [53] L. A. Tracy, T. W. Hargett, and J. L. Reno. Few-hole double quantum dot in an undoped GaAs/AlGaAs heterostructure. *Applied Physics Letters*, 104(12), mar 2014. ISSN 00036951. doi: 10.1063/1.4868971.
- [54] Jie You, Hai Ou Li, Gang Cao, Guang Wei Deng, Ming Xiao, and Guo Ping Guo. Measuring the coherence of charge states in undoped GaAs/AlGaAs double quantum dots with photon-assisted tunneling. *EPL*, 111(1), jul 2015. ISSN 12864854. doi: 10.1209/0295-5075/111/17001.
- [55] R Hanson, L P Kouwenhoven, J R Petta, S Tarucha, and L M K Vandersypen. Spins in few-electron quantum dots. *Rev. Mod. Phys.*, 79(4):1217–1265, oct 2007. ISSN 00346861. doi: 10.1103/RevModPhys.79.1217. URL <http://link.aps.org/doi/10.1103/RevModPhys.79.1217>.
- [56] Leo Kouwenhoven and Charles Marcus. Quantum dots. *Physics World*, 11(6):35–40, 1998. ISSN 0953-8585.
- [57] Stephanie M. Reimann and Matti Manninen. Electronic structure of quantum dots, oct 2002. ISSN 00346861.
- [58] J van Der Heijden, G Tettamanzi, and S Rogge. Dynamics of a single-atom electron pump. *arXiv.org*, 7(1), 2016. ISSN 20452322. doi: 10.1038/srep44371.
- [59] Joanna Waldie. *Electrical current at the single electron level*. PhD thesis, 2015.
- [60] Lukas Hanschke, Kevin Fischer, Stefan Appel, Daniil Lukin, Jakob Wierzbowski, Shuo Sun, Rahul Trivedi, Jelena Vučković, Jonathan Finley, and Kai Müller. Quantum dot single photon sources with ultra-low multi-photon probability. *arXiv.org*, 4(1), 2018. ISSN 20566387. doi: 10.1038/s41534-018-0092-0.
- [61] Andrew J. Shields, Martin P. O’Sullivan, Ian Farrer, David A. Ritchie, Mark L. Leadbeater, Nalin K. Patel, Richard A. Hogg, Carl E. Norman, Neil J. Curson, and Michael Pepper. Single photon detection with a quantum dot transistor. *Japanese Journal of Applied Physics, Part 2: Letters*, 40(3 B):2058–2064, 2001. ISSN 00214922. doi: 10.1143/jjap.40.2058.
- [62] Fabio Pulizzi. Semiconductor devices: A quantum dot thermometer. *Nature Nanotechnology*, 2014. ISSN 1748-3387. doi: 10.1038/nnano.2014.205.
- [63] Xin Zhang, Hai Ou Li, Ke Wang, Gang Cao, Ming Xiao, and Guo Ping Guo. Qubits based on semiconductor quantum dots, feb 2018. ISSN 20583834.
- [64] Stefan Birner, Tobias Zibold, Till Andlauer, Tillmann Kubis, Matthias Sabathil, Alex Trellakis, and Peter Vogl. Nextnano: General purpose 3-D simulations. *IEEE Transactions on Electron Devices*, 54(9):2137–2142, sep 2007. ISSN 00189383. doi: 10.1109/TED.2007.902871.
- [65] I Vurgaftman, J R Meyer, and L R Ram-Mohan. Band parameters for III–V compound semiconductors and their alloys. *Journal of Applied Physics*, 89(11):5815–5875, jun

2001. ISSN 0021-8979. doi: 10.1063/1.1368156. URL <https://doi.org/10.1063/1.1368156>.
- [66] J Batey and S L Wright. Energy band alignment in GaAs:(Al,Ga)As heterostructures: The dependence on alloy composition. *Journal of Applied Physics*, 59(1):200–209, jan 1986. ISSN 0021-8979. doi: 10.1063/1.336864. URL <https://doi.org/10.1063/1.336864>.
- [67] Miyoko Oku Watanabe, Jiro Yoshida, Masao Mashita, Takatosi Nakanisi, and Akimichi Hojo. Band discontinuity for GaAs/AlGaAs heterojunction determined by C - V profiling technique. *Journal of Applied Physics*, 57(12):5340–5344, 1985. ISSN 0021-8979. doi: 10.1063/1.334852.
- [68] Ugo Siciliani de Cumis. *Towards a complete laboratory for transport and optical studies of electron-hole interactions*. PhD thesis, 2016.
- [69] D Taneja, F Sfigakis, A F Croxall, K D Gupta, Vijay Narayan, Joanna Waldie, I Farrer, and David Ritchie. N-type ohmic contacts to undoped GaAs/AlGaAs quantum wells using only front-sided processing: Application to ambipolar FETs. 2016.
- [70] Michael J Manfra. *Molecular Beam Epitaxy of Ultra-High Quality AlGaAs/GaAs Heterostructures: Enabling Physics in Low-Dimensional Electronic Systems*. 2013.
- [71] Lindhard and J. ON THE PROPERTIES OF A GAS OF CHARGED PARTICLES. *Kgl. Danske Videnskab. Selskab Mat.-fys. Medd.*, Vol: 28, N, jan 1954.
- [72] D Laroche, S Das Sarma, G Gervais, M P Lilly, and J L Reno. Scattering mechanism in modulation-doped shallow two-dimensional electron gases. *Appl. Phys. Lett.*, 96(16), aug 2010. ISSN 00036951. doi: 10.1063/1.3402765. URL <http://arxiv.org/abs/0908.2104><http://dx.doi.org/10.1063/1.3402765>.
- [73] E H Hwang and S Das Sarma. Limit to two-dimensional mobility in modulation-doped GaAs quantum structures: How to achieve a mobility of 100 million. *Physical Review B*, 77(23):235437, jun 2008. doi: 10.1103/PhysRevB.77.235437. URL <https://link.aps.org/doi/10.1103/PhysRevB.77.235437>.
- [74] R H Harrell, J H Thompson, D A Ritchie, M Y Simmons, G A C Jones, and M Pepper. Very high quality 2DEGS formed without dopant in GaAs/AlGaAs heterostructures. *Journal of Crystal Growth*, 201:159–162, 1999. ISSN 0022-0248. doi: 10.1016/S0022-0248(98)01316-5.
- [75] K Das Gupta, A F Croxall, W Y Mak, H E Beere, C A Nicoll, I Farrer, F Sfigakis, and D A Ritchie. Linear non-hysteretic gating of a very high density 2deg in an undoped metal–semiconductor–metal sandwich structure. *Semiconductor Science and Technology*, 27(11):115006, 2012. ISSN 0268-1242. doi: 10.1088/0268-1242/27/11/115006.
- [76] S Sarkozy, K Das Gupta, C Siegert, A Ghosh, M Pepper, I Farrer, H E Beere, D A Ritchie, and G A C Jones. Low temperature transport in undoped mesoscopic structures.

- Applied Physics Letters*, 94(17):172105, apr 2009. ISSN 0003-6951. doi: 10.1063/1.3097806. URL <https://doi.org/10.1063/1.3097806>.
- [77] W Pan, N Masuhara, N S Sullivan, K W Baldwin, K W West, L N Pfeiffer, and D C Tsui. Impact of Disorder on the $\nu=5/2$ Fractional Quantum Hall State. *Phys. Rev. Lett.*, 106(20):206806, may 2011. doi: 10.1103/PhysRevLett.106.206806. URL <https://link.aps.org/doi/10.1103/PhysRevLett.106.206806>.
- [78] R L Willett, L N Pfeiffer, and K W West. Simple-layered high mobility field effect heterostructured two-dimensional electron device. *Applied Physics Letters*, 89(24):242107, 2006. ISSN 00036951. doi: 10.1063/1.2403183. URL <http://scitation.aip.org/content/aip/journal/apl/89/24/10.1063/1.2403183>.
- [79] Michael R. Melloch. Molecular beam epitaxy for high electron mobility modulation-doped two-dimensional electron gases. *Thin Solid Films*, 231(1-2):74–85, aug 1993. ISSN 00406090. doi: 10.1016/0040-6090(93)90704-S.
- [80] Y Tokura, T Saku, S Tarucha, and Y Horikoshi. Anisotropic roughness scattering at a heterostructure interface. *Phys. Rev. B*, 46(23):15558–15561, dec 1992. doi: 10.1103/PhysRevB.46.15558. URL <https://link.aps.org/doi/10.1103/PhysRevB.46.15558>.
- [81] G Weimann and W Schlapp. Molecular beam epitaxial growth and transport properties of modulation-doped AlGaAs-GaAs heterostructures. *Applied Physics Letters*, 46(4):411–413, feb 1985. ISSN 0003-6951. doi: 10.1063/1.95916. URL <https://doi.org/10.1063/1.95916>.
- [82] P T Coleridge. Correlation lengths for scattering potentials in two-dimensional electron gases. *Semiconductor Science and Technology*, 12(1):22–28, jan 1997. ISSN 02681242. doi: 10.1088/0268-1242/12/1/005. URL <http://stacks.iop.org/0268-1242/12/i=1/a=005?key=crossref.afdef81cebec99316a3bbe66166b8425>.
- [83] W Pan, H L Stormer, D C Tsui, L N Pfeiffer, K W Baldwin, and K W West. Experimental evidence for a spin-polarized ground state in the $\nu=5/2$ fractional quantum Hall effect. *Solid State Communications*, 119(12):641–645, 2001. ISSN 0038-1098. doi: 10.1016/S0038-1098(01)00311-8.
- [84] B E Kane, L N Pfeiffer, K W West, and C K Harnett. Variable density high mobility two-dimensional electron and hole gases in a gated GaAs/Al_xGa_{1-x}As heterostructure. *Appl. Phys. Lett.*, 63(15):2132–2134, 1993. ISSN 00036951. doi: 10.1063/1.110563. URL <http://scitation.aip.org/content/aip/journal/apl/63/15/10.1063/1.110563>.
- [85] Tadashi Saku, Koji Muraki, and Yoshiro Hirayama. High-Mobility Two-Dimensional Electron Gas in an Undoped Heterostructure: Mobility Enhancement after Illumina-

- tion. *Japanese Journal of Applied Physics*, 37(Part 2, No. 7A):L765–L767, 1998. ISSN 00214922. doi: 10.1143/JJAP.37.L765.
- [86] Y Hirayama, K Muraki, A Kawaharazuka, K Hashimoto, and T Saku. Backgated layers and nanostructures. *Physica E: Low-dimensional Systems and Nanostructures*, 11(2-3): 155–160, 2001. ISSN 1386-9477. doi: 10.1016/S1386-9477(01)00194-1.
- [87] S Das Sarma and E H Hwang. Metallicity and its low-temperature behavior in dilute two-dimensional carrier systems. *Phys. Rev. B*, 69(19):195305, may 2004. doi: 10.1103/PhysRevB.69.195305. URL <https://link.aps.org/doi/10.1103/PhysRevB.69.195305>.
- [88] E H Hwang and S Das Sarma. Limit to two-dimensional mobility in modulation-doped GaAs quantum structures: How to achieve a mobility of 100 million. *Phys. Rev. B*, 77(23):235437, jun 2008. doi: 10.1103/PhysRevB.77.235437. URL <https://link.aps.org/doi/10.1103/PhysRevB.77.235437>.
- [89] Loren Pfeiffer, K W West, H L Stormer, and K W Baldwin. Electron mobilities exceeding 10^7 cm² / Vs in modulation-doped GaAs, 1989.
- [90] V Umansky, R De-Picciotto, and M Heiblum. Extremely high-mobility two dimensional electron gas: Evaluation of scattering mechanisms. *Applied Physics Letters*, 71(5):683–685, aug 1997. ISSN 0003-6951. doi: 10.1063/1.119829. URL <https://doi.org/10.1063/1.119829>.
- [91] A Matthiessen and C Vogt. Ueber den Einfluss der Temperatur auf die elektrische Leitungsfähigkeit der Legierungen. *Annalen der Physik*, 198(5):19–78, 1864. ISSN 0003-3804. doi: 10.1002/andp.18641980504.
- [92] J C Garcia, A Barski, J P Contour, and J Massies. Dimer arsenic source using a high efficiency catalytic cracking oven for molecular beam epitaxy. *Applied Physics Letters*, 51(8):593–595, 1987. ISSN 0003-6951. doi: 10.1063/1.98987.
- [93] S Yamada, J Okayasu, S Gozu, C U Hong, and H Hori. Dependencies of low-temperature electronic properties of MBE-grown GaAs/AlGaAs single heterojunctions upon arsenic species. *Journal of Crystal Growth*, 201:800–804, 1999. ISSN 0022-0248. doi: 10.1016/S0022-0248(98)01474-2.
- [94] C R Stanley, M C Holland, A H Kean, M B Stanaway, R T Grimes, and J M Chamberlain. Electrical characterization of molecular beam epitaxial GaAs with peak electron mobilities up to 4×10^5 cm² V⁻¹ s⁻¹. *Applied Physics Letters*, 58(5): 478–480, 1991. ISSN 0003-6951. doi: 10.1063/1.104613.
- [95] J H Neave, P K Larsen, J F van Der Veen, P J Dobson, and B A Joyce. Effect of arsenic species (As₂ OR As₄) on the crystallographic and electronic structure of mbe-grown GaAs(001) reconstructed surfaces. *Surface Science*, 133(1):267–278, 1983. ISSN 0039-6028. doi: 10.1016/0039-6028(83)90495-8.

- [96] H Künzel, J Knecht, H Jung, K Wüstel, and K Ploog. The effect of arsenic vapour species on electrical and optical properties of GaAs grown by molecular beam epitaxy. *Materials Science and Processing*, 28(3):167–173, 1982. ISSN 0947-8396. doi: 10.1007/BF00617982.
- [97] J H Neave, P Blood, and B A Joyce. A correlation between electron traps and growth processes in n-GaAs prepared by molecular beam epitaxy. *Applied Physics Letters*, 36(4):311–312, feb 1980. ISSN 0003-6951. doi: 10.1063/1.91474. URL <https://doi.org/10.1063/1.91474>.
- [98] Naresh Chand, T D Harris, S N G Chu, E A Fitzgerald, J Lopata, M Schnoes, and N K Dutta. Performance of a valved arsenic cracker source for MBE growth. *Journal of Crystal Growth*, 126(4):530–538, 1993. ISSN 0022-0248. doi: 10.1016/0022-0248(93)90802-4.
- [99] B J Wu, Y J Mii, M Chen, K L Wang, and J J Murray. Reduced silicon donor incorporation in MBE grown GaAs layers using cracker-generated dimer arsenic. *Journal of Crystal Growth*, 111(1):252–259, 1991. ISSN 0022-0248. doi: 10.1016/0022-0248(91)90980-J.
- [100] J J Harris, C T Foxon, D E Lacklison, and K W J Barnham. Scattering mechanisms in (Al, Ga)As/GaAs 2DEG structures. *Superlattices and Microstructures*, 2(6):563–568, 1986. ISSN 0749-6036. doi: [https://doi.org/10.1016/0749-6036\(86\)90116-3](https://doi.org/10.1016/0749-6036(86)90116-3). URL <http://www.sciencedirect.com/science/article/pii/0749603686901163>.
- [101] J J Harris, C T Foxon, K W J Barnham, D E Lacklison, J Hewett, and C White. Two-dimensional electron gas structures with mobilities in excess of $3 \times 10^6 \text{cm}^2 \text{V}^{-1} \text{s}^{-1}$. *Journal of Applied Physics*, 61(3):1219–1221, feb 1987. ISSN 0021-8979. doi: 10.1063/1.338174. URL <https://doi.org/10.1063/1.338174>.
- [102] C T Foxon. Optimisation of (al,ga)as/gaas two-dimensional electron gas structures for low carrier densities and ultrahigh mobilities at low temperatures. *Semiconductor Science and Technology*, 4(7):582–585, 1989. ISSN 0268-1242. doi: 10.1088/0268-1242/4/7/016.
- [103] Tadashi Saku, Yoshiji Horikoshi, and Yasuhiro Tokura. Limit of electron mobility in AlGaAs/GaAs modulation-doped heterostructures. *Japanese Journal of Applied Physics, Part 1: Regular Papers and Short Notes and Review Papers*, 35(1 A):34–38, 1996. ISSN 00214922. doi: 10.1143/JJAP.35.34.
- [104] C.-T. Liang, Yen Shung Tseng, Jau-Yang Wu, Sheng-Di Lin, Chun-Kai Yang, Yu-Ru Li, Kuang Yao Chen, Po-Tsun Lin, and Li-Hung Lin. Huge positive magnetoresistance in a gated AlGaAs/GaAs high electron mobility transistor structure at high temperatures. *Applied Physics Letters*, 92(13), 2008. ISSN 0003-6951. doi: 10.1063/1.2906360.

- [105] C.-T. Liang, Yu-Ru Li, Li-Hung Lin, Po-Tsun Lin, Chun-Kai Yang, Yen Shung Tseng, Kuang Yao Chen, N R Cooper, M Y Simmons, and D A Ritchie. Electron heating and huge positive magnetoresistance in an AlGaAs/GaAs high electron mobility transistor structure at high temperatures. *Applied Physics Letters*, 92(15), 2008. ISSN 0003-6951. doi: 10.1063/1.2912526.
- [106] Charles A Bishop. 19 - Atomic Layer Deposition. pages 331–336. William Andrew Publishing, Oxford, 2011. ISBN 978-1-4377-7867-0. doi: <https://doi.org/10.1016/B978-1-4377-7867-0.00019-2>. URL <http://www.sciencedirect.com/science/article/pii/B9781437778670000192>.
- [107] Chapter 6 - Thin Films on Silicon. In Markku Tilli, Teruaki Motooka, Veli-Matti Airaksinen, Sami Franssila, Mervi Paulasto-Kröckel, Veikko B T Handbook of Silicon Based MEMS Materials Lindroos, and Technologies (Second Edition), editors, *Micro and Nano Technologies*, pages 124–205. William Andrew Publishing, Boston, 2015. ISBN 978-0-323-29965-7. doi: <https://doi.org/10.1016/B978-0-323-29965-7.00006-3>. URL <http://www.sciencedirect.com/science/article/pii/B9780323299657000063>.
- [108] Ugo Siciliani de Cumis, Joanna Waldie, Andrew F. Croxall, Deepyanti Taneja, Justin Llandro, Ian Farrer, Harvey E. Beere, and David A. Ritchie. A complete laboratory for transport studies of electron-hole interactions in GaAs/AlGaAs ambipolar bilayers. *Applied Physics Letters*, 110(7), feb 2017. ISSN 00036951. doi: 10.1063/1.4976505.
- [109] Richard O. Duda and Peter E. Hart. Use of the Hough Transformation to Detect Lines and Curves in Pictures. *Communications of the ACM*, 15(1):11–15, jan 1972. ISSN 15577317. doi: 10.1145/361237.361242.
- [110] D Taneja, F Sfigakis, A F Croxall, K Das Gupta, V Narayan, J Waldie, I Farrer, and D A Ritchie. N-type ohmic contacts to undoped GaAs/AlGaAs quantum wells using only front-sided processing: application to ambipolar FETs. *Semicond. Sci. Technol.*, 31(6):65013, jun 2016. ISSN 0268-1242. doi: 10.1088/0268-1242/31/6/065013. URL <http://stacks.iop.org/0268-1242/31/i=6/a=065013?key=crossref.c001a5b5e6314e09fd7d6bdb2dfb3f4c>.
- [111] H H Berger. Models for contacts to planar devices. *Solid-State Electronics*, 15(2):145–158, 1972. ISSN 0038-1101. doi: [https://doi.org/10.1016/0038-1101\(72\)90048-2](https://doi.org/10.1016/0038-1101(72)90048-2). URL <http://www.sciencedirect.com/science/article/pii/0038110172900482>.
- [112] G K Reeves and H B Harrison. Obtaining the specific contact resistance from transmission line model measurements. *IEEE Electron Device Letters*, 3(5):111–113, 1982. ISSN 1558-0563 VO - 3. doi: 10.1109/EDL.1982.25502.

- [113] Raymond T Tung. The physics and chemistry of the Schottky barrier height. *Applied Physics Reviews*, 1(1):11304, jan 2014. doi: 10.1063/1.4858400. URL <https://doi.org/10.1063/1.4858400>.
- [114] M J Iqbal, D Reuter, A D Wieck, and C H van der Wal. Robust recipe for low-resistance ohmic contacts to a two-dimensional electron gas in a GaAs/AlGaAs heterostructure. 2014.
- [115] A Ketterson, F Ponse, T Henderson, J Klem, and H Morkoç. Extremely low contact resistances for AlGaAs/GaAs modulation-doped field-effect transistor structures. *Journal of Applied Physics*, 57(6):2305–2307, mar 1985. ISSN 0021-8979. doi: 10.1063/1.334330. URL <https://doi.org/10.1063/1.334330>.
- [116] Armin Richter, Jan Benick, Martin Hermle, and Stefan W. Glunz. Excellent silicon surface passivation with 5 Å thin ALD Al₂O₃ layers: Influence of different thermal post-deposition treatments. *Physica Status Solidi - Rapid Research Letters*, 5(5-6):202–204, jun 2011. ISSN 18626254. doi: 10.1002/pssr.201105188. URL <http://doi.wiley.com/10.1002/pssr.201105188>.
- [117] Annett Winzer, Nadine Szabó, Andre Wachowiak, Paul Matthias Jordan, Johannes Heitmann, and Thomas Mikolajick. Impact of postdeposition annealing upon film properties of atomic layer deposition-grown Al₂O₃ on GaN. *Journal of Vacuum Science & Technology B, Nanotechnology and Microelectronics: Materials, Processing, Measurement, and Phenomena*, 33(1), 2015. ISSN 2166-2746. doi: 10.1116/1.4904968.
- [118] L G Gosset, J.-F Damlencourt, O Renault, D Rouchon, Ph Holliger, A Ermolieff, I Trimaille, J.-J Ganem, F Martin, and M.-N Séméria. Interface and material characterization of thin Al₂O₃ layers deposited by ALD using TMA/H₂O. *Journal of Non-Crystalline Solids*, 303(1):17–23, 2002. ISSN 0022-3093. doi: 10.1016/S0022-3093(02)00958-4.
- [119] P F Carcia, R S Mclean, and M H Reilly. High-performance ZnO thin-film transistors on gate dielectrics grown by atomic layer deposition. *Applied Physics Letters*, 88(12), 2006. ISSN 0003-6951. doi: 10.1063/1.2188379.
- [120] P D Ye, G D Wilk, J Kwo, B Yang, H.-J.L Gossmann, M Frei, S N G Chu, J P Mannaerts, M Sergent, M Hong, K K Ng, and J Bude. GaAs MOSFET with oxide gate dielectric grown by atomic layer deposition. *IEEE Electron Device Letters*, 24(4):209–211, 2003. ISSN 0741-3106. doi: 10.1109/LED.2003.812144.
- [121] Martin M Frank, Glen D Wilk, Dmitri Starodub, Torgny Gustafsson, Eric Garfunkel, Yves J Chabal, John Grazul, and David A Muller. Hf O₂ and Al₂O₃ gate dielectrics on GaAs grown by atomic layer deposition. *Applied Physics Letters*, 86(15), 2005. ISSN 0003-6951. doi: 10.1063/1.1899745.

- [122] Bockelmann, Abstreiter, Weimann, and Schlapp. Single-particle and transport scattering times in narrow GaAs/Al_xGa_{1-x}As quantum wells. *Physical review. B, Condensed matter*, 41(11):7864, 1990. ISSN 0163-1829. doi: 10.1103/PhysRevB.41.7864.
- [123] Tsuneya Ando, Alan B. Fowler, and Frank Stern. Electronic properties of two-dimensional systems. *Reviews of Modern Physics*, 54(2):437–672, apr 1982. ISSN 00346861. doi: 10.1103/RevModPhys.54.437. URL <https://link.aps.org/doi/10.1103/RevModPhys.54.437>.
- [124] Enrico Fermi. *Nuclear physics : a course given by Enrico Fermi at the University of Chicago / notes compiled by Jay Orear, A.H. Rosenfeld, and R.A. Schluter*. [s.l.] : [s.n.], 1949., s.l.], 1949.
- [125] A Kastalsky and J C M Hwang. Study of persistent photoconductivity effect in n-type selectively doped AlGaAs/GaAs heterojunction. *Solid State Communications*, 51(5): 317–322, 1984. ISSN 0038-1098. doi: 10.1016/0038-1098(84)90696-3.
- [126] Eric W Weisstein. Fourier Transform – from Wolfram MathWorld, 2001. ISSN 00280836. URL <https://mathworld.wolfram.com/FourierTransform.html><http://mathworld.wolfram.com/FourierTransform.html>.
- [127] Tsuneya Ando. Self-Consistent Results for a GaAs/Al_xGa_{1-x}As Heterojunction. II. Low Temperature Mobility. *Journal of the Physical Society of Japan*, 51(12):3900–3907, 1982. ISSN 0031-9015. doi: 10.1143/JPSJ.51.3900.
- [128] Jurgen H Smet, Clifton G Fonstad, and Qing Hu. Intrawell and interwell intersubband transitions in multiple quantum wells for far-infrared sources. *Journal of Applied Physics*, 79(12):9305–9320, 1996. ISSN 0021-8979. doi: 10.1063/1.362607.
- [129] P (Paul) Harrison. *Quantum wells, wires, and dots : theoretical and computational physics of semiconductor nanostructures / Paul Harrison*. Chichester : Wiley, c2009 (2010 printing), Chichester, 3rd ed. edition, 2010.
- [130] David Bohm and David Pines. A Collective Description of Electron Interactions. I. Magnetic Interactions. *Phys. Rev.*, 82(5):625–634, jun 1951. doi: 10.1103/PhysRev.82.625. URL <https://link.aps.org/doi/10.1103/PhysRev.82.625>.
- [131] David Pines and David Bohm. A Collective Description of Electron Interactions: II. Collective vs Individual Particle Aspects of the Interactions. *Phys. Rev.*, 85(2):338–353, jan 1952. doi: 10.1103/PhysRev.85.338. URL <https://link.aps.org/doi/10.1103/PhysRev.85.338>.
- [132] David Bohm and David Pines. A Collective Description of Electron Interactions: III. Coulomb Interactions in a Degenerate Electron Gas. *Phys. Rev.*, 92(3):609–625, nov 1953. doi: 10.1103/PhysRev.92.609. URL <https://link.aps.org/doi/10.1103/PhysRev.92.609>.

- [133] Bin Yang, Yong Hai Cheng, Zhan Guo Wang, Ji Ben Liang, Qi Wei Liao, Lan Ying Lin, Zhan Ping Zhu, Bo Xu, and Wei Li. Interface roughness scattering in GaAs-AlGaAs modulation-doped heterostructures. *Applied Physics Letters*, 65(26):3329–3331, 1994. ISSN 00036951. doi: 10.1063/1.112382. URL <https://doi.org/10.1063/1.112382><http://aip.scitation.org/toc/apl/65/26>.
- [134] B R Nag, Sanghamitra Mukhopadhyay, and Madhumita Das. Interface roughness scattering-limited electron mobility in AlAs/GaAs and Ga_{0.5}In_{0.5}P/GaAs wells. *Journal of Applied Physics*, 86(1):459–463, jun 1999. ISSN 0021-8979. doi: 10.1063/1.370752. URL <https://doi.org/10.1063/1.370752>.
- [135] Tsuneya Ando. Screening Effect and Quantum Transport in a Silicon Inversion Layer in Strong Magnetic Fields. *Journal of the Physical Society of Japan*, 43(5):1616–1626, 1977. ISSN 0031-9015. doi: 10.1143/JPSJ.43.1616.
- [136] J W Harrison and J R Hauser. Alloy scattering in ternary III-V compounds. *Physical Review B*, 13(12):5347–5350, 1976. ISSN 0556-2805. doi: 10.1103/PhysRevB.13.5347.
- [137] F. F. Fang and W. E. Howard. Negative field-effect mobility on (100) Si surfaces. *Physical Review Letters*, 16(18):797–799, may 1966. ISSN 00319007. doi: 10.1103/PhysRevLett.16.797. URL <http://link.aps.org/doi/10.1103/PhysRevLett.16.797>.
- [138] P Virtanen, R Gommers, T E Oliphant, M Haberland, T Reddy, D Cournapeau, E Burrowski, P Peterson, W Weckesser, J Bright, S J van Der Walt, M Brett, J Wilson, K J Millman, N Mayorov, A R J Nelson, E Jones, R Kern, E Larson, and C J Carey. SciPy 1.0: fundamental algorithms for scientific computing in Python: 24 February 2020 : An amendment to this paper has been published and can be accessed via a link at the top of the paper. *Nature Methods*, 17(3):261–272, 2020. ISSN 15487091. doi: 10.1038/s41592-019-0686-2.
- [139] Andrew Y Ng. Preventing "Overfitting" of Cross-Validation Data. In *Proc. Fourteenth Int. Conf. Mach. Learn.*, ICML '97, pages 245–253, San Francisco, CA, USA, 1997. Morgan Kaufmann Publishers Inc. ISBN 1-55860-486-3. URL <http://dl.acm.org/citation.cfm?id=645526.657119>.
- [140] T Tsuji, H Yonezu, and N Ohshima. Reduction of surface roughness of an AlAs/GaAs distributed Bragg reflector grown on Si with strained short-period superlattices. *Journal of Crystal Growth*, 201-202:1010–1014, 1999. ISSN 0022-0248. doi: [https://doi.org/10.1016/S0022-0248\(99\)00031-7](https://doi.org/10.1016/S0022-0248(99)00031-7). URL <http://www.sciencedirect.com/science/article/pii/S0022024899000317>.
- [141] R Zhang, S F Yoon, K H Tan, Z Z Sun, and Q F Huang. Effects of carbon tetrabromide flux, substrate temperature and growth rate on carbon-doped GaAs grown by molecular

- beam epitaxy. *Journal of Crystal Growth*, 262(1):113–118, 2004. ISSN 0022-0248. doi: <https://doi.org/10.1016/j.jcrysgro.2003.10.087>. URL <http://www.sciencedirect.com/science/article/pii/S0022024803019699>.
- [142] J A Dura, J G Pellegrino, and C A Richter. X-ray reflectivity determination of interface roughness correlated with transport properties of (AlGa)As/GaAs high electron mobility transistor devices. *Applied Physics Letters*, 69(8):1134–1136, 1996. ISSN 0003-6951. doi: 10.1063/1.117082.
- [143] Jiang Li, A Mirabedini, L J Mawst, D E Savage, R J Matyi, and T F Kuech. Effect of interface roughness on performance of AlGaAs/InGaAs/GaAs resonant tunneling diodes. *Journal of Crystal Growth*, 195(1):617–623, 1998. ISSN 0022-0248. doi: [https://doi.org/10.1016/S0022-0248\(98\)00581-8](https://doi.org/10.1016/S0022-0248(98)00581-8). URL <http://www.sciencedirect.com/science/article/pii/S0022024898005818>.
- [144] A Khatiri, T J Krzyzewski, C F McConville, and T S Jones. Atomic hydrogen cleaning of low-index GaAs surfaces. *Journal of Crystal Growth*, 282(1):1–6, 2005. ISSN 0022-0248. doi: <https://doi.org/10.1016/j.jcrysgro.2005.04.046>. URL <http://www.sciencedirect.com/science/article/pii/S0022024805005051>.
- [145] T Noda, M Tanaka, and H Sakaki. Characterization of lateral correlation length of interface roughness in MBE grown GaAs/AlAs quantum wells by mobility measurement. *Journal of Crystal Growth*, 111(1):348–352, 1991. ISSN 0022-0248. doi: [https://doi.org/10.1016/0022-0248\(91\)90999-L](https://doi.org/10.1016/0022-0248(91)90999-L). URL <http://www.sciencedirect.com/science/article/pii/002202489190999L>.
- [146] Andrew R Conn, Nicholas I M Gould, and Philippe L Toint. *Trust Region Methods*. Society for Industrial and Applied Mathematics, 2000. ISBN 0898714605-9780898714609.
- [147] Y. Xiang and X. G. Gong. Efficiency of generalized simulated annealing. *Physical Review E - Statistical Physics, Plasmas, Fluids, and Related Interdisciplinary Topics*, 62(3 B):4473–4476, sep 2000. ISSN 1063651X. doi: 10.1103/PhysRevE.62.4473.
- [148] Yasutami Takada and Yasutada Uemura. Subband Structures of N-Channel Inversion Layers on III–V Compounds –A Possibility of the Gate Controlled Gunn Effect–. *Journal of the Physical Society of Japan*, 43(1):139–150, 1977. ISSN 0031-9015. doi: 10.1143/JPSJ.43.139.
- [149] A F Croxall, B Zheng, F Sfigakis, K Das Gupta, I Farrer, C A Nicoll, H E Beere, and D A Ritchie. Demonstration and characterization of an ambipolar high mobility transistor in an undoped GaAs/AlGaAs quantum well. *Appl. Phys. Lett.*, 102(8):82105, 2013. ISSN 00036951. doi: 10.1063/1.4793658. URL <http://scitation.aip.org/content/aip/journal/apl/102/8/10.1063/1.4793658>.

- [150] A Isihara and L Smrcka. Density and magnetic field dependences of the conductivity of two-dimensional electron systems. *Journal of Physics C: Solid State Physics*, 19(34): 6777–6789, 1986. ISSN 0022-3719. doi: 10.1088/0022-3719/19/34/015.
- [151] P T Coleridge. Small-angle scattering in two-dimensional electron gases. *Phys. Rev. B*, 44(8):3793–3801, aug 1991. doi: 10.1103/PhysRevB.44.3793. URL <https://link.aps.org/doi/10.1103/PhysRevB.44.3793>.
- [152] Qi Qian, James Nakamura, Saeed Fallahi, Geoffrey Gardner, John Watson, Silvia Luscher, Joshua Folk, Gabor Csathy, and Michael Manfra. Quantum Lifetime in Ultra-High Quality GaAs Quantum Wells: Relationship to $\Delta_{5/2}$ and Impact of Density Fluctuations. *arXiv.org*, 96(3), 2017. ISSN 24699950. doi: 10.1103/PhysRevB.96.035309.
- [153] B Rössner, D Chrastina, G Isella, and H von Känel. Scattering mechanisms in high-mobility strained Ge channels. *Applied Physics Letters*, 84(16):3058–3060, apr 2004. ISSN 0003-6951. doi: 10.1063/1.1707223. URL <https://doi.org/10.1063/1.1707223>.
- [154] B Fluegel, R N Kini, A J Ptak, D Beaton, K Alberi, and A Mascarenhas. Shubnikov-de Haas measurement of electron effective mass in GaAs_{1-x}Bi_x. *Applied Physics Letters*, 99(16):162108, oct 2011. ISSN 0003-6951. doi: 10.1063/1.3655198. URL <https://doi.org/10.1063/1.3655198>.
- [155] V A Kulbachinskii, L N Oveshnikov, R A Lunin, N A Yuzeeva, G B Galiev, and E A Klimov. Shubnikov de Haas Effect and Electron Mobilities in the Isomorphic InGaAs Quantum Well With the InAs Insert on the InP Substrate, 2014.
- [156] R G Mani and J R Anderson. Study of the single-particle and transport lifetimes in GaAs/Al_xGa_{1-x}As. *Phys. Rev. B*, 37(8):4299–4302, mar 1988. doi: 10.1103/PhysRevB.37.4299. URL <https://link.aps.org/doi/10.1103/PhysRevB.37.4299>.
- [157] Sarah J MacLeod, Theodore P Martin, Adam P Micolich, and Alex R Hamilton. Single particle and momentum relaxation times in two-dimensional electron systems (updated May 14, 2008). In *Proc.SPIE*, volume 6800, jan 2008. doi: 10.1117/12.759655. URL <https://doi.org/10.1117/12.759655>.
- [158] S Macleod, K Chan, T Martin, A Hamilton, A See, A Micolich, M Aagesen, and P Lindelof. The role of background impurities in the single particle relaxation lifetime of a two-dimensional electron gas. *arXiv.org*, 80(3), 2009. ISSN 10980121. doi: 10.1103/PhysRevB.80.035310.
- [159] Tse-Ming Chen, C.-T. Liang, M Y Simmons, Gil-Ho Kim, and D A Ritchie. Transport and quantum lifetime dependence on electron density in gated GaAs/AlGaAs het-

- erostructures. *Physica E: Low-dimensional Systems and Nanostructures*, 22(1):312–315, 2004. ISSN 1386-9477. doi: <https://doi.org/10.1016/j.physe.2003.12.009>. URL <http://www.sciencedirect.com/science/article/pii/S1386947703008506>.
- [160] A D C Grassie, K M Hutchings, M Lakrimi, C T Foxon, and J J Harris. Shubnikov-de Haas effect in submicron-width GaAs/Ga_{1-x}As_x heterojunction wires. *Phys. Rev. B*, 36(8):4551–4554, sep 1987. doi: 10.1103/PhysRevB.36.4551. URL <https://link.aps.org/doi/10.1103/PhysRevB.36.4551>.
- [161] Richard Rennie and Jonathan Law. magnetocaloric effect, 2019. URL <http://www.oxfordreference.com/view/10.1093/acref/9780198821472.001.0001/acref-9780198821472-e-1820>.
- [162] D V Dmitriev, I S Strygin, A A Bykov, S Dietrich, and S A Vitkalov. Transport relaxation time and quantum lifetime in selectively doped GaAs/AlAs heterostructures. *JETP Letters*, 95(8):420–423, 2012. ISSN 1090-6487. doi: 10.1134/S0021364012080048. URL <https://doi.org/10.1134/S0021364012080048>.
- [163] P Wisniewski, T Suski, E Litwin-Staszewska, G Brunthaler, and K Köhler. Mobility and quantum lifetime in a GaAs/AlGaAs heterostructure: tuning of the remote-charge correlations. *Surface Science*, 361-362:579–582, 1996. ISSN 0039-6028. doi: [https://doi.org/10.1016/0039-6028\(96\)00473-6](https://doi.org/10.1016/0039-6028(96)00473-6). URL <http://www.sciencedirect.com/science/article/pii/0039602896004736>.
- [164] B Das, S Subramaniam, M R Melloch, and D C Miller. Single-particle and transport scattering times in a back-gated GaAs/Al_xGa_{1-x}As modulation-doped heterostructure. *Phys. Rev. B*, 47(15):9650–9653, apr 1993. doi: 10.1103/PhysRevB.47.9650. URL <https://link.aps.org/doi/10.1103/PhysRevB.47.9650>.
- [165] R Taboryskit and P E Lindelof. Semiconductor Science and Technology Weak localisation and electron-electron interaction in modulation-doped GaAs/AlGaAs heterostructures. Technical report, 1990. URL <http://iopscience.iop.org/article/10.1088/0268-1242/5/9/003/pdf>.
- [166] I Tângring, H Q Ni, B P Wu, D H Wu, Y H Xiong, S S Huang, Z C Niu, S M Wang, Z H Lai, and A Larsson. 1.58 μ m InGaAs quantum well laser on GaAs. *Applied Physics Letters*, 91(22), 2007. ISSN 0003-6951. doi: 10.1063/1.2803756.
- [167] Tae-Woo Kim, Hyuk-Min Kwon, Seung Heon Shin, Chan-Soo Shin, Won-Kyu Park, Eddie Chiu, Manny Rivera, Jae Ik Lew, Dmitry Veksler, Tommaso Orzali, and Dae-Hyun Kim. Impact of H₂ High-Pressure Annealing Onto InGaAs Quantum-Well Metal-Oxide-Semiconductor Field-Effect Transistors With Al₂O₃/HfO₂ Gate-Stack. *IEEE Electron Device Letters*, 36(7):672–674, 2015. ISSN 0741-3106. doi: 10.1109/LED.2015.2438433.

- [168] Takashi Ueda, Sachiko Onozawa, Masahiro Akiyama, and Masaaki Sakuta. Heteroepitaxy of InGaAs on GaAs substrate with InAlAs intermediate layer. *Journal of Crystal Growth*, 93(1):517–522, 1988. ISSN 0022-0248. doi: [https://doi.org/10.1016/0022-0248\(88\)90576-3](https://doi.org/10.1016/0022-0248(88)90576-3). URL <http://www.sciencedirect.com/science/article/pii/S0022024888905763>.
- [169] D C Radulescu, W J Schaff, L F Eastman, J M Ballingall, G O Ramseyer, and S D Hersee. Influence of substrate temperature and InAs mole fraction on the incorporation of indium during molecular-beam epitaxial growth of InGaAs single quantum wells on GaAs. *Journal of Vacuum Science & Technology B: Microelectronics Processing and Phenomena*, 7(1):111–115, jan 1989. ISSN 0734-211X. doi: 10.1116/1.584432. URL <https://avs.scitation.org/doi/abs/10.1116/1.584432>.
- [170] Takuo Sasaki, Hidetoshi Suzuki, Akihisa Sai, Masamitsu Takahashi, Seiji Fujikawa, Itaru Kamiya, Yoshio Ohshita, and Masafumi Yamaguchi. Growth temperature dependence of strain relaxation during InGaAs/GaAs(001) heteroepitaxy. *Journal of Crystal Growth*, 323(1):13–16, 2011. ISSN 0022-0248. doi: <https://doi.org/10.1016/j.jcrysgro.2010.10.005>. URL <http://www.sciencedirect.com/science/article/pii/S0022024810007359>.
- [171] Ryota Deki, Takuo Sasaki, and Masamitsu Takahashi. Strain relaxation and compositional separation during growth of InGaAs/GaAs(001). *Journal of Crystal Growth*, 468:241–244, 2017. ISSN 0022-0248. doi: <https://doi.org/10.1016/j.jcrysgro.2017.01.028>. URL <http://www.sciencedirect.com/science/article/pii/S0022024817300362>.
- [172] Brian R Bennett, Theresa F Chick, J Brad Boos, James G Champlain, and Adrian A Podpirka. Strained InGaAs/InAlAs quantum wells for complementary III–V transistors. *Journal of Crystal Growth*, 388:92–97, 2014. ISSN 0022-0248. doi: <https://doi.org/10.1016/j.jcrysgro.2013.11.035>. URL <http://www.sciencedirect.com/science/article/pii/S0022024813007884>.
- [173] M R Astley, M Kataoka, C J B Ford, C H W Barnes, M D Godfrey, I Farrer, D A Ritchie, D Anderson, G A C Jones, M Pepper, and S N Holmes. Quantized acoustoelectric current in an InGaAs quantum well. *Journal of Applied Physics*, 103(9), 2008. ISSN 0021-8979. doi: 10.1063/1.2906330.
- [174] G Bastard. Energy levels and alloy scattering in InP-In (Ga)As heterojunctions. *Applied Physics Letters*, 43(6):591–593, 1983. ISSN 0003-6951.
- [175] T. Walther, A.G. Cullis, D.J. Norris, and M. Hopkinson. Nature of the Stranski-Krastanow transition during epitaxy of InGaAs on GaAs. *Physical Review Letters*, 86(11):2381–2384, 2001. doi: 10.1103/PhysRevLett.86.2381.
- [176] Takahiro Kitada, Satoshi Shimomura, and Satoshi Hiyamizu. Surface segregation of indium atoms during molecular beam epitaxy of InGaAs/GaAs superlattices on

- (n11)A GaAs substrates. *Journal of Crystal Growth*, 301-302:172–176, 2007. ISSN 0022-0248. doi: <https://doi.org/10.1016/j.jcrysgro.2006.11.170>. URL <http://www.sciencedirect.com/science/article/pii/S0022024806015016>.
- [177] R Contreras-Guerrero, A Guillen-Cervantes, Z Rivera-Alvarez, A Pulzara-Mora, S Gallardo-Hernandez, Y Kudriatsev, V M Sanchez-Resendiz, J S Rojas-Ramirez, E Cruz-Hernandez, V H Méndez-García, L Zamora-Peredo, and M Lopez-Lopez. Study of AlGaAs/GaAs quantum wells grown by molecular beam epitaxy on GaAs substrates subjected to different treatments. *Journal of Crystal Growth*, 311(7):1666–1670, 2009. ISSN 0022-0248. doi: <https://doi.org/10.1016/j.jcrysgro.2008.11.010>. URL <http://www.sciencedirect.com/science/article/pii/S0022024808012311>.
- [178] Vinicio Tarquini, Talbot Knighton, Zhe Wu, Jian Huang, Loren Pfeiffer, and Ken West. Degeneracy and effective mass in the valence band of two-dimensional (100)-GaAs quantum well systems. *Applied Physics Letters*, 104(9), 2014. ISSN 0003-6951. doi: 10.1063/1.4867086.
- [179] Evan O Kane. Band structure of indium antimonide. *Journal of Physics and Chemistry of Solids*, 1(4):249–261, 1957. ISSN 0022-3697. doi: [https://doi.org/10.1016/0022-3697\(57\)90013-6](https://doi.org/10.1016/0022-3697(57)90013-6). URL <http://www.sciencedirect.com/science/article/pii/0022369757900136>.
- [180] U Rössler. Nonparabolicity and warping in the conduction band of GaAs. *Solid State Communications*, 49(10):943–947, 1984. ISSN 0038-1098. doi: 10.1016/0038-1098(84)90299-0.
- [181] J. Schliemann. Spin Hall effect. *International Journal of Modern Physics B*, 20(9): 1015–1036, 2006. doi: 10.1142/S021797920603370X.
- [182] John Schliemann and Daniel Loss. Anisotropic transport in a two-dimensional electron gas in the presence of spin-orbit coupling. *Phys. Rev. B*, 68(16):165311, oct 2003. doi: 10.1103/PhysRevB.68.165311. URL <https://link.aps.org/doi/10.1103/PhysRevB.68.165311>.
- [183] Sadao Adachi. *Physical properties of III-V semiconductor compounds : InP, InAs, GaAs, GaP, InGaAs, and InGaAsP*. New York, New York, 1992.
- [184] S D Bystrov, A M Kreshchuk, S V Le Tuan, T A Novikov, and I G Polyanskaya. Savel'ev, and A. Ya. Shik. *Fiz. Tekh. Poluprovodn*, 28:91, 1994.
- [185] I B Berkutov, V V Andrievskii, Yu. F Komnik, O A Mironov, M Mironov, and D R Leadley. Shubnikov-de Haas oscillations of the conductivity of a two-dimensional gas in quantum wells based on germanium and silicon. Determination of the effective mass and g factor. *Low Temperature Physics*, 35(2):141–145, feb 2009. ISSN 1063-777X. doi: 10.1063/1.3075945. URL <https://doi.org/10.1063/1.3075945>.

- [186] Q Qian, J Nakamura, S Fallahi, G C Gardner, J D Watson, S Lüscher, J A Folk, G A Csáthy, and M J Manfra. Quantum lifetime in ultrahigh quality GaAs quantum wells: Relationship to $\Delta_{5/2}$ and impact of density fluctuations. *Phys. Rev. B*, 96(3): 35309, jul 2017. doi: 10.1103/PhysRevB.96.035309. URL <https://link.aps.org/doi/10.1103/PhysRevB.96.035309>.
- [187] S N Holmes, P J Newton, J Llandro, R Mansell, C H W Barnes, C Morrison, and M Myronov. Spin-splitting in p-type Ge devices. *Journal of Applied Physics*, 120(8):85702, 2016. doi: 10.1063/1.4961416. URL <https://doi.org/10.1063/1.4961416>.
- [188] F F Fang, P J Wang, B S Meyerson, J J Nocera, and K E Ismail. Two-dimensional hole gas in Si/SiGe heterostructures. *Surface Science*, 263(1):175–178, 1992. ISSN 0039-6028. doi: [https://doi.org/10.1016/0039-6028\(92\)90331-Y](https://doi.org/10.1016/0039-6028(92)90331-Y). URL <http://www.sciencedirect.com/science/article/pii/003960289290331Y>.
- [189] I L Drichko, I Yu. Smirnov, A V Suslov, O A Mironov, and D R Leadley. Magnetoresistivity in a tilted magnetic field in p-Si/SiGe/Si heterostructures with an anisotropic g-factor. Part II. *Journal of Experimental and Theoretical Physics*, 115(3):480–484, 2012. ISSN 1090-6509. doi: 10.1134/S1063776112080067. URL <https://doi.org/10.1134/S1063776112080067>.
- [190] R B Dunford, R Newbury, V A Stadnik, F F Fang, R G Clark, R H McKenzie, R P Starrett, E E Mitchell, P J Wang, J O Chu, K E Ismail, and B S Meyerson. Low temperature magnetotransport of 2D electron and hole systems in high-mobility Si/Si_{1-x}Ge_x heterostructures. *Surface Science*, 361-362:550–555, 1996. ISSN 0039-6028. doi: [https://doi.org/10.1016/0039-6028\(96\)00467-0](https://doi.org/10.1016/0039-6028(96)00467-0). URL <http://www.sciencedirect.com/science/article/pii/0039602896004670>.
- [191] Tsuneya Ando and Yasutada Uemura. Theory of Oscillatory g Factor in an MOS Inversion Layer Under Strong Magnetic Fields. *Journal of the Physical Society of Japan*, 37(4):1044–1052, oct 1974. ISSN 13474073. doi: 10.1143/JPSJ.37.1044. URL <http://journals.jps.jp/doi/10.1143/JPSJ.37.1044>.
- [192] Th. Englert, D. C. Tsui, A. C. Gossard, and Ch. Uihlein. g-Factor enhancement in the 2D electron gas in GaAs/AlGaAs heterojunctions. *Surface Science*, 113(1-3):295–300, jan 1982. ISSN 00396028. doi: 10.1016/0039-6028(82)90604-5. URL <https://www.sciencedirect.com/science/article/pii/0039602882906045>.
- [193] C Morrison, P Wiśniewski, S D Rhead, J Foronda, D R Leadley, and M Myronov. Observation of Rashba zero-field spin splitting in a strained germanium 2D hole gas. *Applied Physics Letters*, 105(18):182401, nov 2014. ISSN 0003-6951. doi: 10.1063/1.4901107. URL <https://doi.org/10.1063/1.4901107>.

- [194] Fabrizio Nichele, Atindra Nath Pal, Roland Winkler, Christian Gerl, Werner Wegscheider, Thomas Ihn, and Klaus Ensslin. Spin-orbit splitting and effective masses in p -type GaAs two-dimensional hole gases. *Phys. Rev. B*, 89(8):81306, feb 2014. doi: 10.1103/PhysRevB.89.081306. URL <https://link.aps.org/doi/10.1103/PhysRevB.89.081306>.
- [195] Sudip Chakravarty and Albert Schmid. Weak localization: The quasiclassical theory of electrons in a random potential. *Physics Reports*, 140(4):193–236, 1986. ISSN 0370-1573. doi: 10.1016/0370-1573(86)90027-X.
- [196] F Rortais, S Oyarzún, F Bottegoni, J. C. Rojas-Sánchez, P Laczkowski, A Ferrari, C Vergnaud, C Ducruet, C Beigné, N Reyren, A Marty, J. P. Attané, L Vila, S Gambarelli, J Widiez, F Ciccacci, H Jaffrès, J. M. George, and M Jamet. Spin transport in p-type germanium. *Journal of Physics Condensed Matter*, 28(16):165801, apr 2016. ISSN 1361648X. doi: 10.1088/0953-8984/28/16/165801. URL <http://stacks.iop.org/0953-8984/28/i=16/a=165801?key=crossref.7865b880d94e8f24eff1cf21d3e09e5f>.
- [197] S A Wolf, D D Awschalom, R A Buhrman, J M Daughton, S. Von Molnár, M L Roukes, A Y Chtchelkanova, and D M Treger. Spintronics: A spin-based electronics vision for the future, nov 2001. ISSN 00368075. URL <http://www.ncbi.nlm.nih.gov/pubmed/11711666>.
- [198] D (David) Awschalom, D (Daniel) Loss, and N (Nitin) Samarth. *Semiconductor spintronics and quantum computation/D. D. Awschalom, D. Loss, N. Samarth (eds.)*. Berlin, Berlin, 2002.
- [199] Igor Žitnik, Jaroslav Fabian, and S Das Sarma. Spintronics: Fundamentals and applications. *Rev. Mod. Phys.*, 76(2):323–410, apr 2004. doi: 10.1103/RevModPhys.76.323. URL <https://link.aps.org/doi/10.1103/RevModPhys.76.323>.
- [200] J D Koralek, C P Weber, J Orenstein, B A Bernevig, Shou-Cheng Zhang, S Mack, and D D Awschalom. Emergence of the persistent spin helix in semiconductor quantum wells. *Nature*, 458(7238):610–613, 2009. ISSN 1476-4687. doi: 10.1038/nature07871. URL <https://doi.org/10.1038/nature07871>.
- [201] F Dettwiler, S Mack, P Weigele, J Egues, D Awschalom, and D Zumbühl. Electrical spin protection and manipulation via gate-locked spin-orbit fields. *arXiv.org*, 2014.
- [202] L J Cui, Y P Zeng, B Q Wang, Z P Zhu, L Y Lin, C P Jiang, S L Guo, and J H Chu. Zero-field spin splitting in $\text{In}_{0.52}\text{Al}_{0.48}\text{As}/\text{In}_x\text{Ga}_{1-x}\text{As}$ metamorphic high-electron-mobility-transistor structures on GaAs substrates using Shubnikov-de Haas measurements. *Applied Physics Letters*, 80(17):3132–3134, apr 2002. ISSN 0003-6951. doi: 10.1063/1.1476055. URL <https://doi.org/10.1063/1.1476055>.

- [203] A. Zduniak, M. Dyakonov, and W. Knap. Universal behavior of magnetoconductance due to weak localization in two dimensions. *Physical Review B - Condensed Matter and Materials Physics*, 56(4):1996–2003, jul 1997. ISSN 1550235X. doi: 10.1103/PhysRevB.56.1996. URL <https://link.aps.org/doi/10.1103/PhysRevB.56.1996>.
- [204] P P Szydlik, S A Alterovitz, E J Haugland, B Segall, T S Henderson, J Klem, and H Morkoc. Shubnikov-de Haas measurements of the 2-D electron gas in pseudomorphic In_{0.1}Ga_{0.9}As grown on GaAs. *Superlattices and Microstructures*, 4(4):619–621, 1988. ISSN 0749-6036. doi: [https://doi.org/10.1016/0749-6036\(88\)90248-0](https://doi.org/10.1016/0749-6036(88)90248-0). URL <http://www.sciencedirect.com/science/article/pii/0749603688902480>.
- [205] M Rosini, E Cancellieri, D Ercolani, G Biasiol, C Jacoboni, and L Sorba. Transport anisotropy in InGaAs 2D electron gases. *Physica E: Low-dimensional Systems and Nanostructures*, 40(5):1392–1394, 2008. ISSN 1386-9477. doi: <https://doi.org/10.1016/j.physe.2007.09.126>. URL <http://www.sciencedirect.com/science/article/pii/S1386947707004614>.
- [206] E Diez, Y P Chen, S Avesque, M Hilke, E Peled, D Shahar, J M Cerveró, D L Sivco, and A Y Cho. Two-dimensional electron gas in InGaAs/InAlAs quantum wells. *Applied Physics Letters*, 88(5):52107, jan 2006. ISSN 0003-6951. doi: 10.1063/1.2168666. URL <https://doi.org/10.1063/1.2168666>.
- [207] W Z Zhou, W Wang, Z G Chang, Y Z Wang, Z Q Lan, L Y Shang, T Lin, L J Cui, Y P Zeng, G X Li, C H Yu, J Guo, and J H Chu. Effects of scattering on two-dimensional electron gases in InGaAs/InAlAs quantum wells. *Journal of Applied Physics*, 112(2), 2012. ISSN 0021-8979. doi: 10.1063/1.4737777.
- [208] Scott Dietrich, Jesse Kanter, William Mayer, Sergey Vitkalov, D V Dmitriev, and A A Bykov. Quantum electron lifetime in GaAs quantum wells with three populated subbands. *Physical Review B*, 92(15), 2015. ISSN 1098-0121. doi: 10.1103/PhysRevB.92.155411.
- [209] X. Fu, A. Riedl, M. Borisov, M. A. Zudov, J. D. Watson, G. Gardner, M. J. Manfra, K. W. Baldwin, L. N. Pfeiffer, and K. W. West. Effect of illumination on quantum lifetime in GaAs quantum wells. *Physical Review B*, 98(19), apr 2019. doi: 10.1103/PhysRevB.98.195403. URL <http://arxiv.org/abs/1904.03146><http://dx.doi.org/10.1103/PhysRevB.98.195403>.
- [210] M Hilke, P Poole, S Studenikin, and D Austing. Phase Diagram of Quantum Hall Breakdown and Non-linear Phenomena for InGaAs/InP Quantum Wells. *arXiv.org*, 98(16), 2018. ISSN 24699950. doi: 10.1103/PhysRevB.98.165434.
- [211] R Danneau, W R Clarke, O Klochan, A P Micolich, A R Hamilton, M Y Simmons, M Pepper, and D A Ritchie. Conductance quantization and the $0.7 \times 2 e^2 / h$ conduct-

- ance anomaly in one-dimensional hole systems. *Applied Physics Letters*, 88(1), 2006. ISSN 0003-6951. doi: 10.1063/1.2161814.
- [212] Florian Bauer, Jan Heyder, Enrico Schubert, David Borowsky, Daniela Taubert, Benedikt Bruognolo, Dieter Schuh, Werner Wegscheider, Jan Von Delft, and Stefan Ludwig. Microscopic origin of the ‘0.7-anomaly’ in quantum point contacts. *Nature*, 501(7465): 73, 2013. ISSN 0028-0836. doi: 10.1038/nature12421.
- [213] H. Hou, Y. Kozuka, Jun Wei Liao, L. W. Smith, D. Kos, J. P. Griffiths, J. Falson, A. Tsukazaki, M. Kawasaki, and C. J.B. Ford. Quantized conductance of one-dimensional strongly correlated electrons in an oxide heterostructure. *Physical Review B*, 99(12), mar 2019. ISSN 24699969. doi: 10.1103/PhysRevB.99.121302.
- [214] B. Roche, P. Roulleau, T. Jullien, Y. Jompol, I. Farrer, D. A. Ritchie, and D. C. Glattli. Harvesting dissipated energy with a mesoscopic ratchet. *Nature Communications*, 6, apr 2015. ISSN 20411723. doi: 10.1038/ncomms7738.
- [215] Pojen Chuang, Sheng-Chin Ho, Luke Smith, F Sfigakis, Michael Pepper, Chin-Hung Chen, Ju-Chun Fan, J P Griffiths, Ian Farrer, Harvey Beere, G A C Jones, David Ritchie, and T-M Chen. All-electric and all-semiconductor spin field effect transistors. *Nature Nanotechnology*, 2014.
- [216] Pengcheng Ma. Using multiplexers to study the statistics of quantum phenomenon in one-dimensional wires, 2018.
- [217] Michael Robert Astley. *Surface-acoustic-wave-defined dynamic quantum dots*. PhD thesis, 2008.
- [218] D Q Wang, A R Hamilton, I Farrer, D A Ritchie, and O Klochan. Double-layer-gate architecture for few-hole gaas quantum dots. *Nanotechnology*, 27(33):334001, 2016. ISSN 0957-4484. doi: 10.1088/0957-4484/27/33/334001.
- [219] A M See, O Klochan, A R Hamilton, A P Micolich, M Aagesen, and P E Lindelof. Al-GaAs/GaAs single electron transistor fabricated without modulation doping. *Appl. Phys. Lett.*, 96(11):112104, 2010. ISSN 00036951. doi: 10.1063/1.3358388. URL <http://scitation.aip.org/content/aip/journal/apl/96/11/10.1063/1.3358388>.
- [220] Denis V Bulaev and Daniel Loss. Spin relaxation and decoherence of holes in quantum dots. *Phys. Rev. Lett.*, 95(7):76805, aug 2005. ISSN 00319007. doi: 10.1103/PhysRevLett.95.076805. URL <http://link.aps.org/doi/10.1103/PhysRevLett.95.076805>.
- [221] F Sfigakis, K Das Gupta, S Sarkozy, I Farrer, D A Ritchie, M Pepper, and G A C Jones. Benefits of using undoped GaAs/AlGaAs heterostructures: A case study of the zero-bias bias anomaly in quantum wires. *Physica E: Low-dimensional Systems and Nanostructures*, 42(4):1200–1204, 2010. ISSN 1386-9477. doi: <https://doi.org/10.1016/>

- j.physe.2009.12.018. URL <http://www.sciencedirect.com/science/article/pii/S138694770900633X>.
- [222] Büttiker. Quantized transmission of a saddle-point constriction. *Physical review. B, Condensed matter*, 41(11):7906, 1990. ISSN 0163-1829. doi: 10.1103/PhysRevB.41.7906.
- [223] D A Pokhabov, A G Pogosov, E Yu. Zhdanov, A A Shevyrin, A K Bakarov, and A A Shklyayev. Lateral-electric-field-induced spin polarization in a suspended GaAs quantum point contact. *Applied Physics Letters*, 112(8), 2018. ISSN 0003-6951. doi: 10.1063/1.5019906.
- [224] Y Komijani, M Csontos, T Ihn, K Ensslin, Y Meir, D Reuter, and A D Wieck. Origins of conductance anomalies in a p -type GaAs quantum point contact. *Phys. Rev. B*, 87(24):245406, jun 2013. doi: 10.1103/PhysRevB.87.245406. URL <https://link.aps.org/doi/10.1103/PhysRevB.87.245406>.
- [225] A Kozikov, R Steinacher, T Ihn, K Ensslin, C Reichl, and W Wegscheider. Mode specific backscattering in a quantum point contact. *arXiv.org*, 15(12), 2015. ISSN 15306984. doi: 10.1021/acs.nanolett.5b03170.
- [226] M Seo and Y Chung. Anomalous conductance quantization observed in a quantum point contact with an asymmetric confinement potential. *Journal of the Korean Physical Society*, 60(11):1907–1910, 2012. ISSN 0374-4884. doi: 10.3938/jkps.60.1907.
- [227] C H Yang, R C C Leon, J C C Hwang, A Saraiva, T Tanttu, W Huang, J Camirand Lemyre, K W Chan, K Y Tan, F E Hudson, K M Itoh, A Morello, M Pioro-Ladrière, A Laucht, and A S Dzurak. Operation of a silicon quantum processor unit cell above one kelvin. *Nature*, 580(7803):350, 2020. ISSN 0028-0836. doi: 10.1038/s41586-020-2171-6.
- [228] W R Clarke, A P Micolich, A R Hamilton, M Y Simmons, K Muraki, and Y Hirayama. Fabrication of induced two-dimensional hole systems on (311)A GaAs. *Journal of Applied Physics*, 99(2):23707, jan 2006. ISSN 0021-8979. doi: 10.1063/1.2163998. URL <https://doi.org/10.1063/1.2163998>.
- [229] A Srinivasan, D S Miserev, K L Hudson, O Klochan, K Muraki, Y Hirayama, D Reuter, A D Wieck, O P Sushkov, and A R Hamilton. Detection and Control of Spin-Orbit Interactions in a GaAs Hole Quantum Point Contact. *Phys. Rev. Lett.*, 118(14):146801, apr 2017. doi: 10.1103/PhysRevLett.118.146801. URL <https://link.aps.org/doi/10.1103/PhysRevLett.118.146801>.
- [230] L Dicarlo, Y Zhang, D McClure, D Reilly, C Marcus, L Pfeiffer, and K West. Shot-Noise Signatures of 0.7 Structure and Spin in a Quantum Point Contact. *arXiv.org*, 97(3), 2006. ISSN 00319007. doi: 10.1103/PhysRevLett.97.036810.

FOURIER ANALYSIS OF SHUBNIKOV DE HAAS OSCILLATIONS

To extract the effective mass and quantum lifetime from the Shubnikov De Haas oscillations a combination of Fourier analysis and amplitude modulation was used to extract the signal peak in frequency space for fitting.

This appendix covers the details of the methods and calculations used to extract the signal peak, the effective mass, and quantum lifetime. I hope that this may be a useful starting point for others who start to go down the rabbit hole that is signal processing.

A.1 Fourier Transform

A simple but important starting point is the Fourier transform. While most physicists will be very familiar with a Fourier transform, there are multiple definitions and there is the added complication that the digital processing of the signal requires use of the discrete Fourier transform (DFT) to approximate the continuous Fourier transform (CFT).

To avoid confusion, the Fourier transform used is defined as;

$$\mathcal{F}(f) \equiv \int_{-\infty}^{\infty} dt y(t) \exp\{-i2\pi ft\} \quad (\text{A.1})$$

because of the more straight forward mapping to the implementation of the DFT.

To show this mapping. Let's make time and frequency discrete with $t_n = t_0 + n\Delta t$, $f_m = m\Delta f$

and $\Delta t \Delta f = 1/N$. With these definition the CFT can be approximated by the following sum,

$$\mathcal{F}(f_m) \approx \frac{\exp\{-i2\pi/N f_s t_0\}}{f_s} \sum_{n=0}^N y(t_n) \exp\left\{-i \frac{2\pi n}{N} m\right\} \quad (\text{A.2})$$

where $f_s = 1/\Delta t$ is the sampling frequency. The sum in this expression is equivalent to the DFT as implemented using the FFT algorithm, note the pre-factor not only scales the DFT by $1/f_s$ but also adds a constant phase due to the time of the signal not necessarily starting at $t = 0$.

The computation of the DFT was handled by standard libraries which returns an array holding the DFT for frequencies between $-f_s/2$ and $f_s/2$ with a spacing of $\Delta f = f_s/N$. While the maximum frequency that can be sample is set by the Nyquist frequency, f_n , the lowest frequency is set by $\Delta f = 2f_n/N$, therefore increasing the number of points in the DFT increases the frequency resolution. This is important as the typical length of the Shubnikov De Haas oscillation is not long enough to give a fine enough frequency resolutions to fit the signal peak.

A.1.1 Zero-Padding and Windowing

To increase the frequency resolution of the DFT the number of points of the signal must be increased. A common method of doing this is to pad the signal with zeros on the left and right. This increases the length of the signal without the padding changing the DFT as the zeros do not change the sum.

If this seems like we get something for nothing and that this is too good to be true it is. By zero padding the signal is effectively multiplied by a top hat function. Therefore from the convolution theorem the Fourier transform of this padded function with the the Fourier transform of the signal convolved with a sinc function. If the width of the non-padding signal is large enough the sinc function is narrow enough to be approximated by a delta function so there is very little affect of the padding. However generally the convolution with the sinc results in spectral leakage, with the secondary lobes of the sinc function widening the peak in the DFT.

To limit the affect of the spectral bleed, a window function can be applied to signal. The window function multiplies the signal reducing the edges of the signal to zeros so that there is no sharp drop to zero which causes a large amount of spectral bleed. While there are many windows to choice from the 'hann' and 'flattop' window demonstrate the two main reasons for choosing a particular window.

The 'hann' window is one of the most commonly used windowing functions and is defined as:

$$w_0(x) \triangleq \begin{cases} \frac{1}{2} \left(1 + \cos\left(\frac{2\pi x}{L}\right)\right) = \cos^2\left(\frac{\pi x}{L}\right), & |x| \leq L/2 \\ 0, & |x| > L/2 \end{cases} \quad (\text{A.3})$$

The affect of using this window is to smoothly reduce the edges of signal to zero. The hann window is normally a good choice of windowing function if nothing is know about the signal, as it produces a sharp peak at the signal frequency, as the side lobes that cause spectral leakage are sharply reduced.

The flattop window is another common window function and is defined as:

$$w[n] = a_0 - a_1 \cos\left(\frac{2\pi n}{N}\right) + a_2 \cos\left(\frac{4\pi n}{N}\right) - a_3 \cos\left(\frac{6\pi n}{N}\right) + a_4 \cos\left(\frac{8\pi n}{N}\right) \quad (\text{A.4})$$

where the constants a_n vary between from implementation. The affect of the flattop window function produces a wide but flat peak so is very useful for determining the amplitude of the signal if the frequency is know.

It is worth being aware that windowing function change the shape of the signal peak. In the two example here the hann window causes the peak to be shorter but sharper so is useful for locating peaks in the spectrum. While the flattop window results in the peak becoming much wider and flatter at the peak. This is good for measuring the amplitude of the peak but at the loss of accuracy in the frequency of the peak.

A.2 Amplitude Modulation

Amplitude modulation is a branch of signal processing where a signal is encoded in the amplitude of a carrier oscillation, usually with a much higher frequency than the bandwidth of the signal being encoded. The Shubnikov De Haas oscillations can be thought of as an amplitude modulation signal with the envelope function being encoded on a carrier oscillation at frequency $f_{1/B}$.

Therefore the envelope function of the Shubnikov oscillations could be obtain by demodulating the oscillations signal. Amplitude modulation is best understood by considering the action of multiplying a signal of know bandwidth with a oscillation at a known frequency f_c , in the frequency domain. The result will be a convolution of the signal spectrum with the oscillation peak at f_c . Assuming a pure cosine oscillations this result in the signal spectrum being copied to a peak centred at f_c .

Demodulation of the signal is achieved by taking the modulated signal at f_c and multiplying by another signal at a known frequency f_b . This will result in a copies of the frequency at $f_c - f_b$ and $f_b - f_c$ which can then be extracted by applying a bandpass filter at f_b .

It is the amplitude demodulation that is of use for the Shubnikov De Haas oscilltion analysis. By modulating the signal with a cosine oscillation with matching phase and frequency

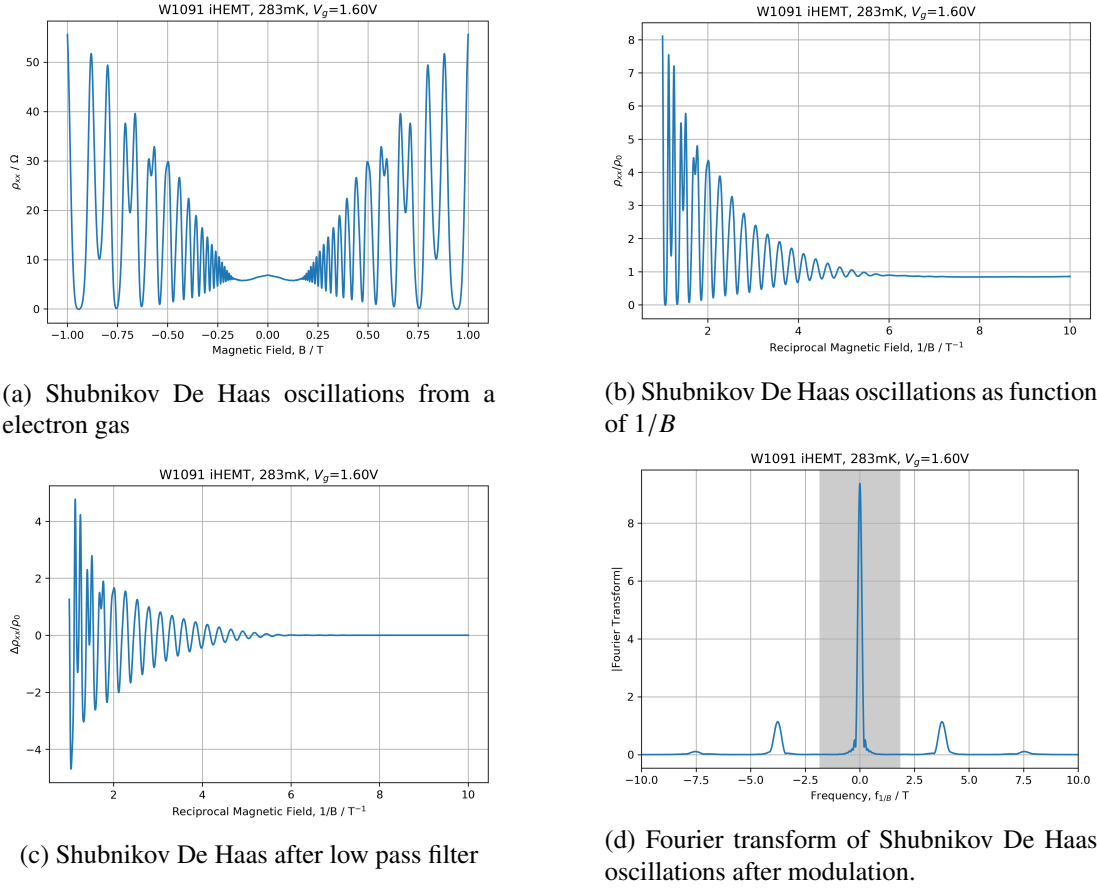


Figure A.1: Shubnikov De Haas oscillations from an electron gas at 283mK. To calculate $\Delta\rho_{xx}/\rho_0$ the signal is converted to a function of $1/B$ and then a high pass filter is used to remove the low frequency components, marked in grey.

a copy of the envelope spectrum will appear at $f = 0$. This can then easily be extracted by applying a lowpass filter.

A.3 Shubnikov De Haas Oscillation Signal

The Shubnikov De Haas oscillations measured over a range of temperatures had a magnetic field range between $\pm 1\text{T}$. The signal could be converted to give ρ_{xx}/ρ_0 as a function of $1/B$ by interpolating the function between $1/B = 1 \rightarrow 10\text{T}^{-1}$. A sampling rate of $f_s = 1000\text{T}$ was used as this gave a nice smooth curve with a resolution of $\Delta(1/B) = 1\text{mT}^{-1}$.

To remove the background from the signal a digital high-pass filter was used with the cutoff frequency set using the bandwidth of the background signal, determined from the Fourier transform of ρ_{xx}/ρ_0 , figure A.1 contains plots showing the result of this procedure.

Based on a sampling rate of 1000T and a range of 9T^{-1} the frequency resolution of the

Fourier transform would be $\approx 0.1T$. This corresponds to between 1-10% of the frequency of the signal based on the Hall coefficient. While this resolution is sufficient to identify the signal peak, it not enough to look at the shape of the signal peak. Therefore zero-padding was used in increase the frequency resolution. It worth noting that at this sampling rate the Nyquist frequency is 500T which is well above the typical frequency of the Shubnikov oscillation which is $<10T$, therefore aliasing is not a problem.

The signal $\Delta\rho_{xx}/\rho_0$ in figure A.1 goes to zero in the limit of low B-field. This makes the end of the signal suitable for zero-padding without the use of a windowing function to limit spectral bleed. However due to the application of a finite B-field, in the high field limit the signal is truncated. Therefore simply zero-padding with cause a large amount of spectral bleeding. As mentioned in A.1.1 window function could be use to limit the impact of spectral bleeding, however this will change the shape of the signal peak. As the aim of this analysis is to extract the quantum lifetime and effective mass from the shape of the signal peak in the spectrum, changing the shape of the peak will impact the extracted parameters. Therefore windowing is not an option to handle the spectral bleed from the truncation of the signal.

To reduce the effect of spectral bleeding without use of a windowing function, the signal was made symmetric in $1/B$ by copying the signal on to the negative domain, figure A.2. At this point the edges of the signal both tend to zero so are ideal for zero-padding without windowing, however the gap in the centre of the signal has to be removed. To remove this gap for $1/|B| < 1/B_{max}$ the largest peak or troughs was taken to be the start of the signal and flipped at this point onto the negative domain. Mathematically this is the same as making the variable substitution $1/B \equiv x \rightarrow |u| + x_0$, where x_0 is the $1/B$ value of the peak or trough. Because the Shubnikov oscillations measured contain odd minimum at sufficiently high magnetic field, in practice the truncation of shifting of the signal described here had to take into account these odd minima, so the peak or trough taken as x_0 was the large peak or trough before the odd minima were observed. The result of this process is a symmetric continuous signal which tends to zero for high $|x| \equiv 1/|B|$ which is suitable for Fourier transforming with zero padding to increase the frequency domain resolution. Because the signal tends to zero at the edges a spectral bleeding from the zero padding should not be an issue so windowing function were not used, so that the changes to the Fourier transform from the window function did not have to be considered. Figure A.2 shows the final signal and its Fourier transform.

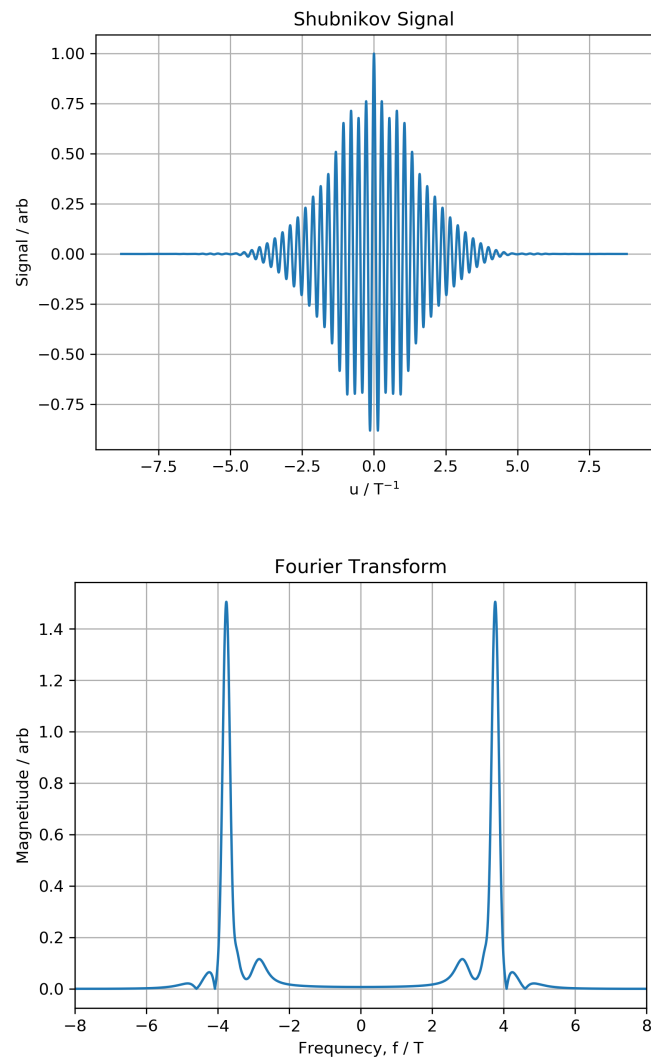


Figure A.2: The final processed symmetric signal from the Shubnikov De Haas oscillations and its Fourier transform.

APPENDIX 

FABRICATION PROCEDURE

The fabrication of induced devices is a little more involved than fabricating a doped device and uses a wider range of fabrication processes to create an ambipolar, double-gated induced device. This appendix provides the detailed steps of all the processes used in the production of the induced device in the thesis. Everything detailed here is specific to the SP clean room at the Cavendish laboratory and the specific equipment used. Unless stated otherwise, all the values quoted should be taken as approximate values with a tolerance of the order 10%.

During the fabrication of an induced device, many of the processing steps are repeated, such as photoresist spinning and patterning and cleaning. These repeat steps are summarised here:

B.1 Sample Cleaning

A full clean for the sample consists of four stages: acetone, IPA, RF ash, and HCL dip. Details are given below:

- Soak in Acetone for 10-20secs, or until chip is clean
- Soak in IPA against for 10-20secs
- Dry with chip with nitrogen
- RF Ash sample for 60s
- 20% HCL Dip for 30s
- Rinse in DI weir until weir runs clean
- Dry chip with N₂

B.2 Photoresist Spinning

- 2 minute bake on the 125°C to dry the chip
- Place chip on spinner set for 5500rpm
- Use nitrogen gun to clear any dust before add resist to chip
- Place S1805 or S1813 on chip, a droplet in each corner of the device (resist age should be < 2 weeks)
- Spin chip at 5500rpm for 60s
- Remove chip from spinner and clean back of chip on acetone wipe to remove resist on back of chip
- Bake chip for 60s at 115°C (If using chlorobenzene bake at 90°C for 120s instead)

B.3 Photoresist Patterning and Development

- Place chip in aligner and bring into firm contact with photomask
- To align pattern and chip use separator to bring chip out of contact with mask and move with micrometers
- Once aligned bring chip into firm contact with mask and expose for 6.5s for S1813 and 3.5s for S1805
- (If using chlorobenzene place chip in chlorobenzene for two minute before removing and drying with N2 gun)
- Develop in MF319 for 60s (S1813) and 30s (S1805).
- Check under microscope to see that pattern has developed, place in MF319 for extra time as needed to completely pattern

B.4 Recessed Ohmics

For induced devices the ohmic contacts are recessed below the surface of the wafer to improve the connection to the carrier gas. Two types of ohmics contacts are used, a layered AuGeNi contacts for N-type contacts and a AuBe alloy for P-type contacts. The precise ohmic recipe varies based on the type of device.

B.4.1 N-type Layered Contact for iHEMTs

For N-type contacts on iHEMTs a layered AuGeNi contacts is used. Because the ohmic is recessed coverage of the ohmic pit's side wall is important. Therefore a rota-tilt at 60° to the normal of the chip surface is used. While the covers the side wall, it also introduces a geometric factors of 1/2 for the thickness deposited on the chip compared to the thickness measured on

the evaporator's crystal. All the thickness here are the values measured on the crystal of the evaporator, therefore the thickness on the chip is 1/2 the value quoted.

The Ni and AuGe are evaporated separately with a 10nm Ni wetting layer, then the AuGe, which is at the eutectic composition 28% by Ge at%, is evaporate. Finally a 120nm Ni cap is evaporated to cap the contact.

- Mix $\text{H}_3\text{PO}_4:\text{H}_2\text{O}:\text{H}_2\text{O}_2$ - 1:20:1 etchant.
- Pattern chip and calibration chip (at least 3mm wide so can be spun easily) with S1813
- After pattern has been developed 60s RF de-scum
- Detak calibration chip to get thickness of the resist, should be $>11\text{k}\text{\AA}$.
- Etch calibration chip for 100s.
- Detak calibration chip again and calculate etch rate, should be $2.5\text{-}3.2\text{nm}\text{s}^{-1}$ depending on mixture, time, wafer contents etc.
- Before etching device chip measure 28nm of Ge and 220mg of Au for evaporator, approximately the eutectic composition for 150-200nm
- Etch device chip for required time for 300nm deep ohmic pit
- Follow etch by DI clean and 30 HCL Dip.
- Load device chip straight into evaporator with 60° rotatilt and load Ni and AuGe. Take care with Ni to tight pack Ni into ceramic boat.
- Pump layered ohmics evaporator for 2 hours for pressure to reach low 10^{-6}mBar / high 10^{-7}mBar .
- Evaporate 10nm Ni, warming the ceramic boat lowly to maximise lifetime of boat
- Evaporate AuGe Mixture, used $0.05\text{nm}\text{s}^{-1}$ rate steps every 10nm e.g. 0-10nm at $0.05\text{nm}\text{s}^{-1}$ 10-20nm at $0.1\text{nm}\text{s}^{-1}$ until a max rate of $0.3\text{nm}\text{s}^{-1}$ at $\geq 50\text{nm}$. Thickness so be between 120nm and 200nm in thickness.
- Leave evaporator to cool for at least 30 mins
- Evaporator 120nm Ni. Again warming and cooling ceramic boat slowly. Maximum rate of $\sim 0.1\text{nm}\text{s}^{-1}$ achievable in Ni boats.
- Remove chip and liftoff in acetone. Take care that metal between ohmic teeth lifts off.
- Anneal contacts using AuGeNi Deepy recipe in RTS600 470C for 1 mins, figure B.1

B.4.2 P-type Contact iHHMT

A AuBe alloy 20% Be by weight is used for the P-type contacts. Due to limitation in the amount of material that can be placed in the P-type evaporator the depth of the etch is 250nm with a target of 200-250nm of AuBe evaporator on the crystal monitor. In this way the AuBe evaporation mirrors the layered AuGeNi contact.

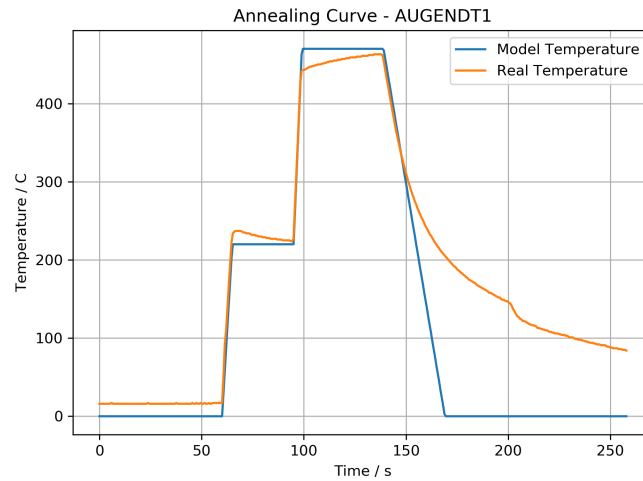


Figure B.1: Output from RTS600 annealing when running AuGeNi Deepy recipe for n-type contacts

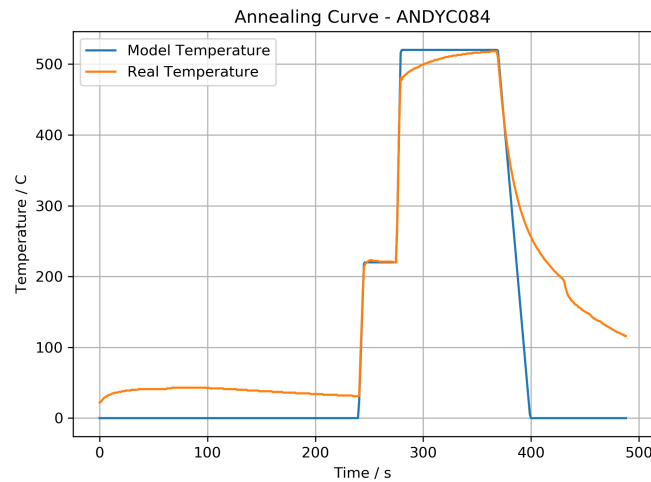


Figure B.2: Output from RTS600 annealing when running AndyC recipe for p-type contacts

- Outgas AuBe evaporator twice, pressure when 'hot' ideally $< 1 \times 10^{-6} mBar$ should be low $10^{-6} mBar$.
- Mix $H_3PO_4:H_2O:H_2O_2$ - 1:20:1 etchant.
- Pattern chip and calibration chip (at least 3mm wide so can be spun easily) with S1813
- After pattern has been developed 60s RF descum
- Detak calibration chip to get thickness of the resist, should be $> 11k\text{\AA}$.
- Etch calibration chip for 100s.
- Detak calibration chip again and calculate etch rate, should be $2.5-3.2nm s^{-1}$ depending on mixture, time, wafer contents etc.
- Before etching device chip, load AuBu into evaporator. Get about 0.8nm per mg.

- Etch device to depth of 250nm
- Follow etch by DI clean and 30 HCL Dip.
- Load into evaporator with rotatilt at 45° (I don't know why but 45° works and 60° doesn't.... It shouldn't make a difference but it did early 2018... Feel free to check)
- Pump for 1-2 hours
- Remove chip and liftoff in acetone. Take care that metal between ohmic teeth lifts off.
- Anneal contacts using ANDYC recipe in RTS600 470C for 1 mins 30s, figure B.2

B.5 Undoped Hall Bars

The follows are the steps to produce an undoped hall bar. There are mask patterns for single gated and double gate devices, but the first three stages are the same. As the MF319 developer used for S1805 and S1813 etched Al_2O_3 when patterning Al_2O_3 surface a double layer PMMA process is used

- MESA etch, 500nm using $\text{H}_3\text{PO}_4:\text{H}_2\text{O}:\text{H}_2\text{O}_2$, 1:20:1 approx 3 nms^{-1} etch rate
- Deposition recessed ohmics and anneal. If ambipolar deposition p-type first, anneal then repeat for n-type
- Deposit 60-65nm Al_2O_3 using 470 cycles of static Al_2O_3 process in Anric AT400 system
- if double gated, extra stages to pattern central gate
 - HF etch of Al_2O_3
 - * Spin S1813 and bake for 2mins 115C
 - * Pattern with windows to etch away Al_2O_3
 - * Etch using BHF for 60s and check ohmics are clean
 - Double layer PMMA
 - * Spin PMMA 495K A7 neat at 4000rpm for 60s
 - * bake for 20min at 150C in oven
 - * Spin PMMA 495K A7 neat at 4000rpm for 60s
 - * bake for 20min at 150C in oven
 - * Spin S1805 and pattern with central gate and bond pads
 - * After development of S1805 expose PMMA in UV O-zone cleaner for 35mins
 - * Develop PMMA using MIBK:MIK:IPA 1:5:15, 10s followed by 60s in IPA
 - * blow dry with N_2
 - Central Gate and Bond pads - deposit Ti 10nm and 50nm Au and liftoff acetone and IPA
 - Deposit 40nm Al_2O_3 using 310 cycles of static Al_2O_3 process in Anric AT400 system
- HF etch of Al_2O_3
 - Spin S1813 and bake for 2mins 115C
 - Pattern with windows to etch away Al_2O_3
 - Etch using BHF for 60s and check ohmics are clean
- Double layer PMMA
 - Spin PMMA 495K A7 neat at 4000rpm for 60s
 - bake for 20min at 150C in oven

- Spin PMMA 495K A7 neat at 4000rpm for 60s
- bake for 20min at 150C in oven
- Spin S1805 and pattern with central gate and bond pads
- After development of S1805 expose PMMA in UV O-zone cleaner for 35mins
- Develop PMMA using MIBK:MIK:IPA 1:5:15, 10s followed by 60s in IPA
- blow dry with N₂
- Deposit Top gate and bond pads, 20nm Ti and 120nm Au
- Liftoff in Acetone and IPA
- Cleave, package and bond devices

B.6 *iQPCs and iQDs*

Fabrication of *iQPCs* and *iQDs* is very similar to the fabrication of undoped Hall bars by with an extra e-beam and optical gate stages.

- MESA etch, 500nm using H₃PO₄:H₂O:H₂O₂, 1:20:1 approx 3 nms⁻¹ etch rate
- Deposition recessed ohmics and anneal. If ambipolar deposition p-type first, anneal then repeat for n-type
- E-beam Lithography
 - Clean samples with 60s RF ash followed by 30s HCL dip
 - Prebake, 5min, 125celsius
 - Spin 4000 rpm PMMA 100K A6 1:1 Anisole, 60s
 - Bake 150celsius 30mins
 - Spin (start spinning within less than 3s) 6000-8000 rpm 950K A11 1:5 MIBK
 - Bake at 115celsius for 5mins
 - submitted chip for e-beam patterning
 - Develop in IPA:MIBK:MEK (15:5:1) for 6-8s, rinse in IPA for 1min, dry
 - Check if developed, RF ash 25s, wash with HCl
- Deposit 10nm of Ti and 25nm of Au
- Long liftoff in Acetone (overnight) followed by IPA
- Optical gates
 - Clean samples with 60s RF ash followed by 30s HCL dip
 - Prebake, 5min, 125celsius
 - Spin LOR5b 5000rpm for 60s
 - Bake 180 °C for 10mins

- Spin S1805 and pattern with optical gates
 - develop for 1min in MF319 and check for visible undercut from LOR
- Deposit Ti 10nm and 50nm Au
- Liftoff in SVC14 60°C followed by acetone and IPA
- Deposit 60-65nm Al₂O₃ using 470 cycles of static Al₂O₃ process in Anric AT400 system
- HF etch of Al₂O₃
 - Spin S1813 and bake for 2mins 115C
 - Pattern with windows to etch away Al₂O₃
 - Etch using BHF for 60s and check ohmics are clean
- Double layer PMMA
 - Spin PMMA 495K A7 neat at 4000rpm for 60s
 - bake for 20min at 150C in oven
 - Spin PMMA 495K A7 neat at 4000rpm for 60s
 - bake for 20min at 150C in oven
 - Spin S1805 and pattern with central gate and bond pads
 - After development of S1805 expose PMMA in UV O-zone cleaner for 35mins
 - Develop PMMA using MIBK:MIK:IPA 1:5:15, 10s followed by 60s in IPA
 - blow dry with N₂
- Deposit Top gate and bond pads, 20nm Ti and 120nm Au
- Liftoff in Acetone and IPA
- Cleave, package and bond devices using wedge bonder for ESD safety

PARAMETER UNCERTAINTIES ESTIMATED FROM χ^2

The fitting of the scattering rate model centres around the minimisation of the objective function χ^2 . While finding the parameters that minimise χ^2 is relatively straight forward, if time consuming, estimating the uncertainties in this parameters is less obvious. This appendix details the mathematics used to generate estimate in the parameter uncertainties once a minimum has be found.

C.1 Find region about minimum that corresponds to a confidence interval

The probability distribution χ^2 is the distribution of the sum of the squared of k independence standard normal random variables. The definition of the objective function is,

$$\chi^2 \equiv \sum_{i=0}^N \left(\frac{y_i - y(\mathbf{p}, x_i)}{\sigma_i} \right)^2 \quad (\text{C.1})$$

where the experimental data \mathbf{y} and \mathbf{x} have an error of σ and are modelled by the function $y(\mathbf{p}, x)$ given a set of parameters \mathbf{p} . Assuming a global minima χ_0^2 exists, then the region about this minima is describe by the relationship,

$$\Delta\chi^2 \equiv \chi^2 - \chi_0^2 = \sum_{i=0}^N \left(\frac{y_i - y(\mathbf{p}, x_i)}{\sigma_i} \right)^2 - \chi_0^2 \quad (\text{C.2})$$

As all values of χ^2 are positive by definition, if χ_0^2 is truly the global minima then the function $\Delta\chi^2$ will range from 0 to infinity. From this definition, providing that the experimental data

points are independent and normally distributed, usually a safe assumption for experimental data, the distribution of $\Delta\chi^2$ will be described by the probability distribution χ^2 with degrees of freedom N - number of parameters, hence the name.

This is useful for finding the region about the minimum that corresponds to a confidence interval, as from the CDF of the χ^2 defined as,

$$CDF(x; k) = \frac{\gamma\left(\frac{k}{2}, \frac{x}{2}\right)}{\Gamma\left(\frac{k}{2}\right)} \equiv P\left(\frac{k}{2}, \frac{x}{2}\right) \quad (C.3)$$

the value of x for a given confidence interval can be calculated. Defining p as the confidence interval, e.g. 90%, 95%, the value of x is defined by the equation,

$$1 - p = 1 - P\left(\frac{k}{2}, \frac{x}{2}\right) = \frac{\Gamma\left(\frac{k}{2}, \frac{x}{2}\right)}{\Gamma\left(\frac{k}{2}\right)} \equiv Q\left(\frac{k}{2}, \frac{x}{2}\right) \quad (C.4)$$

This equation can be solve numerical using standard root finding functions. The value of x that solves this equation is the maximum value that $\Delta\chi^2$ can taken and still be within a parameter space region with a confidence interval of p . Therefore, the region is defined by the equation,

$$\Delta\chi^2 = \sum_{i=0}^N \left(\frac{y_i - y(\mathbf{p}, x_i)}{\sigma_i} \right)^2 - \chi_0^2 \leq x \quad (C.5)$$

From the Taylor expansion of the of the objective function χ^2 about the point χ_0^2 ,

$$\chi^2 \approx \chi_0^2 + \mathbf{p} \cdot \nabla\chi^2 + \frac{1}{2}\mathbf{p} \cdot \nabla\nabla\chi^2 \cdot \mathbf{p} + \dots \quad (C.6)$$

Working to second order and assuming that the first derivatives are small as χ_0^2 is a minimum, the Taylor expansion combine with the equation that defined the region of interest give the following relationship,

$$2\Delta\chi^2 \approx \begin{pmatrix} p_1 & \dots & p_n \end{pmatrix} \begin{pmatrix} \frac{\partial^2\chi^2}{\partial p_1\partial p_1} & \dots & \frac{\partial^2\chi^2}{\partial p_1\partial p_n} \\ \vdots & \ddots & \vdots \\ \frac{\partial^2\chi^2}{\partial p_n\partial p_1} & \dots & \frac{\partial^2\chi^2}{\partial p_n\partial p_n} \end{pmatrix} \begin{pmatrix} p_1 \\ \vdots \\ p_n \end{pmatrix} = x \quad (C.7)$$

here define the parameter vector $\mathbf{p} \equiv (p_1 \ \dots \ p_n)$ and the matrix of mixed derivative as \mathbf{H}

This equation describes an n th dimensional surface equivalent to a conic section. In 2D and 3D the surfaces would be an ellipse or ellipsoid. Note that here were are assuming a close surface as this would make sense in the context of confidence interval, but the equation does allow for the equivalent of n th dimensional hyperbola.

This equation is most easily understood by considering the eigenvalue decomposition,

$$2\Delta\chi^2 = \mathbf{p} \cdot \mathbf{H} \cdot \mathbf{p} = \mathbf{p} \cdot \mathbf{R}\mathbf{\Lambda}\mathbf{R}^{-1} \cdot \mathbf{p} \equiv \mathbf{q} \cdot \mathbf{\Lambda} \cdot \mathbf{q} = \sum_i \Lambda_{ii} q_i^2 \quad (C.8)$$

where the principle axis of the ellipsoid are given by $\mathbf{R}^{-1} \cdot \mathbf{p}$. Putting this relationship in the standard form for an ellipsoid,

$$\sum_i \frac{\Lambda_{ii}}{2\Delta\chi^2(p)} q_i^2 = 1 \quad (\text{C.9})$$

it can be seen that the length of the principle axes are proportional to the size of $\Delta\chi^2$, as $a_i = 2\Delta\chi^2(p)/\Lambda_{ii}$. Therefore to find the region corresponding to a confidence interval p about a minimum χ_0^2 the Hessian matrix, \mathbf{H} must be evaluated at the position of the minimum. This is done numerically using finite difference methods. With the Hessian matrix and the value of $\Delta\chi^2$ calculated given the value of p the principle axes of the ellipsoid can be calculated from the eigenvalues of the Hessian matrix.

It was noted earlier that only closed surfaces make sense of a confidence interval, but that mathematically hyperbola surface are allowed. These surface can quickly be checked for by checking for sign difference in the eigenvalues of the Hessian matrix. If there is a sign difference that correspond to at least one hyperbola solution in one of the principle axes. This suggests that the found minimum is not a global minimum.

At this point it looks like the problem is solve and the confidence interval has been found, however this is not quite the case. The ellipsoid defined here generally will be rotate with respect to the parameter space axes. While the ellipsoid does describe the confidence region to estimate the uncertainties in the parameters the ellipsoid is of less interest than the bounding cube that encloses the ellipsoid. The bounding box of the ellipsoid describes the range of value each individual parameter can take in the region and therefore is a better description of the uncertainty in each parameter. The follow section outline how the bound box of an n dimensional ellipsoid is found.

C.2 Bounding Box of N Dimensional ellipsoid

To find the bounding box of an N dimensional ellipsoid is a relatively straight forward calculation. In 2D and 3D this calculations can be done by hand but quickly become long a tedious. Here, the number of dimensions can change depending on the number of parameters being used in the fit. Rather than having to compute by hand the relationship between the principle axes and the bound box size for dimension a more general solution would be very useful. Such a solution makes use of the mathematics of quadric hypersurfaces. To illustrate the mathematics here, the bounding box of an ellipsoid will be calculated, but this method generalises relatively simply.

Starting with a unit sphere defined by $x^2 + y^2 + z^2 = 1$, the quadric representation of this

sphere is to solutions to a 4D quadratic defined by,

$$\mathbf{p}^T \mathbf{S} \mathbf{p} = 0 \quad (\text{C.10})$$

where the point \mathbf{p} in 4D space is $\mathbf{p} = [x, y, z, 1]^T$ and the matrix \mathbf{S} is,

$$\mathbf{S} = \begin{pmatrix} 1 & 0 & 0 & 0 \\ 0 & 1 & 0 & 0 \\ 0 & 0 & 1 & 0 \\ 0 & 0 & 0 & -1 \end{pmatrix} \quad (\text{C.11})$$

to generalise this to any N dimensional ellipsoid the transformation matrix \mathbf{M} is introduced which maps the unit sphere to the ellipsoid in question,

$$(\mathbf{M}^{-1} \mathbf{p})^T \mathbf{S} (\mathbf{M}^{-1} \mathbf{p}) = \mathbf{p}^T (\mathbf{M}^{-T} \mathbf{S} \mathbf{M}^{-1}) \mathbf{p} = 0 \quad (\text{C.12})$$

therefore the general ellipsoid is described by $\mathbf{p}^T \mathbf{Q} \mathbf{p} = 0$, where $\mathbf{Q} \equiv \mathbf{M}^{-T} \mathbf{S} \mathbf{M}^{-1}$.

In this representation a plane can be described by a vector \mathbf{u} such that $\mathbf{u} \cdot \mathbf{p} = 0$ e.g. $\mathbf{u} = [1, 1, 1, 0]$, $\mathbf{u} \cdot \mathbf{p} = x + y + z = 0$. To find the tangent plane the vector \mathbf{u} must both intersect the surface defined by $\mathbf{p} \cdot \mathbf{Q} \cdot \mathbf{p} = 0$ at a single point only. For the plane to intersect the surface it must solve $\mathbf{u} \cdot \mathbf{p} = 0$ and satisfy $\mathbf{p} \cdot \mathbf{Q} \cdot \mathbf{p} = 0$ simultaneously. One such solution is $\mathbf{u} = \mathbf{p}^T \mathbf{Q}$ with the intersection point at \mathbf{p} . The intersection can be shown to be unique by considering $\mathbf{q} = \mathbf{p} + \mathbf{r}$ and showing that $\mathbf{r} = 0$ in order for both \mathbf{q} and \mathbf{p} to lie on the surface.

With the plane $\mathbf{u} = \mathbf{Q} \cdot \mathbf{p}$ found a more useful relation for the planes is $\mathbf{u}^T \cdot \mathbf{Q}^{-1} \cdot \mathbf{u} = 0$. The plane perpendicular to x is given by $\mathbf{u} = [1, 0, 0, -x]$ most easily seen by considering the unit sphere, as $\mathbf{u} \cdot \mathbf{p} = [1, 0, 0, -x] \cdot [x, y, z, 1] = 0$ and with $\mathbf{p} = \mathbf{Q}^{-1} \mathbf{u} = [1, 0, 0, x]$ the point of intersection is $\mathbf{p} \cdot \mathbf{Q} \cdot \mathbf{p} = 1 - x^2 = 0$, hence $x = \pm 1$.

For a general ellipsoid, defining $\mathbf{R} \equiv \mathbf{Q}^{-1}$ the equation for the x tangent plane is,

$$\begin{aligned}
\mathbf{u}^T \mathbf{R} \mathbf{u} &= \begin{bmatrix} 1 & 0 & 0 & -x \end{bmatrix} \mathbf{R} \begin{bmatrix} 1 \\ 0 \\ 0 \\ -x \end{bmatrix} \\
&= \begin{bmatrix} 1 & 0 & 0 & -x \end{bmatrix} \begin{bmatrix} \mathbf{R}_{1,1} - \mathbf{R}_{1,4} x \\ \mathbf{R}_{2,1} - \mathbf{R}_{2,4} x \\ \mathbf{R}_{3,1} - \mathbf{R}_{3,4} x \\ \mathbf{R}_{4,1} - \mathbf{R}_{4,4} x \end{bmatrix} \\
&= \mathbf{R}_{4,4} x^2 - (\mathbf{R}_{1,4} + \mathbf{R}_{4,1}) x + \mathbf{R}_{1,1} \\
&= \mathbf{R}_{4,4} x^2 - 2 \mathbf{R}_{1,4} x + \mathbf{R}_{1,1} \\
&= 0. \\
x &= \frac{\mathbf{R}_{1,4} \pm \sqrt{\mathbf{R}_{1,4}^2 - \mathbf{R}_{1,1} \mathbf{R}_{4,4}}}{\mathbf{R}_{4,4}}.
\end{aligned}$$

with similar solutions for y and z . To generalise this relation to the N dimensional ellipsoid from the fitting problem, consider the equation defining the ellipsoid.

$$2\Delta\chi^2 = \mathbf{p} \cdot \mathbf{H} \cdot \mathbf{p} \quad (\text{C.13})$$

Therefore the matrix \mathbf{Q} for this matrix is,

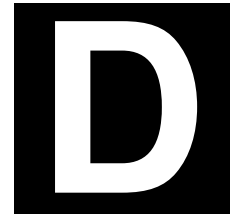
$$\mathbf{Q} = \begin{pmatrix} \mathbf{H} & \mathbf{0} \\ \mathbf{0} & -2\Delta\chi^2 \end{pmatrix} \quad (\text{C.14})$$

and therefore the matrix \mathbf{R} is:

$$\mathbf{R} \equiv \mathbf{Q}^{-1} = \begin{pmatrix} \mathbf{H}^{-1} & \mathbf{0} \\ \mathbf{0} & -\frac{1}{2\Delta\chi^2} \end{pmatrix} \quad (\text{C.15})$$

Therefore noting that $R_{i4} = 0$ unless $i = 4$ the relationship for the bound box sides reduces to,

$$x_i = \pm \sqrt{2R_{i,i}\Delta\chi^2} = \pm \sqrt{2H_{i,i}\Delta\chi^2} \quad (\text{C.16})$$



EXAMPLE SCATTERING RATE MODELLING INPUT FILE

This appendix contains an example input file for the scattering rate model calculated in python. It is included here for future reference for the syntax of the input file.

```
"""
Python script to fit the experimental data from W1088 a 100nm
AsII iHEMT and W1089 a 50nm AsII iHEMT
"""
# Imports
import sys
import os.path
import numpy as np
import logging
sys.path.append('..')

# Import
from cryomeas import stdassess
from twodesmobility import Devices
from twodesmobility import CrossValidation
from twodesmobility import MobilityIO as mio
from twodesmobility import PhysicalConstants as pc
```

```

#
#####

# Set options
#
#####

# Experimental data file
exp_directory = [
    './ data/W1088_Device_4/' ,
    './ data/W1089_Device_1/'
]

# Output files
data_directory = './ data/W1088_and_W1089/'
plot_directory = './ Plots/W1088_and_W1089/'
file_root = 'W1088-W1089-Numba'

# Wave function
wf = Devices.WaveFunction.FANGHOWARD

# Scattering types
st = \
    (
        ( # W1088 Device 4 - Common background, surface
          charge and interface roughness
          (Devices.ScatteringType.SURFACECHARGE, (-110 * pc.
            nm2a0,)),
          (Devices.ScatteringType.IMPURITYDOPANTS, (-110 *
            pc.nm2a0, 1000 * pc.nm2a0)),
          (Devices.ScatteringType.INTERFACEROUGHNESS,)
        ),
        ( # W1089 Device 1 - Common background, surface
          charge and interface roughness
          (Devices.ScatteringType.SURFACECHARGE, (-60 * pc.
            nm2a0,)),
    )

```

```

        (Devices.ScatteringType.IMPURITYDOPANTS, (-60 * pc
            .nm2a0, 1000 * pc.nm2a0)),
        (Devices.ScatteringType.INTERFACEROUGHNESS,)
    )
)

# Fitting index
fit_dictionary = \
    (
        { # W1088 Device 4 - Common interface parameters
            (Devices.ScatteringType.SURFACECHARGE, 0): 0,
            (Devices.ScatteringType.IMPURITYDOPANTS, 0): 1,
            (Devices.ScatteringType.INTERFACEROUGHNESS, 0):
                (2, 3)
        },
        { # W1089 Device 1 - Common interface parameters
            (Devices.ScatteringType.SURFACECHARGE, 0): 0,
            (Devices.ScatteringType.IMPURITYDOPANTS, 0): 1,
            (Devices.ScatteringType.INTERFACEROUGHNESS, 0):
                (2, 3)
        }
    )

# Common fit dictionary holding all parameter for outputting
# fitted parameter
common_fit_dictionary = {
    (Devices.ScatteringType.SURFACECHARGE, 0): 0,
    (Devices.ScatteringType.IMPURITYDOPANTS, 0): 1,
    (Devices.ScatteringType.INTERFACEROUGHNESS, 0): (2, 3)
}

# Fit parameter intial guess
x0 = [1e10 * pc.cm2a0, 1e20 * pc.m3a0, 0.1 * pc.nm2a0, 10 * pc
    .nm2a0]
low_bnds = [1e8 * pc.cm2a0, 1e19 * pc.m3a0, 0.01 * pc.nm2a0,
    0.1 * pc.nm2a0]

```

```
upp_bnds = [1e12 * pc.cm2a0, 1e21 * pc.m3a0, 1 * pc.nm2a0, 100
            * pc.nm2a0]
```

```
# K-fold parameter
```

```
k_fold = True
```

```
foldes = 5
```

```
runs = 1
```

```
#
```

```
#####
```

```
# Create directories if not there
```

```
#
```

```
#####
```

```
for d in [data_directory , plot_directory]:
```

```
    if not os.path.exists(d):
```

```
        os.mkdir(d)
```

```
#
```

```
#####
```

```
# Setup logging
```

```
#
```

```
#####
```

```
# Create logger
```

```
logging.basicConfig(level=logging.INFO, format='% (message)s')
```

```
logger = logging.getLogger('Fitting_Log')
```

```
# create a file handler
```

```
handler = logging.FileHandler(data_directory + file_root + '.log', 'w')
```

```
    log', 'w')
```

```
handler.setLevel(logging.INFO)
```

```
# add the handlers to the logger
```

```

logger.addHandler(handler)

#
#####

# Data loading and device creation
#
#####

# Read in data from data file
data = []
for e in exp_directory:
    logger.info('Loading Data File: {}'.format(e + e.split(
        '/')[-2] + '.dat'))

    # Look for Data file and create if missing
    if not os.path.exists(e + e.split('/')[2] + '.dat'):
        stdassess.createModellingDataFile(e + 'Cryomeas/',
            filename=e + e.split(
                '/')[-2] + '.dat
                ')

    # Read in data from data file
    data.append(mio.readMobilityTxtFile(e + e.split('/')[2] +
        '.dat'))

# Create device
logger.info('Creating devices')
devices = []
for i in range(2):
    devices.append(Devices.Heterostructure(wf))

# Set carrier density
devices[-1].setCarrierDensity(data[i][:, 0])

# Set experimental data

```

```

devices[-1].setExperimentalData(data[i][:, 1], data[i][:,
    2])

# Set scattering
for s in st[i]:
    if len(s) > 1:
        devices[-1].setScatteringType(s[0], *s[1])
    else:
        devices[-1].setScatteringType(s[0])

# Intialise device
logger.info('Calculating_scattering_rate_integrals')
for i, d in enumerate(devices):
    logger.info('Device_' + str(i + 1) + '_of_' + str(len(
        devices)))
    d.calScatteringIntegrals(verbose=True)
    print()

#
#####

# Fitting
#
#####

logger.info('Fitting_experimental_data')
# Set parameter for fitting
for i, d in enumerate(devices):
    d.setParameterDictionary(fit_dictionary[i])

# Intialise experimental data
d.intialiseExperimentalData()

# Run fitting
if k_fold:
    parameters, parameter_errors, chi_sq_values = \

```

```

        CrossValidation.kfoldDevices(devices , x0, (low_bnds ,
            upp_bnds), folds , runs , logger)

    p, p_err = CrossValidation.averageParameterByChiSq(
        parameters , chi_sq_values)
else :
    p, p_err = CrossValidation.fitDevices(devices , x0, (
        low_bnds , upp_bnds))
print()

# Output parameter to log
mio.writeParametersToTerminal(p, p_err , common_fit_dictionary ,
    logger)
print()

#
#####

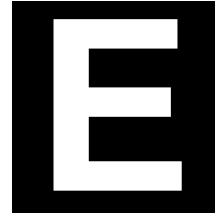
# Generate fit parameter
#
#####

logger.info('Generate_fitted_curves')
for i, d in enumerate(devices):
    logger.info('Device_' + str(i + 1) + '_of_' + str(len(
        devices)))
    d.setFittedParameters(p)
    mio.genFittedMobilityPlot(p, d, plot_directory + '-' .join(
        exp_directory[i].split('/')[ -2].split('_')) + '-Fit')
    mio.mobilityTextFile(d, data_directory + '-' .join(
        exp_directory[i].split('/')[ -2].split('_')) + '-Fit')
    print()

if k_fold:
    logger.info('Writing_parameter_files')

```

```
mio.writeOptimisationFile(data_directory + file_root + '-  
Fit-Parameters',  
                           parameters, parameter_errors,  
                           chi_sq_values,  
                           common_fit_dictionary)  
mio.genParameterPlot(parameters, common_fit_dictionary,  
plot_directory + file_root + '-Fit-Parameters')
```



NEXTNANO INPUT FILE FOR UNDOPED STRUCTURES

Nextnano has been used extensively throughout this thesis to calculate the band structure and wave function of undoped devices to assist the understanding of the behaviour of the devices. Included here is an example input file for nextnano, used to calculate the bandstructure in an undoped AlGaAs/GaAs heterostructure.

```
#-----  
# Nextnano simulation of a doped hemt  
# Within the AlGaAs/GaAs system  
#-----  
# Structure Parameters  
$ALLOY = 0.33      # Fraction of Al in  
$CAP = 10         # GaAs Cap thickness in nm  
$SPACE_ALGAAS = 100 # Spacer AlGaAs layer thickness in nm  
$BUFFER_GAAS = 1000 # GaAs Buffer thickness in nm  
$DOPANTS = 00e14  # Dopant density per cm-3  
  
# Physical parameters  
$BARRIER = 0.7   # GaAs Surface Barrier in eV  
$BIAS = 0.5       # Bias of surface gate in V  
$TEMPERATURE = 1.2 # Temperature in K  
  
# Nextnano parameters
```

```

$NUMEV = 10          # Number of eigen values to solve for
$QZSTART = -20 # Distance from interface at z = 0 to start
                  quantum region
$QZSTOP = 100       # Distance from interface at z = 0 to
                  stop quantum region
$QGRID = 0.1        # Quantum grid step size

# Output parameters
$EV_OUT = 5         # Number of eigenstates to output
$OUTPUT = "X:\nextnano\Output\iHEMT-Gate-Sweep" # Output
                  directory

#-----
# Global
#-----
global{
    simulate1D{ }

    temperature = $TEMPERATURE

    substrate{ name = "GaAs" }

    crystal_zb{ x_hkl = [1, 0, 0] y_hkl = [0, 1, 0] }
}

#-----
# Grid - Variable sized grid with
# z = 0 at interface
#-----
grid{
    xgrid{
        # Max and min position
        min_pos = -$CAP - $SPACE_ALGAAS- 1
        max_pos = $BUFFER_GAAS + 1

        # Define variable grid

```

```

line{ pos = - $CAP - $SPACE_ALGAAS - 1 spacing = 1 } #
    Region for top contacts
line{ pos = - $CAP - $SPACE_ALGAAS spacing = 1 } # End
    of top contact spacing

line{ pos = - $CAP - $SPACE_ALGAAS spacing = 5} #
    Region of cap and spacer layer
line{ pos = $QZSTART spacing = 5} # End of this spacing

line{ pos = $QZSTART spacing = $QGRID } # Quantum region
line{ pos = $QZSTOP spacing = $QGRID} # Quantum region

line{ pos = $QZSTOP spacing = 10 } # Start of Buffer
    spacing
line{ pos = $BUFFER_GAAS spacing = 10 } # End of buffer
    spacing

line{ pos = $BUFFER_GAAS spacing = 0.5 } # Start of back
    contact
line{ pos = $BUFFER_GAAS + 1 spacing = 0.5 } # End of
    back contact
}
}

#-----
# Dopants - Fully ionized Si
#-----
impurities{
    donor{ name = "Si" energy = -10 degeneracy = 2 } # fully
        ionized
}

#-----
# Contacts
#-----
contacts{

```

```

schottky{
    name = "Gate"
    bias = $BIAS
    barrier = $BARRIER
}

fermi{
    name = "Interface"
    bias = 0
}

charge_neutral{
    name = "Backgate"
    bias = 0
}
}

#-----
# Structure
#-----
structure{
    output_material_index{}
    output_contact_index{}
    output_impurities{}

# Default
    region{
        everywhere{} # default material
        binary{ name = "GaAs" }
    }

# Top contact
    region{
        line{ x = [ -$CAP - $SPACE_ALGAAS - 1, -$CAP -
            $SPACE_ALGAAS ] }
        binary{ name = "GaAs" }
    }
}

```

```

    contact{ name = "Gate" }
}

# GaAs cap
region{
  line{ x = [ -$CAP - $SPACE_ALGAAS, - $SPACE_ALGAAS] }
  binary{ name = "GaAs" }
}

# Spacer layer
region{
  line{ x = [ -$SPACE_ALGAAS, -$QGRID] }
  ternary_constant{ name = "Al(x)Ga(1-x)As" alloy_x =
    $ALLOY }
}

region{
  line{ x = [-$QGRID, $QGRID] }
  binary{ name = "GaAs" }
  contact{ name = "Interface" }
}

# GaAs substrate
region{
  line{ x = [$QGRID, $BUFFER_GAAS] }
  binary{ name = "GaAs" }
}

# Back gate (ohmic contact)
region{
  line{ x = [$BUFFER_GAAS , $BUFFER_GAAS + 1] }
  contact{ name = "Backgate" }
}
}

#-----

```

```
# Simulation
```

```
#-----
```

```
classical{
```

```
  Gamma{}
```

```
  HH{}
```

```
  LH{}
```

```
  SO{}
```

```
  output_bandedges{}
```

```
  output_carrier_densities{}
```

```
}
```

```
quantum {
```

```
  region{
```

```
    name = "2DEG"
```

```
    x = [$QZSTART, $QZSTOP]
```

```
    Gamma{
```

```
      num_ev = $NUMEV
```

```
      dispersion{
```

```
        lines{ name = 'lines' spacing = 0.01 k_max = 1 }
```

```
        output_dispersions{max_num = 5}
```

```
        output_masses{max_num = 5}
```

```
      }
```

```
    }
```

```
    output_wavefunctions{ probabilities = yes amplitudes =
```

```
      yes max_num = $EV_OUT }
```

```
  }
```

```
}
```

```
poisson{
```

```
  output_potential{}
```

```
}
```

```
currents {
  output_fermi_levels {}
}

#-----
# Output and Run
#-----

run {
  solve_current_poisson {}
  solve_quantum {}
  outer_iteration {
    output_log = yes
    alpha_fermi = 0.4
  }
}
```

